EXPERIMENTAL INVESTIGATIONS OF FLUID – STRUCTURE INTERACTION OF BLUFF BODIES SUBJECTED TO A CROSS-FLOW

Wang Zhi-Jin

A thesis submitted for Degree of
Doctor of Philosophy in Mechanical Engineering
at The Hong Kong Polytechnic University

Hong Kong 2002

I hereby certify that the work embodied in this thesis is the result of original research and has not been submitted for a higher degree to any other University or Institution.

(Signed).....

Acknowledgement

I would like to express my deep gratitude to my supervisor, Dr. Y. Zhou for his many ideas and insights that have had such a strong influence on this thesis. His precise manner and diligence impress me very much, and it will benefit me in my future career. I would also like to express my gratitude to Professor R. M. C. So, my co-supervisor, for many useful suggestions and counsels. I thank them for giving me the opportunity to learn so much at The Hong Kong Polytechnic University, and giving me encouragement and support throughout the duration of this project.

I would also like to give my special thanks to Dr. W. Jin for his useful suggestions and assistance with the FBG sensing system. Thanks are due to many other people for contribution to this work, including Mr. H. J. Zhang, Mr. S. J. Xu, Mr. K. Y. Ng, Dr. H. G. Xu and Dr. M. H. Liu.

Finally, I wish to express my thanks to my families for their love, patience and support for all the years I was away from home.

ABSTRACT

This thesis presents an experimental study of fluid-structure interactions of bluff bodies subjected to a uniform cross-flow. The investigation concentrates mainly on the fluid-structure interactions of two side-by-side circular cylinders in a cross-flow. However, the flow separation effects on the structural dynamic response are also investigated. Four topics are covered.

First, the flow behind two side-by-side circular cylinders in a cross-flow was studied using laser-illuminated flow-visualization, laser Doppler anemometer and hot-wire techniques. Three typical T/d values, i.e. 3.00, 1.70 and 1.13, were investigated, where T is the centre-to-centre cylinder spacing and d is the cylinder diameter. The vortex formation, interaction and downstream evolution are examined in detail in the three different flow regimes. With the WAG (window average gradient) detection method, the relative probability of the two typical flow pattern, symmetrical and anti-symmetrical vortex arrangement, at large cylinder spacing, T/d = 3.00, is estimated. Specific attention was given to the asymmetrical flow regime, T/d = 1.70, including the dominant frequencies, the stability of the deflected gap flow and its random changeover from one side to another. Based on the observation, a mechanism is proposed for the stability of the deflected gap flow. An explanation is put forward for the existence of two different dominant frequencies associated with the narrow and the wide wake, respectively. The role gap bleeding plays in the vortex formation and downstream development for very small spacing between the cylinders, T/d = 1.13, was also investigated in detail.

Second, free vibrations and the associated non-linear fluid-structure interactions of two side-by-side elastic cylinders with fixed support at both ends placed in a cross-flow were experimentally investigated using FBG sensors, hot wire

technique and flow visualization. Three *T/d* ratios, identical with those mentioned above, were investigated. The structural vibration behaviour at each typical flow regime, i.e. *T/d* = 3.00, 1.70 and 1.13, was examined in detail. The characteristics of the system modal damping ratios, including both structural and fluid damping, and natural frequencies were also addressed using an auto-regressive moving average (ARMA) technique. For example, the dependence on *T/d* and U_r of the system natural frequency and the effective and fluid damping ratios were investigated thoroughly, in particular, at and near resonance, thus throw a new light on the fluid-structure interaction behaviour.

Third, the nonlinear interplay between the simultaneous vibrations of two side-by-side elastic cylinders in a cross-flow, at three identical transverse spacing ratios as mentioned above, were experimentally investigated using FBG sensor, laser vibrometer and hot wire technique. The emphasis was on the structural dynamics and the vibration characteristics. The strain-displacement relationship associated with the two interfering cylinders at each *T/d* values were established and was compared with that of an isolated cylinder. Interference effects on behaviours of the system natural frequencies, the vibration amplitude and the correlation coefficient between the two interfering cylinders at each *T/d* value were also investigated in detail. It was found that, in general, the correlation coefficient ρ_{12} between fluctuating strains measured from the two cylinder increases as *T/d* decreases, suggesting an increasing interference.

Finally, the effect of the nature (fixed or oscillating point) of flow separation on fluid-structure interactions was experimentally investigated. Flow field and structural vibrations of both square and circular cylinders, associated with fixed and moving flow separation points, respectively, were investigated using hot wire and FBG sensors. The vibration characteristics, resonance behaviour, system modal

damping ratios and natural frequencies associated both square and circular cylinder cases were investigated in an effort to understand the effect of flow separation on fluid-structure interactions. Furthermore, the incidence angle effects on the fluid-structure interaction behaviour associated with the square cylinder were also studied in detail.

Nine publications, including 5 refereed journal papers and 4 refereed conference proceedings, have been produced out of this work.

Contents

NOMENCLATURE

A	cross section area of a cylinder.
C_D	drag coefficient $\equiv 2D/(\rho U_\infty^2)$.
C_L	lift coefficient $\equiv 2L/(\rho U_\infty^2)$.
c_m	added mass coefficient.
C_p	pressure coefficient $\equiv 2\Delta p/(\rho U_\infty^2)$.
C_{pb}	base pressure coefficient.
d	diameter of circular cylinder. d also denote the height of the square cylinder (mm).
d'	cross flow cylinder dimension, $d' = (\sin\alpha + \cos\alpha)d$ for square cylinder (mm).
d_h	hydraulic diameter of cylinders (mm).
D	mean drag.
E	Young's modulus of the cylinders.
EI	structural stiffness.
$E_\alpha(f)$	spectrum of fluctuation α (α represents either ε_x, ε_y, X, Y or u), normalised so that $\int_0^\infty E_\alpha(f)df = 1$.
f	frequency in spectrum analysis (Hz).
$f_0^{(n)}$	nth mode structural natural frequency (Hz), n = 1, 2, 3, ...
$f_x^{(n)}$, $f_y^{(n)}$	nth mode inline and cross-flow natural frequencies, respectively, of the fluid-cylinder system (Hz), n = 1, 2, 3,...
f_s	vortex shedding frequency of a stationary cylinder (Hz).

f_{SL}	frequency of the shear layer instability (Hz).
I	area moment of inertia.
L	mean lift.
m	cylinder mass per unit length = $\rho_s A$.
M	sum of added mass and the cylinder unit length mass = $(c_m + 1)\rho_s A$.
M^*	mass ratio = $M/\rho d^2$.
$P(\phi)$	relative probability.
Re	Reynolds number $\equiv U_\infty d/\nu$.
s	cylinder span (mm)
S_t	Strouhal number = $f_s d_h / U_\infty$
t	time (sec).
T	Centre-to-centre cylinder spacing.
u, v	streamwise and cross-flow fluctuation velocity, respectively (m/sec).
U_∞	free stream velocty (m/sec).
U_r	reduced velocity $\equiv U_\infty / f_0^{(1)} d$.
x, y	co-ordinates in streamwise and lateral directions, respectively.
X, Y	displacements of the cylinder in the x and y directions, respectively, measured at midspan of the cylinder by laser vibrometer. X and Y also denote the displacements derived from the dynamic strain signals measured at midspan of the cylinder using fibre-optic Bragg grating (FBG) sensors (μm).
X', Y'	bending displacements of the square cylinder estimated from the strain signals ε_1 and ε_2, respectively (μm).
X_{rms}, Y_{rms}	root mean square values of X and Y, respectively (μm).

Greek Symbols

α	incidence angle of free stream velocity, zero when the flow is normal to one face of the square cylinder.
ρ	fluid density.
ρ_{12}	correlation coefficient between dynamic strains measured from the two cylinders, simultaneously.
ρ_s	structural density.
ε_1, ε_2	dynamic strains of the square cylinder measured by FBG sensor 1 and sensor 2, respectively ($\mu\varepsilon$).
$\varepsilon_{1,rms}$, $\varepsilon_{2,rms}$	root mean square values of ε_1 and ε_2, respectively ($\mu\varepsilon$).
ε_x,ε_y	dynamic strains due to drag and lift, respectively, measured by fibre-optic Bragg grating (FBG) sensors ($\mu\varepsilon$).
$\varepsilon_{x,rms}$,$\varepsilon_{y,rms}$	root mean square values of ε_x *and* ε_y, respectively ($\mu\varepsilon$).
$\zeta_0^{(1)}$	the first-mode structural damping ratio.
ζ_e	effective damping ratio of a fluid-cylinder system.
$\zeta_s^{(n)}$	nth mode structural damping ratio, n = 1, 2, 3,...
ζ_f	fluid damping ratio.
$\zeta_{x,f}^{(n)}$, $\zeta_{y,f}^{(n)}$	nth mode inline and cross-flow fluid damping ratios, respectively, n = 1, 2, 3,...
$\zeta_{x,e}^{(n)}$, $\zeta_{y,e}^{(n)}$	nth mode inline and cross-flow effective (or system) damping ratios, respectively, n = 1, 2, 3, ...
θ	azimuthal angle around a cylinder with the origin at the forward stagnation point.

θ_R	angle of resultant force.
Δp	mean pressure difference between the wall pressure and a reference pressure.
Γ_s	vortex shed circulation.
ν	fluid kinematic viscosity.
ϕ	phase.
Φ_{12}	spectral phase shift at f_s between the ε_y (or ε_x) signals obtained from the two cylinders.
$\Phi_{u_1u_2}$	spectral phase angle at f_s between simultaneously measured hot wire signals.

Superscript

*	denote dimensionless parameter normalised by d/d_h and U_∞ unless otherwise stated.

Subscript

1,2	represent the hot wire number in Chapter 2. Subscript 1, 2 also denote the cylinder number (Chapters 3 and 4) or the fibre-optic Bragg grating (FBG) sensor number (Chapter 5).

CHAPTER 1

INTRODUCTION

1.1 Background

Fluid-structure interactions are of common occurrence in many branches of engineering, i.e. turbo-machines, off shore pilings, large buildings, tube bundle heat exchangers, etc. In general, when bluff bodies are exposed to a uniform or unsteady stream, fluid excitation forces acting on the structure are created by vortex shedding (Chen 1972a, b and c; Blevins and Burton 1976; Achenbach and Heinecke 1981; Perry *et al.* 1982; Chen 1987; Hara 1989; Blackburn and Melbouren 1996). These unsteady forces cause the structures to vibrate (Sarpkaya 1979; Chen 1986; Price *et al.* 1987; Weaver and Fitzpatrick 1988; Brika and Laneville 1993). The resultant structural motions may, in turn, change the flow field through the moving boundary conditions, thus giving rise to a change in the flow-induced forces, which will affect the vibration characteristics of the structure. Consequently, fluid and structure are coupled, modifying both the frequency and the magnitude of the forces on the structure. The coupling is in general a highly non-linear function of both structural motion and flow velocity. Earlier investigations of fluid-structure interaction problems have been concentrated mainly on the measurement of the fluctuating forces, the dynamic strain and the bending displacements (e. g. Griffin 1980; Paidoussis 1982; Schewe 1983; Parkinson 1989; Luo and Teng 1990). There were few measurements carried out simultaneously with the flow field to study the fluid-structure interactions. Exceptions are the work of Williamson and Roshko (1988), Ongoren and Rockwell (1988a and b), Baban *et al.* (1989) and Baban and So (1991). Williamson and Roshko (1988) and Ongoren and Rockwell (1988a and b) focused

mainly on the forced vibration problem rather than the free vibration case, while the latter two investigations (Baban *et al.* 1989; Baban and So 1991) concentrated mainly on rigid structures. Therefore, knowledge of the tightly coupled fluid-structure interaction effects in a free vibration problem is very limited. In this thesis, the fluid-structure interactions, where only vortex shedding generates the excitation forces on the structure, referred to here as free vibration problems. While the problems in which the structure vibration is excited by external excitation forces, which are independent of vortex shedding and structural motions, are considered as forced vibration.

A common fluid-structure interaction problem is the flow-induced vibrations caused by vortex shedding from structures. The flow-induced vibrations could cause structural fatigue and even lead to drastic failure of the structures. For example, in the design of bridges, if the flow-induced vibration and its structural effect are not taken into account in their design, the result could be quite drastic. A good example is the collapse of the Tacoma Bridge during a violent windstorm. Accordingly, interest in understanding the associated physics and predicting the structural motions is rapidly growing (Blevins 1994; Ziada and Staubli 2000). The flow-induced vibration of a two-dimensional bluff body in a cross-flow is a simple and classical version of this class of fluid-structure interaction problems which have been extensively investigated in the past (Chen 1972a and b; Griffin and Ramberg 1974; Sarpkaya 1979; Griffin 1980; Schewe 1983; Chen 1987; Brika and Laneville 1993; Blackburn and Melbouren 1996; Zhou *et al.* 1999a; Zhou *et al.* 2000a). Even then, it is governed by a number of major parameters, such as the reduced velocity, the reduced damping and mass ratio (Chen 1987). Each of these parameters plays a different role in the dynamic response of the cylinder. For example, damping is responsible for the limit cycle oscillation behaviour of the cylinder at resonance

(Zhou *et al.* 1999a) because effective damping does not decrease to zero as resonance is approached. The fluid-structure interaction problem is further complicated by the presence of an identical neighbouring cylinder, such as in the case of two side-by-side cylinders. Here, besides the parameters mentioned above, the problem is also governed by the ratio of the centre-to-centre cylinder spacing T to diameter d. Varying this ratio could lead to the formation of a single or multiple wakes (Landweber 1942; Spivac 1946; Ishigai *et al.* 1972; Bearman and Wadcock 1973; Zdravkovich 1985; Zhou *et al.* 2000b) and this, in turn, could affect the dynamic response and the resonance behaviour of the cylinders. Furthermore, the nonlinear interplay between the simultaneous vibrations of the two cylinders and the fluid as a result of flow-induced forces is a far more complicated process than the fluid-cylinder interaction in the single cylinder case. The present experimental investigations concentrated mainly on the fluid-structure interactions of two side-by-side circular cylinders in a cross-flow. In addition, the effects of the flow separation characteristics from bluff bodies on the structural dynamic response are also investigated in detail.

1.2 A Brief Literature Review

1.2.1 Flow dynamics around two side-by-side cylinder/bluff bodies

Flow dynamics around two side-by-side cylinders subjected to a uniform cross-flow has received considerable attention in the past (e.g. Biermann and Herrnstein 1933; Landweber 1942; Ishigai *et al.* 1972; Zdravkovich 1977; Williamson 1985; Chang and Song 1990; Kolář *et al.* 1997; Sumner *et al.* 1999) because of its inherent importance and practical significance in many branches of engineering. In this configuration, the ratio T/d is known to be a very important

parameter. The wake pattern, Strouhal number, lift and drag coefficients experience series changes in this case (Chang and Song 1990). When *T/d* is larger than about 6.0, virtually no interactions are generated between the two Karman vortex streets (Biermann and Herrnstein 1933; Landweber 1942; Spivac 1946; Hori 1959). When *T/d* less than about 6.0, vortices shed from the two cylinders interact dynamically (Chang and Song 1990). The lift and drag coefficients measurements carried out by Zdravkovich and Pridden (1977) indicates that the sum of the low and high drag generated by the two cylinders was always less than twice the drag of a single cylinder.

When *T/d* is in the range 2.0 - 6.0, for each cylinder, vortices shed alternately at gap side and free-stream side with a frequency same as that of a single cylinder, indicating a relatively small interaction between the two cylinders (Landweber 1942; Spivac 1946; Ishigai *et al.* 1972). The vortex formation and shedding from the two cylinders exists either in symmetrical (anti-phase) or anti-symmetrical (in-phase) form (Chang and Song 1990). It has been observed that the symmetrical vortex shedding is predominant over the anti-symmetrical vortex shedding (Ishigai *et al.* 1972; Williamson 1985). When $1.2 < T/d < 2.0$, flow dynamics around two side-by-side cylinders subjected to a cross-flow is characterized as 'asymmetrical'. The gap flow is mostly deflected toward one cylinder and may changeover to the other side from time to time (Spivack 1946; Ishigai *et al.* 1972; Bearman and Wadcock 1973; Kamemoto 1976, Kiya *et al.* 1980; Kim and Durbin 1988; Sumner *et al.* 1999). Bearman and Wadcock (1973) measured the base pressure simultaneously on both cylinders, and found that the cylinders always experienced different based pressure in the range of spacing *T/d* between 1.2 and 2.0. He also found that the cylinder, toward which the gap flow is deflected, has a lower base pressure and a higher C_D, whereas the other cylinder has a higher base pressure and a lower C_D. Similar

phenomena were also observed by Quadflieg (1977). For very small cylinder spacing, i.e. $T/d < 1.2$, no vortex is generated in the gap between the two cylinders; vortices are mostly alternately formed from the free-stream sides of the two cylinders with a frequency half of that of a single cylinder (Ishigai *et al.* 1972; Williamson 1985; Sumner *et al.* 1999).

1.2.2 Vibration characteristics of two cylinders subjected to a cross-flow

The vortex-induced vibration characteristics of two side-by-side cylinders in a cross-flow are generally related to the flow dynamics around the cylinders, which has also been investigated extensively in the past (Chen 1975; Bokaian and Geoola 1984b and c; Zdravkovich 1984; Chang and Song 1990; Meneghini *et al.* 2001). For large cylinder spacing, i.e. $T/d > 2.0$, the coupling due to fluid flow is small, therefore, each cylinder responds similarly to that of an isolated cylinder (Chen 1986). At $T/d < 2$, flow dynamics around the two cylinders are asymmetrical and there are multiple vortex frequencies (Bearman and Wadcock 1973; Williamson 1985; Kim and Durbin 1988), therefore, the cylinder vibration characteristics become extremely complicated. For example, Livesey and Dye's (1962) investigation indicates that the two cylinders may vibrate in either out-of-phase or in-phase at intermediate cylinder spacing ($T/d < 2.0$). They further conjectured that the out-of-phase and in-phase modes maybe related to the resonance of the corresponding vortex frequencies. A detailed study, including natural frequencies, damping, displacements and vibration orbit, of flow-induced vibration of two side-by-side circular cylinders in a cross-flow at the bi-stable flow regime, i.e. $T/d = 1.5$ and 1.75, has been carried out by Jendrzejczyk *et al.* (1979). They found that the tube response frequencies in the drag and lift direction are the same at low flow velocities. As the flow velocity increases, tube response frequencies in the lift direction decrease while those in the drag direction increase. They ascribed this observation to two reasons.

First, the drag force induced displacement may tend to change the end conditions of the tube. Second, the added mass is not constant but varies with flow velocity. Later, Chen (1986) further pointed out that the effect of fluid damping and fluid stiffness forces may be also partially responsible to the tube response frequencies or natural frequency variations observed by Jendrzejczyk *et al.* (1979). When the two cylinders are fairly close, i.e. $T/d < 1.2$, the two cylinders are strongly coupled by flow field, acting like a single structure (Chen 1986).

1.2.3 Flow field behind two side-by-side cylinders

The characteristics of flow field behind two side-by-side cylinders subjected to a uniform cross-flow depend to a great extent on the ratio T/d among many other parameters, e.g. initial conditions, pressure gradient and Reynolds number (e.g. Zdravkovich 1977; Williamson 1985; Kolář *et al.* 1997; Sumner *et al.* 1999). For relatively large cylinder spacing, i.e. $T/d > 2.0$, two distinct vortex streets are generated behind each cylinder (Landweber 1942) with the same vortex frequency as that behind a single cylinder (Spivac 1946). The two streets are coupled and dominated by antiphase or symmetrical behaviour (Ishigai *et al.* 1972), though the inphase or anti-symmetrical arrangement between the two streets was also observed (Williamson 1985). As the two cylinders approach each other to an intermediate cylinder spacing, i.e. $1.2 < T/d < 2.0$, the gap flow between the cylinders is deflected towards one cylinder and may change over intermittently from one side to another. The deflection leads to the formation of one narrow and one wide wake, which are associated with high and low vortex frequency, respectively (Spivack 1946; Ishigai *et al.* 1972; Bearman and Wadcock 1973; Kamemoto 1976; Kiya *et al.* 1980; Kim and Durbin 1988; Sumner *et al.* 1999). For very small cylinder spacing, i.e. $T/d <$ 1.2, the two cylinders behave like a single structure, that is, vortices are mostly

alternately shed from the outer side only, nearer to the free stream, of the two cylinders, forming a single vortex street (Sumner *et al.* 1999).

1.2.4 Fluid damping of fluid-structure system

Damping is an important issue in fluid-structure interaction problems, which is in general a highly non-linear function of both structural motion and flow characteristics. Damping may arise from fluid surrounding the structure as well as from the structure. While structural damping is related to the properties of the structure itself, fluid damping originates from viscous dissipation and fluid drag, i.e. the result of viscous shearing of the fluid at the surface of the structure and flow separation. As a result, fluid damping is motion dependent and is difficult to estimate, especially for multi-degree-of-freedom dynamic systems (Weaver and Fitzpatrick 1988; Granger *et al.* 1993).

Previous experimental work on fluid damping mostly focused on liquid-structure systems where the induced force is large and the vibration amplitude is of the order of the hydraulic diameter of the structure (Chen and Jendrzejczyk 1979 and 1981; Chen *et al.* 1995). From the measurements of a circular cylinder in a liquid cross flow, Chen and Jendrzejczyk (1979) inferred modal damping ratios along the lift and drag directions. Similar measurements of the damping ratios of a tube in an array have also been carried out (Chen and Jendrzejczyk 1981). On the theoretical side, Chen *et al.* (1995) presented an unsteady flow theory for vortex-induced vibration of a structure in a cross flow. According to this theory, resonance (or lock-in resonance), where the natural frequency of the combined fluid-structure system coincides with the frequency of fluid excitation forces, is a coupled instability and forced vibration problem. As the flow passes through the lock-in region, the modal damping might become negative, resulting in an unstable system. Once the

amplitude becomes large, the modal damping also increases and the system will be stabilized.

Recently, Mittal and Kumar (1999), Mendes and Branco (1999) and Zhou *et al.* (2000a) studied the flow-induced vibration of a single cylinder in a cross-flow numerically assuming a two-dimensional flow and a two-degree-of-freedom (2-dof) dynamics approach over a range of Reynolds number, $200 \leq Re < 500$. Zhou *et al.* (2000a) extracted fluid damping ratios from the calculated signals of the lift and drag and their respective vibration amplitudes. The damping ratios thus deduced showed a trend quite similar to the experimental measurements of Griffin and Koopmann (1977). These measurements, which were obtained from an elastically mounted rigid cylinder in a wind tunnel, showed that there is a marked decrease in fluid damping ratio in the lock-in region. An attempt to compare the calculated and measured damping ratio for the first vibration mode has been made by So *et al.* (2000a). The comparison was made with the measurements of So *et al.* (2000a) at an *Re* of about 3340. Agreement between calculations and measurements was fair. There are many reasons for the less than good comparison, major among them are errors in the measured lift signal, the 2-dof dynamics model and the two-dimensional laminar flow assumption for the upstream flow and wake. An attempt to relax the 2-dof assumption has been made by Wang *et al.* (2001), but the modal damping ratio comparison with measurements was not so good as the 2-dof result. These studies, therefore, suggest that there is a real need to verify the experimental data and improve on their measurements.

On the other hand, Newman and Karniadakis (1997), Evangelinos and Karniadakis (1999) and Evangelinos *et al.* (2000) carried out direct numerical simulation of this simple fluid-structure interaction problem at *Re* ranging from 200 to 1000. Their calculations took into account the effect of turbulence in the wake

flow and the three-dimensional nature of the shed vortices and the wake. In principle, therefore, the lift and transverse displacement signals were more reasonable than those obtained under the two-dimensional laminar approach of So *et al.* (2000a) and Wang *et al.* (2001). However, their studies were mainly concentrated on the wake flow and the structural motions. Little attempt has been made to deduce damping information and the associated change in damping ratios over the range of reduced velocity, U_r, investigated.

1.2.5 Flow separation characteristics from bluff bodies

The excitation force originates from vortex shedding in the free vibration case. Naturally, the nature (fixed or oscillating) of flow separation could affect the dynamics of the freely vibrating elastic cylinder. In the case of a circular cylinder, the separation point is not fixed, but keeps moving on the cylinder surface. The excursion of the separation point is usually within 10° and varies from 75° to 85° (the angle measures from the forward stagnation point) for the Reynolds number $Re = 1.06 \times 10^5$ (Dwyer e*t al.* 1973). The mean location of flow separation varies with *Re* (Chen 1987). Higuchi *et al.* (1989) found that the separation point moved between 87° and 95° at $Re = 1.96 \times 10^5$, while Achenbach (1968)'s measurements indicated that boundary layer separation occurred at 78° for $Re = 10^5$ and shifted to 94° for $Re = 3 \times 10^5$. Flow separation and structural vibration are also related. Mei and Currie (1969) examined the boundary layer separation from a stationary and a vibrating cylinder. Their results showed that the separation point oscillated over an arc of the cylinder surface. The arc length varied with the frequency and the amplitude of the cylinder vibration; it reached a peak when the cylinder frequency was about 0.9 times the wake frequency and then decreased with further increase of the wake frequency. On the other hand, vortex shedding from a square cylinder is

characterized by a fixed separation point. The way the flow separates is linked to the rotation angle of the cylinder. When the square cylinder is normal to the free stream velocity, i.e. the angle of incidence α = 0°, the flow separates from the upstream corners of the cylinder and will not reattach on the side surfaces (Nguyen and Naudascher 1991; Naudascher and Wang 1993). When α increases to 13° ~ 45°, the flow might separate from one upstream corner and one trailing corner for Re = 3000 ~ 21000 (Chen and Liu 1999). Evidently, separation behaviour of the square cylinder differs from that of the circular cylinder.

1.2.6 Issues identified

As reviewed above, the fluid-structure interactions of two side-by-side cylinder/bluff bodies has been investigated extensively in the past (Landweber 1942; Spivac 1946; Ishigai *et al.* 1972; Bearman and Wadcock 1973; Chen 1975; Bokaian and Geoola 1984b andc; Zdravkovich 1984; Chang and Song 1990; Kolář *et al.* 1997; Sumner *et al.* 1999; Meneghini *et al.* 2001). These studies have greatly improved our understanding of the fluid-structure characteristics of two side-by-side cylinder/bluff bodies subjected a uniform cross-flow. Nevertheless, as a fully coupled problem, investigation of the fluid-structure interactions of this fluid-structure configuration is far from complete. There are still a number of important issues have yet to be addressed. For example, at relatively large T/d (>2.0), why is the symmetric vortex shedding predominant over the anti-symmetric shedding? What is the ratio between the two spatial arrangements? What triggers the transition of the two vortex streets from the in-antiphase to the in-phase mode? At asymmetric flow regime ($1.2<T/d<2.0$), physics behind the formation and stability of a narrow and a wide wake is unclear. Furthermore, what triggers the changeover of the gap flow deflection from one side to another? Why does the dominant frequency in the narrow wake triple that in the wide wake? How do the vortices in both wakes evolve

downstream? For very small cylinder spacing (T/d <1.2), the possible role the gap bleeding plays in vortex formation and downstream evolution has yet to be clarified.

On the other hand, previous studies were mostly concerned with the behaviour of the wake flow and the flow-induced vibrations on rigid cylinders. Even in the free vibration case, the cylinders, flexibly mounted at both ends, were relatively rigid. Here, a rigid cylinder is defined as one having infinite structural stiffness. The dynamic characteristics of an elastic cylinder, defined as one with finite structural stiffness, can be quite different from a rigid one (Zhou *et al.* 1999a, So *et al.* 2000a). There have been relatively few studies on two side-by-side elastic cylinders in a cross-flow. Consequently, the fluid-structure interaction characteristics of two side-by-side elastic cylinders subjected to a uniform cross-flow have yet to be well documented.

In previous studies of fluid damping (Chen and Jendrzejclyk 1979 and 1981; Chen *et al.* 1995; Jendrzejclyk *et al.* 1979; Granger and Paidoussis 1995; Newman and Karniadakis 1997; Evangelinos and Karniadakis 1999), the mean flow velocity was relatively small. As a result, the range of U_r covered was quite limited and the observation revealed resonance with the first vibration mode. In other word, only the first modal damping was deduced or considered in the data analysis. Damping ratios of other modes of vibration of an elastic cylinder in a cross-flow are scarce. Consequently, many aspects of resonance associated with these modes have yet to be clarified, for example, how the damping ratios would behave at higher mode resonance, and how interference between two side-by-side cylinders affects the damping ratio. Furthermore, the issue of the effect of flow separation on fluid-structure interactions has yet to be addressed.

1.3 Objectives

The present work aims to investigate experimentally the fluid-structure interactions of bluff bodies subjected to a uniform cross-flow. The study is concentrated mainly on the configuration of two side-by-side circular cylinders in a cross-flow. The reason for choosing this configuration is that, in spite of the extensive investigations in the past, there are still a number of important issues have yet to be addressed. Specific objectives are stated as follows:

(i) To study the flow around two side-by-side cylinders subjected to a uniform cross-flow so as to gain a better understanding of the vortex generation, interaction, topology (vortex pattern) and downstream evolution at different flow regimes.

(ii) To investigate the free vibration of two side-by-side elastic cylinders placed in a cross-flow and the associated non-linear fluid-structure interactions.

(iii) To study the interference effect on the structural dynamics and vortex-induced vibration characteristics of two side-by-side fix-supported elastic cylinders.

(iv) To investigate the effect of flow separation characteristics on the free vibration of an elastic cylinder, with fixed-fixed end conditions, subjected to a uniform cross-flow.

1.4 Experimental Instruments

In these experimental investigations, the fluid dynamics was investigated using constant temperature hot-wire anemometers and laser-illuminated flow visualization technique, while the mean drag and lift acting on the structures were

obtained by applying a wall pressure tap and a pressure transducer. A number of techniques are available for the measurement of dynamic strain and displacement of a vibrating structure. However, most of them are intrusive and would alter the structural dynamic characteristics, i.e. the strain gauges (Weaver and Yeung 1984; Andjelic and Popp 1089) and capacitive type displacement transducer (Laneville and Mazouzi 1995). In this study, a Polytec Series 3000 Dual Laser Beam Vibrometer (Trethewey *et al.* 1993) was employed to measure the fluctuating displacement of the structures. The laser vibrometer is a non-intrusive technique, which has been successfully employed by So *et al.* (2000b) to study the dynamic behaviour of an elastic cylinder in a cross-flow and the fluid-structure interactions at synchronization. However, it is very difficult to measure the dynamic displacement of the structure in the streamwise direction applying laser vibrometer (So *et al.* 2000b; Zhou *et al.* 1999b). Therefore, a new technique, Fibre-optic Bragg Grating (FBG) sensor, was also applied to measure the dynamic strains of the structures.

Figure 1-1 shows the generic sensing concept using FBG sensor (Kersey *et al.* 1997). An FBG is formed inside the core of an optical fibre by introducing periodic changes in refractive index along the fibre. Assuming input signal is broadband light incident on the grating, a narrow band signal is reflected back at the Bragg resonance wavelength $\lambda_B = 2n\Lambda$, where Λ is the grating pitch and n the averaged fibre refractive index. Any perturbation, say due to applied strain variation ε, of the grating results in a variation in Λ and n, and therefore a shift $\Delta\lambda_B$ in λ_B. The value of $\Delta\lambda_B$ is related to ε by $\Delta\lambda_B = K\varepsilon$, where K is a scale factor and can be determined by a calibration process. Using a wavelength detection device, the $\Delta\lambda_B$ can be converted into the variation of light intensity. The intensity variation is subsequently converted into an electric current or voltage through a photo-detector. The variation of strain is therefore related to that of the electric signal. The FBG sensor has many unique features. For

example, its diameter could be as small as 80 μm. Therefore, its attachment to the structure would not seriously alter the flow around the structure and, in addition, it has a negligible effect on the structural dynamic characteristics. Zhou *et al.* (1999b) and Jin *et al.* (2000) have successfully used the FBG sensor to measure the dynamic strain on one or two circular cylinders in a cross flow. They have established that the measured root mean square (rms) strain is linearly correlated to the rms bending displacement provided that the displacement is small. This empirical relationship allows the dynamic strain measurements to be interpreted in terms of the displacement.

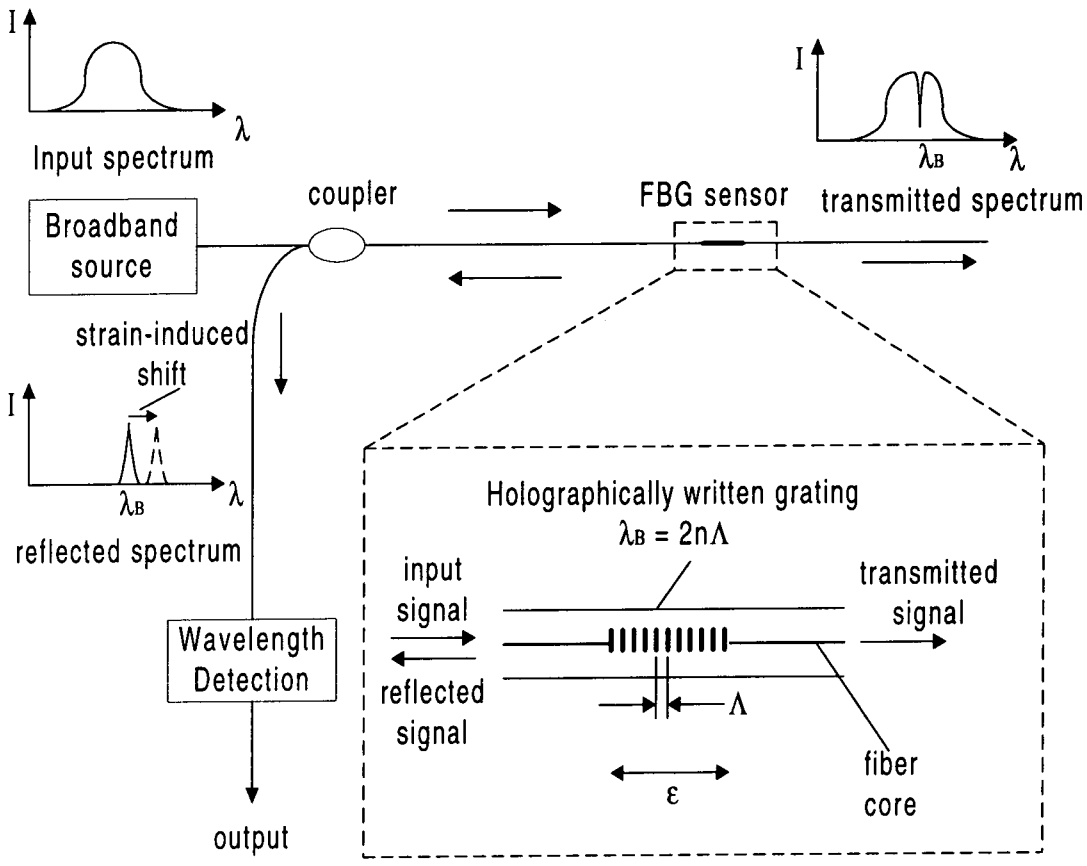

Figure 1-1 A schematic of the Fibre-optic Bragg Grating (FBG) sensing concept, from Kersey *et al.* (1997).

For easier reference, the estimated experimental uncertainties are provided in Table 1-1.

Table 1-1 Summary of the estimated experimental uncertainties.

Hot-wire Anemometry	Pressure tap	Pressure transducer	Pitot tube	Laser Doppler Anemometry	Laser Vibrometer	FBG sensing system
± 4.8%	± 3.5%	± 0.01%	± 3.0%	± 1.5%*	± 7.5%	± 8.0%

* The measuring volume has a minor axis of 1.18mm and a major axis of 2.48mm.

1.5 Synopsis of the thesis

The experimental work presented here is mainly concentrated on the fluid-structure interaction characteristics of two side-by-side circular cylinders subjected to a uniform cross-flow. In addition, the flow separation effects on fluid-structure interaction behaviours of a single elastic cylinder in a cross-flow were also included. There are six chapters in the thesis. Chapter 1 is an introduction to this work.

The flow dynamics behind two side-by-side circular cylinders subjected to a uniform cross-flow, which is essential to study the fluid-structure interaction effects, are examined in Chapter 2 using laser-illuminated flow-visualization, laser Doppler anemometer and hot wire technique. Details include the vortex formation, topology (flow pattern) and downstream evolution at each typical cylinder spacing, i.e. T/d = 3.00, 1.70 and 1.13, respectively. The relative probability of the two typical flow patterns, symmetrical and anti-symmetrical vortex arrangement, at large cylinder spacing, T/d = 3.00, is estimated by simultaneously measuring wake velocities at symmetrical spatial positions about the flow centerline using hot wire anemometers. The vortex shedding behaviour, formation of a narrow wake and a wide wake, changeover process of the deflected gap flow and downstream evolution of the vortices behind the two cylinders at intermediate cylinder spacing, T/d = 1.70, were

examined in detail in this chapter. Based on the flow visualization and hot wire measurements, a mechanism is proposed for the stability of the deflected gap flow. An explanation is put forward for the existence of two different dominant frequencies associated with the narrow and the wide wake, respectively. In addition, the role the gap bleeding plays in determining the flow characteristics at small cylinder spacing, $T/d = 1.13$, are also investigated.

Chapter 3 studies the free vibrations of two side-by-side elastic cylinders with fixed support at both ends placed in a cross-flow. Two FBG sensors were used to measure the dynamic strains associated with each cylinder, simultaneously, in both transverse and streamwise directions. A hot wire and flow visualization were employed to examine the flow field around the cylinders. Three typical T/d ratios, identical with that in the studies presented in Chapter 2, were investigated. The measured structural vibration behaviour is closely linked to the flow characteristics obtained in Chapter 2. For example, At $T/d = 3.00$, the cross-flow root mean square strain distribution shows a very prominent peak at the reduced velocity $U_r \approx 26$ when the vortex shedding frequency f_s coincides with the third-mode natural frequency of the combined fluid-cylinder system. When $T/d < 3.00$, the vibration is suppressed because of the weakening strength of the vortices. The characteristics of the system modal damping ratios, including both structural and fluid damping, and natural frequencies are also addressed using an auto-regressive moving average (ARMA) technique. It is found that both parameters depend on T/d. Furthermore, they vary slowly with U_r, except near resonance where a sharp variation occurs. The sharp variation in the natural frequencies of the combined system is dictated by the vortex shedding frequency, in contrast with the lock-in phenomenon, where the forced vibration of a structure modifies the vortex shedding frequency, thus throw a new light on the fluid-structure interaction behaviours.

The nonlinear interplay between the simultaneous vibrations of the two side-by-side elastic cylinders, fixed at both ends in a cross-flow, is investigated in Chapter 4. Two FBG sensors and a laser vibrometer were employed to measure the dynamic response of the cylinders. Simultaneously, a single hot wire was used to measure the velocity in the wake. Three identical transverse spacing ratios with that mentioned in Chapters 2 and 3 were investigated. The strain-displacement relationship associated with the two interfering cylinders at each *T/d* values were established and was compared with that of an isolated cylinder. Interference effects on behaviours of the natural frequencies of the fluid-cylinder system, the vibration amplitude and the correlation coefficient between the two interfering cylinders at each *T/d* value were also investigated in this chapter.

Chapter 5 addresses the effect of the nature (fixed or oscillating point) of flow separation on fluid-structure interactions. Flow field and structural vibrations of both square and circular cylinders, associated with fixed and moving flow separation points, respectively, are investigated using hot wire and FBG sensors. The vibration characteristics, resonance behaviour, system modal damping ratios and natural frequencies associated both square and circular cylinder cases are investigated in an effort to understand the effect of flow separation on fluid-structure interactions. Furthermore, the incidence angle effects on the fluid-structure interaction behaviour associated with the square cylinder were also studied in this Chapter.

Summary and conclusions are given in Chapter 6.

CHAPTER 2

VORTEX STREETS BEHIND TWO SIDE-BY-SIDE CYLINDERS

2.1 Introduction

Flow around two side-by-side cylinders has received considerable attention in the past (e.g. Zdravkovich 1977; Williamson 1985; Kolář *et al.* 1997; Sumner *et al.* 1999) because of its inherent importance and practical significance in many branches of engineering. This flow depends to a great extent on the ratio T/d (T is the centre-to-centre cylinder spacing and d is the cylinder diameter) among many other parameters, e.g. initial conditions, pressure gradient and Reynolds number.

For a relatively large spacing, i.e. $T/d > 2$, two distinct vortex streets occur (Landweber 1942). The two streets are coupled, with a definite phase relationship (e.g. Kim and Durbin 1988); they are characterised by a single frequency (Spivac 1946). This frequency was further found to be the same as the frequency measured in the single cylinder wake. A Schlieren optical method was used by Ishigai *et al.* (1972) to visualize the flow behind two side-by-side cylinders. They observed a remarkably symmetric vortex formation and shedding for T/d = 2.5 and 3.0. Based on flow-visualization data at the Reynolds number Re ($\equiv U_\infty d/\nu$, where ν is the kinematic viscosity) = 100 ~ 200, Williamson (1985) demonstrated that the two streets may occur in phase (anti-symmetric vortex formation) or in antiphase (symmetric vortex formation). The in-phase streets eventually merged downstream to form a single street, while the antiphase streets remained distinct farther downstream. He observed a predominant antiphase vortex shedding for $2 < T/d < 6$. These studies have greatly improved our understanding of the flow behind two side-

by-side cylinders for relatively large T/d (≥ 2). However, some aspects of the flow remain unclear. For example, why is the symmetric vortex shedding predominant over the anti-symmetric shedding? What is the ratio between the two spatial arrangements? What triggers the transition of the two vortex streets from the in-antiphase to the in-phase mode?

At an intermediate cylinder spacing, i.e. $1.2 < T/d < 2.0$, the interaction between the wakes associated with the two cylinders is expected to intensify; the gap flow between the cylinders is deflected, forming one narrow and one wide wake. Ishigai *et al.* (1972) ascribed the gap flow deflection to Coanda effects. However, Bearman and Wadcock (1973) measured different base pressures behind two side-by-side flat plates and inferred that the gap flow was deflected. Therefore, they argued that the gap flow deflection was not caused by the boundary layer separation; instead, it was a near-wake phenomenon. Their argument was further supported by Williamson (1985)'s flow visualisation data, which showed a deflected gap flow behind two side-by-side flat plates. It has been found that the vortex frequency associated with the narrow wake approximately triples that for the wide wake (e.g. Bearman and Wadcock 1973; Sumner *et al.* 1999). The deflected gap flow may change over intermittently from one side to another and is bi-stable. The bi-stability is nominally independent of the Reynolds number (Kim and Durbin 1988). Nevertheless, a number of important issues have yet to be clarified of the asymmetric flow regime. Typically, physics behind the formation and stability of a narrow and a wide wake is unclear. Furthermore, what triggers the changeover of the gap flow deflection from one side to another? Why does the dominant frequency in the narrow wake triple that in the wide wake? How do the vortices in both wakes evolve downstream?

For very small spacing, i.e. $T/d < 1.2$, no vortex is generated in the gap between the cylinders; vortices are alternately shed from the free-stream side only of the two cylinders, generating a single vortex street. Sumner *et al.* (1999) observed that the alternate vortex shedding was supplanted from time to time by the symmetric shedding. They further pointed out that the gap bleeding was usually associated with higher momentum, acting to increase the streamwise extent of the vortex formation region. However, the possible role the gap bleeding plays in vortex formation and downstream evolution has not been thoroughly investigated.

This Chapter aims to study the flow around two side-by-side cylinders based on flow visualization, laser Doppler anemometer (LDA) and hot wire measurements, specifically, to gain a better understanding of the vortex generation, interaction and downstream evolution in the three different flow regimes. Specific attention is given to the asymmetrical flow regime ($T/d = 1.5 \sim 2.0$), including the stability of the deflected gap flow and its random changeover from one side to another. The role gap bleeding plays in the vortex formation and downstream development for very small spacing between the cylinders is examined in detail.

2.2 Experimental Details

2.2.1 Laser-illuminated flow visualisation

Experiments were carried out in a water tunnel with a square working section (0.15m × 0.15m) of 0.5m long. The water tunnel is a recirculating single reservoir system (Fig. 2-1a). A centrifugal pump delivers water from the reservoir to the tunnel contraction. The area ratio of the contraction is 10:1 over a length of 0.6m. A honeycomb is used to remove any large-scale irregularities prior to the contraction. The flow variation is controlled by a regulator valve, up to a maximum velocity of

about 0.32m/s in the working section, which is made up of four 20mm thick Perspex panels.

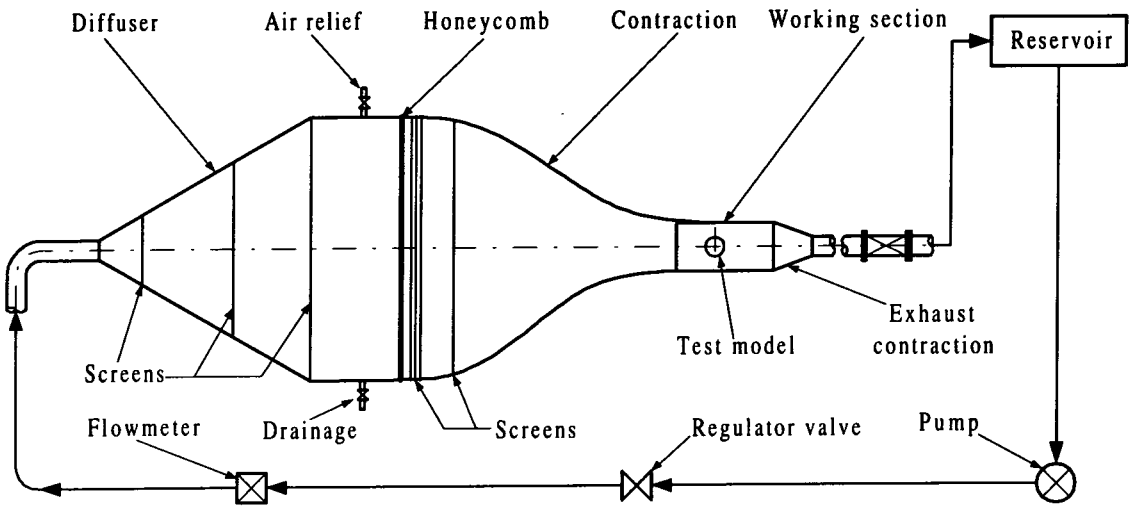

(a)

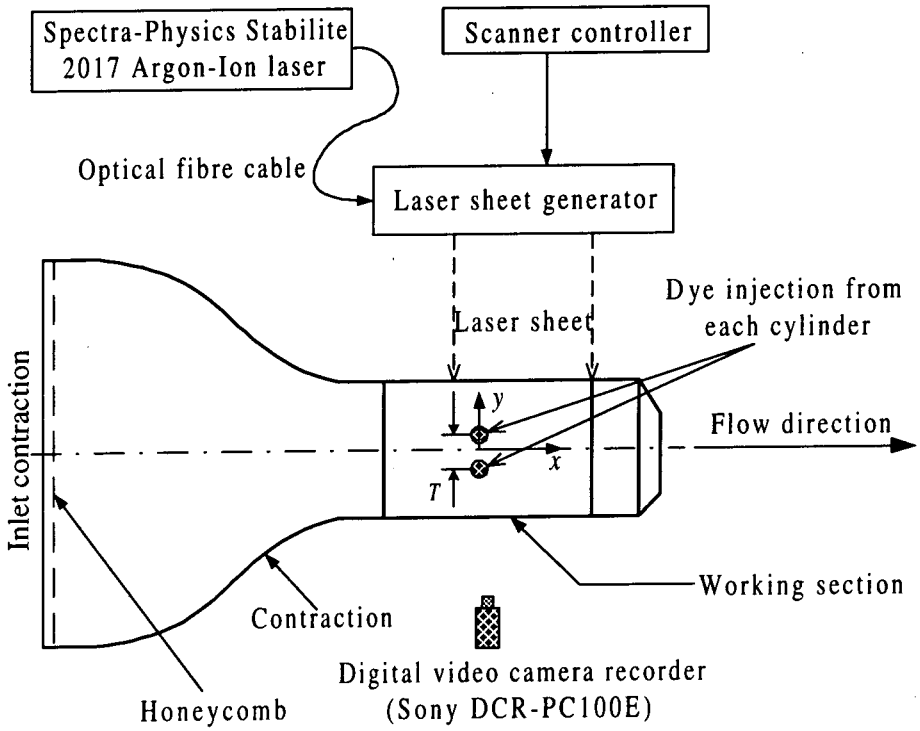

(b)

Figure 2-1 (a) Schematic diagram of the water tunnel. (b) Experimental set-up.

Two side-by-side acrylic circular tubes of an identical diameter of 10 mm were horizontally mounted 0.20m downstream of the exit plane of the tunnel contraction and placed symmetrically about the mid-plane of the working section (Fig. 2-1b). They spanned the full width of the tunnel, resulting in a blockage of 13.3%. Three transverse spacing ratios were used, i.e. T/d = 3.00, 1.70 and 1.13, respectively. These ratios were chosen because the flow regimes thus resulted were representative of the different proximity effects for two side-by-side circular cylinders (Zdravkovich 1985).

Dye (Rhodamine 6G 99%) was chosen to be the flow marker, which had a faint red colour and became metallic green when excited by laser. For each cylinder, dye was introduced through 2 injection pinholes of 0.5mm in diameter at the mid-span of the cylinder. The two pinholes were located at 90°, clockwise and anti-clockwise, respectively, from the forward stagnation point.

A thin laser sheet, which was generated by laser beam sweeping, provided illumination vertically at the mid-plane of the working section. A Spectra-Physics Stabilite 2017 Argon Ion laser with a maximum power output of 4 watts was used to generate the laser beam. A digital video camera recorder (Sony DCR-PC100E) was used to record the dye-marked vortex streets at a framing rate of 25 frames per second. The recording duration was typically 10 min. Flow-visualisation was carried out in the Re range of 120 to 2000 over $0 \leq x/d \leq 8$. At larger Re and x/d, the dye diffused too rapidly to be an effective marker of vortices.

2.2.2 Hot-wire measurements

Experiments were carried out in a closed circuit wind tunnel with a 2.0 m long square cross section of 0.6 m × 0.6 m. Two brass circular cylinders of 12.7 mm diameter were installed side-by-side in the mid-plane and spanned the full width of the working section (Fig. 2-2). The cylinders were located at 0.20 m downstream of

the exit plane of the contraction, resulting in a maximum blockage of about 4.2% and an aspect ratio of 47. Three transverse spacing ratios, identical to those in flow visualization investigations, were used. The longitudinal turbulence intensity in the free-stream was measured to be approximately 0.4%. Measurements were carried out over $0 \leq x/d \leq 10$ and $-5.0 < y/d < 5.0$. The Reynolds number Re was 5900.

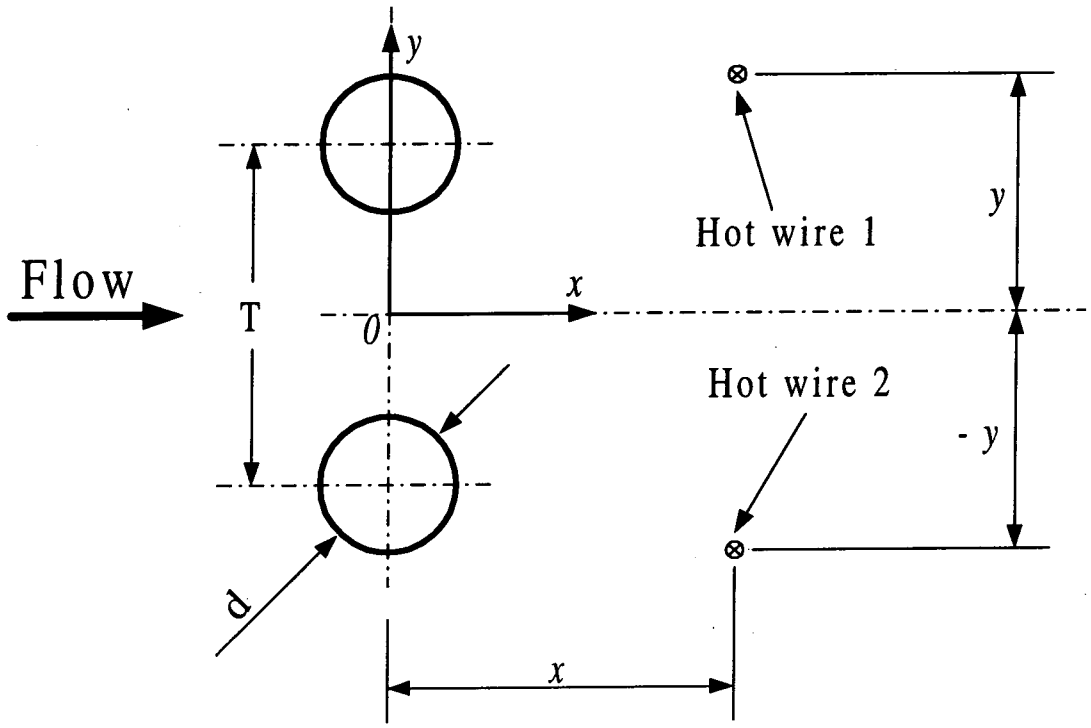

Figure 2-2 Experimental arrangement of hot-wire measurements.

Two single hot-wires were placed symmetrically about the midway of the gap between the cylinders, which was chosen to be the origin for the x and y coordinates (Fig. 2-2). In this Chapter, we define $y/d = 0$ as the flow centreline. Hot wires 1 and 2, moveable along both x and y directions, measured simultaneously the velocity fluctuations on both sides of the flow centreline. The wires were operated at an overheat ratio of 1.8 with two constant temperature anemometers. Signals from the two anemometers were simultaneously offset, amplified and then digitised using a

12bit A/D board and a personal computer at a sampling frequency of 6.0 *kHz* per channel. Unless otherwise stated, the duration of each record was about 20s.

2.2.3 LDA measurements

The wind tunnel and other experimental conditions were the same as those used for the hot-wire measurements. In order to obtain the quantitative information on the flow field at a close vicinity downstream of the cylinders, a two-component LDA (Dantec Model 58N40 two component LDA with enhanced FVA signal processor) was used to measure velocities at x/d = 1.5, 5 and 10 in the plane of mean shear. The measuring volume has a minor axis of 1.18mm and a major axis of 2.48mm. Thus, the measured mean velocity was estimated to have an error of less than 3% and the corresponding error for the measured root mean square value was less than 10%. The seeding of the flow was provided by smoke generated by a Dantec SAFEX 2010 fog generator from Dantec fog fluid (standard). The LDA system comes with the necessary software for data processing and analysis. Therefore, besides the mean field, the data could also be processed to yield information on the Reynolds stresses.

2.3 Flow Characteristics for Large Cylinder Spacing

2.3.1 Mean velocity and Reynolds stresses

Figure 2-3 shows the cross-stream distributions of the mean velocity $\overline{U}^*$, Reynolds stresses $\overline{u^2}^*$, $\overline{v^2}^*$ and Reynolds shear stress $\overline{uv}^*$ measured at x/d = 1.5. In this Chapter, an overbar denotes time averaging. An asterisk indicates normalization by U_∞ and/or d. This normalisation is used for convenience only because the velocity fields of the present flow are not self-preserving. The distributions on each

side of the flow centreline, i.e. $y/d = 0$, are similar to those behind a single cylinder (Zhou and Antonia 1993), indicating the occurrence of two vortex streets.

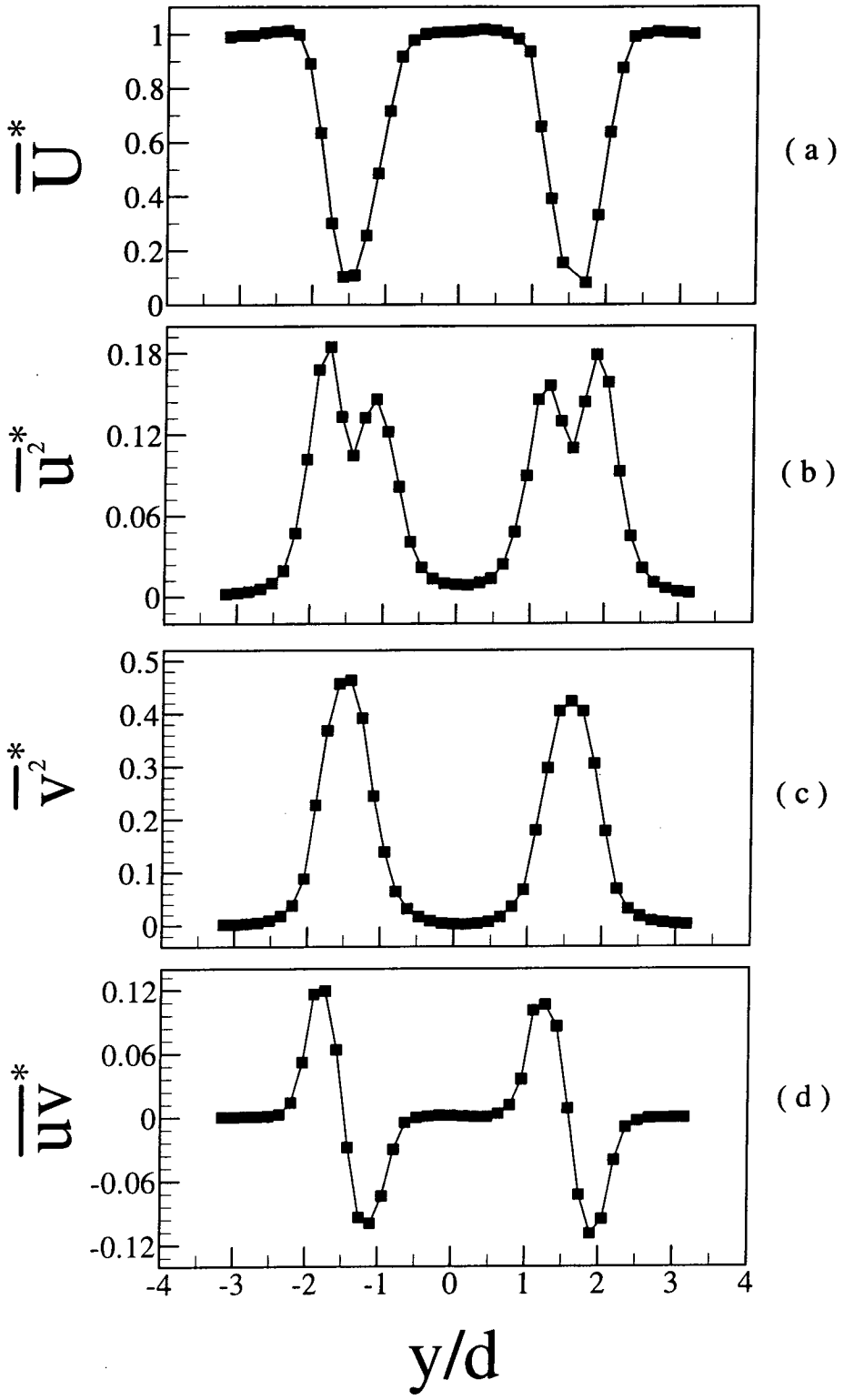

Figure 2-3 Cross-flow distributions of mean velocity, Reynolds normal stresses and shear stress: (a) $\overline{U}^*$, (b) $\overline{u^2}^*$, (c) $\overline{v^2}^*$, (d) $\overline{uv}^*$. $T/d = 3.00$, $x/d = 1.5$.

The peaks in $\overline{u^2}^*$, close to y/d = 0, are relatively small in magnitude, compared with those towards the free-stream. This suggests that the inner vortices, shed from the side of cylinders near the centreline, could be weaker than the outer vortices generated from the free-stream side of a cylinder. Kolář *et al.* (1997) conducted ensemble-averaging of LDA data measured in the near-wake of two side-by-side square cylinders (x/d < 10, T/d = 3.0, where d is the height of square cylinders) and noted a weak strength and fast decay in inner vortices. Based on the examination of effective turbulent vorticity flux density vector (Hussain 1986), they proposed that the interaction between the inner vortices shed from the different cylinders was mainly responsible for the fast decay in inner vortices. The present measurement, at such a close proximity to the cylinder, further suggests that the inner vortices could be shed with smaller circulation.

Assuming a steady and symmetric flow, the shed circulation Γ_s from an isolated circular cylinder can be estimated (Roshko 1954) by

$$\frac{\Gamma_s}{U_\infty d} = \frac{1}{2St}\left(\frac{u_s}{U_\infty}\right)^2,$$

where u_s is the velocity just outside the boundary layer at the separation point. Because of a relatively large T/d, the outer boundary layer nearer to the free stream may behave quite similarly to the counterpart of an isolated cylinder, the corresponding u_s being approximated by $1.45U_\infty$ (Cantwell and Coles 1983). Noting an identical Strouhal number St for both inner and outer row vortices, a smaller Γ_s associated with the inner boundary layer may then imply a smaller u_s but higher pressure than in the outer boundary layer.

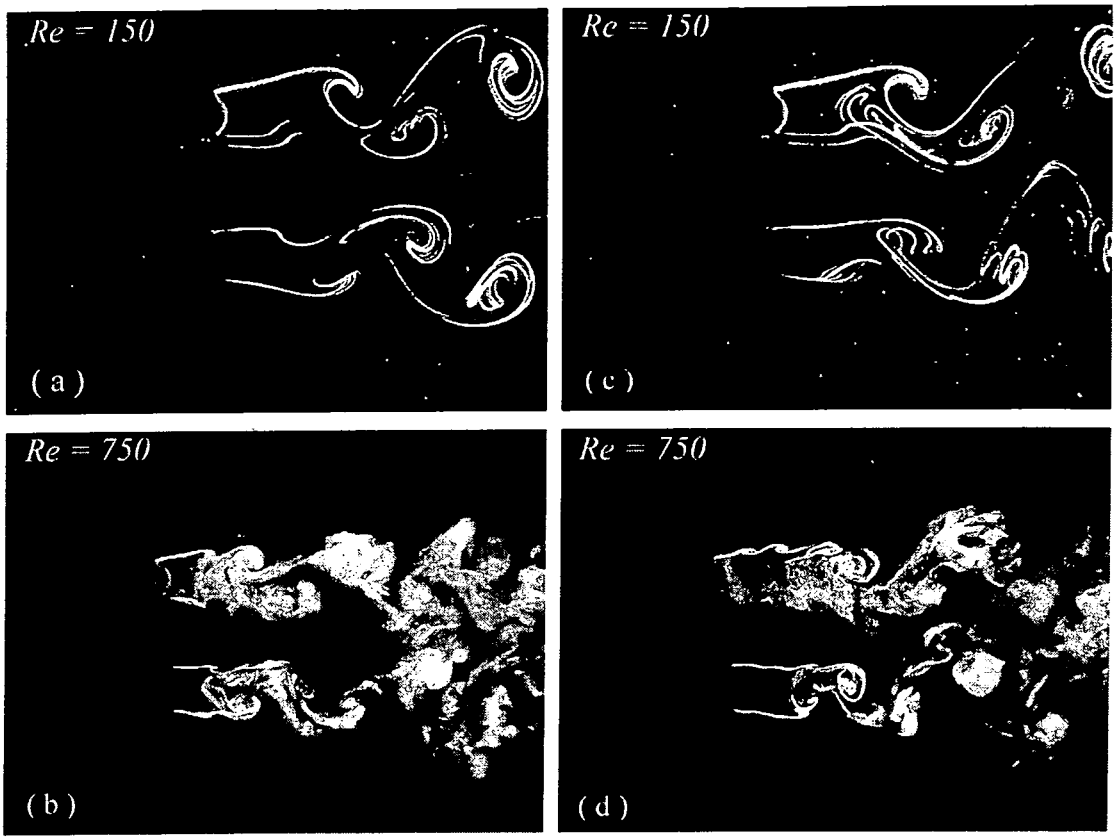

Figure 2-4 Typical flow patterns at T/d = 3.00. (a ~ b) Symmetric vortex shedding; (c ~ d) anti-symmetric vortex shedding. Flow is from left to right.

2.3.2 Flow patterns

The flow behind two cylinders at T/d = 3.00 display two distinct vortex streets, consistent with the LDA measurements. The vortices are mostly shed in symmetric pairs or the antiphase mode (Figs. 2-4a, b), irrespective of the laminar or turbulent flow regime. The spectrum (not shown) of the hot-wire signal exhibits a pronounced peak at an identical frequency, $f_s^* = f_s d / U_\infty \approx 0.2$ for both streets, which is identified with the vortex shedding frequency. The above observation is consistent with previous reports (e.g. Ishigai *et al.* 1972; Bearman and Wadcock 1973; Williamson 1985). Figure 2-5 presents the streamwise variation of the spectral phase angle $\Phi_{u_1u_2}$ at f_s^* between simultaneously measured hot-wire signals. The two hot wires were located symmetrically about the flow centreline. The values of $\Phi_{u_1u_2}$

are close to zero for $0 \leq x/d \leq 10$ irrespective of the lateral location of the hot wires. This observation suggests a predominantly symmetric arrangement of vortices, or in-antiphase mode vortex streets, persists at least up to $x/d = 10$.

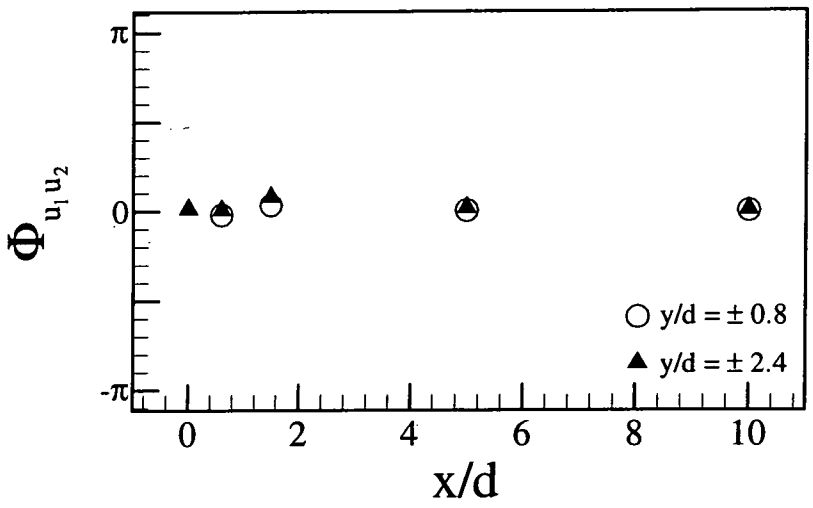

Figure 2-5 Streamwise variation of the spectral phase angle $\Phi_{u_1u_2}$ at the vortex shedding frequency f_s^* between simultaneously measured hot-wire signals. The two hot wires were located symmetrically about the flow centreline, i.e. at $y/d = \pm 0.8$ and ± 2.4. $T/d = 3.00$, $Re = 5900$.

Weaver and Abd-Rabbo (1984) and Granger *et al.* (1993) observed a symmetric vortex shedding in a square array of tubes in a cross flow. Weaver and Abd-Rabbo (1984) proposed that a symmetric-mode jet instability mechanism might have caused or at least triggered this phenomenon. Granger *et al.* (1993) suggested that the inline cylinder motion caused a symmetric oscillation of separation points at the surface of the moving cylinder and could be responsible for the symmetric vortex shedding. In the present investigation, the inline cylinder motion is unlikely to be responsible for the symmetric vortex shedding since vortex-induced vibration of the cylinders is negligibly small. The pressure measurement around the two cylinders, which will be presented later in Chapter 3, indicates that the pressure upstream of the gap between the cylinders was higher than that close to the free stream because of flow retardation. As a result, it can be inferred that there was a pressure difference on

the two sides of each cylinder in the cross-flow direction, in consistent with our earlier suggestion (Section 2.3.1) that the pressure of the inner boundary layer may be higher than that of the outer boundary layer. The difference may be symmetrical with respect to $y/d = 0$, as supported by the numerical calculation of the pressure field around two side-by-side cylinders at $T/d = 3$ and 4 (Meneghini *et al.* 2001). Such a pressure distribution is likely to suppress the anti-symmetrical or in-phase vortex shedding and induce the symmetric behaviour.

The anti-symmetric or inphase vortex shedding (Figs. 2-4c,d) occurs from time to time in the Re range investigated. The mode change from antiphase to inphase or vice versa is not well understand. Figure 2-6 shows the sequential photographs ($Re = 450$). The real time index is given by the first three numbers on the upper left-hand corner in the photographs and the sequential order is indicated by the fourth number. Initially, vortices were shed in symmetrical pairs (Plate 1). However, the two gap vortices, as marked by arrows in Plate 2, were formed with a small phase deviation from the antiphase vortex shedding. This is not unexpected especially in the context of a turbulent flow since a constant phase shift between the two gap vortices is highly unlikely. The gap vortices are fairly close to each other and therefore interaction between them may occur. Such interaction could encourage the formation of the staggered vortices. Furthermore, as the vortices grow downstream, the interaction is expected to intensify, resulting in an increased phase deviation from the antiphase mode (Plates 3 ~ 5). As a result, the following vortices were shed in phase from the two cylinders (Plates 5 and 6). Eventually, we see the two vortex streets arranged spatially in the in-phase mode (Plate 6). The two vortex streets in the inphase mode are however less stable and soon become somewhat disorganized; the formation of the upper gap vortex appears suppressed (Plates 7 ~ 11). The vortex streets restore to the in-antiphase mode within two shedding periods

(Plates 12-15). It may be concluded that, while the symmetric vortex shedding is relatively stable, the anti-symmetric vortex shedding, which may be initiated by a small phase deviation between the gap vortices, is unstable. The observation is likely attributed to a possibly symmetrical pressure differentiation about the flow centreline.

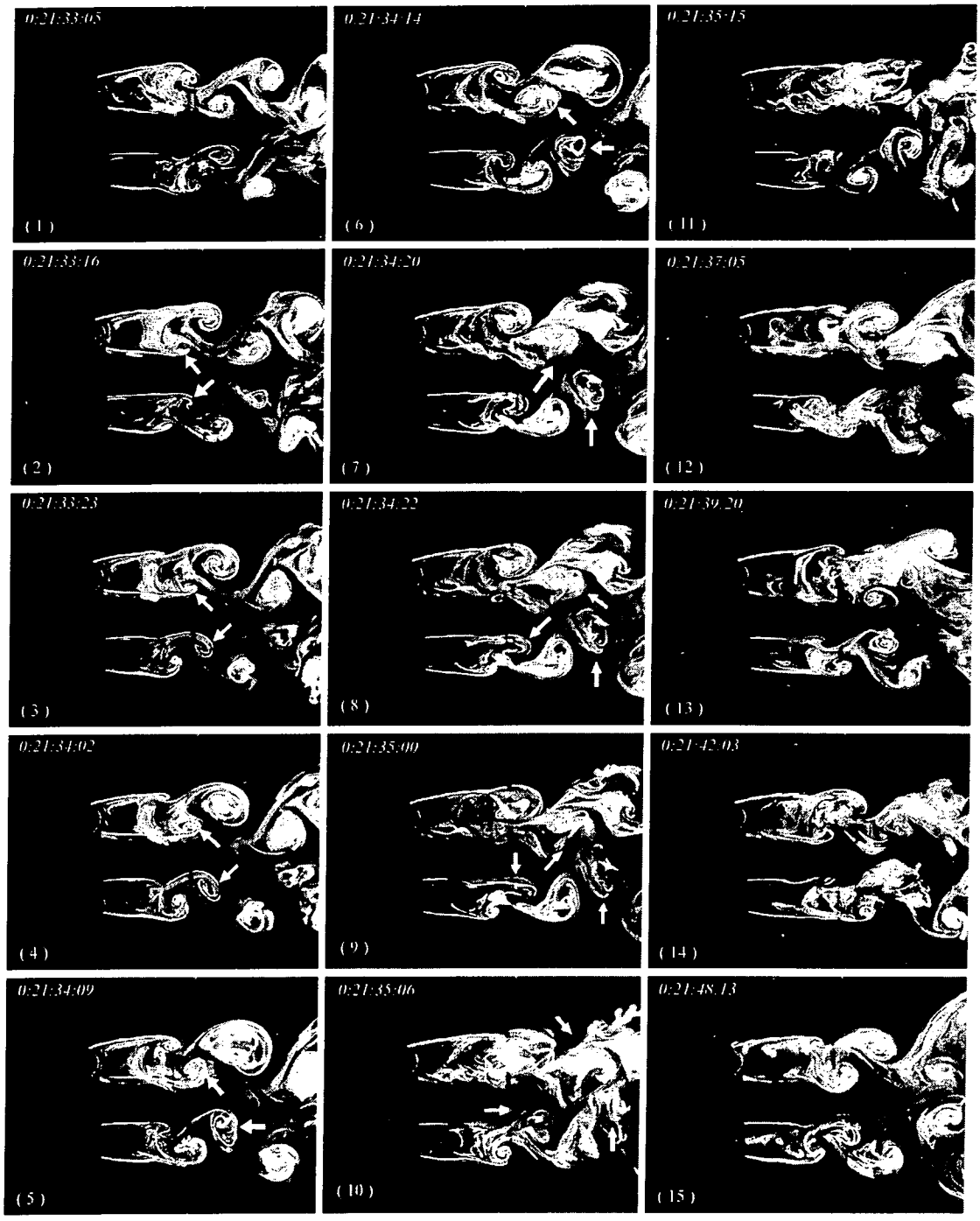

Figure 2-6 Sequential photographs from laser-illuminated flow-visualization: transition from the antiphase to inphase mode vortex shedding. T/d = 3.00, Re = 450.

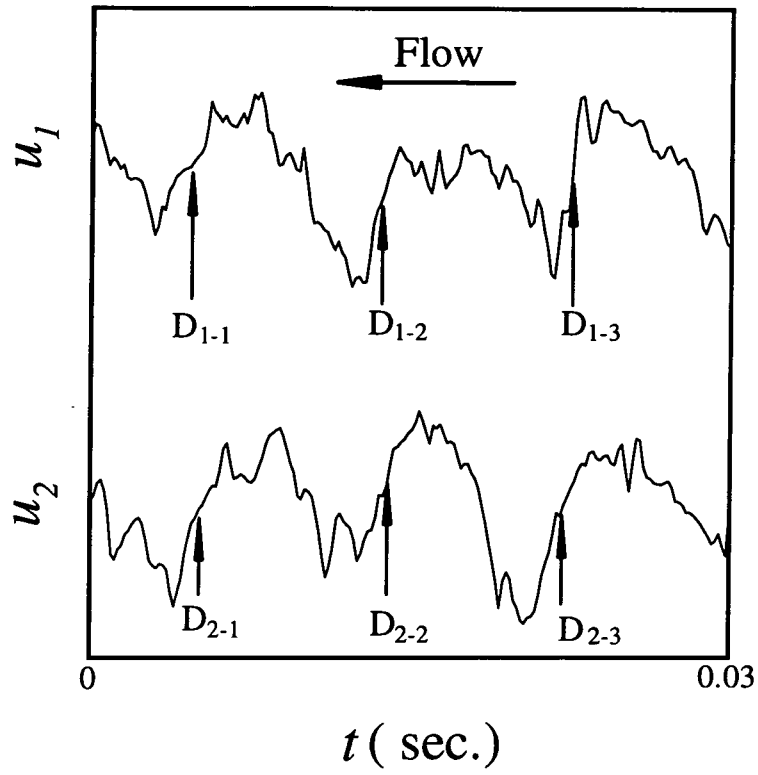

Figure 2-7 Detections using *WAG* technique (D_{1-1}, D_{1-2}, D_{1-3}, D_{2-1}, D_{2-2} and D_{2-3} denote detections). Hot-wire signals were obtained at x/d = 10 and $y/d = \pm 2.4$ ($T/d = 3.00$).

It is useful to quantify the contribution to the flow from the in-antiphase and in-phase mode streets. A window average gradient (*WAG*) method was used for detecting vortical structures. This method was described in Antonia and Fulachier (1989) and interested readers may refer to their paper for details. Briefly, this scheme examines the u- or v-signal and identifies an increase (or decrease) in average signal level over a specified time interval. The increase is associated with the occurrence of vortices. This technique proves to be quite adequate for the detection of vortical structures (e.g. Bisset *et al.* 1990; Zhou and Antonia 1992; Zhang *et al.* 2000). The lower and upper outer row vortices, shed from the free-stream side of a cylinder, were detected based on the signals obtained at $y/d = \pm 2.4$, respectively. A total of about 1100 events, which represent about one half of total vortices, were detected. Figure 2-7 illustrates the detections at x/d = 10 using the *WAG* method. The relative

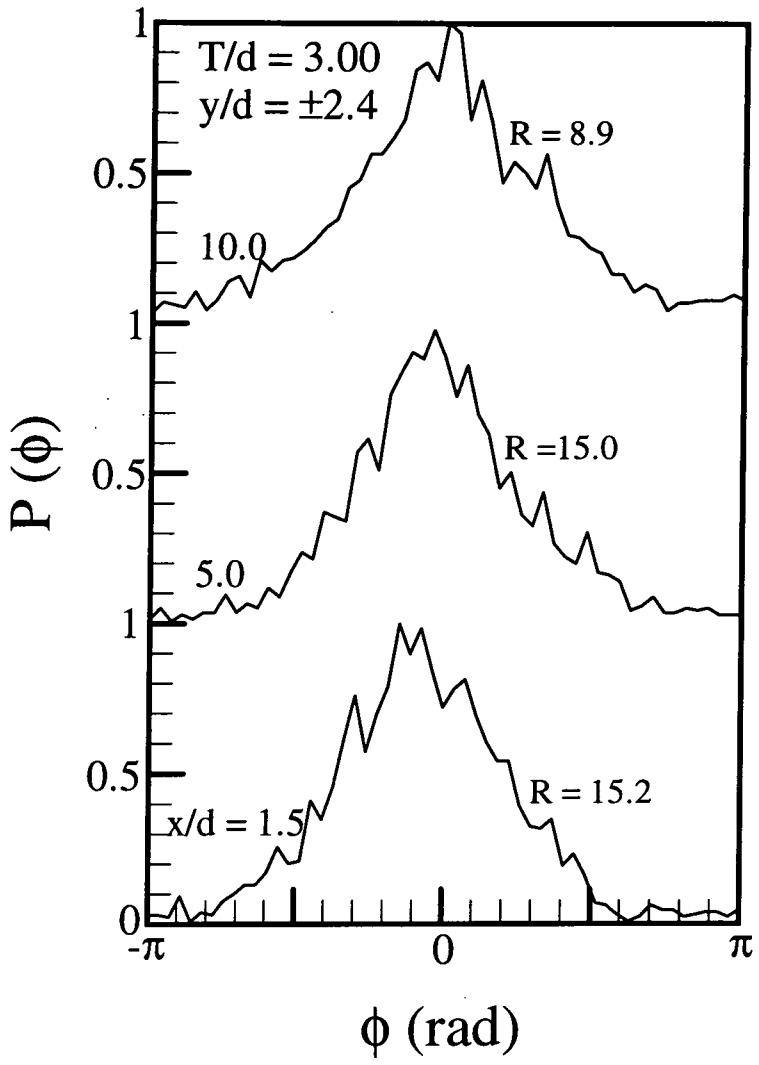

Figure 2-8 Relative probability $P(\phi)$ of the phase shift between detections from the simultaneously measured hot-wire signals at $y/d = \pm 2.4$. $T/d = 3.00$. $R = \int_{-\pi/2}^{\pi/2} P(\phi)d\phi / (\int_{-\pi}^{-\pi/2} P(\phi)d\phi + \int_{\pi/2}^{\pi} P(\phi)d\phi)$ indicates the ratio of the in-antiphase to in-phase mode streets.

probability $P(\phi)$ of the phase shift ϕ between the two sets of detections is presented in Figure 2-8. The probability has been normalised so that the maximum is 1. One prominent peak occurs at $\phi = 0$, indicating a predominantly symmetrical arrangement of the two outer row vortices, or vortex streets predominantly in antiphase mode. The probability is minimum but non-zero at $\phi = \pm\pi$, apparently due to the occurrence of staggered vortices or the in-phase vortex streets. If we refer to the events occurring

over $-\frac{\pi}{2} < \phi < \frac{\pi}{2}$ as the in-antiphase mode streets and those over $-\pi < \phi < -\frac{\pi}{2}$ or $\frac{\pi}{2} < \phi < \pi$ as the in-phase mode streets, then the ratio between the two modes may be estimated as $R = \frac{\int_{-\pi/2}^{\pi/2} P(\phi)d\phi}{\int_{-\pi}^{-\pi/2} P(\phi)d\phi + \int_{\pi/2}^{\pi} P(\phi)d\phi}$. The R value (Fig. 2-8) is well above unity, indicating a predominance of the in-antiphase mode streets. Furthermore, R slowly decreases as x/d increases, especially, at x/d > 5.0, i.e. R decreases from 15.2 at x/d = 1.5 to 8.9 at x/d = 10.0, suggesting an increase in in-phase streets. The inner vortices, shed from the side of cylinders close to the flow centreline were also detected based on the signals obtained at $y/d = \pm 0.8$ using the *WAG* technique. The result (not shown) is essentially the same as those obtained from the outer vortices and internally consistent with both the flow visualisation and the spectral phase shift (Fig. 2-5) at f_s^* between the hot-wire signals.

2.4 Asymmetrical Flow for Intermediate Cylinder Spacing

Previous research (Spivack 1946; Ishigai *et al.* 1972; Bearman and Wadcock 1973; Kamemoto 1976; Kiya *et al.* 1980; Kim and Durbin 1988; Sumner *et al.* 1999) on the flow behind two cylinders at intermediate cylinder spacing, i.e. at T/d = 1.2 ~ 2.0, has revealed that the gap flow between the two cylinders is deflected, thus forming one narrow and one wide wake. The narrow and wide wakes are associated with the high and the low vortex frequencies, respectively. The ratio of the two frequencies is close to but less than 3. The gap flow deflection may switch, in a random manner, from one side to the other and is stable in either side. This is reconfirmed in the present investigation. This section will focus on the following issues, that is, why the gap flow is stably deflected, what causes the changeover of

the gap flow from one side to the other and why the dominant frequency in the narrow wake triples that in the wide wake.

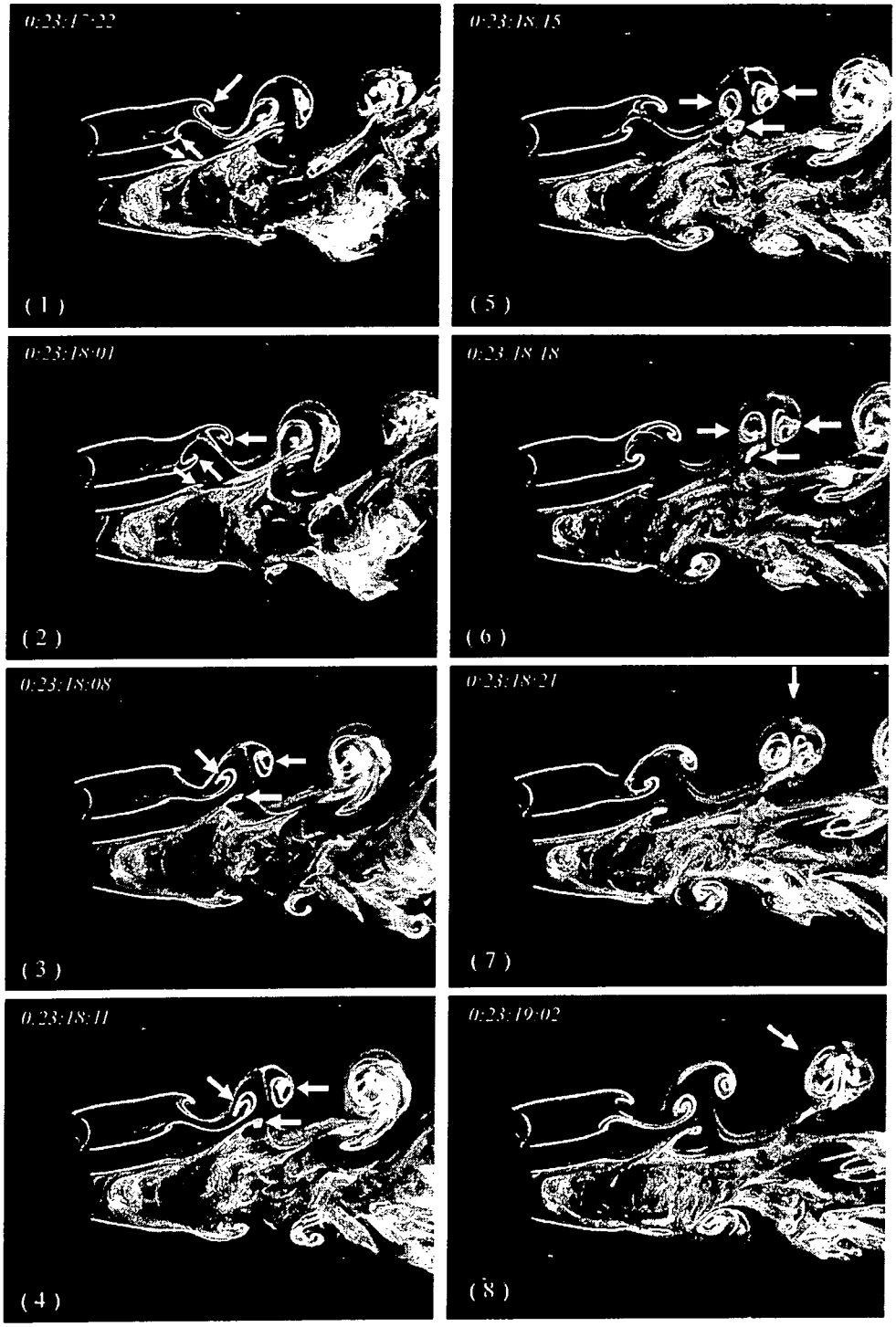

Figure 2-9 Sequential photographs from laser-illuminated flow-visualization: the pairing opposite-signed vortices in the narrow wake draw in the gap vortex in the wide wake. $T/d = 1.70$, $Re = 450$.

2.4.1 Stably deflected gap flow

Since the two cylinders are relatively close, interactions between the wakes generated by individual cylinders are expected to be strong. The interactions may naturally influence the behaviours of the gap flow and contribute to its stable deflection. Figure 2-9 presents typical sequential photographs from laser-illuminated flow-visualization at $T/d = 1.70$ ($Re = 450$). Two rows of vortices in the narrow wake appear pushed by the wide wake so that their lateral spacing is very small. Initially (Plates 1 ~ 3), the longitudinal spacing between two opposite-signed vortices in the narrow wake, as marked by arrows, is large. However, Plates 4 and 5 show a reduced spacing, both longitudinally and laterally, between the vortices. It is likely that the gap vortex travels faster than the outer vortex, possibly carried by the gap flow jet of a higher mean velocity. The two approaching counter-rotating vortices could create a region between them, where the lateral velocity (upwards) is relatively high and pressure being low. The low-pressure region induces the two vortices to further approach each other and subsequently pair with each other (Plates 5 and 6). In the meantime, the low-pressure region probably also draws in fluid in the wide wake. This is evident from the movement of the gap vortex generated in the wide wake, also marked by an arrow. This gap vortex appears approaching the region between the pairing vortices (Plates 3 ~ 6). As a matter of fact, the gap vortex amalgamated with the two pairing vortices and eventually formed a single structure (Plates 7 ~ 8). This observation was found to be quite typical in the Re range presently investigated.

The gap flow deflection and the formation of wide and narrow wakes behind a row of bluff bodies for $T/d = 1.5 \sim 2.0$ have been reported by a number of previous studies (e.g. Ishigai *et al.* 1972; Moretti 1993; Williamson 1985). Ishigai *et al.* and Moretti attributed the phenomenon to the Coanda effect (Englar 1975). However,

Bearman and Wadcock (1973) and also Williamson (1985) observed the deflected gap flow between two parallel flat plates as well as circular cylinders. The observation did not support the proposition that the Coanda effect was responsible for the deflected gap flow. One may surmise that, since a straight flow between abrupt two-dimensional bluff bodies tends to be unstable, the initial deflection of the gap flow may occur due to perturbations such as non-symmetric vortex shedding from the two cylinders. A number of factors may contribute to the stably deflected gap flow. Firstly, the gap flow is associated with a relatively high momentum. Therefore, the base pressure behind the cylinder, towards which the gap flow is deflected, should be low, and that behind the other cylinder, where fluid has a relatively low momentum, would be high. Secondly, the vortices shed from the cylinder in the narrow wake are generally characterized by a high frequency and perhaps relatively weak strength. Those generated in the wide wake could be even weaker (Fig. 2-9). Therefore, the fluctuation of the velocity or pressure field could have a limited strength, generally not strong enough to force the gap flow to change over from one side to another. Thirdly, carried by the gap flow jet of relatively high mean velocity, the gap vortex in the narrow wake possibly travels downstream faster than the outer vortex. The approaching two counter-rotating vortices could result in a low-pressure region between them. Meneghini *et al.* (2001) conducted a numerical study of the flow behind two side-by-side cylinders. At $T/d = 1.5$ ($Re = 200$), the two counter-rotating vortices (their Figure 15a) in the relatively narrow (lower) wake appeared fairly close. The pressure corresponding to the region between the two vortices (their Figure 14a) was low and hence drew in the fluid from the other wake (their Figure 15a). The present data further indicates that the low-pressure region draws in the gap vortex as well as fluid in the wide wake, thus acting to stabilise the formed narrow and wide wake.

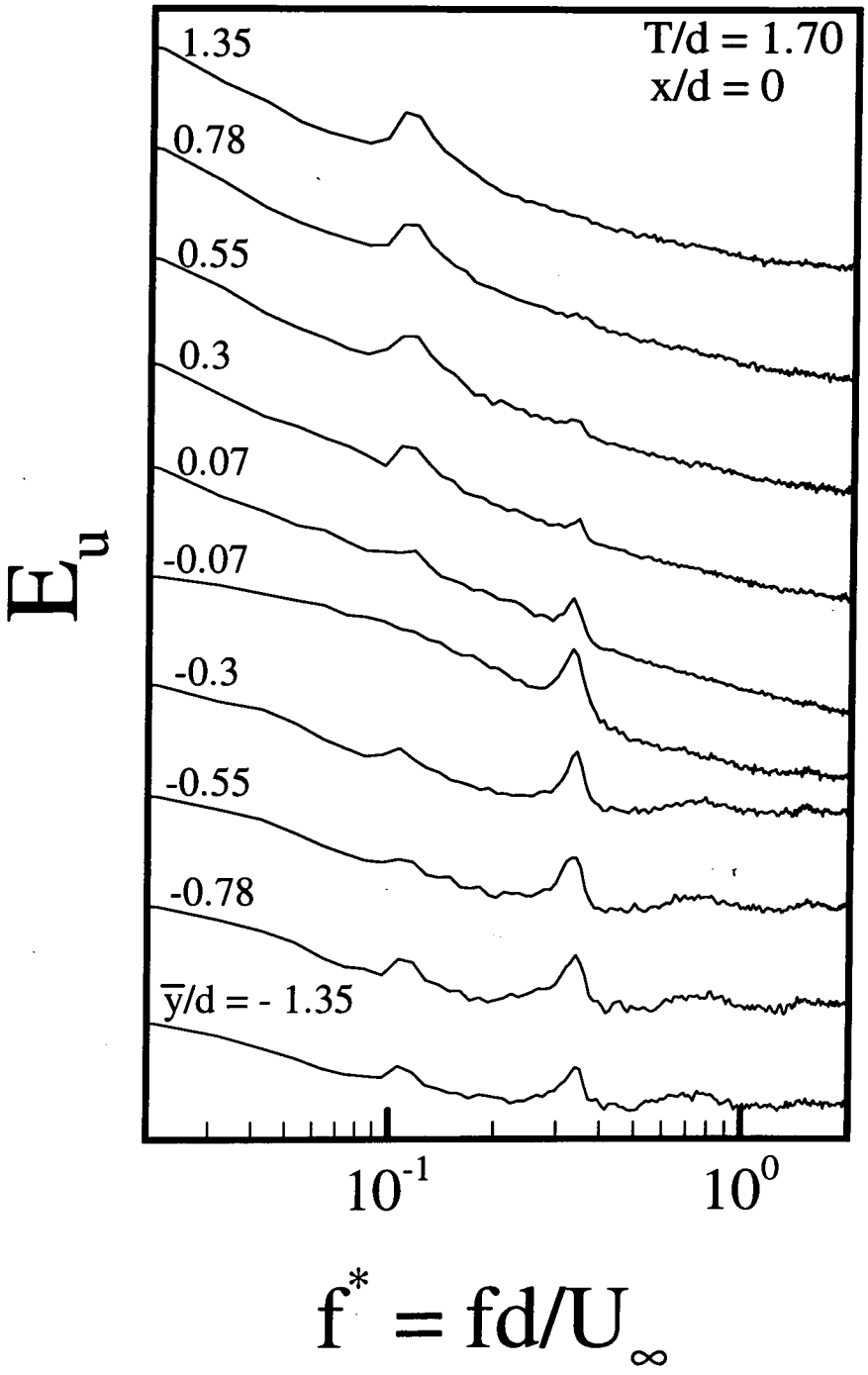

Figure 2-10 Power spectrum E_u of the hot-wire signals simultaneously measured in the two outer shear layers associated with the two cylinders. Here $\bar{y}/d$ is the distance from the cylinder surface at $x/d = 0$, given by $y/d - 1.35$ for the upper cylinder and $y/d + 1.35$ for the lower cylinder. $T/d = 1.70$.

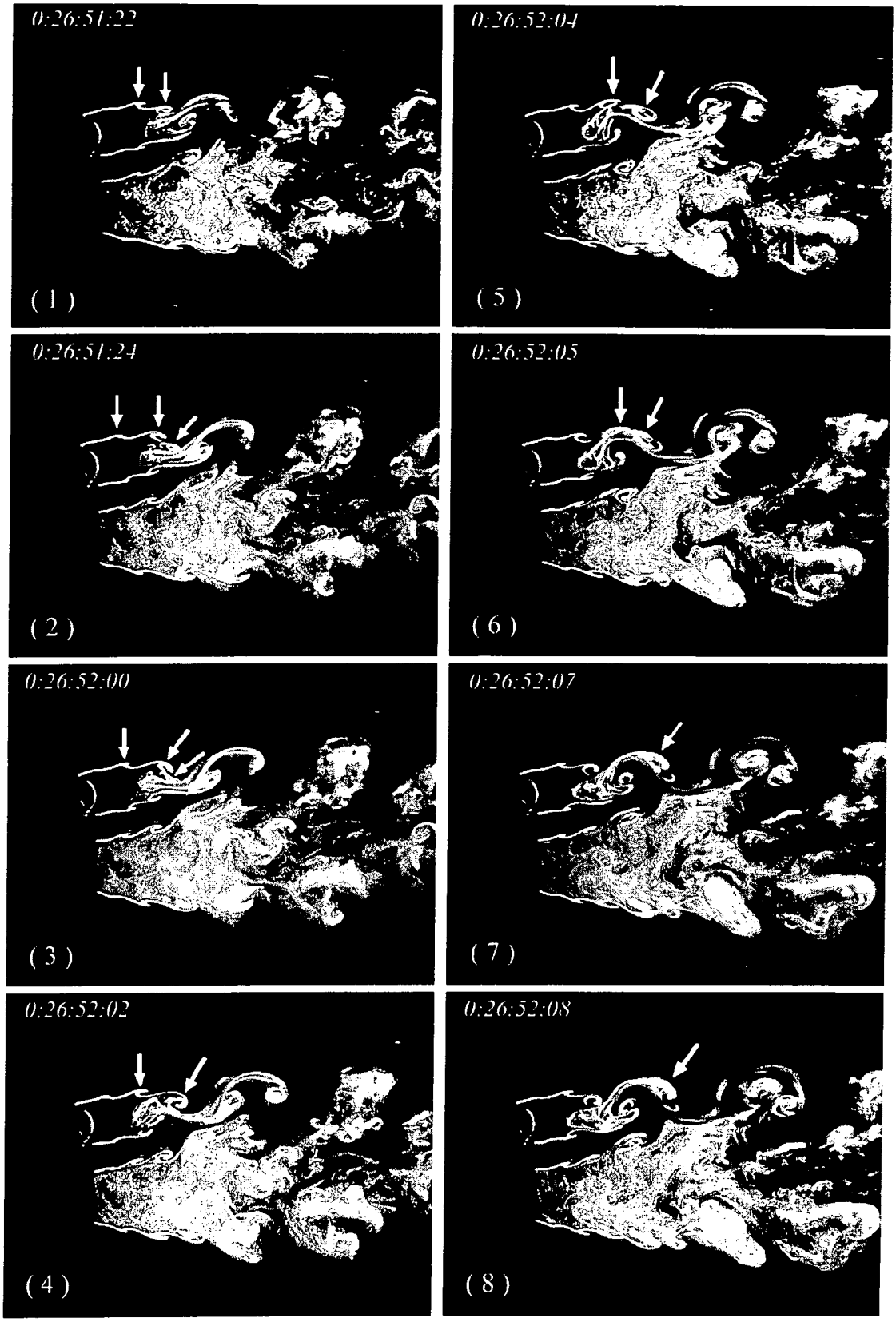

Figure 2-11 Sequential photographs from laser-illuminated flow-visualization: the coalescence of the small-scale secondary vortices. T/d = 1.70, Re = 600.

2.4.2 Dominant frequencies in each wake

It has been previously reported that the narrow and wide wakes observed in flow visualisation were associated with the high and low vortex frequencies, respectively (Spivack 1946; Ishigai *et al.* 1972; Bearman and Wadcock 1973; Kamemoto 1976; Kiya *et al.* 1980; Kim and Durbin 1988; Sumner *et al.* 1999). The ratio of the two frequencies was close to but less than 3 (Kim and Durbin 1988). The physics behind the occurrence of two different frequencies is not clear; some researchers (Kim and Durbin 1988; Sumner *et al.* 1999) referred to the frequencies as vortex-shedding frequencies. Based on flow visualisation at a low Re ($\leq$ 200), Williamson (1985) proposed that the two frequencies resulted from the existence of harmonic vortex-shedding modes. But Kim and Durbin (1988)'s data at Re = 3300 did not support this conjecture.

To gain a better understanding of the multiple dominant frequencies, two hot wires were placed, symmetrically with respect to y/d = 0, at x/d = 0 in the two outer shear layers (close to the free-stream), which were associated with the two cylinders, respectively. Figure 2-10 presents the power spectrum E_u of two simultaneously obtained hot-wire signals, where $\overline{y}/d$ is the distance for the cylinder surface, given by y/d – 1.35 for the upper cylinder and y/d + 1.35 for the lower cylinder. Two peaks are identifiable at $f^* \approx 0.1$ and 0.3, respectively, in each shear layer, though the strengths of the peaks are different from one shear layer to the other. For example, the peak at $f^* \approx 0.3$ is more pronounced in the shear layer associated with the lower cylinder, but weaker in the shear layer associated with the upper cylinder.

The question is naturally raised: which is the vortex shedding frequency? It is well known that the separating shear layer from a cylinder becomes unstable for Re > 1000 and small-scale structures or secondary vortices emerge (Wei and Smith 1986;

Prasad and Williamson 1997). The coalescence of the small-scale secondary vortices will increase the scale and decrease the frequency of shear layer instability to the Strouhal frequency (Winant and Browand 1974; Brown and Roshko 1974; Roshko 1976; Ongoren and Rockwell 1988a and b). The secondary vortices are discernible at Re = 450 and become evident in the present flow visualisation for $Re \geq 600$. These vortices are seen coalescing to form a larger vortex. Figure 2-11 show sequential photographs from flow visualisation. Two small-scale vortices, marked by arrows, are discernible in the narrow wake (Plate 1). They approach each other and form a larger structure (Plates 2 ~ 4). In the meantime, another small-scale vortex occurs (Plates 2 ~ 4) and catches up with the larger structure (Plates 5 ~ 6). They eventually coalesce and roll up into a single vortex in the narrow wake (Plates 7 ~ 8). The frequencies of the secondary vortices and the vortices shed from the cylinder in the narrow wake were estimated by means of counting consecutive vortices (about 20 pair) for a certain period. It is rather difficult to count accurately the secondary vortices and thus determined frequency (normalised) scattered over the range of 0.2 to 0.5. But for the relatively large-scale vortices shed from the cylinder, the frequency estimate was less scattered, ranging between $f^* = 0.10$ and 0.13 for Re = 600. Similar results were obtained for other Re. The observation suggests that, while the vortex shedding may be responsible for the peak at $f^* \approx 0.1$ in the narrow wake, the secondary vortices could account for the peak at $f^* \approx 0.3$.

The most dominant frequency in the wide wake is $f^* \approx 0.1$ (Fig. 2-12b). The vortex rolling-up frequency was also estimated by counting consecutive vortices (about 20 pair) for a certain period on flow visualisation data. The result is consistent with that from the spectrum E_u. For example, f^* was about 0.11 at Re = 450. Note that the vortex rolling-up in the wide wake occurs quite far away from the cylinder

(Figs. 2-9 and 2-11), apparently different from the vortex shedding from a cylinder. Furthermore, the peak at $f^* \approx 0.1$ grows downstream (Fig. 2-12b). The observations suggest that the vortical structures in the wide wake may be formed under the effect of shear layer instability.

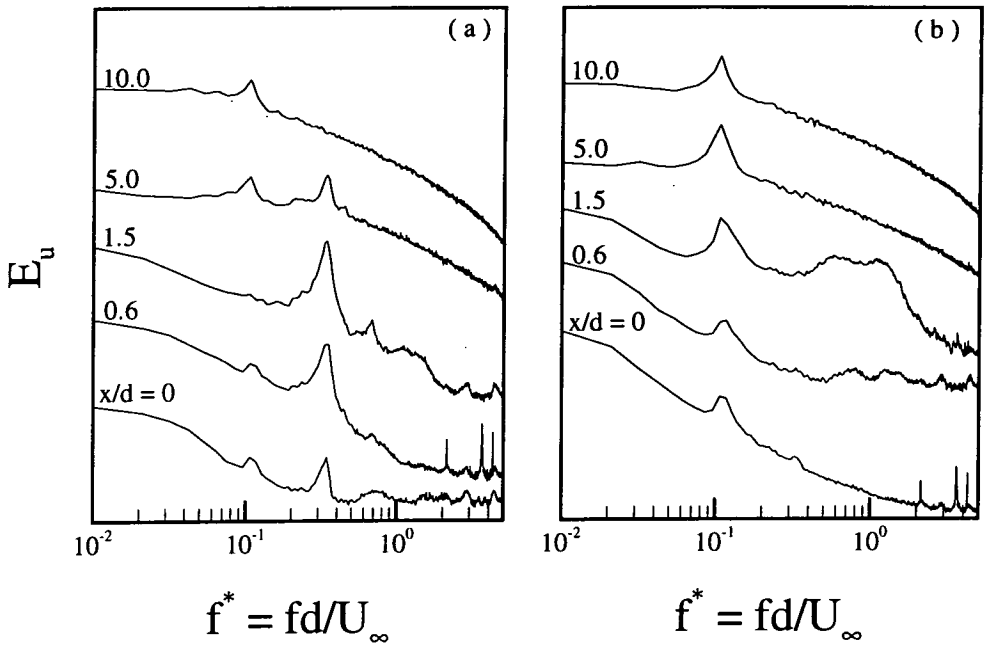

Figure 2-12 Downstream evolution of the power spectrum E_u of hot-wire signals simultaneously measured at $y/d = \pm 2.0$: (a) the narrow wake; (b) the wide wake. $T/d = 1.70$, $Re = 5900$.

Figure 2-12a shows the downstream evolution of the power spectrum E_u in the narrow wake. The peak at $f^* \approx 0.3$ reaches maximum at $x/d = 1.5$ and then is considerably reduced at $x/d = 5$. By $x/d = 10$, there is no presence of the peak at $f^* \approx 0.3$. Flow visualisation data (e.g. Fig. 2-11) indicates that the vortex rolling-up appears complete near $x/d = 3$ for the Reynolds number of 600. However, the peak at $f^* \approx 0.3$ in E_u is still identifiable at $x/d = 5$. As discussed in Section 2.4.1.1, the two rows of vortices in the narrow wake appear squeezed by the wide wake so that their

lateral spacing is very small. Furthermore, the two opposite-sign vortices draw in the approaching gap vortex in the wide wake. Note that the vortex shedding frequency in the narrow wake might be the same as the vortex rolling-up frequency in the wide wake. Because of the small lateral spacing between the three vortices, the hot wire could measure a frequency tripling that in the wide wake.

It is interesting to note that the frequencies of the shear layer instability at x/d = 0 are the same as those predominant in the vortex streets downstream. This may not be coincidental. Based on the published data (Norberg 1987; Bloor 1964; Okamoto *et al.* 1981; Kourta *et al.* 1987; Wei and Smith 1986; Maekawa and Mizuno 1967) and their own measurement, Prasad and Williamson (1997) obtained an empirical correlation between Re and the frequency, f_{SL}, of the shear layer instability for a single cylinder in a cross flow, that is, $f_{SL}/f_S = 0.0235 \times Re^{0.67}$. This correlation would predict $f_{SL}^* = 0.789$ for the present Reynolds number, significantly higher than the measurement. Although strong interactions between shear layers associated with different cylinders may contribute to the deviation, the upstream influence from the downstream vorticity dynamics should not be overlooked. This influence may have an impact upon the initial evolution of the shear layer instability (Rockwell 1983; Ho and Huerre 1984). Michalke (1984) further suggested that the initial shear layer instability was controlled by downstream vorticity dynamics. Roshko (1954) proposed a universal Strouhal number $St_u = \frac{f_s d_w}{U_w}$, where d_w is the wake width and $U_w = U_\infty (1 - C_{pw})^{1/2}$, where C_{pw} is the pressure in the wake. St_u is a constant, about 0.16 in a single cylinder wake. The Strouhal number St was then written as $St = St_u \frac{d}{d_w}(1 - C_{pw})^{1/2}$. Evidently, d_w or the shear layer thickness and St are inversely related. Presumably, this relationship is also valid in the wide wake, where the vortical structures are probably generated by the shear layer instability.

This implies that the vortical structure frequency $f^* \approx 0.1$ might be dictated by the shear layer thickness. This frequency may feed back upstream and excites the instability of shear layers around the cylinders, thus inducing the vortex shedding at $f^* \approx 0.1$ from the cylinder, behind which the narrow wake is formed.

The interaction between vortices in the streets may be responsible for peak at $f^* \approx 0.3$ in the hot-wire spectrum. As proposed earlier, the two cross-stream vortices in the narrow wake and the gap vortex in the wide wake approach laterally as well as longitudinally in the process of amalgamation, acting to produce a dominant frequency $f^* \approx 0.3$. This frequency could also feed back upstream and excite the shear layer instability. Because of vorticity cancellation between oppositely signed structures, the vortical structure formed from the amalgamation of the three vortical structures is probably weak in strength, compared with that in the wide wake. Consequently, the peak in the spectrum E_u (Fig 2-10) at $f^* \approx 0.1$ is significant in the shear layers associated with both cylinders, whereas the peak at $f^* \approx 0.3$ is not so evident in the shear layer associated with the cylinder, which is relatively far away and responsible for the generation of the wide wake.

It is worthwhile commenting on the dependence of the vortex formation length on the Reynolds number. It is well known that the vortex formation length behind an isolated cylinder reduces as Re increases (Gerrard 1966). This is also evident in the flow behind two cylinders. For instance, Figure 2-13 indicates that the vortex formation length at $T/d = 1.70$ is greatly reduced at $Re = 1100$, compared with $Re = 150$ or 450. The observation implies that the gap vortex in the wide wake may amalgamate with the pairing opposite-sign vortices in the narrow wake at a location closer to the cylinders for a large Reynolds number. Noting that the amalgamation occurs near $x/d = 5$ for $Re = 450$ (Fig. 2-9), it would not be surprised to see the amalgamation appreciably before $x/d = 5$ for $Re = 5900$. This may explain why the

peak at $f^* \approx 0.3$ in the hot-wire spectrum (Fig. 2-12) is more pronounced at x/d = 1.5 than that at x/d = 5. A reduced vortex formation length is also consistent with a larger gap deflection angle (Fig. 2-13) as Re increases.

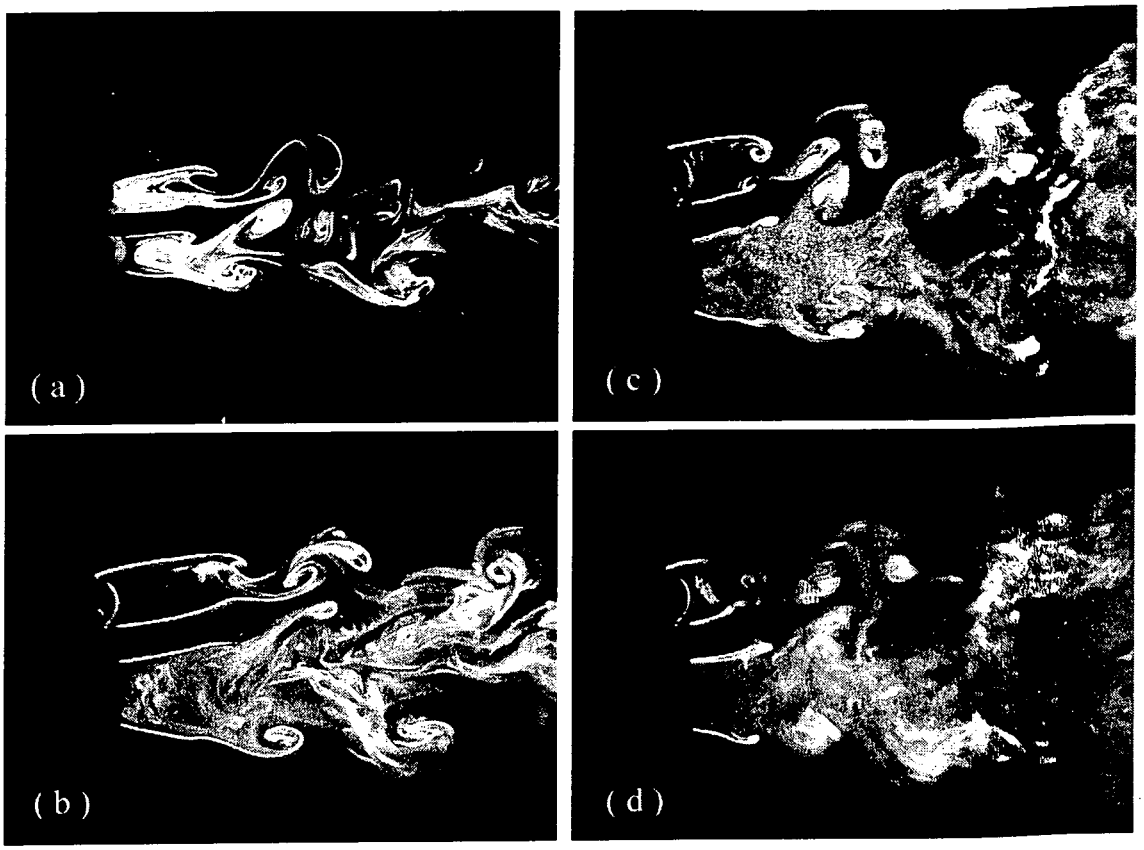

Figure 2-13 Dependence of the vortex formation length on Re: (a) Re = 150, (b) 450, (c) 750, (d) 1100. T/d = 1.70.

2.4.3 Changeover of the gap flow

It is well known that for $1.2 < T/d < 2.0$ the biased gap flow is bi-stable and intermittently changes over from one side to another, forming two asymmetric vortex streets of different frequencies (e.g. Ishigai *et al.* 1972; Bearman and Wadcock 1973; Kim and Durbin 1988). However, physics behind the changeover is so far not well understood. A close examination of the present flow-visualization data unveils that the changeover of the deflected gap flow from one side to another is often associated

with the occurrence of unusually large gap vortices, as marked by an arrow in Figure 2-14 for *Re* = 150, 230 and 300.

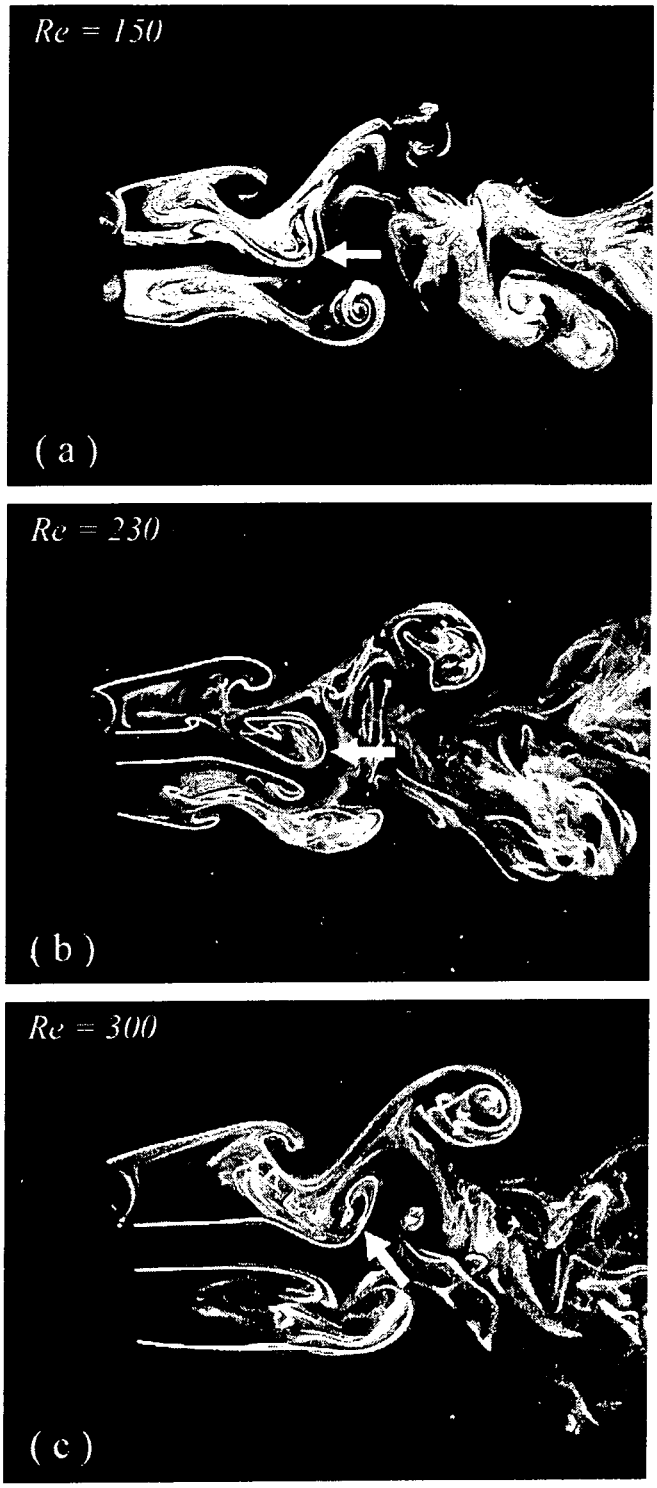

Figure 2-14 The changeover of the gap flow deflection from one side to another at *T/d* = 1.70 is associated with an exceptionally large gap vortex. (a) *Re* = 150; (b) *Re* = 230; (c) *Re* = 300.

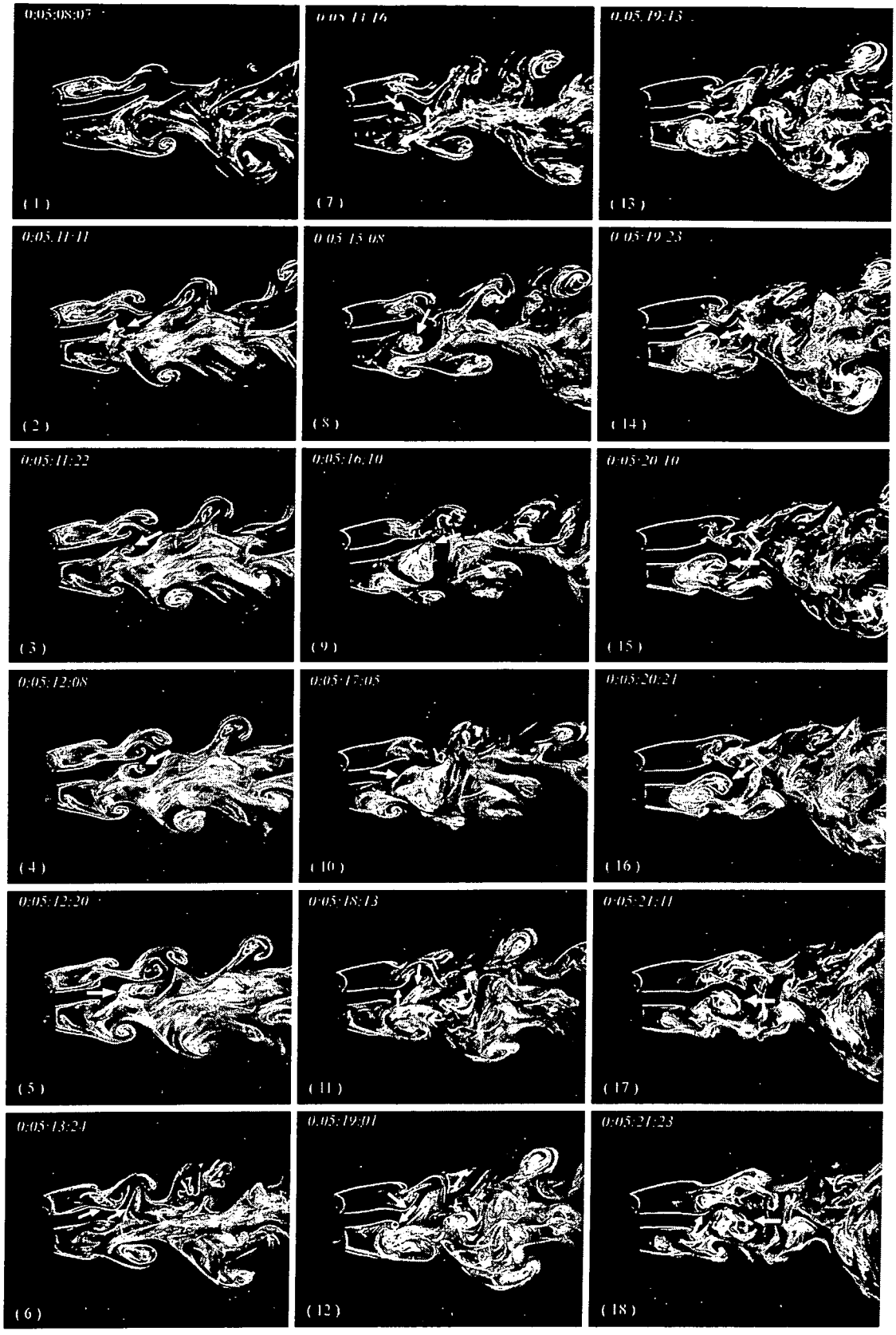

Figure 2-15 Sequential photographs from laser-illuminated flow-visualization: the changeover of the gap deflection from one side to another. T/d = 1.70, Re = 230.

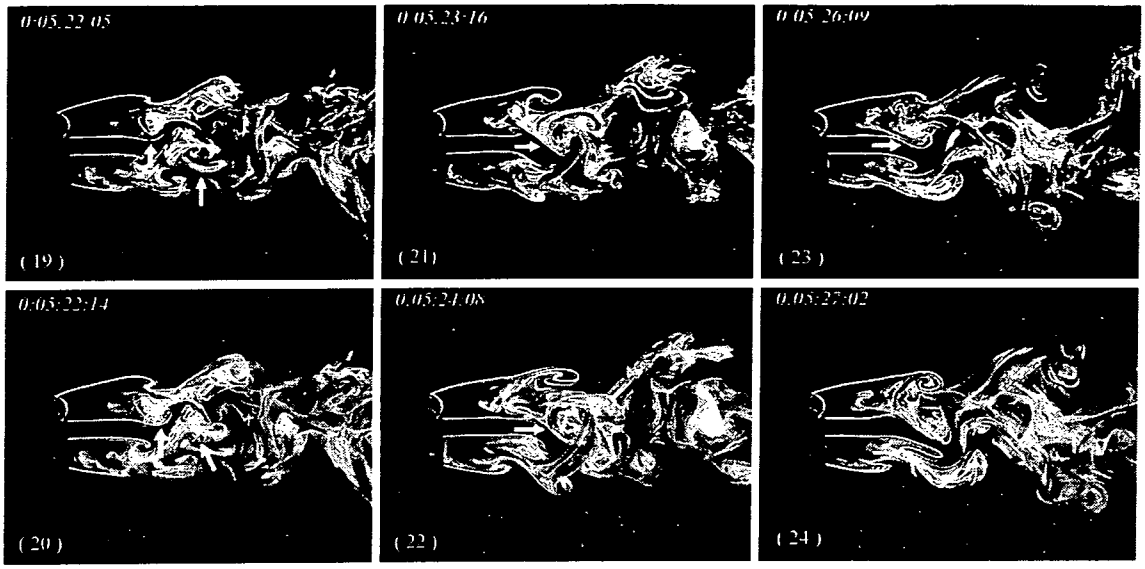

Figure 2-15 (Continue)

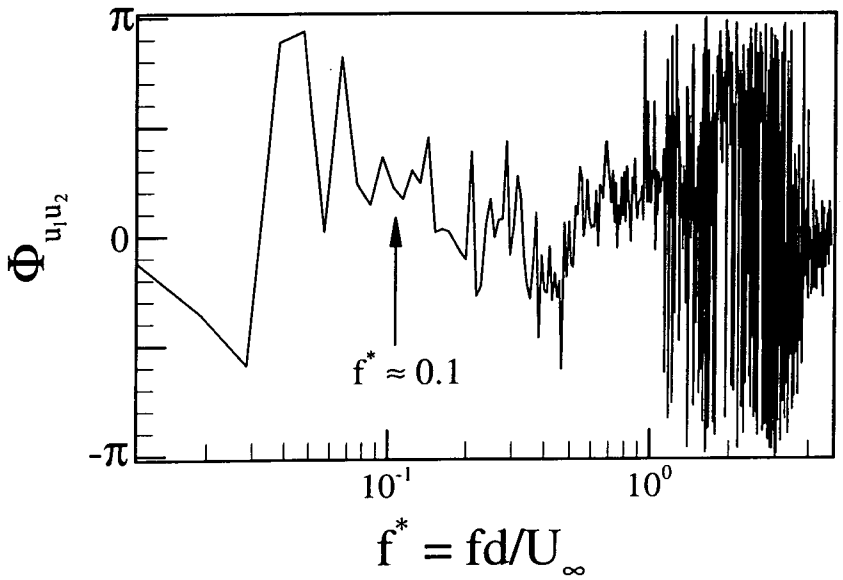

Figure 2-16 Spectral phase angles $\Phi_{u_1u_2}$ between simultaneously measured hot-wire signals. The hot wires were placed at $y/d = \pm 0.4$. $T/d = 1.70$, $x/d = 1.5$.

In order to gain insight into this phenomenon, Figure 2-15 presents sequential photographs at Re = 230 of the changeover process. Initially, the gap flow was deflected upwards (Plate 1). The gap vortices in the two wakes appear in-antiphase.

See Figure 2-9 for example. This is supported by the spectral phase angle $\Phi_{u_1u_2}$ (Fig. 2-16) of near zero at $f^* \approx 0.1$ between simultaneously measured hot wire signals u_1 at y/d = + 0.4 and u_2 at y/d = - 0.4 (T/d = 1.70, x/d = 1.5). Here, u_1 and u_2 have been identified to be associated with wide and narrow wakes, respectively, based on the prominent frequencies in the power spectra, E_{u_1} and E_{u_2} (not shown). The spectral phase angle is calculated from the Fourier transform of the correlation $\overline{u_1(t+\tau)u_2(t)}$. A positive phase angle indicates that u_1 leads u_2, and a negative phase angle means that u_2 leads u_1. $\Phi_{u_1u_2}$ at $f^* \approx 0.1$ is greater than zero (Fig. 2-16), indicating that u_1 leads u_2 at this frequency, that is, the gap vortex in the wide wake generally leads that in the narrow wake. The gap vortex in the wide wake, as marked by arrows in Plate 2 (Fig. 2-15), failed to amalgamate with the vortices pairing in the narrow wake (Plates 3 ~ 4), perhaps because of an unfavourable phase shift between the two gap vortices. As a matter of fact, the gap vortex in the wide wake appears lagging behind that in the narrow wake (Plate 4). Subsequently, this vortex (Plate 4) grew unusually large (c.f. Figure 2-9), but quickly 'collapsed' (Plates 5), probably due to the increased interaction with the narrow wake. The collapse of this gap vortex could momentarily alleviate the interaction between the narrow and the wide wake, allowing the narrow wake to swing towards the wide wake (Plates 6 ~ 7). Meanwhile, the weak interaction also encouraged the fast growth of the following gap vortex in the wide wake (Plates 6 ~ 8), which subsequently collapsed again (Plates 9 ~ 10). Similar cycles were repeated (Plates 11 ~ 19 and Plates 20 ~ 24). In each cycle, the gap vortex in the wide wake lagged behind that in the narrow wake and experienced a rapid growth and then collapse. On the other hand, the gap vortex in the narrow wake became larger after these cycles, as Plates 20 and 23~24 indicated, and eventually pushing over the gap flow to the other side (Plates 24), and then we see an

upper wide wake and a lower narrow wake. Note that in the whole changeover process, the gap vortex in the wide wake had no chance to amalgamate with the pairing vortices in the narrow wake, possibly because of a phase lag behind that in the narrow wake. The observation is consistent with the suggestion that the amalgamation of the three vortices could be important for maintaining the existing narrow and wide wakes.

In conclusion, the gap vortices in the two wakes tend to be in antiphase, but the one in the wide wake mostly leads slightly that in the narrow wake and amalgamates with the pairing vortices in the narrow wake. The changeover of the gap flow deflection starts with a phase lag of the gap vortex in the wide wake behind that in the narrow wake. Once lagging behind (compared with antiphase), the gap vortex in the wide wake could be prevented from amalgamation with the pairing vortices in the narrow wake. The gap vortex in the wide wake is subsequently likely to grow fast but quickly collapses. The collapse alleviates the interaction between the two wakes, thus allowing the narrow wake to be widened and eventually causing the changeover of the gap flow deflection. The whole process typically needs three to four vortex shedding cycles in the narrow wake. Speculatively, the 'phase lag' results from interactions between the two wakes. It is therefore not surprising to see the random changeover of gap flow deflection.

2.5 Role of Gap Bleeding for Small Cylinder Spacing

2.5.1 Mean velocity and Reynolds stresses

Figure 2-17 presents the cross-flow distributions of the mean velocity, Reynolds stresses. $\overline{U}^*$ at x/d = 1.5 displays two troughs, as the case of T/d = 1.70. The peak between the troughs occurs significantly away from y/d = 0, indicating a

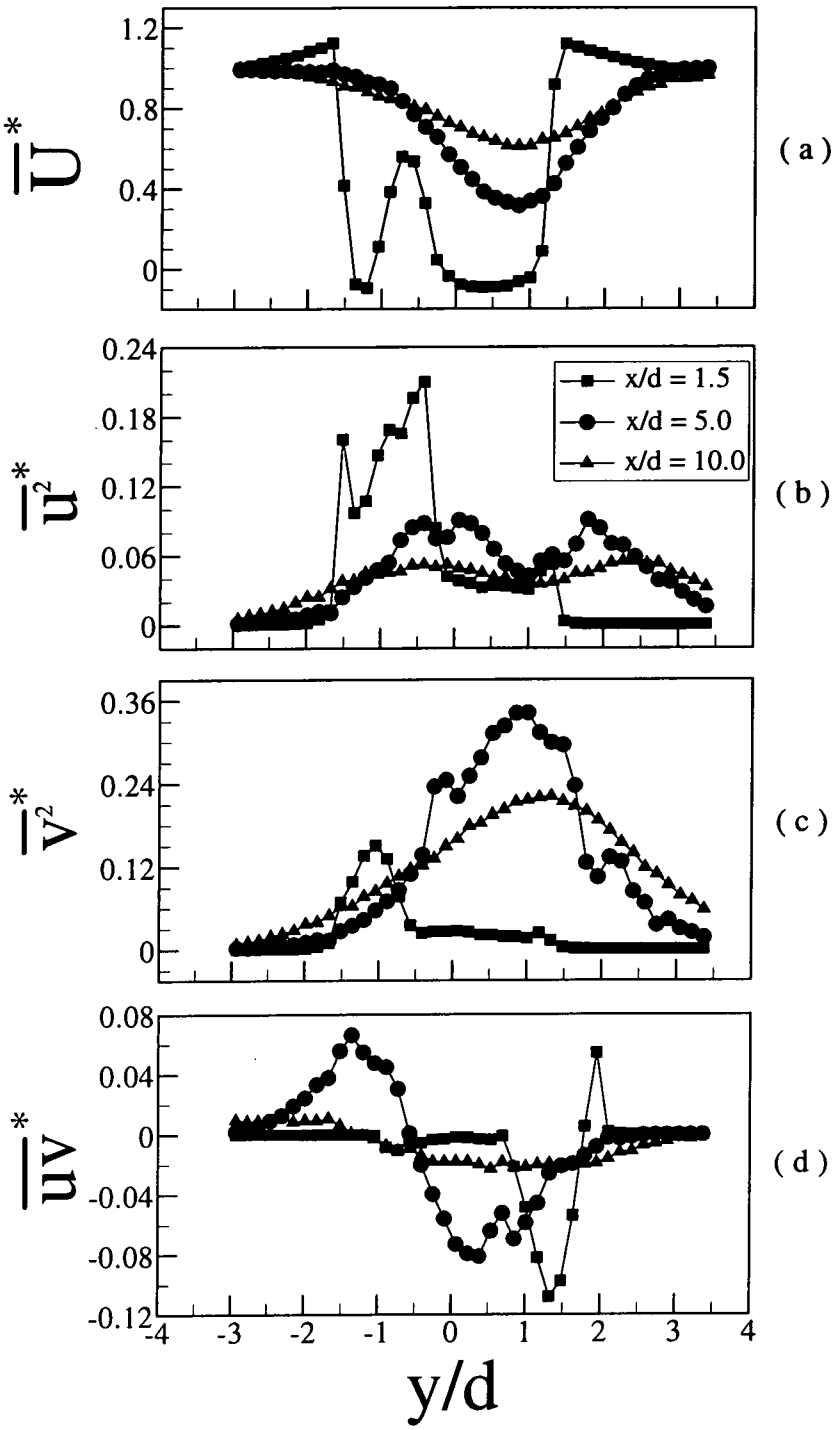

Figure 2-17 Cross-flow distributions of mean velocity, Reynolds normal stresses and shear stress at various stations: (a) $\overline{U}^*$; (b) $\overline{u^2}^*$; (c) $\overline{v^2}^*$; (d) $\overline{uv}^*$. T/d = 1.13.

deflected gap bleeding. The distributions of $\overline{u^2}^*$, $\overline{v^2}^*$ and $\overline{uv}^*$ corresponding to the narrow trough are different from those at T/d = 3.00, suggesting the absence of

vortex shedding. For $x/d \geq 5$, $\overline{U}^*$ shows one trough only; $\overline{u^2}^*$, $\overline{v^2}^*$ and $\overline{uv}^*$ all point to the existence of one single vortex street. However, these distributions are asymmetrical about $y/d = 0$, evident at $x/d = 10$. The asymmetry probably results from the biased gap bleeding. The effect of the bleeding persists beyond $x/d = 10$, contrary to the perception that two side-by-side cylinders of a small spacing may behave like a single structure, generating a Kármán-type vortex street (e.g. Sumner *et al.* 1999).

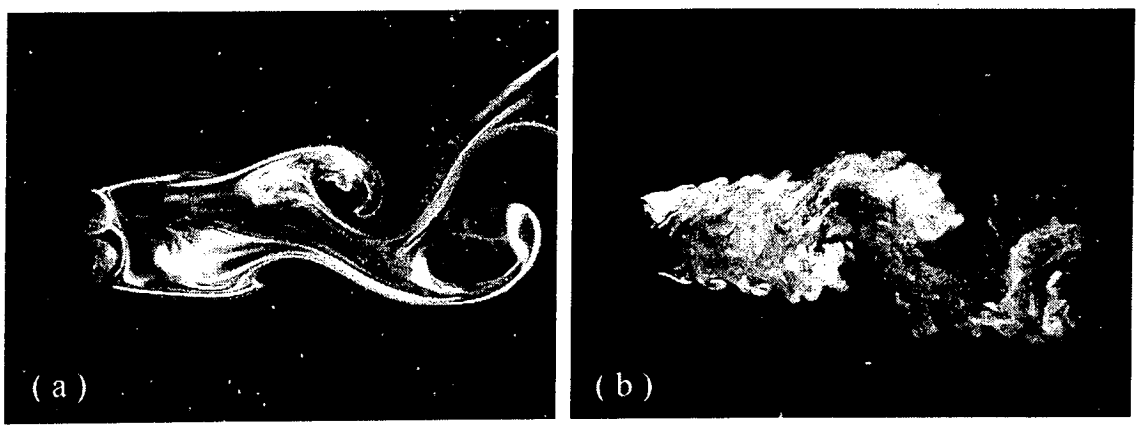

Figure 2-18 Typical flow patterns at $T/d = 1.13$. (a) $Re = 150$; (b) $Re = 750$.

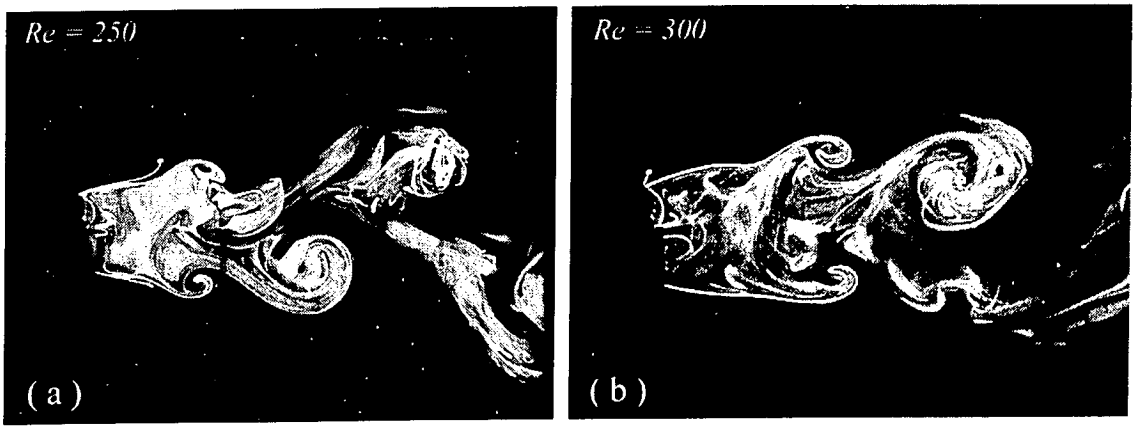

Figure 2-19 Symmetric vortex shedding at $T/d = 1.13$. (a) $Re = 250$; (b $Re = 300$.

2.5.2 Flow pattern

There is no vortex generated between the two cylinders and the vortices are generally shed alternately from the free-stream sides of the cylinders, thus generating a single vortex street (Fig. 2-18). The gap flow or bleeding is deflected or biased towards the lower cylinder in Figure 2-18a and towards the upper cylinder in Figure 2-18b. The behaviour of the gap bleeding is quite different between the laminar and turbulent flows. In the laminar case (Fig. 2-18a), the gap bleeding appeared swerving almost around the cylinder. The bleeding is biased to a smaller degree in the turbulent case (Fig 2-18b), possibly due to higher momentum or inertia. The higher momentum of the gap bleeding is also likely responsible for the increased streamwise extent of the vortex formation region (Sumner *et al.* 1999).

The symmetric vortex shedding occurs occasionally, as illustrated in Figure 2-19 (Re = 250 and 300). In this case, it is found that the gap bleeding is not biased. The observation is reasonable. As earlier discussed, the pressure upstream of the gap between the cylinders is higher than that close to the free stream, forming a pressure differentiation on the two sides of each cylinder in the cross-flow direction. The pressure differentiation is symmetrical about the flow centreline. This symmetry is likely to be sustained when the gap flow is not significantly biased, thus resulting in the symmetric vortex shedding (Fig. 2-19). The symmetric vortex shedding appears unstable for T/d = 1.13 and, in general, quickly reverts to the alternate vortex shedding mode.

It is worthwhile comparing the wake of two side-by-side cylinders of small spacing with that of an isolated cylinder in terms of the spatial arrangement of vortices. Both hot-wire and flow visualisation measurements were conducted behind a single cylinder. Both flows are characterised by a single vortex street. As noted earlier, the flow behind the two cylinder case is asymmetrical about y/d = 0, while

the other is anti-symmetrical. Using the *WAG* technique on two simultaneously measured hot-wire signals, the vortical structures were detected for both vortex rows. For T/d = 1.13, the relative probability (not shown) of the phase shift between the two sets of detections shows a prominent peak at $\phi = \pm \pi$, but non-zero at $\phi = 0$, corroborating the occurrence of the symmetrical spatial arrangement of vortices. Following the definitions of symmetrical and anti-symmetrical arrangements of vortices in Section 2.3.2, the symmetrical arrangement of vortices was estimated to be about 1.6% of the total detections at x/d = 1.5. In contrast, the symmetrical arrangement of vortices is practically zero for the single cylinder case. Evidently, the gap bleeding plays a significant part in the vortex formation, which is probably the essence of the difference between a single bluff body and the two cylinders of small spacing.

Within the same vortex street, due to the interaction between vortices, the symmetric arrangement of vortices is likely to be less stable than the anti-symmetric arrangement; even in the symmetric vortex shedding case, the vortices downstream still exhibit an anti-symmetrical spatial arrangement (Fig. 2-19a). Figure 2-20 presents sequential photographs at Re = 250 in order to gain a better understanding of the relationship between the gap bleeding and the near-wake vortex pattern. Initially, the gap flow was not deflected and two vortices, as marked by arrows in Plate 1, started to form on the free-stream sides of the two cylinders, respectively, in a symmetrical manner. As they move downstream, the vortex rolling up from the lower cylinder appears travelling faster than not only its counterpart from the upper cylinder but also the one shed earlier from the same cylinder (Plates 2 ~ 3). As a result, the two consecutive vortices of the same sign merged, forming a larger structure (see Plates 4 ~ 5). On the other hand, the symmetrically formed upper vortex fell behind. Meanwhile, two more vortices following started to roll up

symmetrically (Plates 4 and 5). The upper one appears moving fast and merging with the one of the same sign, shed earlier (Plates 6 and 7). Eventually, an anti-symmetrical spatial arrangement is displayed (Plates 7 ~ 9). Note that the gap bleeding starts to deflect and the anti-symmetric vortex shedding resumes.

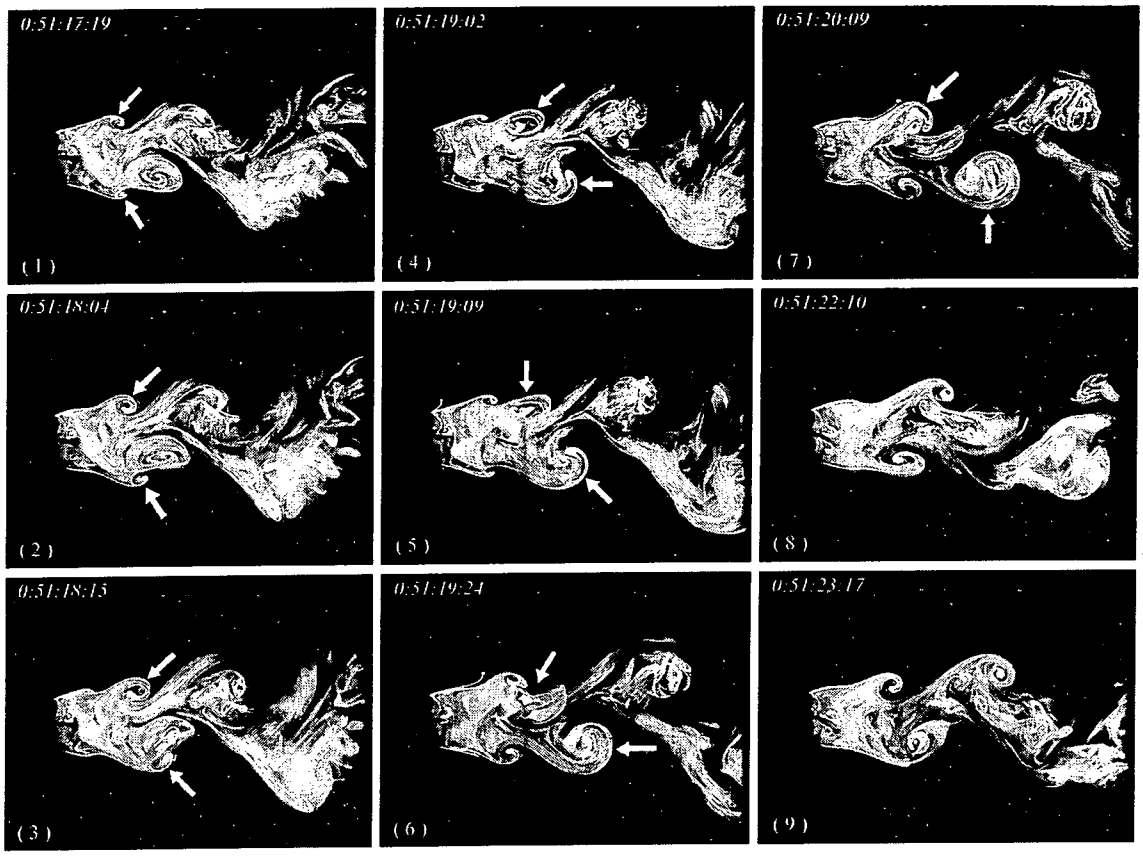

Figure 2-20 Sequential photographs from laser-illuminated flow-visualization: transition from the symmetric to anti-symmetric vortex shedding at $T/d = 1.13$ ($Re = 250$).

2.6 Discussions

The vortex formation and downstream evolution behind two side-by-side circular cylinders of representative spacing is summarised in Figure 2-21, based on the present measurements.

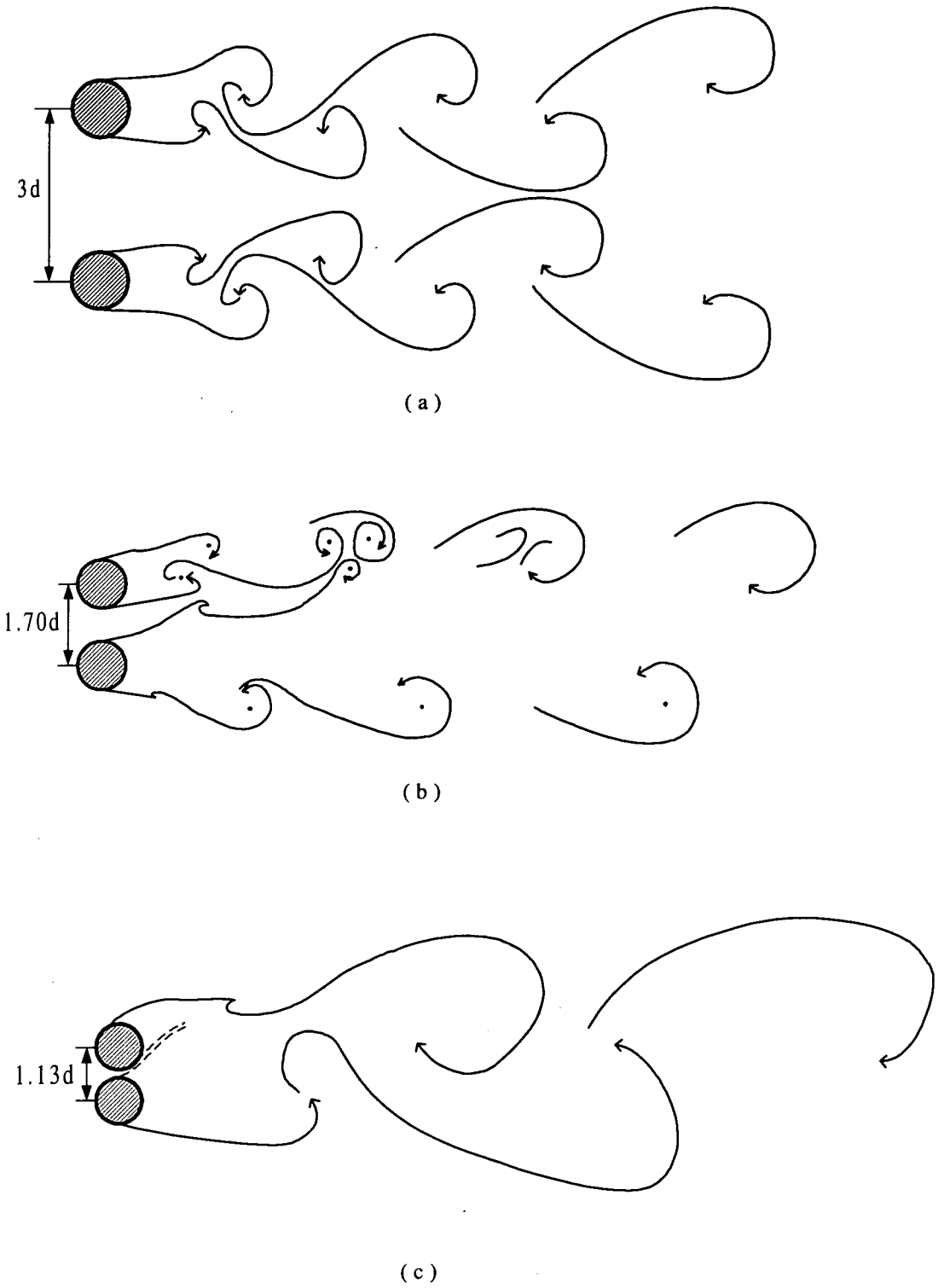

Figure 2-21 Summary sketch for the vortex formation and evolution in the near wake of two side-by-side circular cylinders. (a) T/d = 3.00; (b) T/d = 1.70; (c) T/d = 1.13.

At large cylinder spacing, i.e. T/d = 3.00, the vortex shedding from the two cylinders is predominantly symmetrical about the flow centreline, resulting in two distinct streets in antiphase mode (Fig. 2-21a). The vortex shedding frequency f_s^* is about 0.2, identical to a single cylinder case. The in-antiphase mode streets persist downstream, at least up to x/d = 10. The anti-symmetrical vortex shedding from the two cylinders occurs from time to time, leading to two in-phase streets. This mode of streets starts with a slight phase deviation from the symmetric vortex shedding from the two cylinders. The subsequent interactions between the two streets may lead to the formation of anti-symmetrical vortex shedding from the two cylinders and hence the inphase mode streets. However, the anti-symmetrical vortex shedding is unstable and soon returns to the symmetric manner (Fig. 2-6).

As the two cylinders approach each other, say at T/d = 1.70, interactions between the two vortex streets are intensified, resulting in a totally different flow topology (Fig. 2-21b). The gap jet is deflected, resulting in the formation of a narrow and a wide wake. In the wide wake, vortical structures do not appear shed from the cylinder. They originate from rolling up far away, e.g. about 5d away at Re = 450 (Fig. 2-9), from the cylinder probably due to the effect of the shear layer instability. The two cross-stream vortices in the narrow wake are engaged in pairing, and may generate a relatively low-pressure region between them, thus drawing in fluid as well as the gap vortex in the wide wake. The amalgamation of the two cross-stream vortices in the narrow wake with the gap vortex in the wide wake is not an isolated observation. A combination of wide and narrow wakes has been observed behind multiple cylinders of various geometrical configurations, for example, a row of cylinders (e.g. Moretti 1993), three side-by-side cylinders of equal (Kumada *et al.* 1984) and unequal cylinder spacing (Zhang and Zhou 2001), two staggered cylinders (Sumner *et al.* 2000). Zhang and Zhou (2001)'s flow visualisation clearly showed the

amalgamation of the two cross-stream vortices in the narrow wake with the gap vortex in the wide wake. Sumner *et al.* (2000)'s data (their Figure 9) also indicated a similar interaction between vortices, though they interpreted that the two gap vortices were pairing, and then enveloped by a vortex in the narrow wake. It is speculated that the amalgamation of the three vortices could occur in all the flows composed of a number of narrow and wide wakes. It is further inferred that the amalgamation of the three vortices could be, at least partly, responsible for the stability of the narrow and wide wakes.

Based on the streamwise evolution of the hot-wire signal spectrum (Fig. 2-12), the amalgamation completes probably before x/d = 10, which implies the merging of the two wakes or a single vortex street further downstream. The two rows of vortices in the new street are likely to be different in many aspects such as in size and vorticity strength because of different formation processes involved. The assertion conforms to the report by Yiu *et al.* (2001), who observed a single asymmetrical vortex street (T/d = 1.5, Re = 5800) at x/d = 10 ~ 40 based on phase-averaged velocity and temperature fields.

As the cylinder spacing is further reduced to T/d = 1.13, no gap vortices were seen; a single vortex street is generated behind the two cylinders. The gap bleeding (Fig. 2-18) between the cylinders imposes a significant influence on the vortex formation and downstream evolution. Sumner *et al.* (1999) suggested that for T/d < 1.2 the gap bleeding was usually associated with higher momentum, acting to increase the streamwise extent of the vortex formation region. They noted that the alternate vortex shedding was supplanted from time to time by the symmetric shedding. The present flow visualisation data unveiled that the alternate vortex shedding is associated with the biased gap bleeding, while the symmetric shedding corresponds to the unbiased gap bleeding. The gap bleeding is characterised by a

substantially reduced mean velocity and is quickly invisible. The bleeding effect is however persistent; the vortex street is asymmetrical about the flow centreline, at least up to x/d = 10, as indicated by the cross-stream distributions of mean velocity and Reynolds stresses (Fig. 2-17). This is in distinct contrast with the wake generated by a single circular cylinder, where mean velocity and Reynolds stresses are symmetrical or anti-symmetrical about the flow centreline (e.g. Zhou and Antonia 1993).

2.7 Conclusions

The vortex formation, topology (patterns) and downstream evolution behind two side-by-side circular cylinders have been investigated for three representative T/d values, i.e. 3.00, 1.70 and 1.13, based on flow-visualization, LDA and hot wire measurements. Other than reconfirming the predominance of two distinct vortex streets in antiphase for large cylinder spacing, the present investigation leads to the following conclusions.

1. In the asymmetrical flow regime (T/d = 1.70), the two cross-stream vortices in the narrow wake tend to pair, creating a relatively low-pressure region between them and drawing in the gap vortex in the wide wake. The amalgamation of the three vortices could be at least partially responsible for the stably deflected gap flow.

2. Two dominant frequencies, i.e. $f^* \approx 0.1$ and 0.3, were detected in the outer shear layer associated with each cylinder. The two frequencies were also identifiable in the narrow wake, but the lower frequency 0.1 only was detected in the wide wake. The flow visualisation data suggests that secondary vortices in the shear layer coalesced to form large-scale vortices, which were shed in

the narrow wake at $f_s^* \approx 0.1$. The shedding frequency coincides with the rolling-up frequency of the vortical structures in the wide wake. Presumably, the vortex frequency in the wide wake is dictated by the shear layer thickness. This frequency could feed back upstream to excite the shear layer instability and further induce the vortex shedding in the narrow wake. On the other hand, the amalgamation of the three vortices in the narrow wake involves a reduced lateral spacing between the structures, producing the frequency 0.3 in the hot-wire spectrum. The upstream influence of this frequency could excite the shear layer instability, thus resulting in a dominant frequency at $f^* \approx 0.3$.

3. The gap vortices in the narrow and wide wakes are generally in antiphase, but the one in the wide wake leads slightly that in the narrow wake and amalgamates with the pairing vortices in the narrow wake. The changeover of the gap flow deflection starts with a phase lag of the gap vortex in the wide wake behind that in the narrow wake. The phase lag may make it difficult to proceed for the gap vortex in the wide wake to amalgamate with the pairing vortices in the narrow wake. This could affect the stability of the gap flow deflection. Indeed, the gap vortex grows unusually large but quickly collapses because of the increased interaction with the narrow wake. The collapse may give rise to a momentarily weak interaction between the two wakes, thus allowing the narrow wake to expand laterally. The process was repeated for a few vortex-shedding cycles and eventually the narrow wake pushes the gap flow to the other side and completes the changeover.

4. At T/d = 1.13, there are no gap vortices generated and the vortices are shed only from the free-stream side of the two cylinders, resulting in a single vortex street. This flow is however different from that behind a single bluff body. The gap bleeding between the cylinders plays a significant role in determining the

flow pattern behind the cylinders. The gap bleeding is mostly biased toward one cylinder. Correspondingly, the vortices are shed alternately from the free-stream side of the two cylinders. When the gap bleeding is unbiased, the symmetric vortex shedding occurs. The bleeding is invisible at about $x/d = 5$. Its effect however persists, giving rise to the asymmetrical distributions of the mean velocity and Reynolds stresses at least up to $x/d = 10$.

CHAPTER 3

FREE VIBRATIONS OF TWO SIDE-BY-SIDE CYLINDERS IN A CROSS FLOW

3.1 Introduction

Flow-induced vibration is governed by a number of major parameters. Among these are the reduced velocity, U_r, the damping ratio and the mass ratio (Chen 1987). Each of these parameters plays a different role in the dynamic response of the cylinder. The damping ratio is the ratio of the energy dissipated by the system to the total system energy. The mass ratio, which is the ratio of the cylinder mass to the displaced fluid mass, provides a measure of the relative importance of the different fluid force components. The reduced velocity U_r, defined by $U_\infty / f_0^{(1)} d$, where U_∞ is the free-stream velocity, d is the cylinder diameter and $f_0^{(1)}$ is the first-mode natural frequency of a stationary cylinder, is linked to the ratio of the vortex shedding frequency f_s to the structural natural frequency. Here, the term structural natural frequency is used loosely to mean the structural natural frequency of any one of the vibration modes, but is usually taken to imply the first mode. The natural frequency is the vibration frequency, with which a structure or system, after an initial disturbance, oscillates without external forces. In a vortex-induced free vibration problem, f_s is responsible for the creation of the unsteady forces. Therefore, the interplay between the two frequencies determines the resultant behaviour of the cylinder dynamics and the wake structure. This is especially true when resonance (or synchronisation) occurs, which can be loosely defined as the situation where f_s is approximately equal to the structural natural

frequency. Strictly speaking, resonance occurs when the natural frequency of the combined fluid-structure system is equal to f_s. However, the natural frequency of the system and, to a certain extent, f_s are not known *a priori*. Therefore, the fluid-structure interaction problem is very complicated and its behaviour at or near resonance is of great interest to engineers.

The free vibration problem is further complicated in the case of two side-by-side cylinders. It has been discussed in Chapter 1 that, besides the parameters mentioned above, the problem is also governed by the ratio of the centre-to-centre cylinder spacing T to diameter d. Varying this ratio could lead to the formation of a single or multiple wakes (Landweber 1942; Spivac 1946; Ishigai *et al.* 1972; Bearman and Wadcock 1973; Zdravkovich 1985; Zhou *et al.* 2000b) and this, in turn, could affect the dynamic response and the resonance behaviour of the cylinders. Furthermore, the nonlinear interplay between the simultaneous vibrations of the two cylinders and the fluid as a result of flow-induced forces is a far more complicated process than the fluid-cylinder interaction in the single cylinder case.

Interference between circular cylinders placed side-by-side in a cross-flow has been investigated extensively in the past (Zdravkovich 1977) because of its inherent importance and practical significance in many branches of engineering. The interference drag measurements of two side-by-side cylinders facing a uniform flow can be traced back to Biermann and Herrnstein (1933). Zdravkovich and Pridden (1977) measured the lift and drag coefficients and noted that the sum of the low and high drag generated by the two cylinders was always less than twice the drag of a single cylinder. Using a photographic method, Landweber (1942) observed a single vortex street for $T/d \leq 1.2$ and two distinct vortex streets for $T/d > 2$. Spivac (1946) measured two different frequencies in the two-cylinder wake for $T/d < 2$ but a single frequency for $T/d > 2$. In the latter case, the frequency was further found to be the

same as that measured in the single cylinder wake. A Schlieren optical method was used by Ishigai *et al.* (1972) to visualise the flow behind two side-by-side cylinders. They observed a remarkably symmetric vortex formation and shedding for $T/d = 2.5$ and 3.0, but a biased gap flow for $1.2 < T/d < 2.0$. The biased flow was bi-stable and intermittently changed over from one side to another, forming two asymmetric vortex streets of different frequencies. Bearman and Wadcock (1973) have made a similar observation in their experiments. Based on flow visualisation at a low Re ($\leq$ 200), Williamson (1985) suggested that the two different frequencies, observed in the asymmetric flow regime ($1.5 \leq T/d \leq 2.0$), were due to the existence of harmonic vortex-shedding modes. On the other hand, the measurements of Kim and Durbin (1988) at $Re = 3300$ did not support this conjecture. Therefore, the mechanism for the two distinct frequencies in the asymmetric flow regime has yet to be better understood.

Previous studies were mostly concerned with the behaviour of the wake flow and the flow-induced vibrations on rigid cylinders. Even in the free vibration case, the cylinders, flexibly mounted at both ends, were relatively rigid. The dynamic characteristics of an elastic cylinder can be quite different from a rigid one. For example, there is only one natural frequency for a rigid cylinder system but more than one associated with an elastic cylinder system (Zhou *et al.* 1999b, So *et al.* 2000b). There have been relatively few studies on two side-by-side elastic cylinders in a cross-flow. Consequently, many issues remain to be resolved. For example, how is the free vibration of an elastic cylinder in a cross-flow affected by the presence of a neighbouring cylinder? In a forced vibration situation, the imposed vibration modifies the vortex shedding frequency. However, in the free vibration case, the vortex shedding generates the excitation forces. Could vortex shedding

modify the natural frequencies of the fluid-cylinder system? Are these frequencies dependent on T/d and U_r?

Damping is another important issue. It models the energy dissipation of the system during vibrations and plays an important role in the stability of a structure and its vibration amplitude. Knowledge of damping is essential if the dynamic behaviour of the structures in a cross flow is to be understood thoroughly. Damping arises from the fluid surrounding the structure as well as from the structure itself. While structural damping is related to the properties of the structure alone, fluid damping originates from viscous dissipation and fluid drag. In other words, fluid damping is the result of viscous shearing of the fluid at the surface of the structure and the behaviour of flow separation. Therefore, it is motion dependent and is much more difficult to estimate, especially for multi-degree-of-freedom dynamic systems (Weaver and Fitzpatrick 1988; Granger *et al.* 1993). Using an auto-regressive moving average (ARMA) analysis technique, Zhou *et al.* (2000a) and So *et al.* (2000a) deduced the effective and fluid damping ratios from the calculated lift and displacement signals of a single cylinder in a cross flow over a range of *Re*. In these studies, the cylinder motion was modelled by a two-degree-of-freedom system. Later, Wang *et al.* (2001) used the same technique to analyse similar signals derived by employing the Euler-Bernoulli beam theory to model the free vibration of a single cylinder. All these studies yield reasonable results compared to measured fluid damping ratios. In particular, the work of Wang *et al.* (2001) was able to deduce the fluid damping ratios for the first and third mode of vibration. However, the issue of how interference between cylinders affects the damping ratios has yet to be addressed. It is not clear whether damping behaviour is, if at all, related to the system natural frequencies.

This chapter aims to investigate experimentally the free vibration of two side-by-side elastic cylinders placed in a cross-flow and the associated non-linear fluid-cylinder interactions. The first objective is to further improve the understanding of the flow structure around the cylinders obtained in Chapter 1, including the mean pressure distribution, the induced lift and drag, and the vortex formation and its evolution at different *T/d* ratios. In particular, the two distinct frequencies in the asymmetric flow regime are examined again based on flow visualisation and hot wire signals. The second objective is to study fluid-structure interactions. The free vibration of the two cylinders due to flow excitation is characterised in detail. The dependence on *T/d* and U_r of the natural frequency of the combined fluid-structure system is investigated thoroughly, in particular, at and near resonance. The effective and fluid damping ratios are evaluated from the measured strain signals using an ARMA technique (Mignolet and Red-Horse 1994).

3.2 A Briefly Description of ARMA Technique

A detailed discussion of the ARMA technique can be found in Mignolet and Red-Horse (1994) and Zhou *et al.* (2000a). Here, a brief discussion of ARMA and some different techniques used by other researchers is given. The ARMA modelling technique is based on the observation that the sampled response of a multi-degree-of-freedom system satisfies a linear recurrence relation. The response can be represented as the output of an ARMA discrete system, the input of which is the sampled excitation. In addition, the characteristics of the continuous system, i.e. natural frequencies, damping ratios and mode shapes, can easily be computed from the auto-regressive part of the ARMA model. Finally, reliable techniques for the estimation of the ARMA model parameters from measurements of the excitation and response of the system considered have been developed so that the entire

methodology is available for structural identification, including damping ratio estimation as needed here.

ARMA modelling is not limited to single-mode behaviour; it identifies all modal characteristics present in the responses including possible outside dynamics, such as turbulence in the incoming flow. Furthermore, the estimation of the ARMA parameters accounts for the presence of modelling noise so that its effect on the computed damping ratios is significantly reduced. Finally, ARMA models have been shown (Jadic *et al.* 1998) to capture some non-linear effects through the modelling of the higher harmonics content present in the response. These advantages of ARMA modelling far outweigh the increase in computational effort required to obtain reliable estimates of the damping ratios. Using the ARMA technique, Zhou *et al.* (2000a) deduced the fluid damping ratios from the structural displacement time series obtained from a numerical simulation of an elastic cylinder in a cross-flow.

Granger (1990) developed a digital signal processing method for modal analysis of fluid-structure systems. Their method is a multi-degree-of-freedom time domain method based on the development in the field of time series analysis. The method was used to deduce fluid damping from the strain data of a cylinder placed in a square in-line tube bundle (Granger *et al.* 1993). Since their test cylinder, which was mounted on flexible support, was rigid, their system is different from that of a flexible cylinder on fixed supports as considered in present investigations. The formulation of Granger (1990) is in fact a specific ARMA model. However, there are some differences between his and the present formulation. For example, Granger (1990) used the same operator for auto-regressive (AR) and moving average (MA), as evident in his Eq. (4), while the present technique has unequal operators for AR and MA and seeks the non-linear maximum likelihood solution. Granger further computed the ARMA coefficients A_k, B_k and C_k (in his Eq. 2) based on the auto-

correlation of the measured signal, i.e. the ARMA model is applied on the correlation and then the noise term w is truly a noise. On the other hand, the present approach works directly with the measured signal. One benefit of this approach is that w denotes any measurement noise plus a fictitious random source that creates the randomness in the response and can physically be associated with the origin of the turbulence in the signal.

In the use of the ARMA technique, a model of a higher order provides in general a better fit to the original time series. However, a higher order model demands more computing time. In the process of analyzing numerical simulation data, Zhou *et al.* (2000a) found that an order of 70 was sufficient. Experimental data is 'noisier' than numerical simulation data. It was further found that the measured strain data requires a higher order model than the displacement data. In the present investigation, consistent results were achieved when an order of 80 was chosen for the displacement data and 190 for the strain data. Note that the large value of the auto-regressive order is partly necessitated by the non-linearity of the fluid-structure system, which implies the presence in the response of a large number of harmonics of the shedding frequency. These frequencies are genuine characteristics of the response and are automatically included in the ARMA model.

3.3 Experimental Details

3.3.1 Experimental setup

Experiments were carried out in a suction-type wind tunnel with a 0.35m × 0.35m square cross-section that is 0.5m long (Fig. 3-1). The wind speed of the working section can be adjusted from 1.5 m/s to 28 m/s. The streamwise velocity is uniform to within 0.05% and the free stream turbulence intensity is 0.2%. In order to

minimise tunnel vibrations, the working section is isolated from the motor and fan through vibration absorbers.

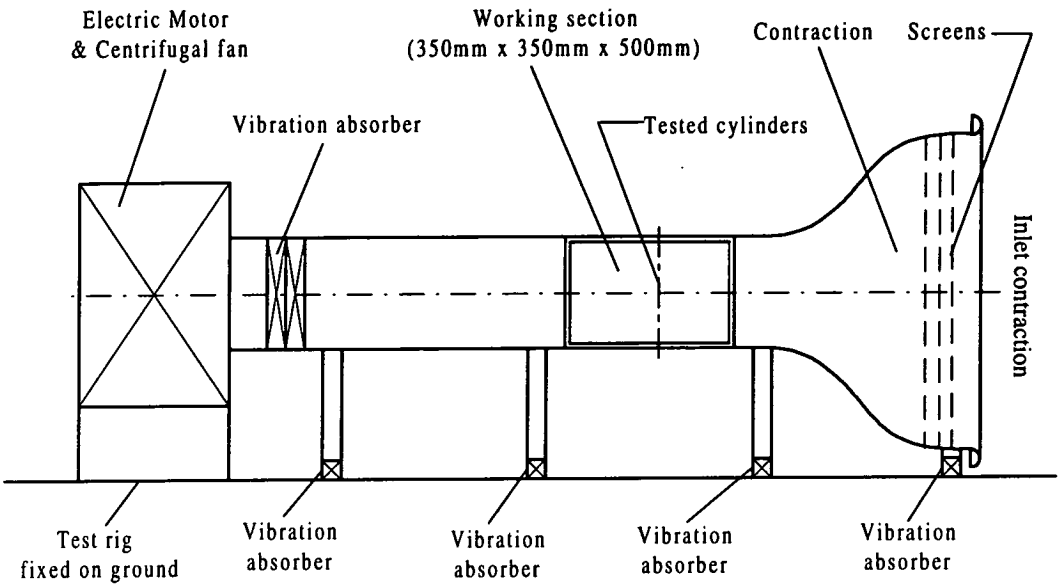

Figure 3-1 Schematic diagram of the test wind tunnel.

Table 3-1. Structural characteristic properties of the cylinders.

Cylinder	EI (Nm^2)	M^*	$\zeta_0^{(1)}$	$f_0^{(1)}$ (Hz)					
				Cross-flow direction T/d			Inline direction T/d		
				1.13	1.70	3.00	1.13	1.70	3.00
1	0.224	565	0.026	104.00	104.00	104.00	98.60	98.60	98.60
2	0.224	565	0.026	94.00	95.00	101.00	95.83	101.50	101.53

Two identical acrylic tubes with a diameter of $d \approx 0.006$m were vertically mounted in a side-by-side arrangement and placed symmetrically to the mid-plane of the working section at 0.20m downstream of the exit plane of the tunnel contraction (Figs. 3-1 and 3-2). The co-ordinate system is attached to Cylinder 1 with y measuring zero at the centre of this cylinder (Fig. 3-2) and the other is labelled Cylinder 2. The two cylinders were built into the walls of the working section, with

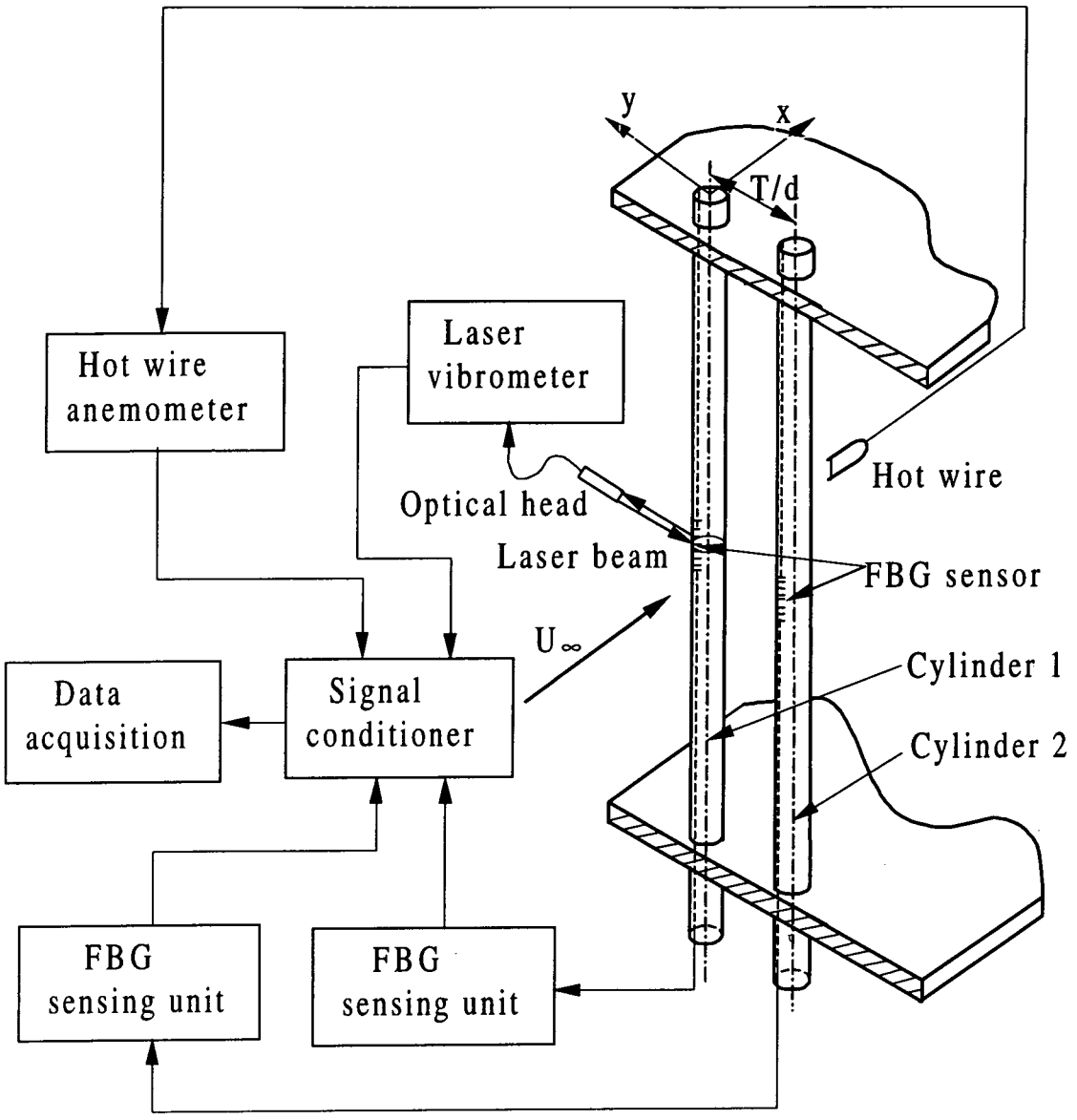

Figure 3-2 Experimental arrangement.

fix-supported boundary conditions at both ends (no rotation and displacement). The structural characteristic properties of the cylinders are summarised in Table 3-1. Here, E is the Young's modulus of the cylinder, I is the area moment of inertia, $\zeta_0^{(1)}$ is the first-mode structural damping ratio and M^* is the mass ratio defined by $M/\rho d^2$, ρ is the fluid density and M is the cylinder mass, and $f_0^{(1)}$ is the first-mode structural natural frequency. The blockage due to the installation of the cylinders was about 3.4%. The Reynolds number, $Re = U_\infty d/\nu$, where ν is the fluid kinematic viscosity, investigated varied from 800 to 10,000. This gives rise to a U_r

range of 3 - 43. In the present *Re* range, the blockage effect on the mean drag is insignificant. Three transverse spacing ratios were investigated, i.e. T/d = 1.13, 1.70, and 3.00. Great care was taken to maintain these ratios along the cylinder span. Furthermore, they were chosen because the flow regimes thus resulted were representative of the different proximity effects for two side-by-side cylinders (Zdravkovich 1985).

3.3.2 Mean drag and lift measurements

The experimental arrangement is shown schematically in Figures. 3-1 and 3-2. Each of the cylinders was instrumented with a single wall pressure tap at the mid-span position. A pressure transducer was connected to the tab to measure the wall static pressure. The cylinder was rotated at an interval of 5° to give the angular distribution of wall static pressure around the cylinder surface and the mean lift and drag on the cylinder were evaluated by integrating the wall static pressure around the cylinder. Measurements of the mean lift and drag were carried out on a single cylinder and on the two side-by-side cylinders at the same *Re*, thus providing a baseline for the evaluation of the interference effects.

3.3.3 Fluctuating velocity measurements

The streamwise fluctuating velocity u was measured by positioning a single hot wire at x/d = 2 and y/d = 1.5, where, x is the streamwise distance measured from the centre of Cylinder 1 (Fig. 3-2). The hot wire was operated at an overheat ratio of 1.8 with a constant temperature anemometer (DISA Type 55M10).

3.3.4 Dynamic strain measurements

Zhou *et al.* (1999b) and Jin *et al.* (2000) used a fibre-optic Bragg grating (FBG) sensor, built in-house, to measure the dynamic strain due to lift on a cylinder

in a cross-flow. The strain thus measured was compared with the transverse displacements obtained from a laser vibrometer. They found that the spectra deduced from the two signals were in excellent agreement with each other in terms of their salient features, such as the vortex shedding frequency and the natural frequency of the fluid-cylinder system, and the two signals showed a complete coherence at these frequencies. They further found that, for small displacements, the root mean square (rms) values of the strain and displacement signals were linearly correlated. A linear correlation is also expected between strain and displacement due to the fluctuating drag and in the presence of another cylinder.

Two FBG sensors were used to simultaneously measure the dynamic strains of the two cylinders along the x or y direction. For measurement along the y-direction, an optical silica fibre of diameter 125 μm built with an FBG sensor was buried in a groove along the span of each cylinder at 90° from the leading stagnation line and flushed with the surface using nail polish. The FBG sensor was located at mid span of the cylinder. Since the sensor grating has a finite length of about 10mm, the measurement represents the average strain over this length. The strain thus measured is designated as ε_y. In principle, ε_y is independent of the streamwise vibration of the structure. If the cylinder is rotated clockwise (or anti-clockwise) by 90°, the FBG sensor will be located at the rear stagnation line (or the leading stagnation line whichever the case may be). In this location, it measures the strain ε_x, due to the drag, which should not depend on the cross-flow vibration of the cylinder. A major source of error comes from the non-linearity effect when calibrating the relation between the output voltage and strain (Zhou *et al.* 1999b, Jin *et al.* 2000). The experimental uncertainty in strain measurements is estimated to be $\pm 8\%$.

In view of the fact that mounting and remounting a cylinder might change the natural frequency of the structure, the mounting of Cylinder 1 was not changed during the entire experiment where the dynamic strain for either the cross-flow or inline direction was measured. Therefore, $f_0^{(1)}$ of Cylinder 1 was constant. Its value is 104 Hz for the cross-flow direction and 98.60 Hz for the inline direction (Table 3-1). This arrangement is important if the interference effect on the natural frequencies of the fluid-cylinder system is to be investigated with confidence. The adjustment of *T/d* was achieved by remounting Cylinder 2 only. Great care was taken to minimise the variation of $f_0^{(1)}$ associated with remounting. The $f_0^{(1)}$ values of Cylinder 2 in both cross-flow and inline directions were given in Table 3-1. Measurements of the bending displacement *Y* and *u* in the wake of a single cylinder carried out by Zhou *et al.* (1999b) indicated a negligible effect on flow separation around the cylinder and on *Y* due to the attachment of the optical fibre.

The signals *u*, ε_{y1} and ε_{y2} or *u*, ε_{x1} and ε_{x2}, where the subscripts 1 and 2 represent the cylinder number, were simultaneously measured. They were offset, amplified and digitised using a 12bit A/D board and a personal computer at a sampling frequency of 6.0 kHz per channel. The record length was about 20s. This record length was sufficiently long for the rms values $\varepsilon_{x,rms}$ of ε_x and $\varepsilon_{y,rms}$ of ε_y to reach their stationary state, with a variation smaller than 1.0%.

3.3.5 Effect of tunnel vibrations

It is important to minimise tunnel vibrations in the present investigation. As pointed out earlier, tunnel vibrations were mainly derived from the fan and motor. Great care has been taken to isolate the working section from the vibration sources through the use of vibration absorber (Fig. 3-1). This vibration isolation is not a sufficient remedy for the laser vibrometer measurement of displacement because the

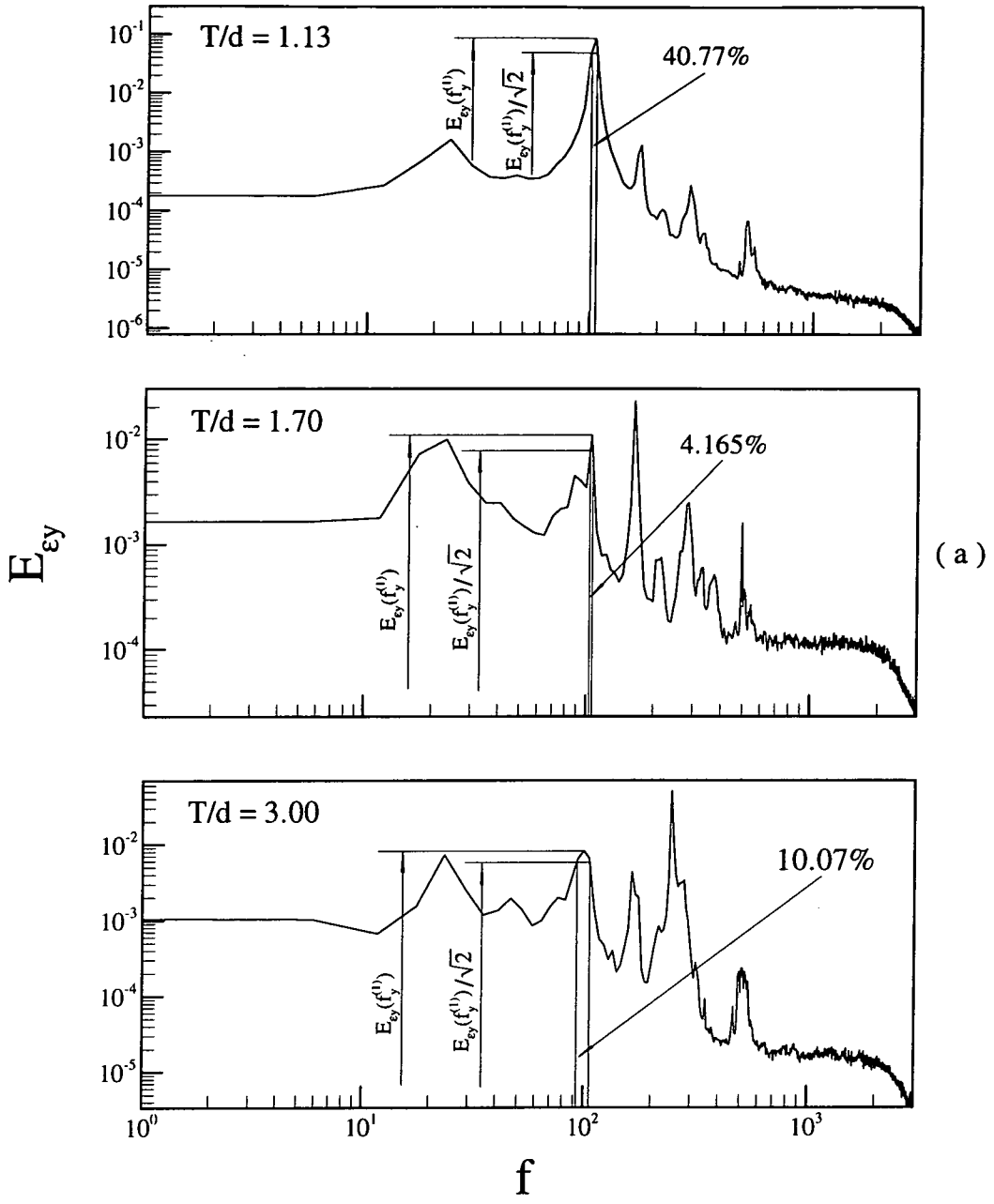

Figure 3-3 Power spectra $E_{\varepsilon y}$ of ε_y: (a) calculated from the measured signal; (b) from the signal filtered with a high pass of 60 Hz. Cylinder 1. U_r = 11.0.

motion of the working section, which can be transmitted through the floor, also affects the measurements (Zhou *et al.* 1999b). The FBG sensor, on the other hand, measures the cylinder deformation. Therefore, it is insensitive to any translational motion of the cylinder, which is associated with the working section vibration.

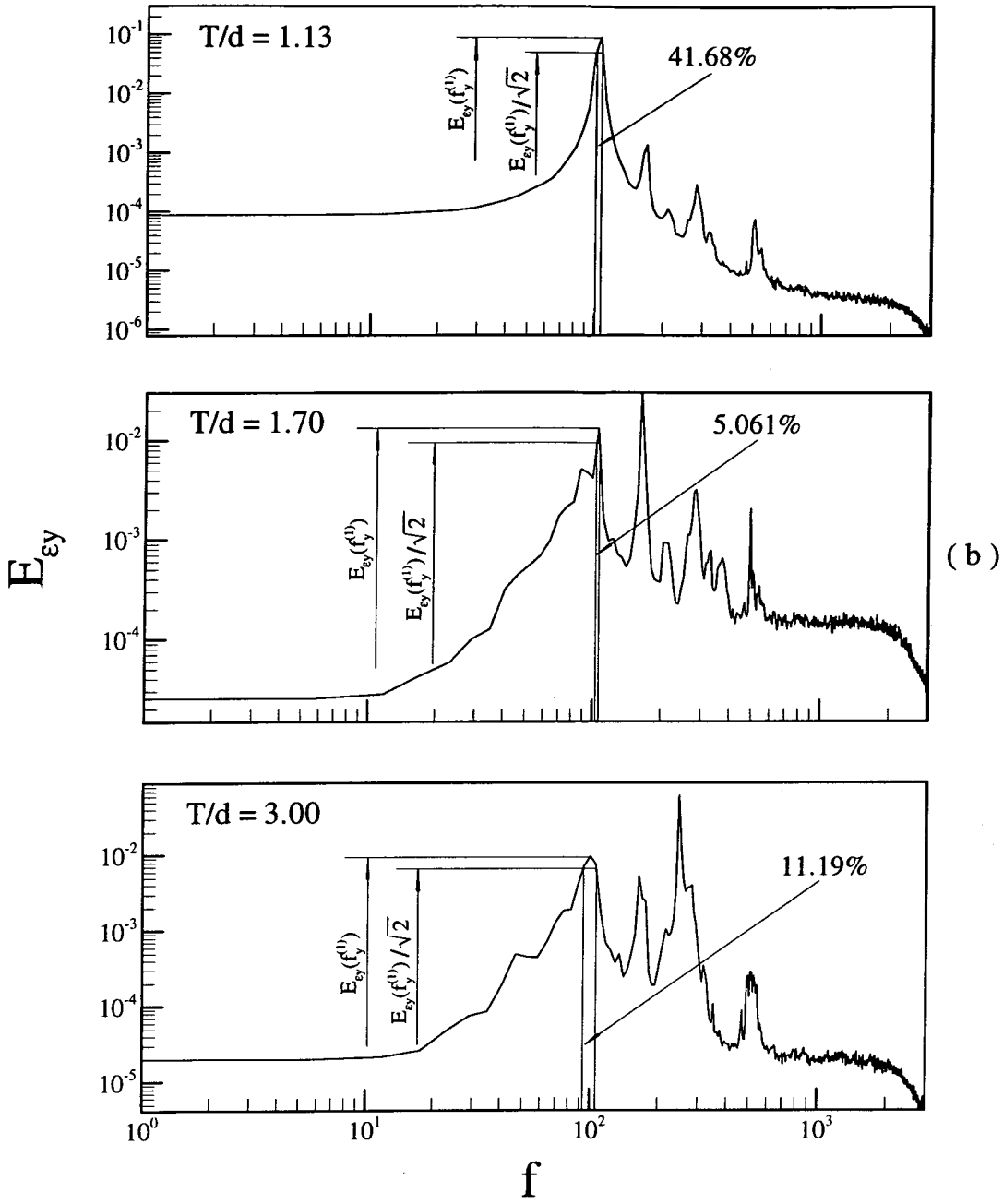

Figure 3-3b

Tunnel vibrations only indirectly affects the FBG sensor measurements through the inertia force. However, this is a secondary effect and is unlikely to have a significant impact on the measurements as demonstrated below.

The effect of tunnel vibrations could be estimated by calculating the variation in energy corresponding to the first-mode natural frequency, with and without tunnel

vibrations. The power spectra $E_{\varepsilon y}$ of ε_y from Cylinder 1 for T/d = 1.13, 1.70 and 3.00 at U_r = 11.0 is shown in Fig. 3-3. Here, $E_{\varepsilon y}$ is normalised so that $\int_0^\infty E_{\varepsilon y}(f)df = 1$. In Fig. 3-3a, $E_{\varepsilon y}$ calculated from the original strain signal is shown. The half-power-bandwidth (HPB) integral at the first-mode natural frequency of the fluid-structure system is 40.77%, 4.17% and 10.07% for T/d = 1.13, 1.70 and 3.00, respectively. The natural frequency of the working section was measured in the range of 20~30 Hz (Zhou *et al.* 1999b). Therefore, the measured ε_y was high-pass filtered at 60 *Hz* to eliminate the noise associated with tunnel vibrations. The $E_{\varepsilon y}$ calculated from the filtered signal is plotted in Fig. 3-3b and the HPB integral at the first-mode natural frequency is 41.68%, 5.06% and 11.19% for T/d = 1.13, 1.70 and 3.00, respectively. The maximum difference between the $E_{\varepsilon y}$ calculated with and without filtering is about 1.1%, indicating a negligible tunnel vibration effect on the FBG sensor measurements.

3.3.6 Flow visualisation

The experimental setup of flow visualisation was identical to those presented in Chapter 2. In view of this, only a brief description of the experimental details is repeated here. Flow visualization was carried out in a water tunnel with a 0.15m × 0.15m square working section of 0.5m long (Fig. 2-1a). The water tunnel is a recirculating single reservoir system. From the reservoir, a centrifugal pump delivers water to the tunnel contraction. A honeycomb is used to remove any large-scale irregularities prior to the contraction. The flow speed is controlled by a regulator valve up to a maximum velocity in the working section of about 0.32 m/s. The working section is made up of four 20mm thick persplex panels. Two side-by-side acrylic circular tubes with an identical diameter of 10 mm were horizontally mounted

0.20m downstream of the exit plane of the tunnel contraction and placed symmetrically to the mid-plane of the working section (Fig. 2-1b). They spanned the full width of the tunnel. The resulting blockage was 13.3%. For the purpose of comparison with the FBG sensor measurements, the same transverse spacing ratios as those used in the wind tunnel were investigated, i.e. T/d = 1.13, 1.70 and 3.00. For each cylinder, dye (Rhodamine 6G 99% which has a faint red colour and will become metallic green when excited by laser) was introduced through injection pinholes located at the mid-span of the cylinder at 90°, by clockwise and anti-clockwise, respectively, from the forward stagnation point. A thin laser sheet, which was generated by laser beam sweeping, provided illumination vertically at the mid-plane of the working section. A Spectra-Physics Stabilite 2017 Argon Ion laser with a maximum power output of 4 watts was used to generate the laser beam and a digital video camera recorder (Sony DCR-PC100E), set perpendicular to the laser sheet, was used to record the dye-marked vortex streets. Investigations of flow visualisation were carried out in the Re range of 120 to 1650 over $0 \leq x/d \leq 10$. At large Re and x/d, the dye diffused too rapidly to be an effective marker of vortices.

3.4 Fluid Dynamics Around Cylinders

3.4.1 Mean pressure, lift and drag

The polar plots of pressure coefficient, $C_p = 2\Delta p/(\rho U_\infty^2)$, around the cylinder for a single as well as two side-by-side arrangements at Re = 6000 are shown in Fig. 3-4. Here, Δp is the mean pressure difference between the cylinder wall and a reference point, i.e. x/d = 10 and y/d = 15, upstream. The resultant force R is calculated from $\sqrt{D^2 + L^2}$ and its direction is given by the angle $\theta_R = \tan^{-1}(L/D)$,

where L and D are the mean lift and drag, respectively. Mean lift and drag of the two cylinders are calculated by integrating the pressure around the cylinders. The respective force coefficients are defined by $C_L = 2L/(\rho U_\infty^2 d)$ and $C_D = 2D/(\rho U_\infty^2 d)$. Their values thus deduced for Re = 3500, 6000 and 10400 are shown in Figs. 3-5a and 3-5b.

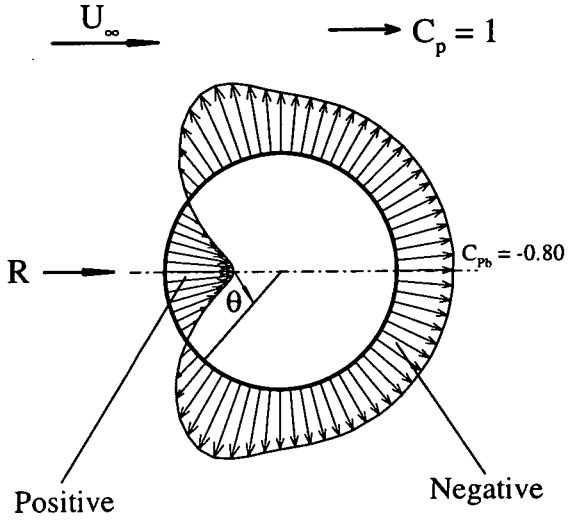

(a)

Figure 3-4 Polar plot of the circumferential distribution of the pressure coefficient at Re = 6000: (a) single cylinder, (b) two cylinders.

The pressure distributions of the two cylinders at T/d = 3.00 exhibit similarity to that for a single cylinder. But the resultant force on each cylinder deviates from the flow direction, probably as a result of flow retardation upstream of the gap between the cylinders, which could give rise to a higher pressure between the cylinders. The θ_R is 3° for Cylinder 1 and – 4° for cylinder 2. The difference in magnitude is probably caused by experimental uncertainty, which is estimated to be about 2.5°. Therefore, the pressure distribution around one cylinder is essentially a mirror reflection of the other. For T/d < 3.00, the pressure distribution around the two cylinders is no longer a mirror reflection of each other, as evidenced by the

difference in θ_R and the base pressure coefficient C_{pb} (θ = 180°) between the cylinders. However, in each case, R is directed approximately through the forward stagnation point, where the pressure is the maximum, and the cylinder centre. The observation is essentially the same as that reported in Bearman and Wadcock (1973). It should be pointed out that the pressure coefficient does not very smoothly behind cylinder 1 at T/d = 1.70 and cylinder 2 at T/d = 1.13 (Fig. 3-4b). This observation could be attributed to the experimental uncertainties, as presented in Table 1-1.

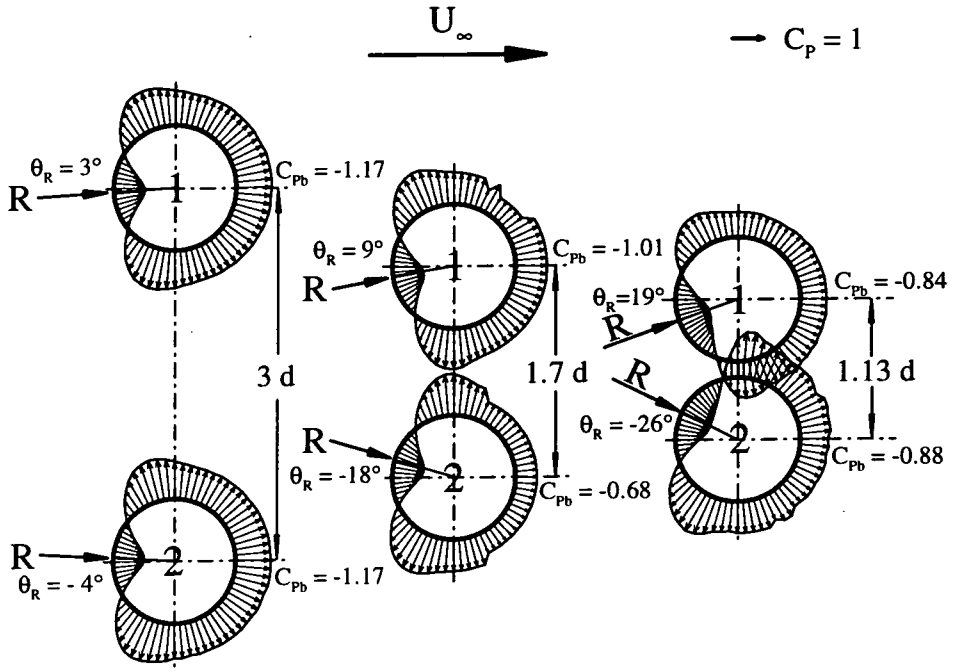

(b)

Figure 3-4b

The C_L value is positive for Cylinder 1 and negative for Cylinder 2 (Fig. 3-5a), showing a repulsive force between the cylinders. Since flow upstream of the gap between the cylinders is further retarded as T/d reduces, the pressure rises between $\theta \approx 0°$ and 90° for Cylinder 1 and between $\theta \approx 270°$ and 360° for Cylinder 1 (Fig. 3-4b). As a result, the repulsive force between the cylinders increases with decreasing T/d.

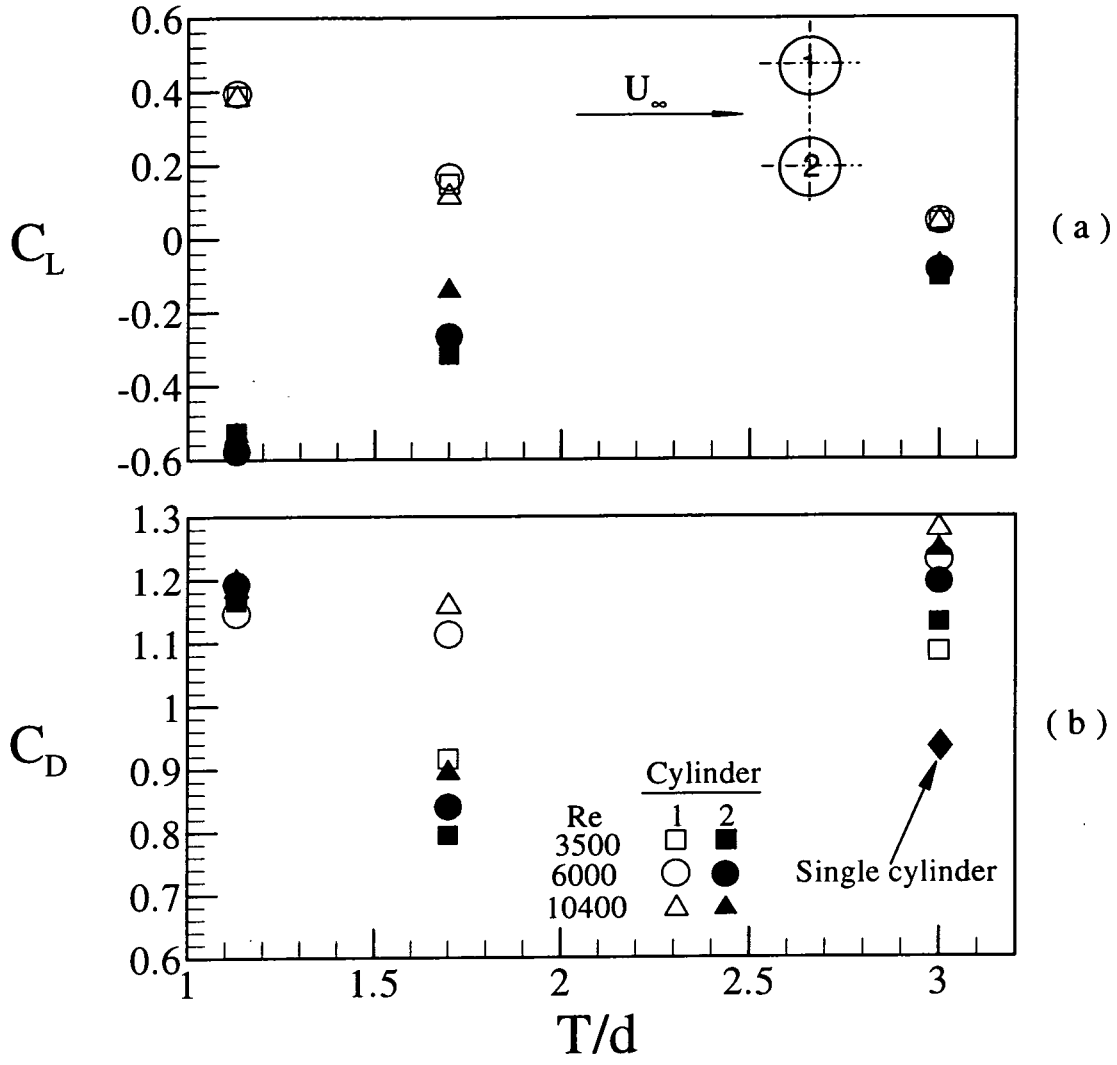

Figure 3-5 Dependence of (a) lift and (b) drag coefficients on the spacing ratio *T/d*.

At T/d = 3.00, C_D is approximately the same for the two cylinders (Fig. 3-5b), ranging from 1.08 to 1.27 when *Re* varies from 3500 to 10400, comparable to that of a single cylinder, 0.93. At T/d = 1.70, the drag coefficients of the two cylinders differentiate. This can be inferred from the base pressure coefficient C_{pb} at $\theta = 180°$. The value is about –1.01 for Cylinder 1 (Fig. 3-4b). The lower value of C_{pb} gives rise to a higher C_D. On the other hand, C_{pb} of Cylinder 2 is about –0.68 (Fig. 3-4b), resulting in a lower C_D. It is well known that, for this T/d, narrow and wide wakes

are formed behind two identical cylinders, respectively, and the gap flow deflects towards the narrow wake (Zdravkovich 1987). Bearman and Wadcock (1973) and Quadflieg (1977) observed that the narrow wake has a lower base pressure and a higher C_D, whereas the wide wake has a higher base pressure and a lower C_D. Thus, it may be inferred that Cylinders 1 and 2 are mostly associated with a narrow and a wide wake, respectively. At T/d = 1.13, C_{pb} shows an increase for both cylinders. However, C_p between 0° ~ 90° for Cylinder 1 and 270° ~ 360° for Cylinder 2 also increases significantly, due to more severe flow retardation upstream of the gap between the cylinders. Consequently, C_D is higher for both cylinders. There is still a difference in the measured C_D between the two cylinders, though less pronounced than that obtained at T/d = 1.70. At such a small T/d, a single vortex street is expected behind the cylinders (Landweber 1942). Photographs from laser-illuminated flow visualisation shown in Section 3-4-2 indicate a biased bleeding between the cylinders. The biased bleeding is probably accountable for the difference in the C_p distribution between the cylinders (Fig. 3-4b), and hence unequal C_D for the two cylinders, as well as the asymmetry of C_L (Fig. 3-5a).

The mean of the low and high C_D values at T/d = 3.00 is 1.2, appreciably higher than that (0.93) of a single cylinder at Re = 6000. The difference cannot be attributed to the experimental uncertainty, which is estimated to be 2%. Further investigation is needed to understand this observation. For T/d < 3.00, this mean is generally less than that determined at T/d = 3.00, in consistence with that reported in Zdravkovich and Pridden (1977). In the near-wake of an isolated cylinder, about 50% of the shed circulation was cancelled as fluid bearing vorticity was drawn across the wake centreline into the growing vortex with an opposite vorticity (Gerrard 1966; Cantwell and Coles 1983). One would expect that the interference between the narrow and wide wakes might cause additional cancellation of vorticity as well as

absorb some flow energy, thus resulting in reduced vortex strength. This, in turn, causes a higher base pressure as exhibited in Fig. 3-4, hence a reduced total drag.

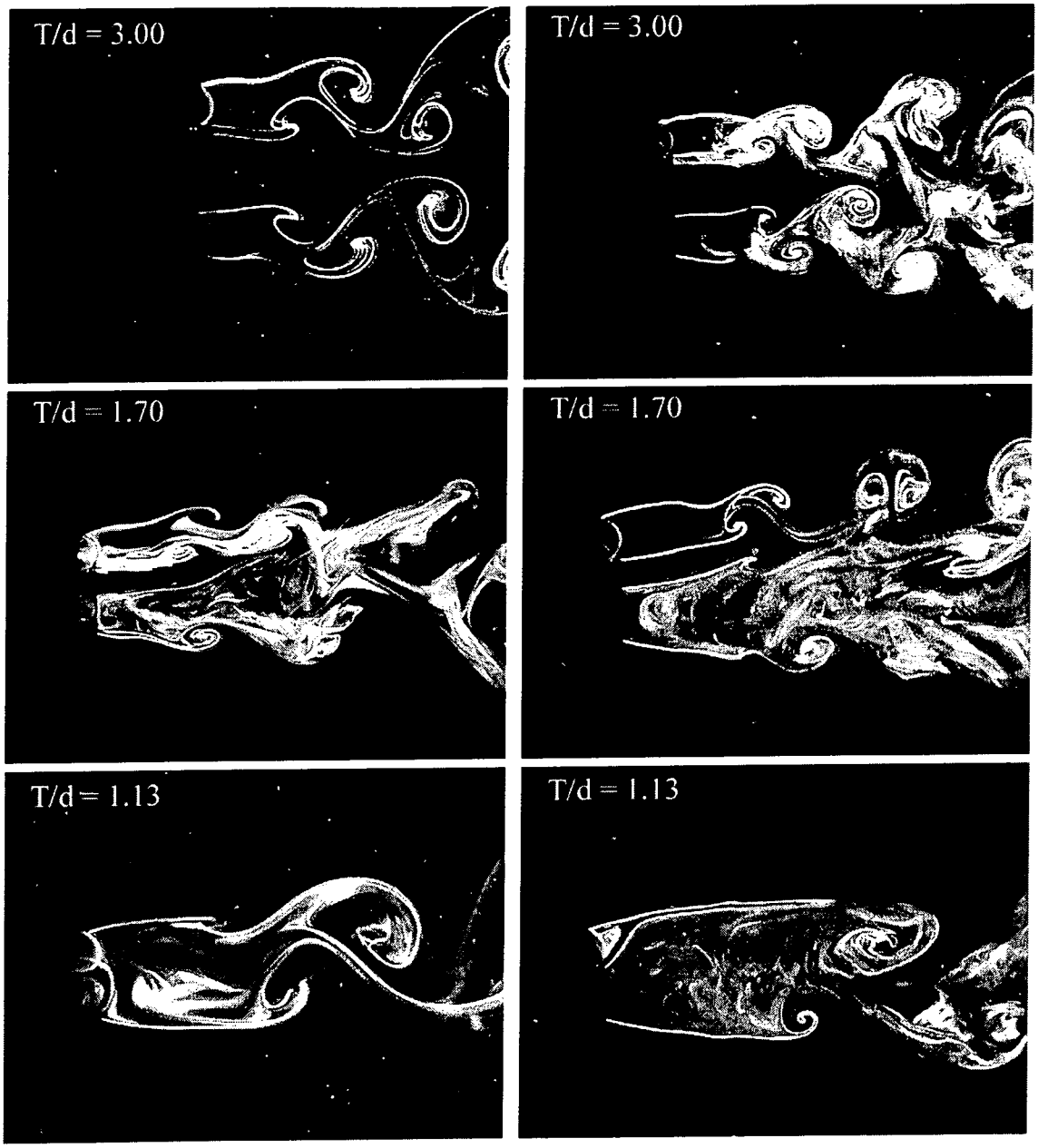

Figure 3-6 Laser-illuminated flow visualisation in the water tunnel behind two side-by-side cylinders. Flow is from left to right.

3.4.2 Flow patterns

The above interpretation is further verified by the observation deduced from the flow visualisation experiment. In this section, flow visualisation results for the

three cases, T/d = 1.13, 1.70 and 3.00, are examined with the aim to gain an understanding of flow physics. The characteristics of the spectral characteristics are discussed later.

T/d = 3.00 The top two plates in Fig. 3-6 present typical photos in the laminar (Re = 150) and turbulent (Re = 450) flow regime, respectively, both exhibiting two anti-phase vortex streets. The pattern is consistent with that obtained in Chapter 2 or reported in the literature. Flow visualisation conducted at Re = 500 by Bearman and Wadcock (1973) showed that two pairs of vortices, when shed from the two cylinders at T/d = 3.00, were in an anti-phase mode. In their experiments, Ishigai *et al.* (1972) observed a remarkably symmetric vortex formation and shedding for T/d = 2.5 and 3.0, but a biased gap flow when T/d was in the range, $1.2 < T/d < 2.0$. The present data suggests that the phenomenon is independent of Re in the range investigated.

The mechanism behind the symmetric vortex shedding behaviour is not clear. Weaver and Abd-Rabbo (1984) and Granger *et al.* (1993) observed a symmetric vortex shedding resonance in a square array of tubes in a cross flow. Weaver and Abd-Rabbo proposed that a symmetric-mode jet instability mechanism might have caused or at least triggered this phenomenon. Noting that during resonance the vibration amplitude was predominant in the streamwise direction, Granger *et al.* (1993) suggested that the inline cylinder motion caused a symmetric oscillation of separation points at the surface of the moving cylinder and could be responsible for the symmetric vortex shedding. This cannot explain the present symmetric vortex shedding at T/d = 3.00. It will be seen in the next section that the cross-flow vibration of the cylinders overwhelms the streamwise vibration when resonance occurs. The inline cylinder motion is unlikely to be, at least not solely, responsible for the present symmetric vortex shedding. When flow separation occurs, the flow

outside the boundary layer is retarded (Prandtl 1976), implying a higher pressure. The pressure upstream of the gap between the cylinders is probably even higher than that close to the free stream, as suggested in Fig. 3-4, thus forming a pressure differential on the two sides of each cylinder in the cross-flow direction. This pressure differential could be symmetrical with respect to the midway of the gap and could tend to suppress the anti-symmetrical vortex shedding and induce the symmetric behaviour.

T/d = 1.70 Typical photographs of the near-wake flow (middle two plates in Fig. 3-6) from flow visualisation in the laminar and turbulent flow regimes indicate a deflected gap flow between the two cylinders, thus forming one narrow and one wide wake. The results are consistent with those for T/d = 1.5 ~ 2.0 previously reported (Spivack 1946; Ishigai *et al.* 1972; Bearman and Wadcock 1973; Kamemoto 1976; Kiya *et al.* 1980; Kim and Durbin 1988; Sumner *et al.* 1999).

T/d = 1.13 The gap vortices were not observed and most vortices were shed alternately from the freestream side of the two cylinders, as evidenced in the photographs (bottom two plates in Fig. 3-6). The photograph at Re = 450 further displays a gap flow or bleeding deflected towards the upper cylinder. The deflected bleeding is likely to cause a difference in p_b between cylinders, thus responsible for the different C_D (Fig. 3-5b). It is worth mentioning that flow visualisation data did show the symmetric vortex shedding from time to time when the gap flow was not deflected, which is consistent with the observation in Chapter 2.

3.4.3 Spectral characteristics

T/d = 3.00 The spectra $E_{\varepsilon y}$ of ε_y from Cylinder 1 and 2 at $U_r \approx 19$ for different T/d values are presented in Fig. 3-7 along with the spectrum E_u of the simultaneously measured streamwise velocity u. No resonance occurs at this

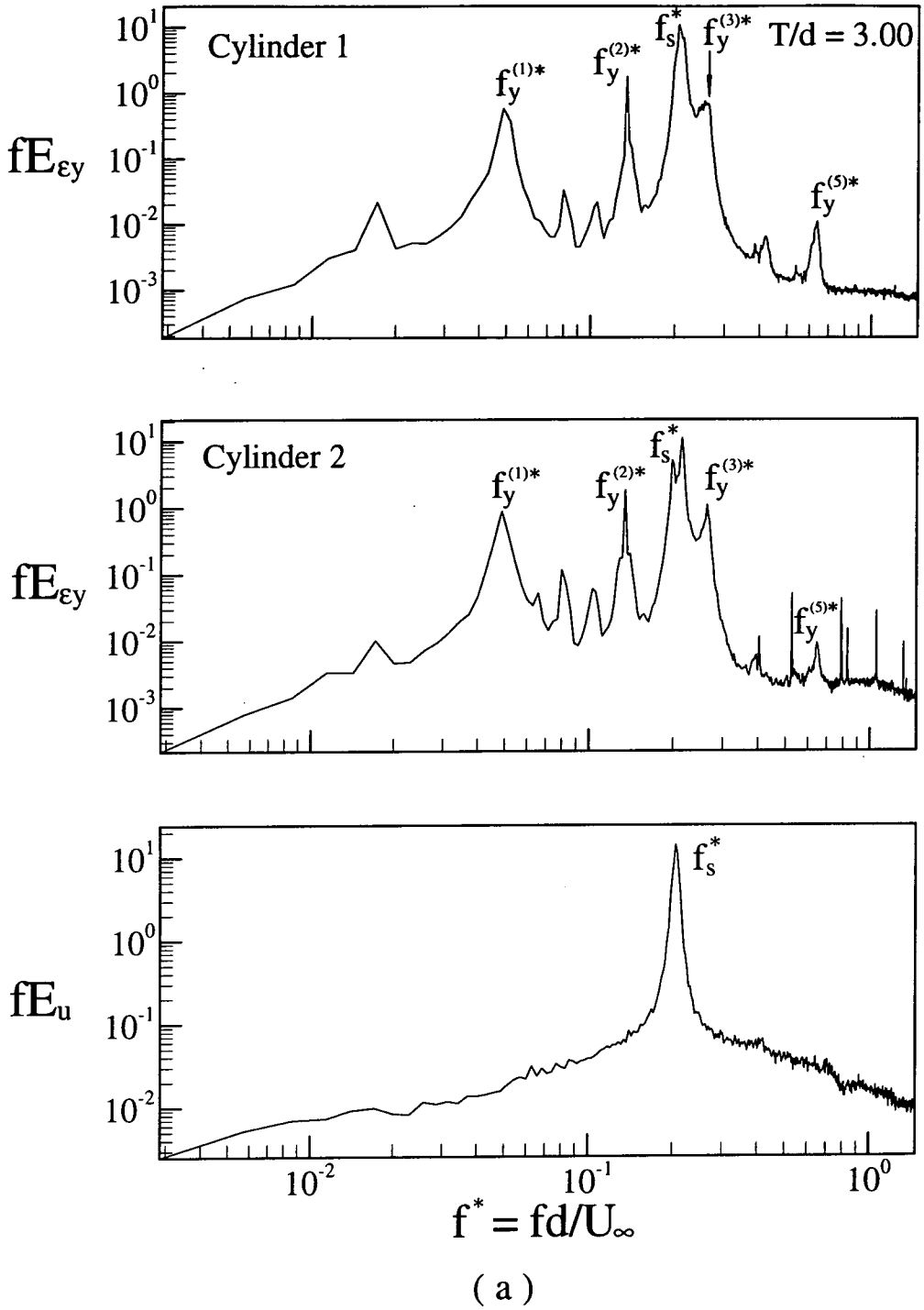

Figure 3-7 Power spectra $fE_{\varepsilon y}$ (upper plate: Cylinder 1; middle plate: Cylinder 2) of the strain ε_y and E_u (lower plate) of the stream-wise velocity u at the off-resonance condition ($U_r \approx 19$, $Re = 4900$). The hot wire was located at $x/d = 2$ and $y/d = 1.5$. (a) $T/d = 3.00$; (b) 1.70; (c) 1.13.

reduced velocity. Here, the focus is on flow-related spectral characteristics, while vibration-related behaviour, such as the prominent peaks in the ε_y-spectrum, is

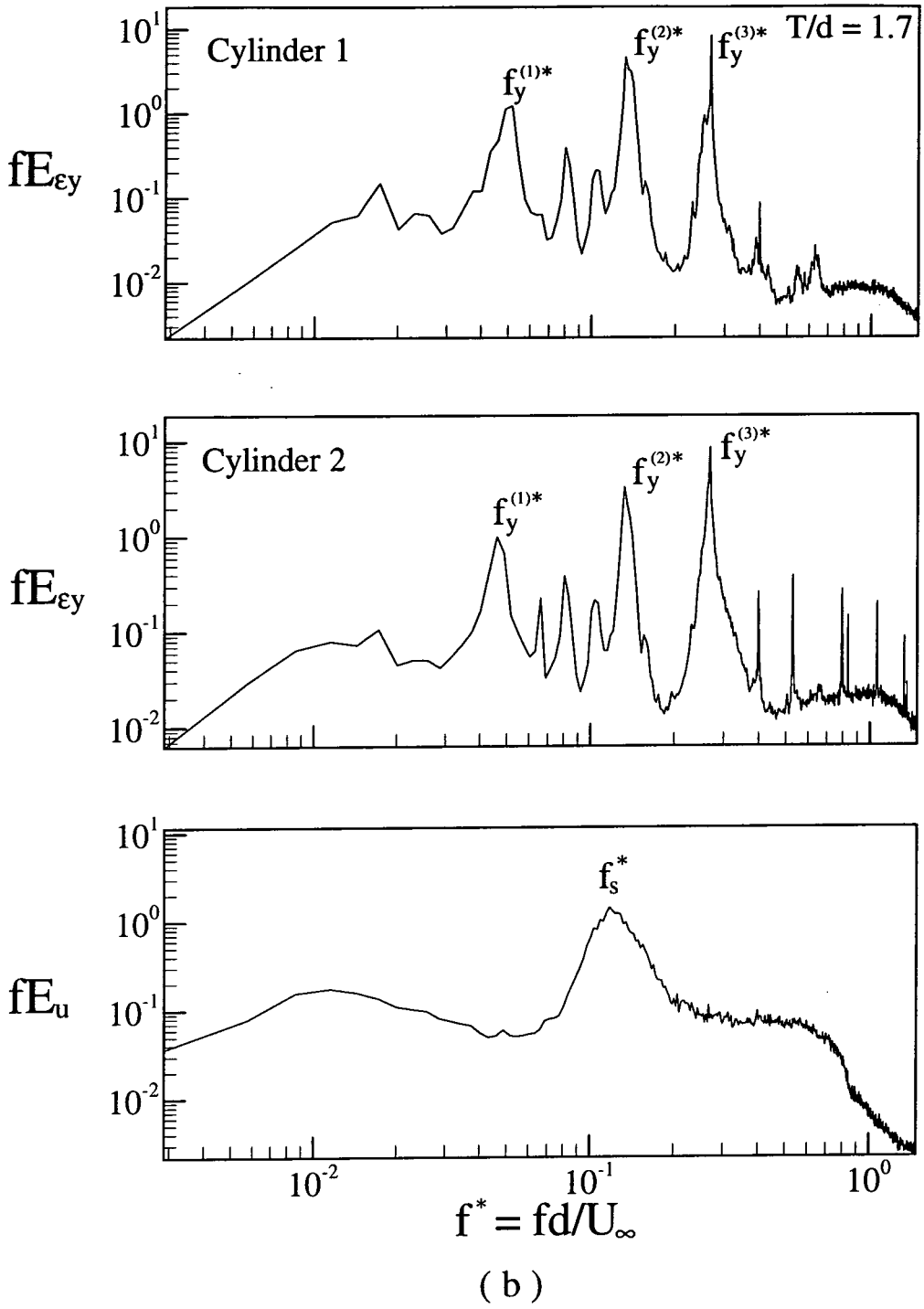

(b)

Figure 3-7b

discussed in Section 3-5. At T/d = 3.00, the u-spectrum (Fig. 3-7a) yields one major peak at $f_s^* = f_s\, d/U_\infty$ = 0.20 which is the same as the normalised vortex shedding frequency (or Strouhal number) of a single cylinder. This peak is also evident in the

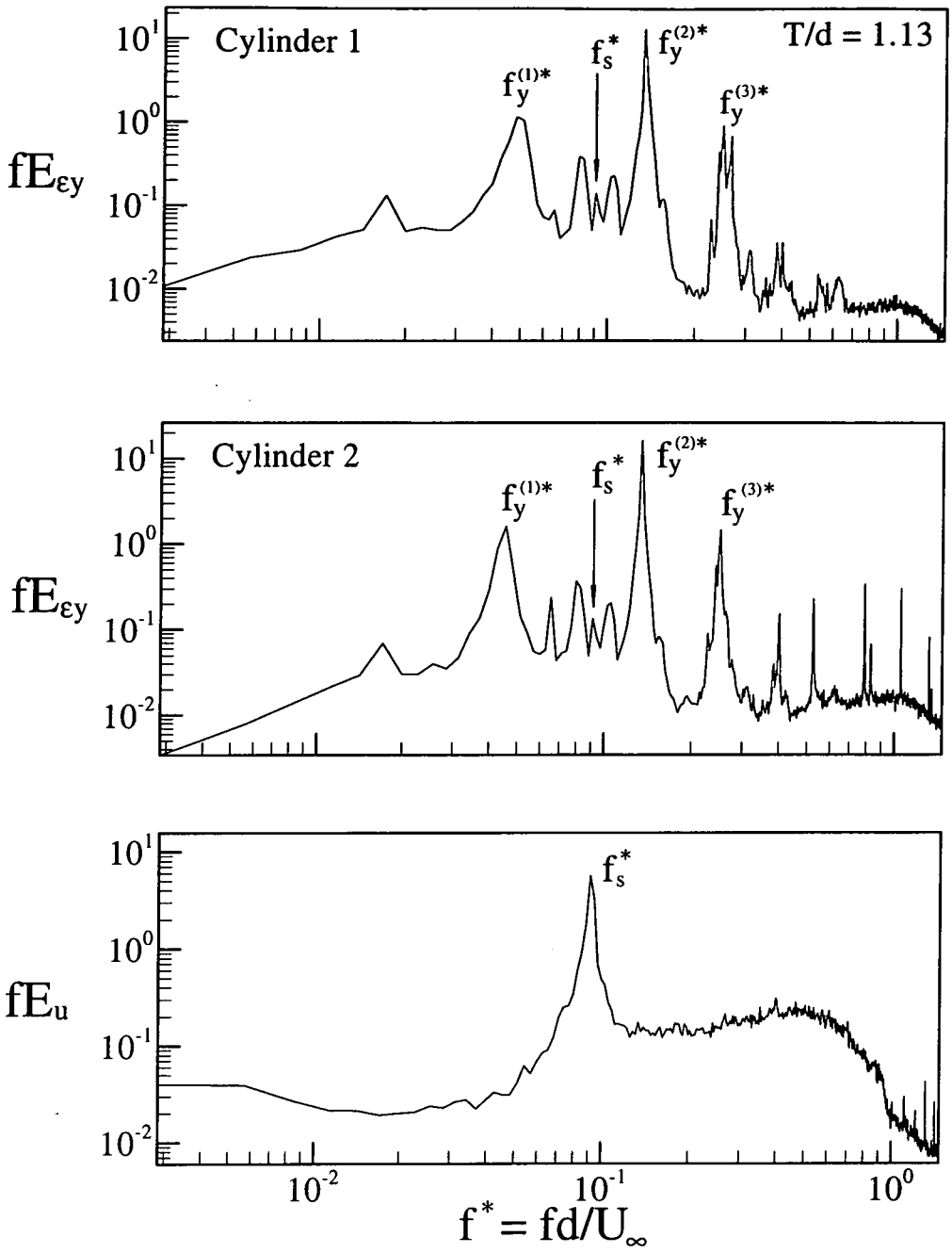

(c)

Figure 3-7c

strain spectra and it occurs at the same frequency for the two strain spectra presented, thus indicating that the shedding frequency for the two cylinders is identical. The spectral phase shift Φ_{12} at f_s between the ε_y signals is generally near + π or - π

(Fig. 3-8a), implying that the two cylinders move in opposite directions. These results conform to the observation from flow visualisation that the vortices are predominantly shed in symmetric pairs or in an anti-phase mode for the two cylinders.

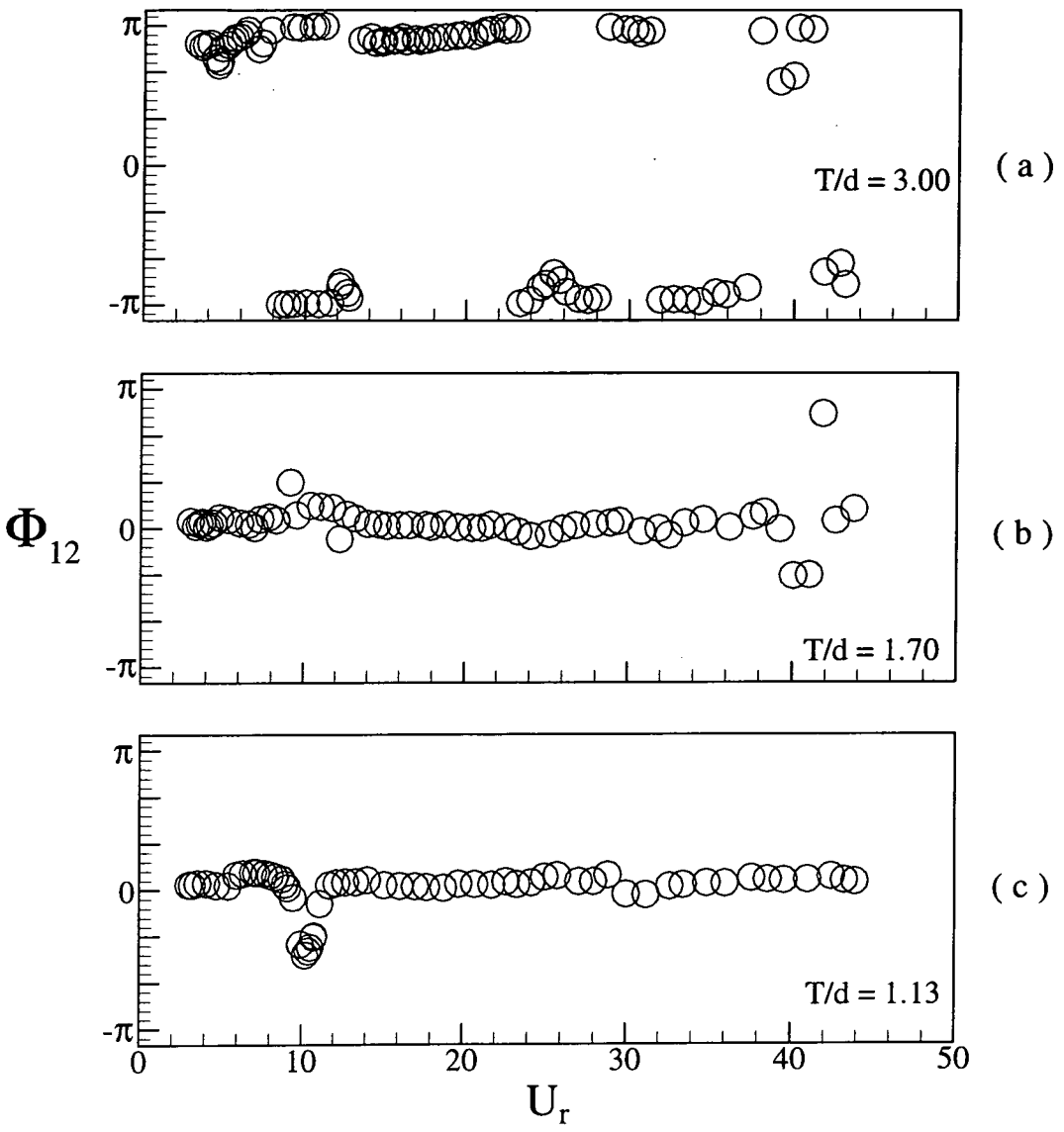

Figure 3-8 Dependence on U_r of the phase shift Φ_{12} at f_s between dynamic strains ε_{y1} and ε_{y2} measured from the two cylinders.

T/d = 1.70 The *u*-spectrum exhibits a broad peak, ranging from 0.08 to 0.20 and centred at $f_s^* = 0.105$ (Fig. 3-7b). This result seems to indicate a frequency range of

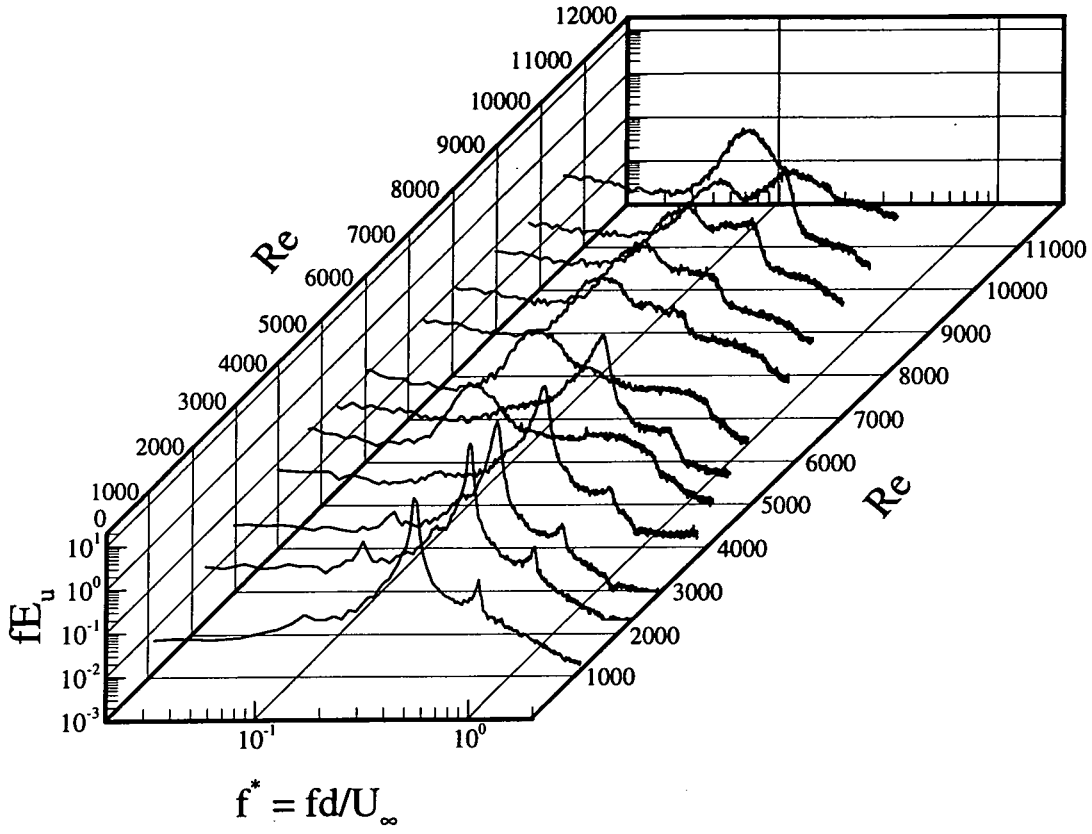

Figure 3-9 Power spectra E_u of u for various Re (T/d = 1.70). The hot wire was located at x/d = 2 and y/d = 1.5.

vortex shedding. It has been reported previously that the narrow and wide wakes observed in flow visualisation were associated with the high and low vortex frequencies, respectively (Spivack 1946; Ishigai *et al.* 1972; Bearman and Wadcock 1973; Kamemoto 1976; Kiya *et al.* 1980; Kim and Durbin 1988; Sumner *et al.* 1999). The ratio of the two frequencies was close to but less than 3 (Kim and Durbin 1988). This is also observed in the present case. The u-spectra for different Re are shown in Fig. 3-9. These spectra show a peak at $f^* \approx 0.1$ or 0.31, or peaks at both frequencies. The physics behind the appearance of two different frequencies was not clear in the past; some researchers (Sumner *et al.* 1999; Kim and Durbin 1988)

suggested two vortex shedding processes or frequencies. Based on flow visualisation at a low *Re* ($\leq$ 200), Williamson (1985) proposed that the two frequencies resulted from the existence of harmonic vortex-shedding modes. On the other hand, the data of Kim and Durbin (1988) at *Re* = 3300 did not support this conjecture. The present flow visualisation in the laminar and turbulent flow regimes in fact suggests another interpretation, which is in consistent with the results presented in Chapter 2.

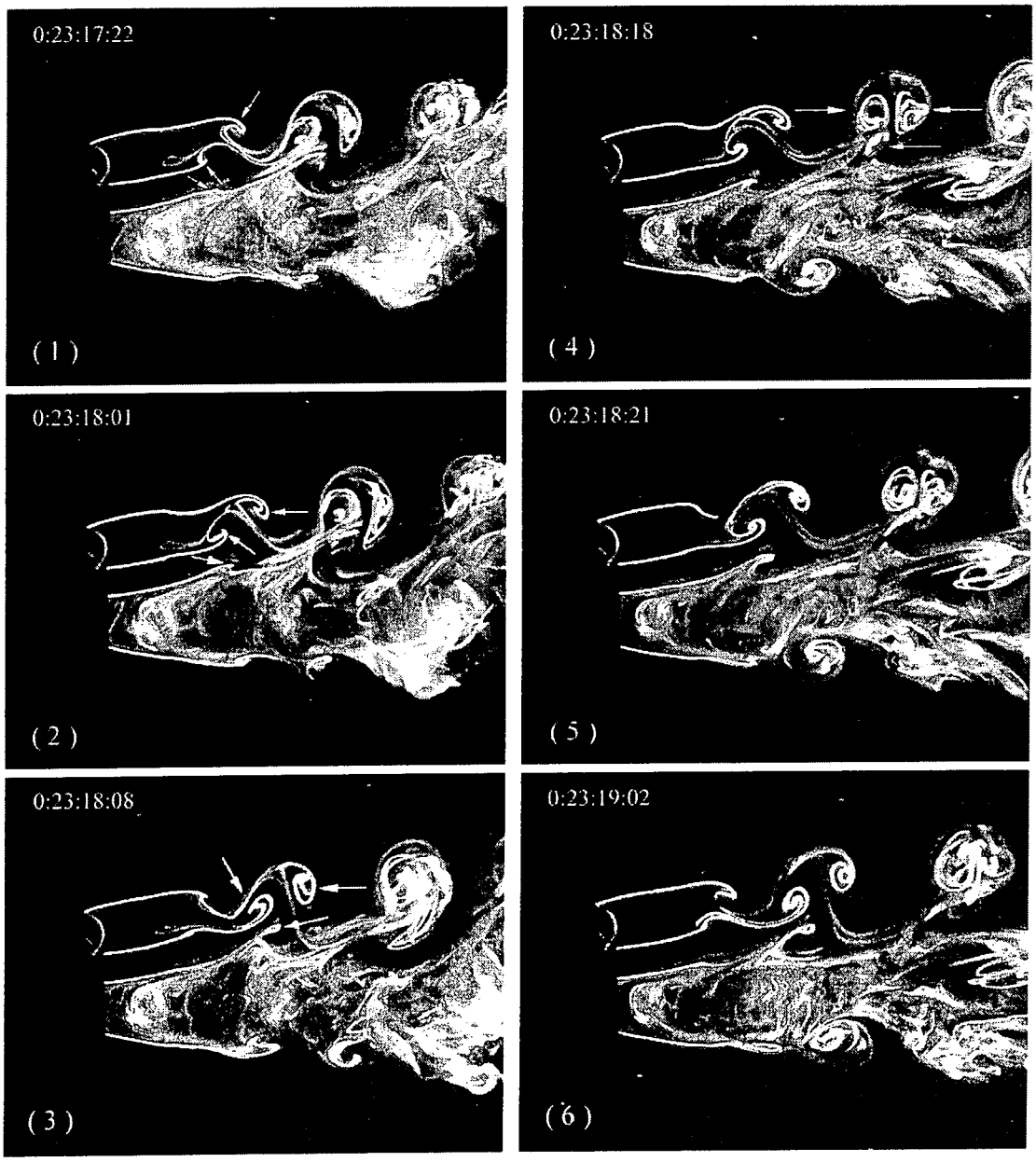

Figure 3-10 Sequential photographs from laser-illuminated flow visualisation (*T/d* = 1.70, *Re* = 450).

In order to understand the two dominant frequencies observed in the velocity spectra, the flow visualisation data was examined in detail. It was noted that vortices were generally shed alternately from both sides of each cylinder, though the gap vortices appeared to be weaker than the outer vortices, which were shed on the freestream side. Playing back the tape and counting consecutive vortices (about 15 pairs) at $x/d \approx 2$ for a certain period, it was noted that the vortices were formed at about the same frequency from the two cylinders. For example, at $Re = 450$, f_s^* was about 0.11 for the lower cylinder and 0.126 for the upper. Similar results were obtained for other Re. This begs the question why the hot wire measured two frequencies and the ratio of the two frequencies was about 3. Sequential photographs at $Re = 450$ are shown in Fig. 3-10. The two rows of vortices in the narrow wake appear squeezed by the wide wake so that their lateral spacing is very small. Initially (Plates 1-3), the longitudinal spacing between two vortices in the narrow wake, as marked by arrows, is large. However, Plates 3 and 4 shows a reduced spacing between the vortices, suggesting that the convection velocity of the outer vortex was smaller than that of the gap vortex, which was possibly carried by the gap flow jet with a higher mean velocity (Sumner *et al.* 1999). As a result, the two opposite-sign vortices were engaged in a pairing process (Plates 4 ~ 6). On the other hand, the gap vortex shed from the lower cylinder, also marked by an arrow, appears pushed into close contact with the pairing vortices by the widening wake. Note that the pairing vortices rotated in opposite directions, acting to 'suck' in the approaching gap vortex (Plates 4-6). Because of the small lateral spacing between the three vortices, the hot wire could measure a frequency tripling that in the wide wake. This observation is consistent with the result obtained in Chapter 2.

The peak in the u-spectrum for $T/d = 1.70$ is considerably less pronounced than that at $T/d = 3.00$. The vortex shedding component is substantially weakened,

thus corroborating the earlier suggestion that the vortex strength is reduced at T/d = 1.70. This reduction is partly attributable to the interference between cylinders, which could be responsible for a decrease in the drag coefficient (Fig. 3-5b). However, the ε_y-spectra, quite similar for the two cylinders, fail to show a strong presence of the vortex excitation at either f_s^* or $3f_s^*$. The spectral phase shift Φ_{12} between the ε_y signals is near zero at $f_s^* = 0.105$ (Fig. 3-8b) but $+\pi$ or $-\pi$ at $3f_s^*$ (not shown). Therefore, it seems that vortices shed from the two cylinders tend to be in-phase at $f_s^* = 0.105$ for $T/d < 2.0$.

T/d = 1.13 When T/d reduces to 1.13, the u-spectrum (Fig. 3-7c) indicates that the vortex shedding frequency is halved, occurring at $f_s^* \approx 0.09$. For such a small transverse spacing, the two cylinders tend to act like a single body and the effective Strouhal number should be really $f_s(2.13d)/U_\infty \approx 0.2$, or $f_s d/U_\infty \approx 0.09$. The phase shift Φ_{12} at f_s^* (Fig. 3-8c) is generally close to zero, indicating that the two cylinders are vibrating in phase in the cross flow direction. It can be inferred that most of the vortices were shed alternately from the free-stream side of the two cylinders, in conformity to the observation from flow visualisation (bottom two plates in Fig. 3-6). Note that at $U_r \approx 11$, Φ_{12} drifts away from zero, displaying a valley. Since $f_s^* \approx 0.09$ (Fig. 3-7c), then the first-mode resonance where $f_0^{(1)} \approx f_s$ occurs at $U_r \approx 1/f_s^* \approx 11$. The natural frequencies of the two cylinders are slightly different (Table 3-1). As a result, while the vibration of one cylinder synchronises with vortex shedding, the other does not. This implies that the two cylinders could respond very differently to the vortex excitation force, thus leading to a phase shift between their vibrations (Fig. 3-8c).

3.5 Fluid-Structure Interactions

3.5.1 Spectral behaviour and root mean square strain

The spectrum $E_{\varepsilon y}$ (Fig. 3-7) of Cylinder 1 exhibits one peak at $f^* \approx 0.049$, irrespective of the transverse spacing. The peak can be identified with the first-mode natural frequency $f_y^{(1)*}$ of the combined fluid-cylinder system for a single cylinder placed in a cross-flow, as verified by the numerical calculation of So *et al.* (2000a). Another peak occurs at $f^* \approx 0.264$. The third-mode natural frequency can be estimated from $f_y^{(3)^*}$ = (121/22.4) $f_y^{(1)*}$ = 0.265 (Chen 1987). Therefore, this peak corresponds to the third-mode natural frequency $f_y^{(3)*}$ of the combined fluid-cylinder system. Similarly, the peak at $f^* = 0.135$ is identified with the second-mode natural frequency of the system. The ε_y-spectrum from Cylinder 2 exhibits a close resemblance to that from Cylinder 1.

The dependence of $\varepsilon_{y,rms}$ and $\varepsilon_{x,rms}$ on U_r from the two cylinders is shown in Figs. 3-11 and 3-12, respectively. The rms values of the measured strain from the two cylinders collapse quite well and generally increase with U_r. At T/d = 3.00, $\varepsilon_{y,rms}$ displays three peaks at $U_r \approx 4.2$, 12.0 and 26.0, respectively, while $\varepsilon_{x,rms}$ shows only one tiny peak at $U_r \approx 26.0$. Note that when $U_r > 33$, $\varepsilon_{x,rms}$ increases faster and becomes larger than $\varepsilon_{y,rms}$.

The peaks in $\varepsilon_{y,rms}$ at $U_r \approx 4.2$, 12.0 and 26.0 (Fig. 3-11a) can be identified from the spectral analysis with resonance occurring when the vortex shedding frequency is equal to the system natural frequencies $f_y^{(1)}$, $f_y^{(2)}$ and $f_y^{(3)}$, respectively. While the peak at $U_r \approx 12$ is barely identifiable, the one at $U_r \approx 26$ is

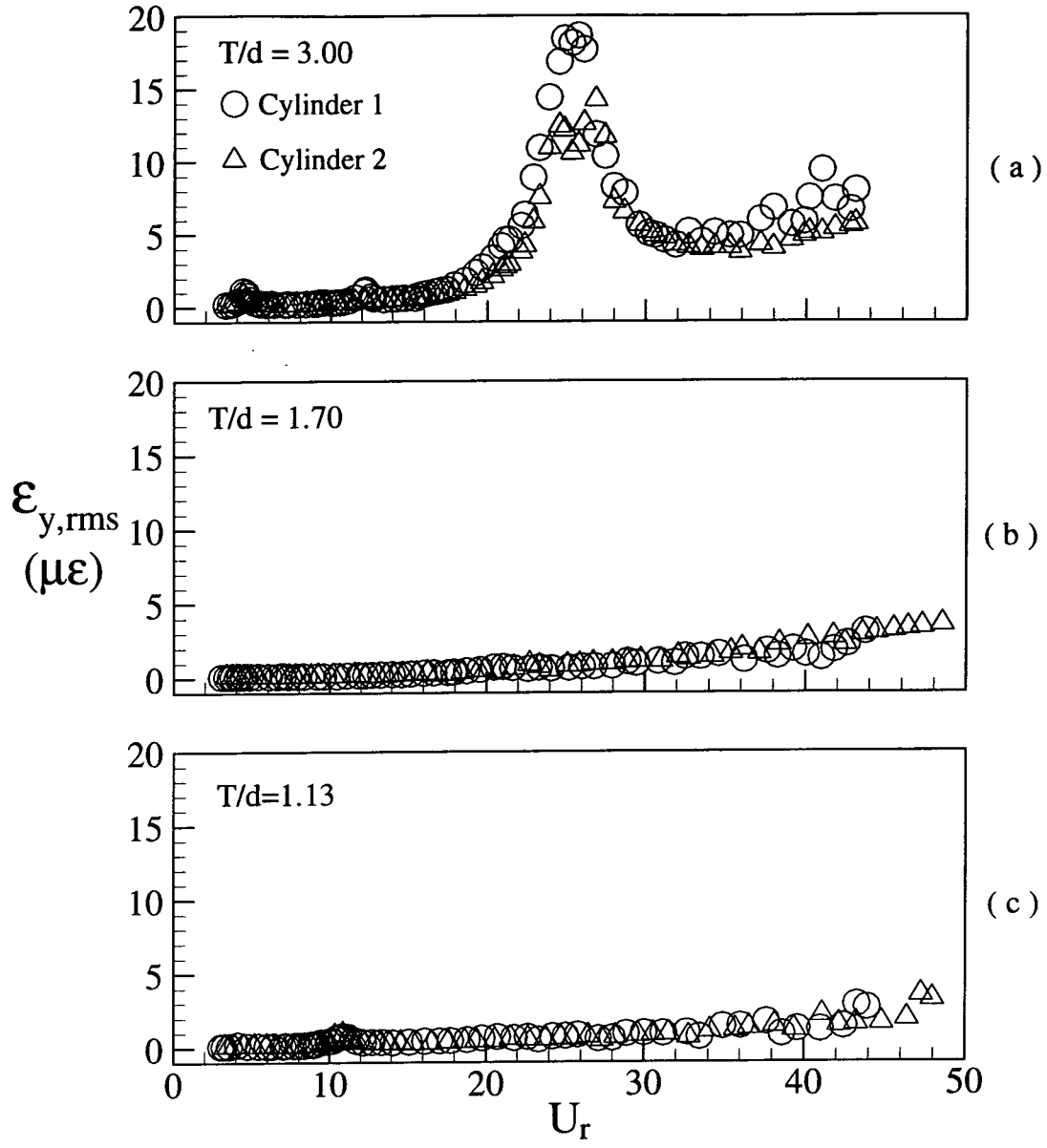

Figure 3-11 Variation of $\varepsilon_{y,rms}$ with U_r at various spacing ratio: (a) T/d = 3.00; (b) T/d = 1.70; (c) T/d = 1.13. O, Cylinder 1; Δ, Cylinder 2.

most prominent. The simultaneously measured $E_{\varepsilon y}$ from the two cylinders at $U_r \approx$ 26 along with E_u are presented in Fig. 3-13. The most prominent peak in $E_{\varepsilon y}$ occurs at $f_y^{(3)*} \approx 0.2$, which coincides with f_s^*, as evidenced in E_u (Fig. 3-13c). The occurrence of resonance is responsible for this prominent peak in $E_{\varepsilon y}$ and hence that

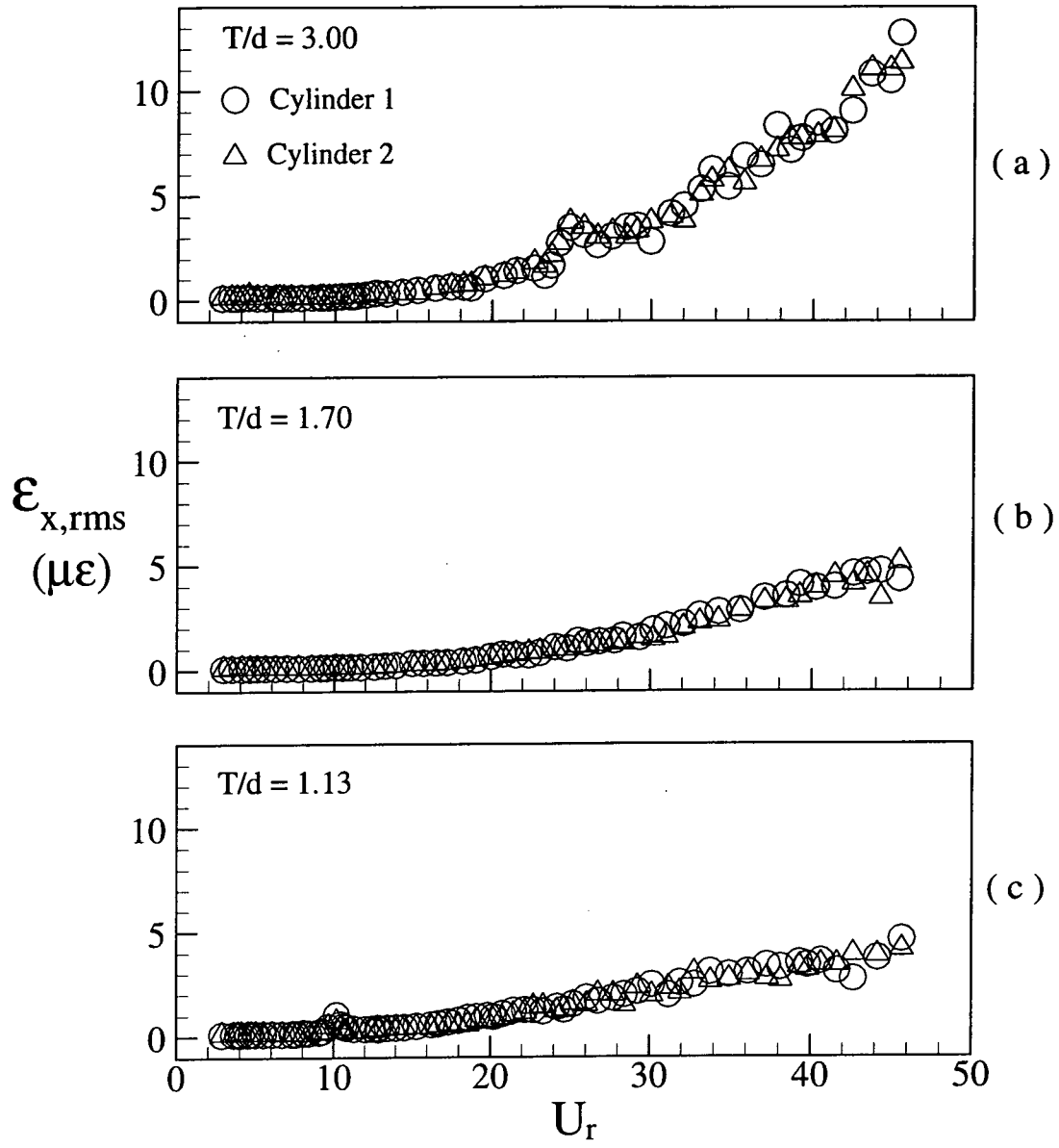

Figure 3-12 Variation of $\varepsilon_{x,rms}$ with U_r at various spacing ratio: (a) T/d = 3.00; (b) T/d = 1.70; (c) T/d = 1.13. O, Cylinder 1; Δ, Cylinder 2.

at $U_r \approx 26$ in $\varepsilon_{y,rms}$. Similarly, the peaks at $U_r \approx 4.2$ and 12 in $\varepsilon_{y,rms}$ could be identified with the result of resonance corresponding to the first- and second-mode natural frequencies of the fluid-cylinder system, respectively.

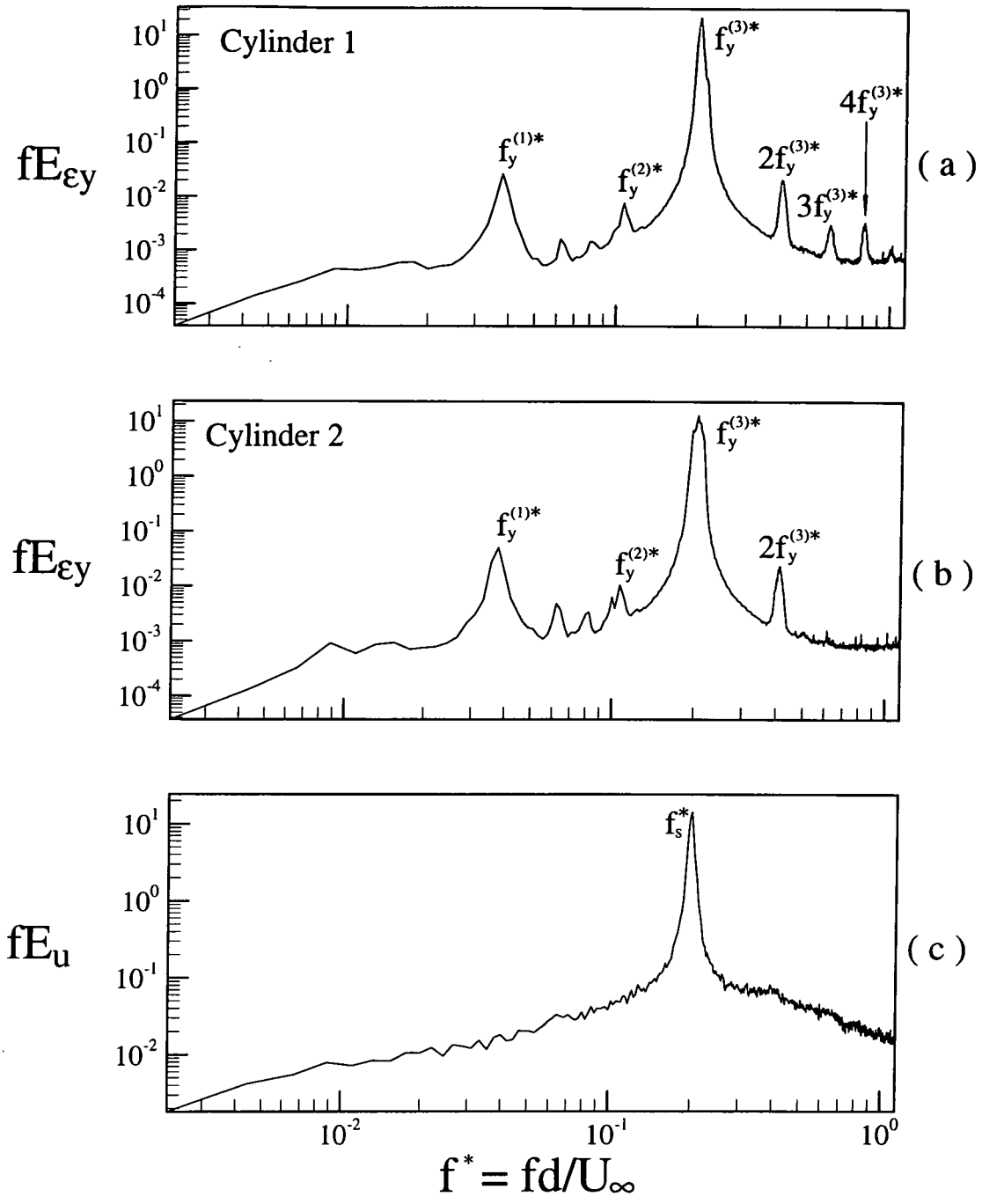

Figure 3-13 Power spectra $fE_{\varepsilon y}$ (upper plate: Cylinder 1; middle plate: Cylinder 2) of the strain ε_y and E_u (lower plate) of the stream-wise velocity u at $U_r \approx 26$ where the third-mode resonance occurs (T/d = 3.00). The hot wire was located at x/d = 2 and y/d = 1.5.

The observation that the peak at $U_r \approx 26$ is far more pronounced than the others may not be surprising. Firstly, resonance corresponding to $f_y^{(3)}$ occurs at a

higher U_r. Flow excitation energy, which is proportional to U_r^2, is therefore much higher. Secondly, it will be seen later in Section 3-5-3 that the deduced effective damping ratio, the sum of the structural and fluid damping ratio, corresponding to $f_y^{(3)}$ is appreciably smaller than that corresponding to $f_y^{(1)}$ or $f_y^{(2)}$. This implies that the energy dissipation, when resonance occurs at $f_s = f_y^{(3)}$, is smallest. Thirdly, the fifth harmonic of $f_y^{(1)*}$ ($\approx$0.0394) is 0.197 and is very close to $f_s^* = 0.2$. This could feed additional energy to the resonance phenomenon. These three effects combined together could lead to a violent vibration or instability at $f_y^{(3)}$ (Fig. 3-11a). This observation suggests that structural flexibility play a significant role in the dynamic analysis. In practice, all structures are flexible; however, structural flexibility has so far been ignored in most previous studies. Consequently, resonance occurring at $U_r \approx 5$ has been extensively investigated, while instability corresponding to $f_y^{(3)}$ has been largely overlooked.

As *T/d* reduces to 1.70, the $\varepsilon_{y,rms}$ values decrease considerably for both cylinders; resonance does not appear to occur at all. In this case, vortices shed from both cylinders are very weak, as seen earlier from the *u*-spectrum. Accordingly, structural vibrations are impeded, even at the occurrence of resonance. This observation is in marked contrast with that at *T/d* = 3.00. The difference is consistent with the observation from the measured spectra, which exhibited a weakening vortex shedding component at *T/d* = 1.70 (Fig. 3-7b), compared with that at *T/d* = 3.00 (Fig. 3-7a). At *T/d* = 1.13, only one peak in $\varepsilon_{y,rms}$ and $\varepsilon_{x,rms}$ is observed at $U_r \approx 11$ because of the first-mode resonance. The third-mode resonance is expected to occur near $U_r \approx (121/22.4)\ 11 = 59.4$, which is beyond the present measurement range, and therefore cannot be observed in Fig. 3-11c.

3.5.2 Natural frequencies of the fluid-cylinder system

The natural frequency $f_y^{(1)}$ identified in Fig. 3-7a of the fluid-cylinder system associated with Cylinder 1 is 101 Hz at T/d = 3.00. This frequency changes to 103.3 Hz at T/d = 1.70 (Fig. 3-7b) and 104.7 Hz at T/d = 1.13 (Fig. 3-7c). Note that the mounting of Cylinder 1 was unchanged throughout the experiments. Therefore, $f_y^{(1)}$ should remain fairly constant. Furthermore, the spectra were deduced using a conventional FFT program, the frequency resolution is fixed by the sampling rate and the record length used in the FFT calculation. It is estimated to be 0.35 Hz. In view of these factors, the variation of $f_y^{(1)}$ noted above cannot be attributed to experimental or calculation errors.

The dependence of $f_y^{(1)}/f_0^{(1)}$ in the cross-flow direction on T/d and U_r is shown in Fig. 3-14. Generally, $f_y^{(1)}/f_0^{(1)}$ rises with decreasing T/d. This is more appreciable when $U_r > 14$. A number of factors could alter the natural frequency of the system other than the repulsive force between the cylinders. As a first-order approximation, a spring-damper-mass model can be used to model the fluid-cylinder system. Both fluid and structure contribute to the system mass, stiffness and the damping ratio. A rise (Fig. 3-5a) in the repulsive force as the cylinders approach each other is equivalent to an increase in fluid rigidity. Alternatively, from a different perspective, an increasing repulsive force between two cylinders should be associated with a tensile axial loading on the cylinder, which was fix-supported at both ends, and subsequently increased the structural rigidity (Weaver *et al.* 1989; Xu *et al.* 2001). As a result, the system natural frequency might increase. This has been qualitatively verified based on the measured lift data. Added mass is another factor that may change the natural frequency of the system. Chen (1987) calculated the added mass on two side-by-side cylinders in a cross flow and found that, in the range

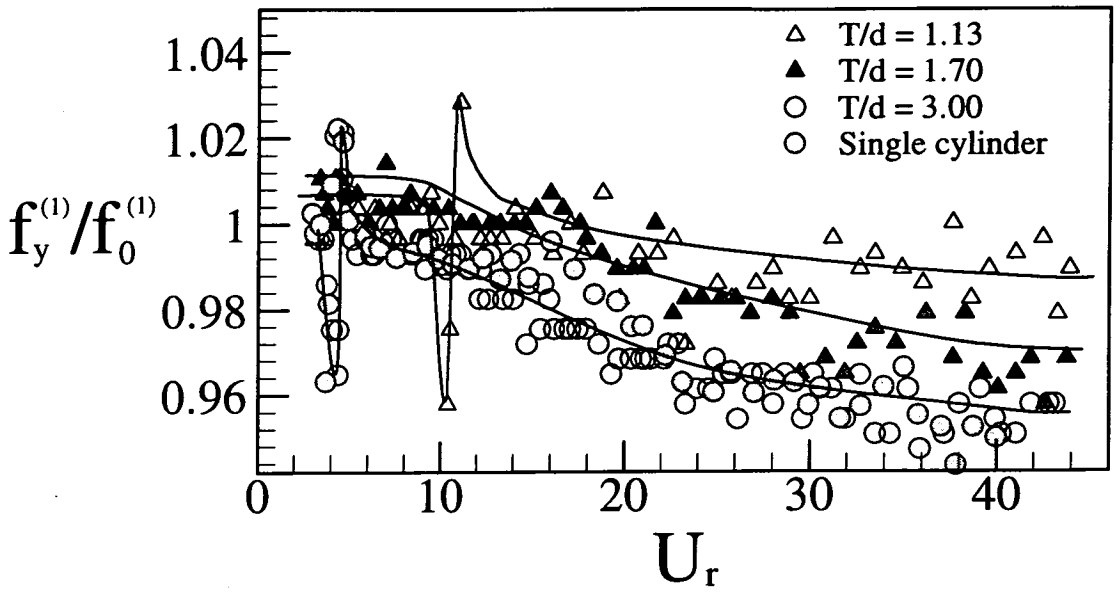

Figure 3-14 Variation of the cross-flow $f_y^{(1)}$ with *T/d* and U_r. Cylinder 1. Δ, *T/d* = 1.13; ▲, 1.70; O, 3.00; ●, single cylinder. The solid line indicates the trend.

of $1.13 < T/d < 4$, the added mass increases as *T/d* decreases, thus contributing to a decrease in the system natural frequency. The system natural frequency may also be affected by the non-linear fluid damping. This effect is however not well understood and subsequently make it difficult to estimate quantitatively the contribution from each factor to the variation in $f_y^{(1)}/f_0^{(1)}$. On the other hand, $f_x^{(1)}/f_0^{(1)}$ in the inline direction appears to decrease for $U_r > 12$ (the corresponding *Re* is 2900) as *T/d* reduces (Fig. 3-15). Again, this could be the combined effect of varying system mass, stiffness and damping ratios with *T/d*.

The value of $f_y^{(1)}/f_0^{(1)}$ and $f_x^{(1)}/f_0^{(1)}$ appears to be slowly decreasing as U_r increases. For the purpose of comparison, the fluctuating displacement data of an isolated elastic cylinder in a cross flow (Zhou *et al.* 1999b) was also analysed. The deduced $f_y^{(1)}/f_0^{(1)}$ is included in Fig. 3-14, which exhibits a behaviour similar to the two cylinder case. It is therefore conjectured that the observation is not directly

related to the interference between cylinders but rather to the fluid-cylinder interaction. A linear analysis of the combined fluid-cylinder system (Zhou *et al.* 2001) indicates that a varying fluid damping, as U_r increases, could be responsible for the slowly evolving system natural frequency.

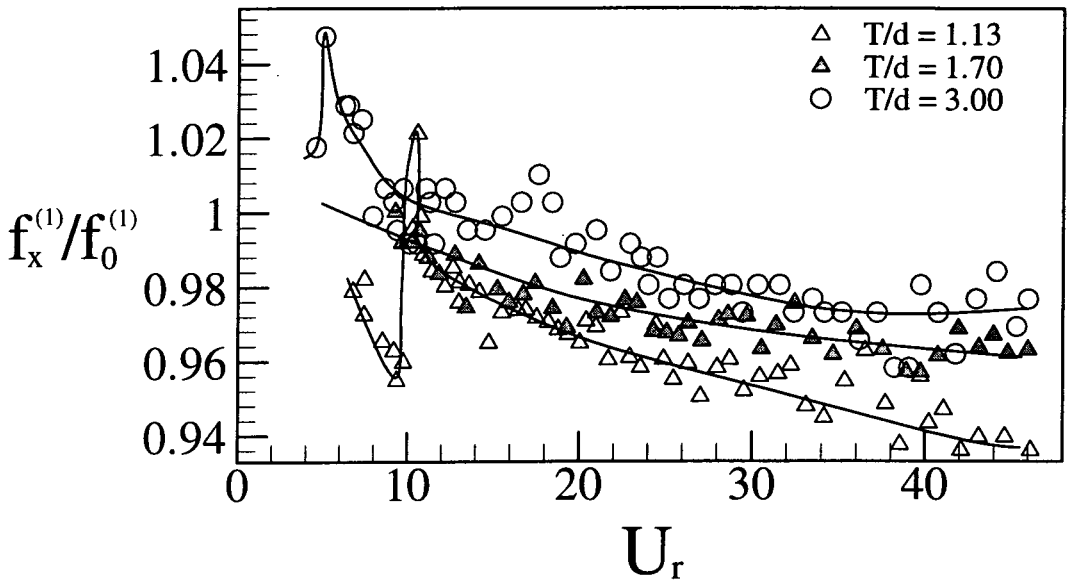

Figure 3-15 Variation of the inline $f_x^{(1)}$ with U_r. Cylinder 1. Δ, T/d = 1.13; ▲, 1.70; O, 3.00. The solid line indicates the trend.

It is interesting to note that, when resonance occurs near $U_r \approx 4.2$ for T/d = 3.00 and $U_r \approx 11.0$ for T/d = 1.13, $f_y^{(1)}/f_0^{(1)}$ falls off sharply and then rises rapidly away from resonance. The variation ranges between 6% and 10% of $f_0^{(1)}$. For Cylinder 2, the dependence of $f_y^{(1)}/f_0^{(1)}$ on U_r (Chapter 4) is quite similar to that presented for Cylinder 1. Price and Paidoussis (1989) measured the free vibration of a cylinder located in a tube bundle in a water cross flow. Their test cylinder was rigid but flexibly mounted at both ends and $U_r < 10$. They observed that near resonance the system natural frequency (or fluidelastic natural frequency) decreased

initially and then increased rapidly as U_r increases. The mechanism behind the observation was not discussed.

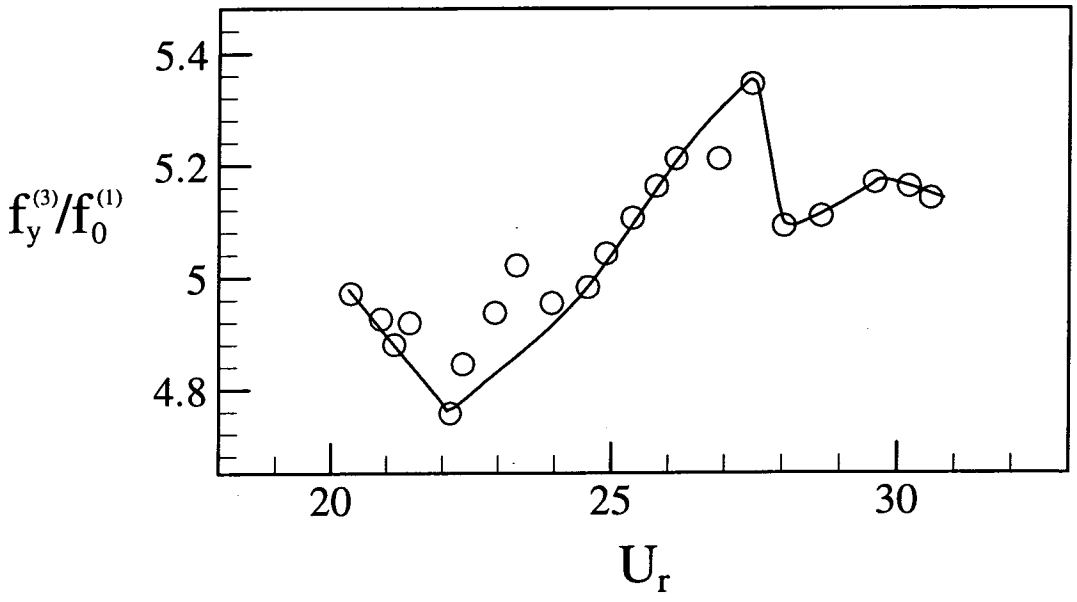

Figure 3-16 Variation of $f_y^{(3)}$ with U_r near resonance. Cylinder 1, T/d = 3.00. The solid line indicates the trend.

There is no drastic change in $f_y^{(1)}/f_0^{(1)}$ near U_r = 26.0 where $\varepsilon_{y,rms}$ is largest. As postulated previously, resonance near U_r = 26.0 occurs as a result of the coincidence of the vortex shedding frequency with $f_y^{(3)}$. A 10% variation in $f_y^{(3)}/f_0^{(1)}$ between U_r = 21 ~ 31 is clearly shown in Fig. 3-16. The observation further corroborates the earlier conjecture that the major mechanism behind the instability, i.e. the prominent peak at $U_r \approx$ 26.0, is the resonance of the vortex shedding frequency with $f_y^{(3)}$. The variation of $f_y^{(3)}/f_0^{(1)}$ follows a similar fashion to that of $f_y^{(1)}/f_0^{(1)}$ near U_r = 4.2 for T/d = 3.00 or U_r = 11 for T/d = 1.13.

It is known that when a structure is forced to vibrate in a cross flow, a lock-in phenomenon occurs when the vortex shedding frequency coincides with the frequency of the imposed excitation force. In free vibration, however, it is the vortex

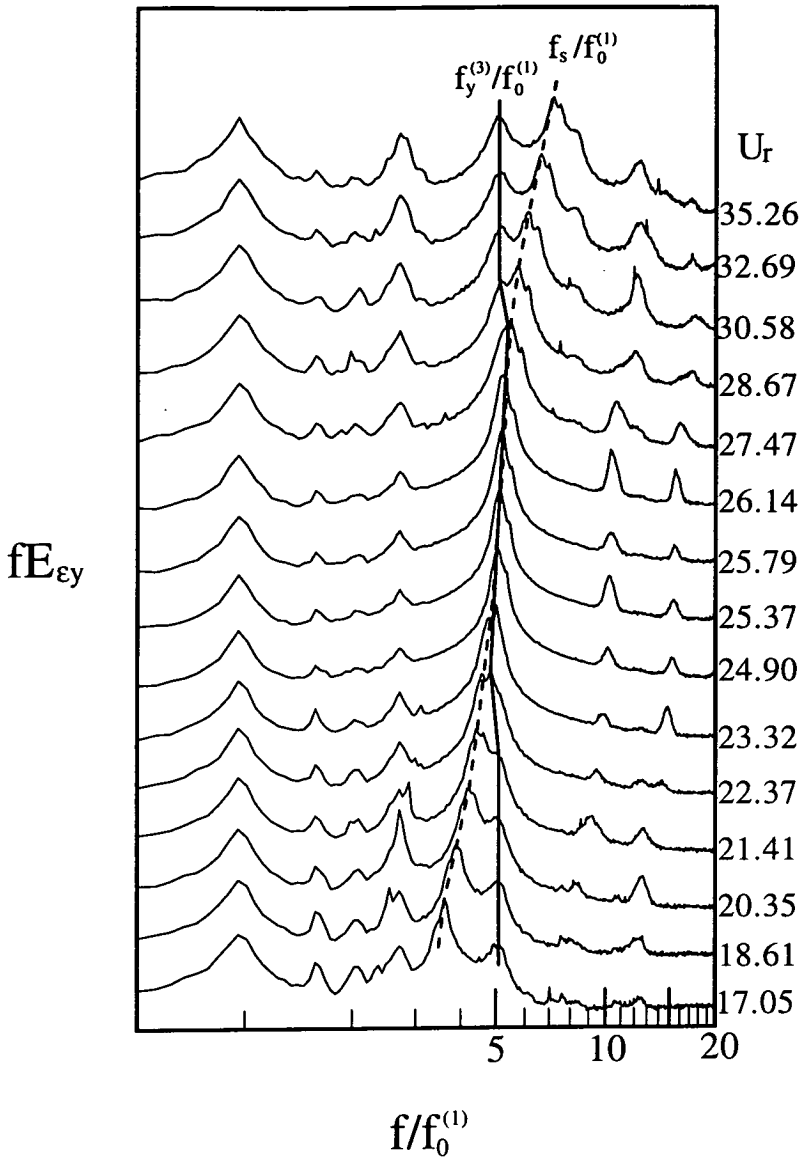

Figure 3-17 Power spectra $fE_{\varepsilon y}$ of the strain ε_y for varying U_r, T/d = 3.00, Cylinder 1. The solid line highlights the trend.

shedding that excites the structure. Therefore, the vortex-induced force dominates. This force has a dominant frequency equal to that of vortex shedding. In the T/d = 3.00 case, the ε_y-spectra for U_r = 17 ~ 35 indicate that the third-mode natural frequency varies near resonance; the variation appears dictated by the vortex shedding frequency (Fig. 3-17). To highlight this point, Fig. 3-18 compares the

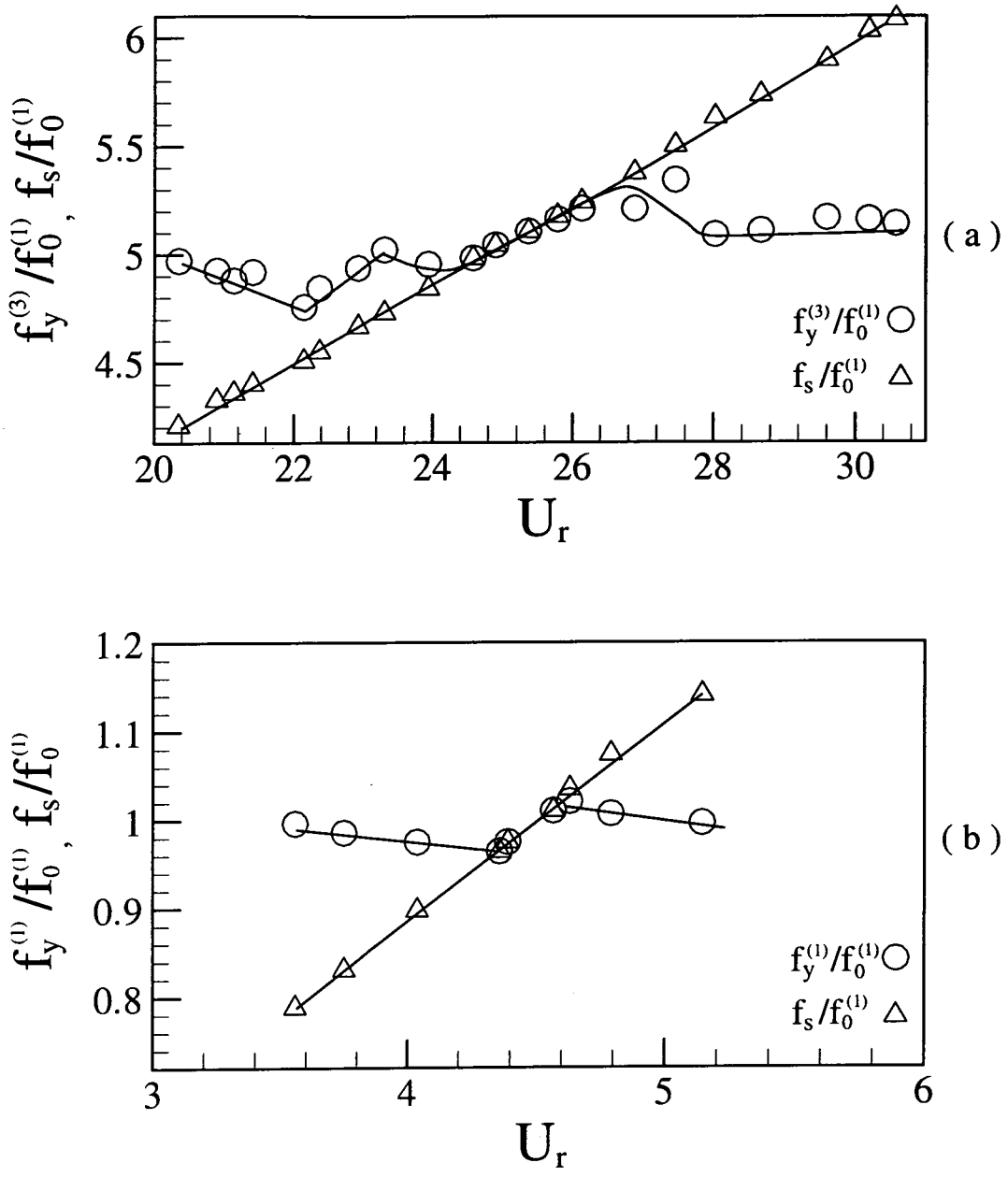

Figure 3-18 Variation of the system's natural frequency (O) and the vortex shedding frequency (Δ) with U_r around resonance: (a) $f_y^{(3)}$ and f_s; (b) $f_y^{(1)}$ and f_s. Cylinder 1, T/d = 3.00. The solid line indicates the trend.

variation of $f_s/f_0^{(1)}$ with that of $f_y^{(3)}/f_0^{(1)}$ (Fig. 3-18a) and $f_y^{(1)}/f_0^{(1)}$ (Fig. 3-18b) near resonance. At U_r = 20.4, $f_s/f_0^{(1)}$ and $f_y^{(3)}/f_0^{(1)}$ are close enough to interact with each other and resonance starts to occur. Influenced by the relatively small

value of $f_s / f_0^{(1)} = 4.2$, $f_y^{(3)} / f_0^{(1)}$ drops from 4.98 to approach $f_s / f_0^{(1)}$. Note that $f_s / f_0^{(1)}$ remains linear with respect to U_r, implying that $f_y^{(3)}$ imposes little influence on f_s. Such interplay between f_s and $f_y^{(3)}$ continues until they are identical or synchronise at $U_r = 24.6$. The system tends to maintain synchronisation. As $f_s / f_0^{(1)}$ increases with increasing U_r, $f_y^{(3)} / f_0^{(1)}$ follows $f_s / f_0^{(1)}$ until eventually $f_s / f_0^{(1)}$ and $f_y^{(3)} / f_0^{(1)}$ are de-coupled from each other at $U_r \approx 26.2$. The interaction between f_s and $f_y^{(1)}$ is quite similar near $U_r = 4.2$ (Fig. 3-18b) or $U_r =$ 11 at $T/d = 1.13$ (not shown). Clearly, vortex shedding dominates the nonlinear interaction between the fluid excitation force and the structural vibration in the free vibration case, thus tuning the natural frequency of the system to the vortex shedding frequency. This observation contrasts with the lock-in phenomenon where the vortex shedding frequency is dictated by the forced vibration frequency of a cylinder.

It is worth pointing out that $f_y^{(3)}$ varies over $U_r \approx 20 \sim 28$, whereas $f_y^{(1)}$ varies over $U_r \approx 3.5 \sim 5$ only. The difference in the U_r range is probably because the fluid excitation force at $U_r \approx 26$ is far greater than that near $U_r \approx 4.2$. It is foreseeable that the U_r range over which the system natural frequency varies will be even greater in the context of a water flow where the excitation force is much greater.

3.5.3 Effective damping ratios

The effective damping ratio of a fluid-cylinder system is made up of fluid and structural damping. The free vibration of an elastic structure has multiple modes with different natural frequencies and effective damping ratios. This section discusses the behaviour of these modal damping ratios and their dependence on U_r

and *T/d*. The modal damping ratios were calculated from the ε_y and ε_x signals using ARMA technique.

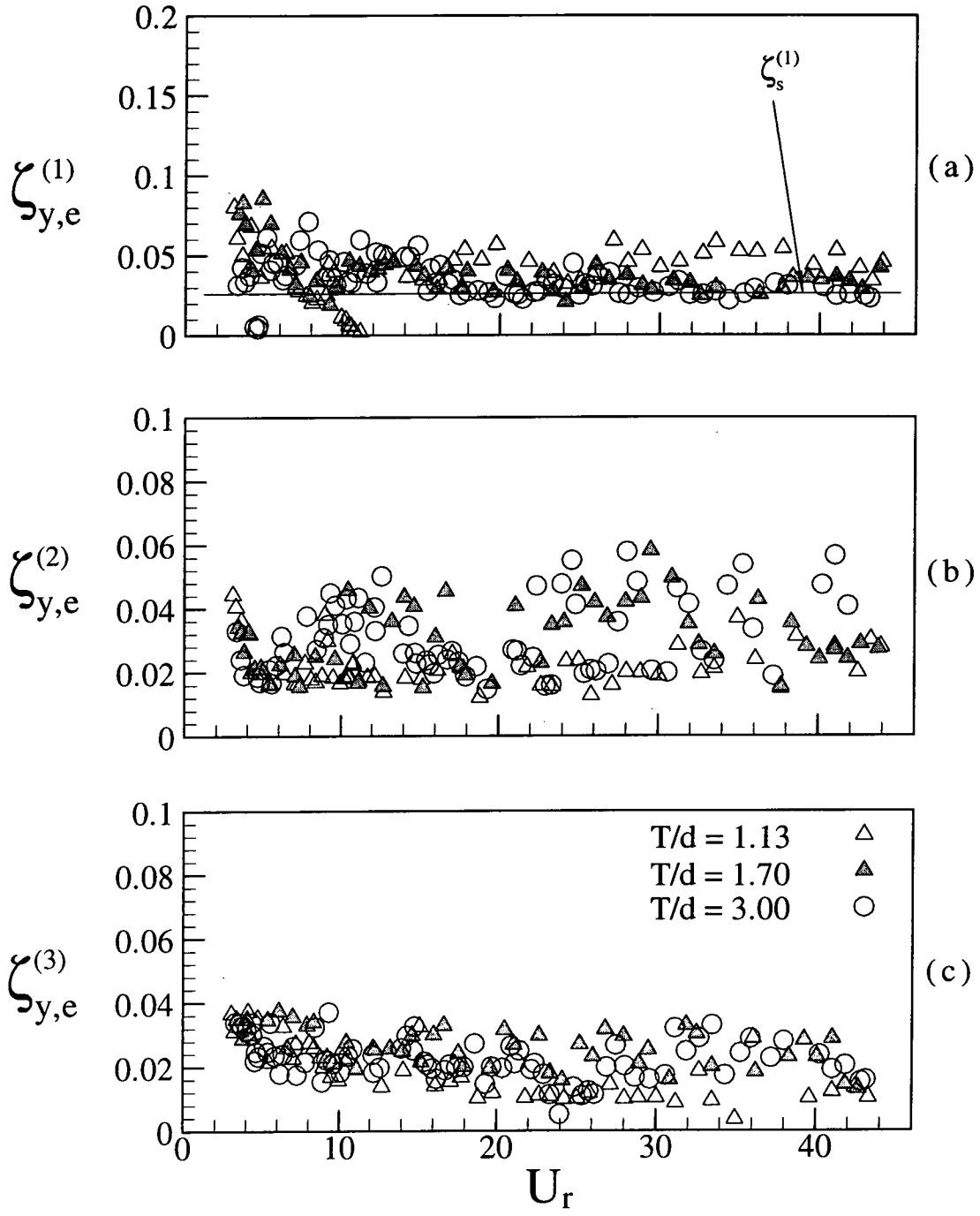

Figure 3-19 Cross-flow effective damping ratios of the fluid-cylinder system: (a) $\zeta_{y,e}^{(1)}$; (b) $\zeta_{y,e}^{(2)}$; (c) $\zeta_{y,e}^{(3)}$. Cylinder 1. Δ, *T/d* = 1.13; ▲, 1.70; O, 3.00.

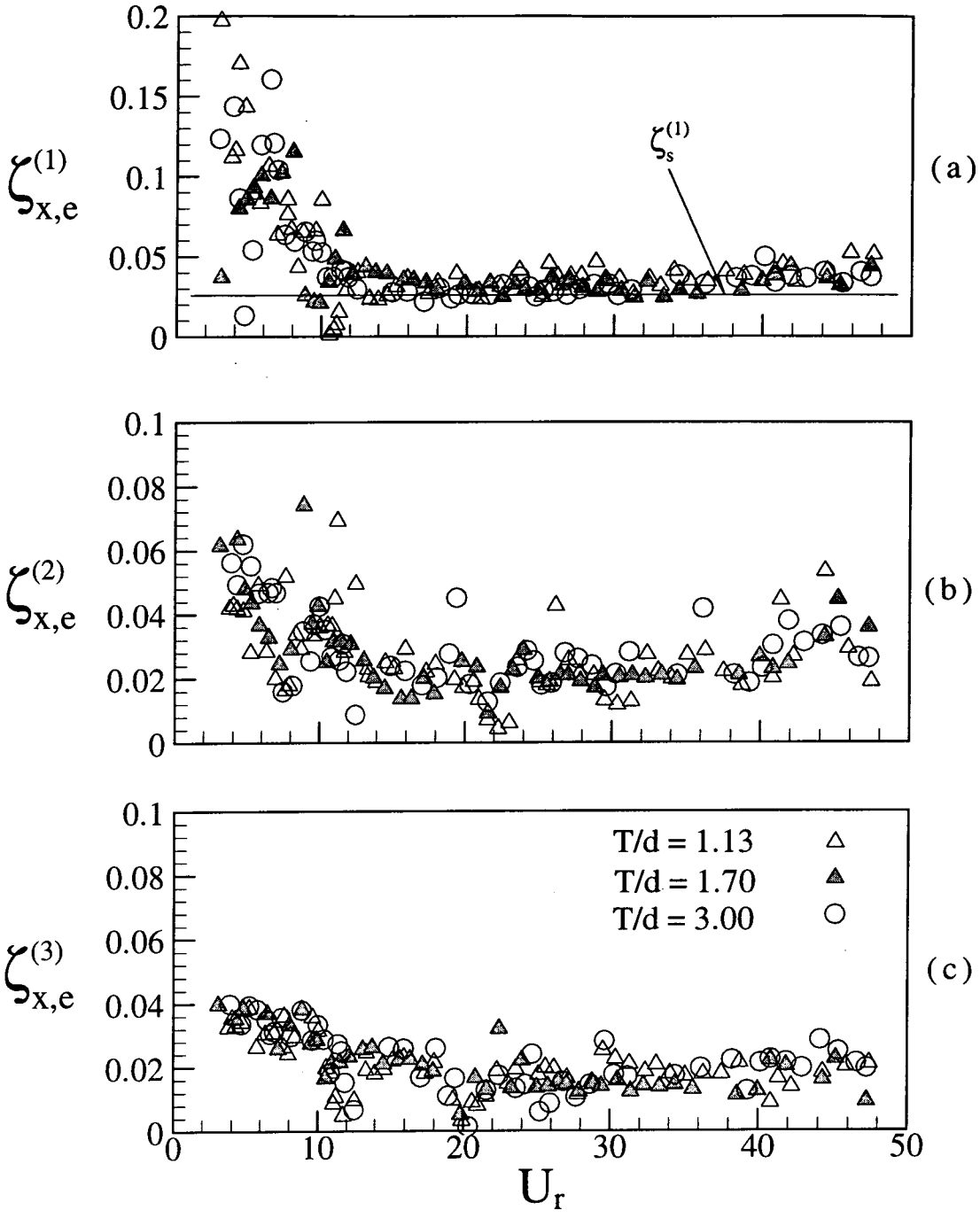

Figure 3-20 Inline effective damping ratios of the fluid-cylinder system: (a) $\zeta_{x,e}^{(1)}$; (b) $\zeta_{x,e}^{(2)}$; (c) $\zeta_{x,e}^{(3)}$. Cylinder 1. Δ, T/d = 1.13; ▲, 1.70; O, 3.00.

Figure 3-19 presents the cross-flow modal damping ratios, $\zeta_{y,e}^{(1)}, \zeta_{y,e}^{(2)}$ and $\zeta_{y,e}^{(3)}$, corresponding to the system natural frequencies $f_y^{(1)}, f_y^{(2)}$ and $f_y^{(3)}$, respectively. The ratios are calculated from the ε_y signals of Cylinder 1. The inline

ratios $\zeta_{x,e}^{(1)}$, $\zeta_{x,e}^{(2)}$ and $\zeta_{x,e}^{(3)}$ are given in Fig. 3-20. In these figures, the solid line represents the first-mode structural damping ratio.

The values of $\zeta_{y,e}^{(2)}$ and $\zeta_{x,e}^{(2)}$ exhibit relatively large scattering. As shown in Fig. 3-11, the resonance corresponding to the second-mode natural frequency of the system is the least violent at $T/d = 3.00$ and fails to occur when $T/d < 3.00$. The ε_y-spectrum (not shown) indicates that even when f_s coincides approximately with $f_y^{(2)}$ at $T/d = 1.13$, the peak at $f_y^{(2)}$ does not appear to be more pronounced than that at $f_y^{(1)}$ and $f_y^{(3)}$. It is evident that the excitation for the second mode of vibration is weak, as compared with that for the first or third mode of vibration. This is reasonable. The assumption of two-dimensional flow and a uniform excitation force along the cylinder span leads to symmetry about mid-span. As a result, the numerical solution cannot admit a second-mode vibration (Wang *et al.* 2001). In a real fluid-cylinder system, however, the vortices shed from the cylinder are not two-dimensional when $Re > 400$ (Bloor 1964; Evangelinos and Karniadakis 1999); their spanwise extent is also limited, typically $1d$ to $3d$ (Zhou and Antonia 1994). This implies a non-uniform excitation force along the cylinder span, thus exciting even mode vibrations (Figs. 3-7 and 3-13). It is possible that excitation due to the three-dimensionality of the shed vortices is small compared with the two-dimensional excitation due to periodic shedding. Therefore, the even-mode resonance could be much weaker in strength than the odd-mode resonance. Consequently, uncertainty in the estimation of even mode damping ratios will increase, resulting in much more scattering in the deduced $\zeta_{y,e}^{(2)}$ and $\zeta_{x,e}^{(2)}$.

A few observations can be made based on the results presented in Figs. 3-19 and 3-20. Firstly, the effective damping ratio approaches zero when resonance occurs. Both $\zeta_{x,e}^{(1)}$ and $\zeta_{y,e}^{(1)}$ decrease sharply near $U_r \approx 11$ for $T/d = 1.13$ and near

$U_r \approx 4.2$ for $T/d = 3.00$ to a level well below the structural damping ratio. This suggests that the fluid damping ratio is negative at resonance. Note that near $U_r \approx 26$, $\zeta_{y,e}^{(3)}$ instead of $\zeta_{y,e}^{(1)}$ or $\zeta_{y,e}^{(2)}$ dips, in further support of the earlier conjecture that the strongest peak in $\varepsilon_{y,rms}$ is mainly due to resonance occurring where f_s coincides with $f_y^{(3)}$.

Secondly, for $T/d = 3.00$, $\zeta_{x,e}^{(1)}$ is generally larger than $\zeta_{y,e}^{(1)}$ in the range $U_r < 8$, implying larger fluid damping. This observation agrees with the finding of Granger *et al.* (1993) for a small flow velocity. Based on a linear assumption that the structural vibration velocity is small relative to the free stream velocity, Blevins (1994) showed that, for a fluid-cylinder dynamic system, the inline fluid damping is twice that in the cross-flow direction. The analysis is expected to be valid for small U_r only. When $8 < U_r < 15$, the trend is reversed; $\zeta_{x,e}^{(1)}$ becomes smaller than $\zeta_{y,e}^{(1)}$. As U_r further increases, $\zeta_{y,e}^{(1)}$ and $\zeta_{x,e}^{(1)}$ are nearly the same, approximately given by the structural damping ratio. On the other hand, $\zeta_{x,e}^{(2)}$ and $\zeta_{x,e}^{(3)}$ are quite comparable in magnitude with their counterparts in the lift direction, probably due to the relatively small contribution from fluid damping. The behaviour of the damping ratios for $T/d = 1.70$ is quite similar to that for $T/d = 3.00$. However, at $T/d = 1.13$, the fluid damping ratio $\zeta_{y,f}^{(1)}$ $(=\zeta_{y,e}^{(1)} - \zeta_s^{(1)})$ increases significantly, accounting for about one half of the effective damping ratio.

Thirdly, $\zeta_{y,e}^{(3)}$ appears to be the smallest, ranging between 0.01 ~ 0.03. Blevins (1975) measured the structural damping ratio of a tube and found that the third-mode structural damping ratio was appreciably smaller than the first and second-mode damping ratios. This may largely account for the relatively small value of $\zeta_{y,e}^{(3)}$ since the fluid damping ratio is small in the present situation. The small $\zeta_{y,e}^{(3)}$

may also contribute to the observation that the third-mode resonance where f_s coincides with $f_y^{(3)}$ is far more violent than the first-mode resonance where f_s approach $f_y^{(1)}$.

Finally, the effective damping ratios rise, though slowly, as U_r increases beyond 15, apparently resulting from increasing fluid damping.

3.6 Conclusions

Fluid-structure interactions of two freely vibrating elastic cylinders in a cross-flow have been experimentally investigated. The following conclusions can be drawn.

1. Vortex formation and its evolution around the cylinders were examined. The spectral phase shift Φ_{12} between the vibrations of the two cylinders is $\pm\pi$ at T/d = 3.00. This observation is consistent with previously reported results (Ishigai *et al.* 1972, Bearman and Wadcock 1973) that vortex pairs are symmetrically formed and shed from the two cylinders for a sufficiently large transverse spacing. Accordingly, the two vortex streets immediately behind the cylinders are predominantly in the anti-phase mode. Furthermore, this finding is found to be independent of *Re*. As T/d reduces to 1.70, one narrow and one wide wake were observed and the corresponding normalised dominant frequencies, as seen from velocity spectra, were 0.31 and 0.105, respectively. Flow visualisation results suggest that vortices might be shed from both sides of each cylinder at the same frequency, i.e., $f_s^* \approx 0.1$. The two vortices across the narrow wake displayed different convection velocity and subsequently underwent pairing. The two counter-rotating pairing vortices further acted to 'suck' in the gap vortex in the wide wake generated by the other cylinder.

Consequently, the three vortices merged and had a small lateral spacing, resulting in a prominent peak in the velocity spectra at $f^* \approx 0.3$. This observation is in further support of the earlier results obtained in Chapter 2. At $T/d = 1.13$, Φ_{12} is generally near zero, indicating a dominance by the alternate vortex shedding, though symmetric shedding is seen from the flow visualisation data from time to time.

2. Vibration characteristics of the elastic cylinders contrast distinctly with those of rigid ones. The instability of a rigid circular cylinder occurs at the first-mode resonance only. For the $T/d = 3.00$ elastic cylinder case, present measurements indicate the occurrence of the first-, second- and third-mode resonance. The third-mode resonance is far more violent due to the combined effect of higher flow energy, smaller effective damping ratio, and synchronisation of vortex shedding with the fifth harmonic of $f_y^{(1)}$. This finding points to the significant role structural flexibility play on structural instability, which has been overlooked in most previous studies. The inline vibration appears to be far less violent for the third-mode resonance than the cross-flow one.

3. The natural frequencies of the combined fluid-cylinder system change as a result of fluid-structure interactions. Firstly, the natural frequencies of the system experience a rather sudden variation, up to 10%, near resonance. The variation always displays the pattern of a dip followed by a rise. In the free vibration case, vortex shedding dominates the non-linear interaction between the fluid excitation force and the structural vibration. As a result, when the vortex shedding and system natural frequency components approach each other, the system natural frequency is modified so as to adapt to the vortex shedding frequency. The observation contrasts with the lock-in phenomenon

where the vortex shedding frequency is tuned to the forced vibration frequency of a cylinder. Secondly, the cross-flow natural frequencies of the system increase when the transverse spacing ratio is decreased. Presumably, the fluid-cylinder system may be modelled by a mass-spring-damper system; both fluid and structures contribute to the stiffness and damping. The observed increase in the repulsive force between the cylinders as they approach each other could be seen as an increase in fluid stiffness, thus causing a rise in the cross-flow natural frequency of the system. Thirdly, the natural frequencies of the fluid-cylinder system appear decreasing, albeit slowly, as U_r increases. The observation, which also persists for the single cylinder case, does not seem to depend on the interference between cylinders.

4. The effective damping ratios of the cylinders with a relatively large mass ratio have been characterised. The values of $\zeta_{y,e}^{(1)}$ approach zero when resonance occurs near $U_r \approx 11$ for $T/d = 1.13$ and near $U_r \approx 4.2$ for $T/d = 3.00$, so is $\zeta_{y,e}^{(3)}$ near $U_r \approx 26$, thus indicating negative fluid damping. At off resonance, the variation of the ratios is consistent with the linear analysis of the fluid-cylinder system for relatively small U_r. When $U_r > 15$, the ratios are quite comparable in the lift and drag directions, probably the result of a small fluid damping in the present case. The cross-flow fluid damping becomes significant at T/d = 1.13, accounting for about one half of the effective damping. The third-mode effective damping ratio $\zeta_{y,e}^{(3)}$ is appreciably smaller than that corresponding to the first- or second-mode. This could be attributed to a substantial decrease of the structural damping ratios for higher modes of vibrations.

CHAPTER 4

VORTEX-INDUCED VIBRATION CHARACTERISTICS OF TWO FIX-SUPPORTED ELASTIC CYLINDERS

4.1 Introduction

It has been discussed in Chapters 1 and 3 that early studies of fluid-structure interaction problems were mostly concentrated on the behaviour of the wake and the induced forces on rigid structures (Richter and Naudascher 1976; So and Savkar 1981; Baban *et al.* 1989). The dynamic characteristics of an elastic cylinder can be quite different from the rigid case. Later investigations dealt with elastic structures because of their importance in many engineering fields (Feireisen *et al.* 1994; West and Apelt 1997; Zhou *et al.* 1999a; Zhou *et al.* 2000b). In spite of these studies, investigations of the interactions between fluid and elastic structures as a fully coupled problem are far from complete. As discussed in Chapter 1, the flow-induced vibration problem of two side-by-side elastic cylinders in a cross flow is further complicated by the ratio T over d. Varying T/d could lead to the formation of a single or multiple wakes (Landweber 1942; Spivac 1946; Ishigai *et al.* 1972; Bearman and Wadcock 1973; Zdravkovich 1985). This, in turn, could affect the dynamic response of the cylinders and their resonance (or synchronisation) behaviour. There have been relatively few studies on two side-by-side elastic cylinders in a cross-flow.

Chapter 3 presents a fairly detailed investigation of the fluid-structure interaction of this particular problem. The emphasis was placed on understanding the fluid dynamics of the wakes and the effects of cylinder vibration on the wake structures. It has been proposed in Chapters 2 and 3 that vortices might shed from

both sides of each cylinder at the same frequency, i.e. $f_s^* \approx 0.1$, at a spacing ratio range of $1.2 < T/d < 2.0$. The two vortices across the narrow wake displayed different convection velocity and subsequently undergo pairing. The two counter-rotating pairing vortices further act to merge with the gap vortex in the wide wake generated by the other cylinder, thus resulting in a prominent peak in the velocity spectra at $f^* \approx 0.3$. It is further found that the natural frequencies vary slowly with U_r, except near resonance where a sharp variation occurs. The sharp variation in the natural frequencies of the combined system is dictated by the vortex shedding frequency, in contrast with the lock-in phenomenon, where the forced vibration of a structure modifies the vortex shedding frequency. Measurements presented in Chapter 3 also showed a very prominent peak in the cross-flow root mean square strain distribution at $T/d = 3.00$ when the vortex shedding frequency f_s coincides with the third-mode system natural frequency. These results have greatly improved the understanding of fluid-structure interaction of two side-by-side cylinders in a cross-flow. However, many other issues remain to be addressed. For example, for large T/d, the cross-flow vibration generally overwhelms the in-line vibration because the fluctuating lift is one order of magnitude lager than the fluctuating drag. Does this trend depend on T/d? If so, what role does the fluid dynamics around the cylinder play? In the free vibration case, vortex shedding generates the excitation forces and modifies the natural frequencies of the fluid-cylinder system near resonance. Is the modification the same on the natural frequencies associated with the different cylinders? How would the correlation behaviour between the dynamic response of the two cylinders be affected by different T/d values?

In order to supplement the understanding of the fluid-structure interaction gained from Chapters 2 and 3, this chapter aims to investigate experimentally the interference effects on the free vibration of two side-by-side cylinders. The emphasis

is on the structural dynamics and the vibration characteristics. This objective is achieved by simultaneously measuring the wake velocity and the structural dynamics using a single hot wire and two FBG sensors. Zhou *et al.* (1999b) and Jin *et al.* (2000) developed the FBG sensing technique for flow-induced vibration measurements. They have found a linear empirical relationship between the root mean square strain and displacement in the lift direction when the displacement is reasonably small. This linearity greatly facilitates the interpretation of the strain data. It is however not very clear whether this linear relationship is also valid in the drag direction. Therefore, the first task is to establish the empirical correlation between strain and displacement in the drag direction. The free vibration of the two cylinders, at different *T/d*, is then investigated in detail based on the measured dynamic strains, including the signal themselves, their spectra and their root mean square (rms) values. Finally, the interference effects on the correlation coefficient and the system natural frequencies are discussed.

4.2 Experimental Details

The experimental set-up and measurement techniques used were identical to those presented in Chapter 3. In view of this, only a brief description of the experimental details is given here.

A schematic mounting of the two acrylic cylinders symmetrically placed about the mid-plane of the tunnel working section is shown in Fig. 3-2. In this experiment, the coordinate system is attached to Cylinder 1 with x and y measuring zero from the centre of this cylinder. The other is labelled Cylinder 2. Both cylinders were fix-supported at the ends. Furthermore, in order to minimise the variation of $f_0^{(1)}$ associated with remounting, *T/d* was changed by moving Cylinder 2

alone. The values of $f_0^{(1)}$ determined for Cylinder 1 were 104 Hz for the lift (or y) direction and 98.60 Hz for the drag (or x) direction. Similarly, $f_0^{(1)}$ for Cylinder 2 were found to be 94, 95 and 101 Hz for the lift direction and 95.83, 101.50 and 101.53 Hz for the drag direction for T/d = 1.13, 1.70 and 3.00, respectively. In the present investigation, it was important to minimise tunnel vibrations, which were mainly derived from the fan and motor. Care was taken to isolate the working section from the vibration sources through the use of vibration absorbers. Furthermore, Chapter 3 had already established that the maximum effect of the tunnel vibration on the spectral energy distribution associated with the first-mode natural frequency was about 1.1%, indicating a negligible tunnel vibration effect on the measurements.

Thus arranged, the blockage was about 3.4% and the Reynolds number Re investigated varied from 800 to 10,000 with a corresponding U_{rr} range of 3 - 43. In the free-stream the longitudinal turbulence intensity was measured to be less than 0.2%. The first-mode structural damping ratio $\zeta_s^{(1)}$ was estimated to be 0.026, with EI = 0.224 Nm^2 and M^* = 565 for both cylinders. In this Re range, the effect of blockage on the mean drag was insignificant. Three spacing ratios were investigated, i.e. T/d = 3.00, 1.70, and 1.13. These ratios were chosen because the flow regimes thus resulted were representative of the different proximity effects for two side-by-side cylinders as observed by Zdravkovich (1985). Great care was taken during experiments to ensure that T/d remained the same along the span of the cylinders.

A single hot wire (Tungsten) was located at x/d = 2 and y/d = 1.5. The wire was operated at an overheat ratio of 1.8 with a constant temperature anemometer (DISA Type 55M10) to measure the streamwise velocity u in the wake. This measurement would provide a check on the vortex shedding frequency that was determined from the strain signals. The bending displacements X and Y along the x

and y direction, respectively, were measured using a Polytec Series 3000 Dual Laser Beam Vibrometer (Fig. 3-2). One laser beam was used to measure the displacement at the mid-span of the cylinder; the other was employed to monitor the tunnel vibration at the same cross-section. The differential signal from the two beams significantly reduced contamination from tunnel vibrations.

The use of the laser vibrometer to measure Y has been discussed in detail (So *et al.* 2000b; Zhou *et al.* 1999b). These studies showed that X was very difficult to measure using a laser vibrometer. There were three reasons for this difficulty. Firstly, the signal-to-noise ratio was relatively weak. Secondly, it was quite difficult to get an accurate measurement of X due to the small curvature of the cylinder and tunnel vibration. Thirdly, the method used to position the optical head of the laser vibrometer was not very reliable and was easily affected by tunnel wall vibration. They further found that it was extremely difficult to obtain a reasonably good signal-to-noise ratio for a 6mm diameter cylinder with $Re > 8{,}000$. Since then, a great part of the difficulties had been overcome and it was possible to measure X with fair accuracy. The optical head of the laser vibrometer was introduced into the tunnel at a location downstream of the cylinder and the laser beam was directed towards the cylinder surface along the x-axis. The overall measurement uncertainty was estimated to be $\pm 7.5\%$. This uncertainty depends on the signal-to-noise ratio, which in turn was affected by the wind speed. For example, the signal-to-noise ratio varied between 1 and 4 in the speed range 5 m/s to 15 m/s for the two side-by-side cylinders. Even though this measurement accuracy was not as good as that deduced for Y (So *et al.* 2000b), the result could be used to establish an approximate strain-displacement relation in the x-direction.

In order to establish the empirical strain-displacement relation in the drag direction, the strain of a single cylinder was measured in the x-direction using one

FBG sensor. The dynamic strains of the two cylinders along the x or y direction were measured simultaneously using two FBG sensors. At the same time, the displacement along the x or y direction was also measured so that a strain-displacement relation could be established. An optical silica fibre of diameter 125 μm built with an FBG sensor was buried in a groove along the span of cylinder. The FBG sensor was located at mid span of the cylinder and at 90° from the leading stagnation line. This arrangement was used to measure the y-direction strain. Since the sensor grating has a finite length of about 10mm, the measurement represents the average strain over this length. The strain thus measured is designated as ε_y. In principle, ε_y is independent of the vibration of the structure along the x direction. However, non-linear fluid-structure interaction could create cross talk between the x and y direction, thus x-direction vibration would affect ε_y and vice versa. If the cylinder was rotated 90° clockwise (or anti-clockwise), the FBG sensor will be located at the rear stagnation line (or the leading stagnation line whichever the case may be). In this arrangement, it measures the x-direction strain ε_x. A major contribution to error came from non-linearity effects when calibrating the relation between the output voltage and strain (Zhou *et al.* 1999b; Jin *et al.* 2000). The experimental uncertainty in strain measurement was estimated to be ±8%. Thus measured, the signals X, ε_x and u or Y, ε_y and u or u, ε_{y1} and ε_{y2} or ε_{x1}, ε_{x2} and u, where the subscripts 1 and 2 represent the cylinder number, were offset, amplified and digitised using a 12bit A/D board and a personal computer at a sampling frequency of 6.0kHz per channel. The record length was about 20s. This record length was sufficiently long for the rms values X_{rms} of X, Y_{rms} of Y, $\varepsilon_{x,rms}$ of ε_x and $\varepsilon_{y,rms}$ of ε_y to reach their stationary state, with a variation smaller than 1.0%.

4.3 Strain-Displacement Relations

For the case of a single cylinder, Zhou *et al.* (1999b) and Jin *et al.* (2000) found that the spectra deduced from the ε_y and Y signals were in agreement with each other in terms of their salient features, such as f_s and $f_y^{(1)}$. Besides, the two signals showed a complete coherence at these frequencies. They further deduced an empirical relation between Y_{rms} and $\varepsilon_{y,rms}$.

It is useful to quantify the ε_y-Y relation for two side-by-side cylinders. The relation could change as the interference from the neighbouring cylinder intensifies. This variation could shed light on the cylinder vibration characteristics and also facilitate the interpretation of strain measurements. Plots of $\varepsilon_{y,rms}$ versus Y_{rms} measured from Cylinder 1 are presented in Fig. 4-1. The Y_{rms}-$\varepsilon_{y,rms}$ relation is generally linear for small Y_{rms}, but the slope changes as the two cylinders approach each other, implying a variation in vibration characteristics for different *T/d* values. When U_r < 20, Y_{rms} < 6 μm, the relation between $\varepsilon_{y,rms}$ and Y_{rms} (Fig. 4-1a) is approximately linear for the *T/d* = 3.00 case, in reasonably good agreement with that reported by Zhou *et al.* (1999b) and Jin *et al.* (2000) for a single cylinder. The result suggests a small interference effect in this case. When U_r > 20, Y_{rms} > 6 μm, $\varepsilon_{y,rms}$ increases faster and the $\varepsilon_{y,rms}$-Y_{rms} relation starts to deviate from linearity. This deviation is not surprising. As will be discussed in Section 4-4, the third-mode resonance occurs near $U_r \approx 26$ where f_s coincides with the third-mode natural frequency of the fluid-cylinder system. At a higher mode of vibration, Y experiences a faster spanwise variation for given amplitude. Consequently, the strain, a second derivative of Y with respect to the spanwise variation, will increase faster than the

displacement. As *T/d* decreases, ε_y reduces for the same *Y*, thus the ε_y-*Y* relation varying. This may be attributed to a different mixture of vibration modes when interference between the cylinders intensifies.

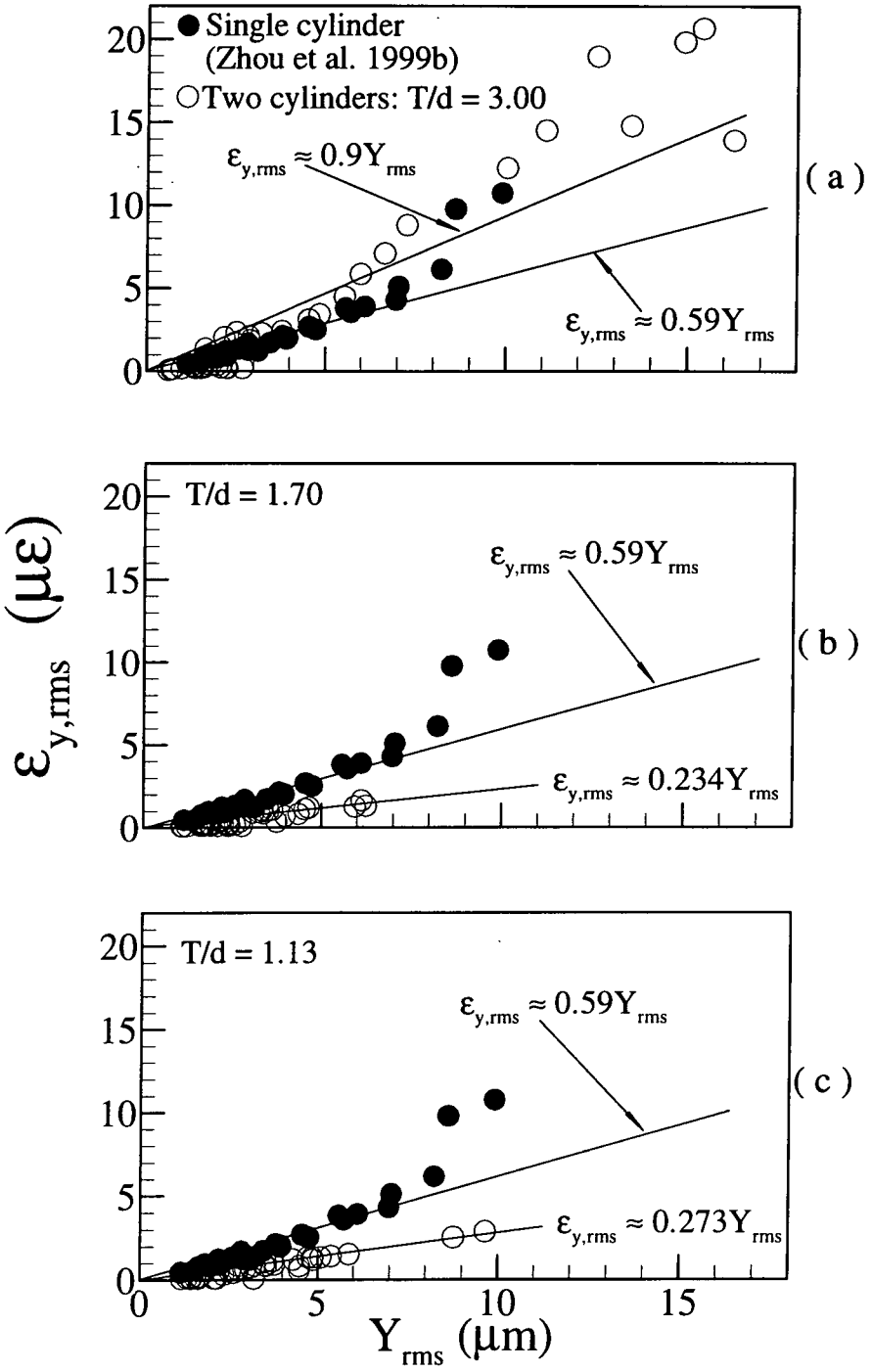

Figure 4-1 Relation between Y_{rms} and $\varepsilon_{y,rms}$ of the same cylinder for different *T/d* ratios: O, present data; ●, single cylinder (Zhou *et al.* 1999b).

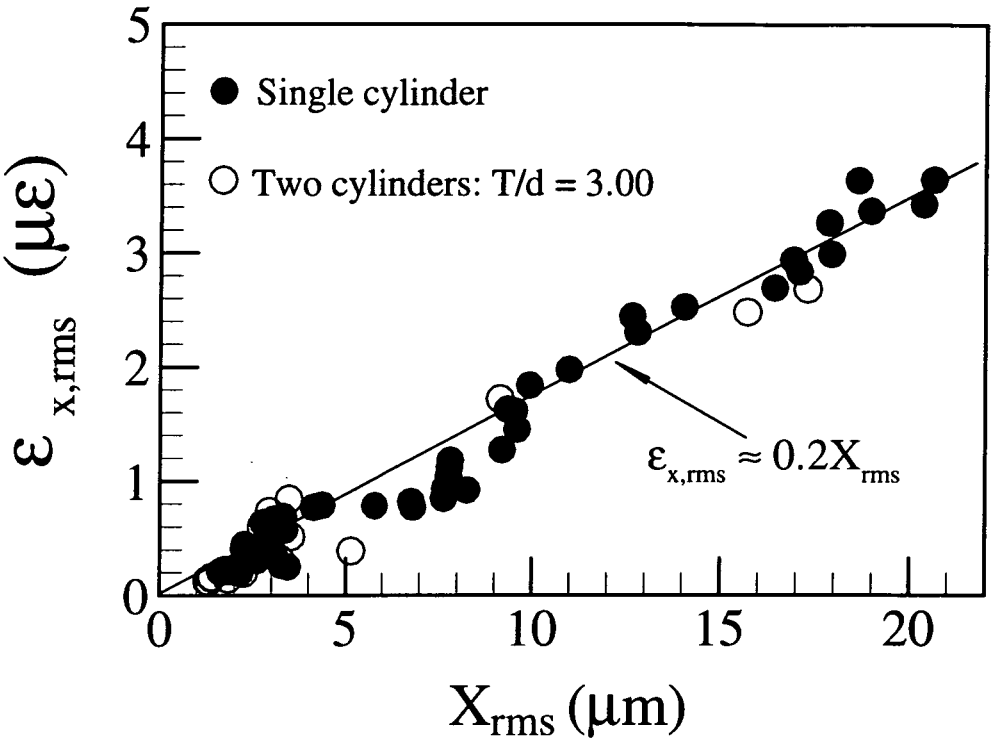

Figure 4-2 Relation between $\varepsilon_{x,rms}$ and X_{rms}: O, two cylinders at T/d = 3.00; ●, single cylinder. Solid line indicates a best fit to the experimental data.

In view of the fact that single cylinder measurements can be used as a benchmark to investigate the interference between two cylinders, the measurements of ε_x and X were conducted for a single cylinder as well as for two side-by-side cylinders. The variations of $\varepsilon_{x,rms}$ with X_{rms} are shown in Fig. 4-2. Again, the relation between $\varepsilon_{x,rms}$ and X_{rms} is linear and can be approximated by $\varepsilon_{x,rms} = 0.2\,X_{rms}$. Since the displacement in the drag direction is much smaller than that in the lift direction, the linear relation between $\varepsilon_{x,rms}$ and X_{rms} is expected to extend beyond that ($U_r \approx 26$) in the lift direction. These results, together with those given by Zhou *et al.* (1999b) for the lift direction, show that the trend of the dynamic response of the cylinder along the drag and lift direction is quite similar for the range of U_r investigated. There is one difference between the results for the drag and lift direction though. While the ε_y-Y relation is only linear for $Y_{rms} < 8$, the ε_x-X

relation remains linear for the range of X_{rms} tested, which is greater than 20. The reason could be attributed to the much smaller fluctuating drag compared to the lift (So and Savkar 1981). As a result, the strain ε_x and the vibration amplitude X are much smaller and non-linear effects have not yet been established.

The measurement of X using the laser vibrometer proved to be difficult for the two-cylinder case, especially at high free stream velocities. Therefore, only a few data points at these velocities were obtained. Nevertheless, the limited data indicates an approximately linear $\varepsilon_{x,rms}$ - X_{rms} relation (Fig. 4-2) at T/d = 3.00, in good agreement with the single cylinder case. For T/d < 3.00, the drag direction vibration was weak, therefore, the signal-to-noise ratio was poor and the measurements were not successful.

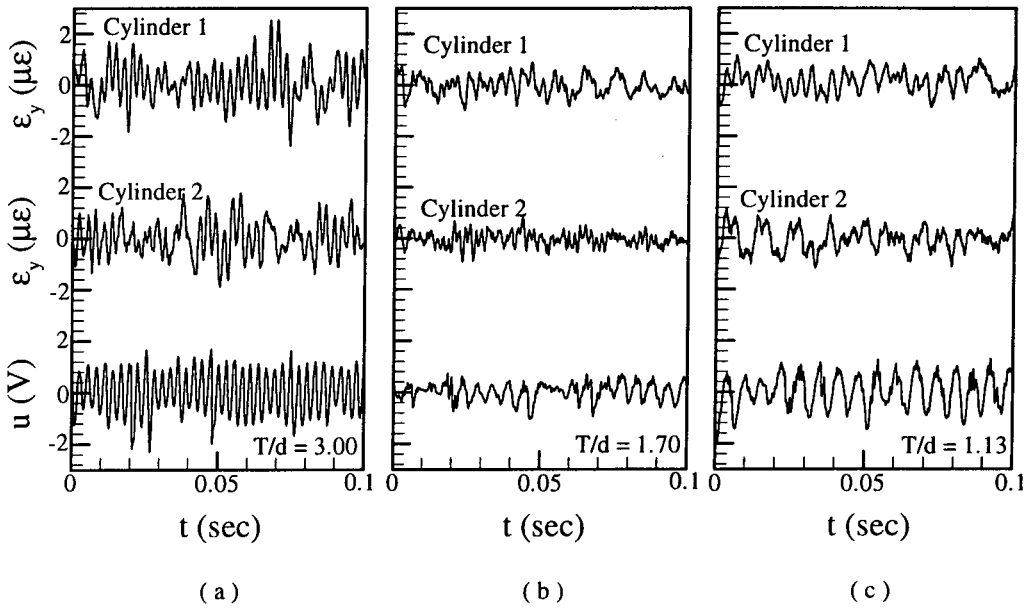

Figure 4-3 Time history of the ε_y (upper trace - Cylinder1, middle trace - Cylinder2) and u (lower trace) signals: (a) T/d = 3.00; (b) 1.70; (c) 1.13. $U_r \approx 16$. The hot wire was located at x/d = 2 and y/d = 1.5.

4.4 Vibration Characteristics

4.4.1 Time series and their spectra

The time histories of ε_y from Cylinder 1 (upper trace) and 2 (middle trace), along with the simultaneously measured u (lower trace), for $U_r \approx 16$ at different T/d values are shown in Fig. 4-3. Resonance fails to occur at this U_r. The corresponding time series of ε_x from the two cylinders and the simultaneously measured u are displayed in Fig. 4-4. The same scales are used in the plots of Fig. 4-4 for the purpose of comparison. Discussion of their behaviour for the different T/d investigated is given below.

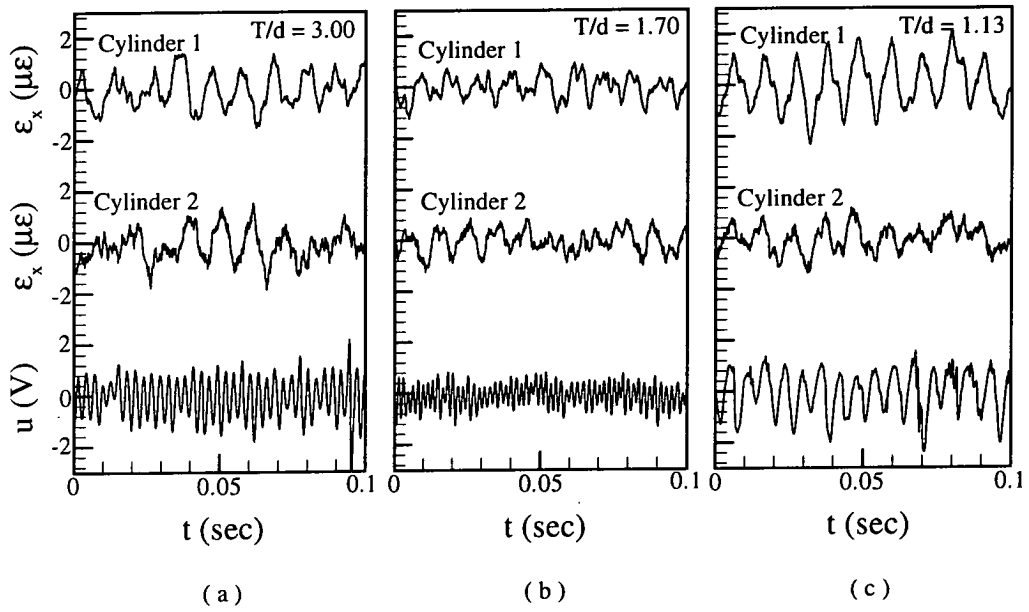

Figure 4-4 Time history of the ε_x (upper trace - Cylinder1, middle trace - Cylinder2) and u (lower trace) signals: (a) T/d = 3.00; (b) 1.70; (c) 1.13. $U_r \approx 16$. The hot wire was located at x/d = 2 and y/d = 1.5.

At T/d = 3.00, the ε_y signals (Fig. 4-3a) show a pseudo-periodic fluctuation, which is also seen in the u signal, apparently due to the excitation of vortex shedding.

However, the ε_x signals (Fig. 4-4a) are quite different from ε_y. A pseudo-periodic fluctuation is also evident, but its frequency is much smaller than that of ε_y and differs from that of the u signal. This periodic fluctuation component corresponds to the first-mode natural frequency of the combined fluid-cylinder system, as confirmed later by the spectral analysis. It should be noted that the ε_y and ε_x signals of Cylinders 1 at T/d = 3.00 are similar to those of Cylinder 2 (Figs. 4-3a and 4-4a). The ε_y signal exhibits a beating behaviour, which could be the result of interaction between vortex shedding and one of the natural frequency components of the cylinder vibration.

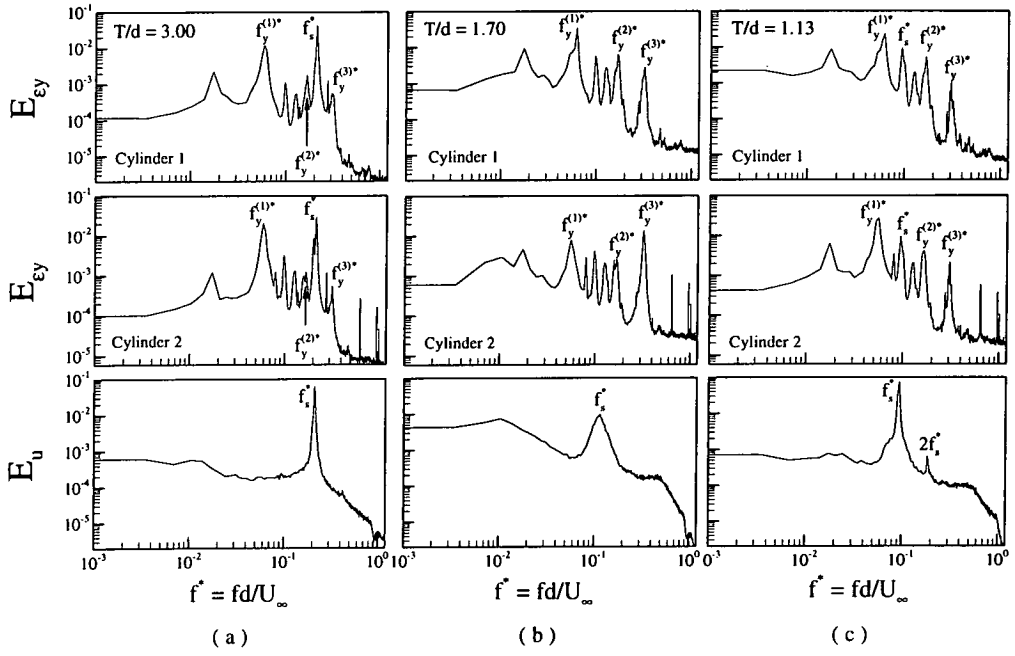

Figure 4-5 Power spectra $E_{\varepsilon y}$ (upper plate - Cylinder1, middle plate - Cylinder2) and E_u (lower plate): $U_r \approx 16$; (a) T/d = 3.00; (b) 1.70; (c) 1.13. The hot wire was located at x/d = 2 and y/d = 1.5.

Spectra E_u, $E_{\varepsilon y}$ and $E_{\varepsilon x}$ corresponding to the strain and velocity signals are shown in Figs. 4-5a and 4-6a. E_u determined from the u-velocity measurement

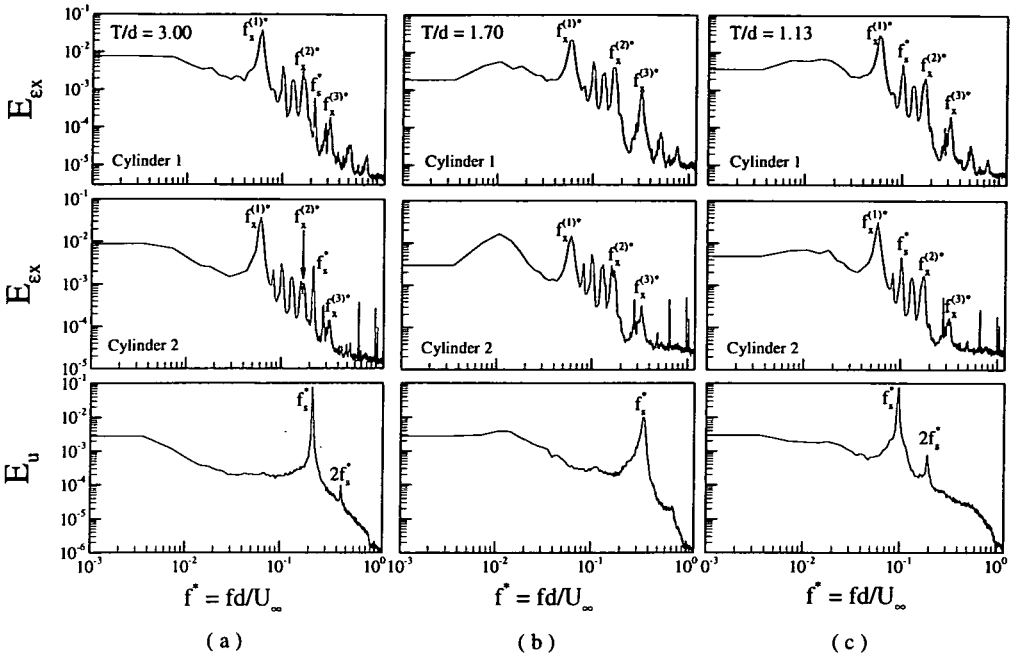

Figure 4-6 Power spectra $E_{\varepsilon x}$ (upper plate - Cylinder1, middle plate - Cylinder2) and E_u (lower plate): $U_r \approx 16$; (a) $T/d = 3.00$; (b) 1.70; (c) 1.13. The hot wire was located at $x/d = 2$ and $y/d = 1.5$.

yields one major peak at $f_s^* = f_s d/U_\infty = 0.20$, which is the same as the vortex shedding frequency of a single cylinder. This peak is also evident in $E_{\varepsilon y}$ (Fig. 4-5a). Furthermore, the peak occurs at the same frequency for $E_{\varepsilon y}$ and $E_{\varepsilon x}$ deduced from the two cylinders, thus suggesting an identical vortex shedding frequency for the cylinders. The peak at $f^* \approx 0.059$ in $E_{\varepsilon y}$ and $E_{\varepsilon x}$ can be identified with the first-mode natural frequency $f_y^{(1)*}$ and $f_x^{(1)*}$ of the fluid-cylinder system in the lift and drag direction, respectively. These frequencies $f_y^{(1)*}$ and $f_x^{(1)*}$ are consistent with the calculated value for a single cylinder system. According to So *et al.* (2000a), the calculated value is given by $f_0^{(1)}/\sqrt{1+\pi\rho d^2/4m}$. Since $m/\rho d^2$ (≈ 450) is quite large in an airflow, the calculated value is virtually identical to $f_0^{(1)}$, based on the theoretical relation. Another peak occurs at $f^* \approx 0.32$. The third-mode natural

frequency can be estimated from $f_y^{(1)}$ and $f_x^{(1)}$ using the formula given in Chen (1987), i.e. (121/22.4)[$f_y^{(1)*}$ (or $f_x^{(1)*}$)] = 0.319. Therefore, this peak is probably due to the third-mode natural frequency $f_y^{(3)*}$ and $f_x^{(3)*}$ of the fluid-cylinder system. Similarly, the peak at f^* = 0.163 is identified with the second-mode natural frequency of the system. $E_{\varepsilon y}$ (also $E_{\varepsilon x}$) from Cylinder 1 exhibits a close resemblance to that deduced from Cylinder 2. The peaks corresponding to $f_y^{(3)*}$ and f_s^* are partially overlapping, which accounts for the beating character observed in the ε_y signals (Fig. 4-3a). Evidently, the most prominent peak occurs at f_s^* = 0.2 for $E_{\varepsilon y}$, but at $f_x^{(1)*}$ for $E_{\varepsilon x}$. This could be attributed to the fact that the vortex excitation forces are substantially weaker in the drag direction than in the lift direction. Consequently, the prominent component appears at $f_x^{(1)*}$ in the drag direction, but at f_s^* in the lift direction.

As *T/d* decreases to 1.70, the ε_y signal (Fig. 4-3b) becomes quite different from that measured at *T/d* = 3.00. The pseudo-periodic fluctuation due to vortex shedding appears very weak. E_u (Fig. 4-5b) exhibits a broad peak at $f^* \approx 0.1$ and its value is about one decade lower than that shown in *T/d* = 3.00. The weak vortex shedding component implies that the vortex strength is impaired at *T/d* = 1.70 because of interference between cylinders. On the other hand, the ε_x signal (Fig. 4-4b) and the corresponding $E_{\varepsilon x}$ (Fig. 4-6b) are quite similar to their counterpart at *T/d* = 3.00, that is, interference between cylinders has little effect on the vibration in the drag direction. It should be pointed out that the *u* signal measured simultaneously with ε_x (Fig. 4-4b) shows a substantial difference from that measured simultaneously with ε_y (Fig. 4-3b). The former displays a much stronger pseudo-

periodic fluctuation; the frequency of the fluctuation is higher than that of the latter, in spite of the fact that the wake velocity was measured at the same U_r and the same spatial location, i. e. x/d = 2 and y/d = 1.5. E_u deduced from the signal simultaneously measured with ε_x displays a more pronounced peak at $f^* \approx 0.3$ (Fig. 4-6b). It was reported previously that the gap flow between the two cylinders is not stable and will deflect for T/d = 1.5 ~ 2.0. The deflection led to the formation of one narrow and one wide wake, which are associated with high and low vortex frequencies, respectively (Spivack 1946; Ishigai *et al.* 1972; Bearman and Wadcock 1973; Kamemoto 1976; Kiya *et al.* 1980; Kim and Durbin 1988; Sumner *et al.* 1999). The deflected gap flow is bi-stable and changes over from one side to the other from time to time. The ratio of the two frequencies is close to but less than 3 (Kim and Durbin 1988). In view of these observations, it can be inferred that, when measuring ε_x, the hot wire was probably located in the narrow wake, thus giving rise to one major peak at $f^* \approx 0.3$ (Fig. 4-6b). On the other hand, when measuring ε_y, the gap flow might have been deflected to the other side and the hot wire would measure the wide wake. Consequently, E_u exhibits a broad peak at $f^* \approx 0.1$ (Fig. 4-5b). Note that in either case, the pseudo-periodic fluctuation, evident in the u-signal, is hardly identifiable, suggesting weak vortex excitation or weak vortex strength. Zhang and Zhou (2001) measured the wake of three side-by-side cylinders. They observed that the deflected gap flows between the cylinders at T/d = 1.5 form one wide and two narrow wakes, which were associated with a lower and a higher vortex shedding frequency, respectively. Based on flow visualisation and downstream evolution of the prominent peaks of the hot-wire spectra, they proposed that the vortex generation mechanisms might be different between the narrow and the wide wakes. While those in the narrow wake may originate from shedding, those in the wide wake could be

generated by the shear layer instability. Their speculation is corroborated by the present observation that the periodicity of vortices is significantly stronger in the narrow wake (Figs. 4-4b and 4-6b) than that in the wide wake (Figs. 4-3b and 4-5b).

When *T/d* is further reduced to 1.13, the behaviour of ε_y and ε_x signals (Figs. 4-3c and 4-4c) are again similar to those at *T/d* = 3.00, showing a clear presence of the vortex shedding component, except with a lower frequency. In such a small *T/d*, the two cylinders behave like a single structure and hence the Strouhal number is $St = [(1+1.13)f_s]/U_\infty \approx 0.2$ or $f_s^* \approx 0.09$ (Figs. 4-5c and 4-6c).

4.4.2 Root mean square strain

The dependence of $\varepsilon_{y,rms}$ and $\varepsilon_{x,rms}$ on U_r at different *T/d* values are shown in Fig. 4-7. A few observations can be made. Firstly, $\varepsilon_{y,rms}$ and $\varepsilon_{x,rms}$ of Cylinder 1 is in general agreement with those of Cylinder 2. Secondly, their values increase with U_r. Thirdly, at *T/d* = 3.00, $\varepsilon_{y,rms}$ displays three peaks at $U_r \approx 4.2$, 12.0 and 26.0, respectively, while $\varepsilon_{x,rms}$ shows only one tiny peak at $U_r \approx 26.0$. The peak at $U_r \approx 12$ is barely discernible, while the one at $U_r \approx 26$ is most prominent. Fourthly, there appears to have no peak for the case *T/d* = 1.70 and there is only one peak at $U_r \approx 11$ for the case *T/d* = 1.13.

In order to understand the different $\varepsilon_{y,rms}$ peaks for the case *T/d* = 3.00, Figure 4-8 gives the time histories of ε_y from Cylinder 1 (upper trace) and 2 (middle trace) along with the simultaneously measured *u* (lower trace) at $U_r \approx 4.2$ and 26. It can be seen that at these U_r values, the ε_y signals exhibit strong periodic fluctuations. These fluctuations have the same period as the excitation forces induced by vortex shedding. The corresponding spectra $E_{\varepsilon y}$ at U_r = 4.2 along with

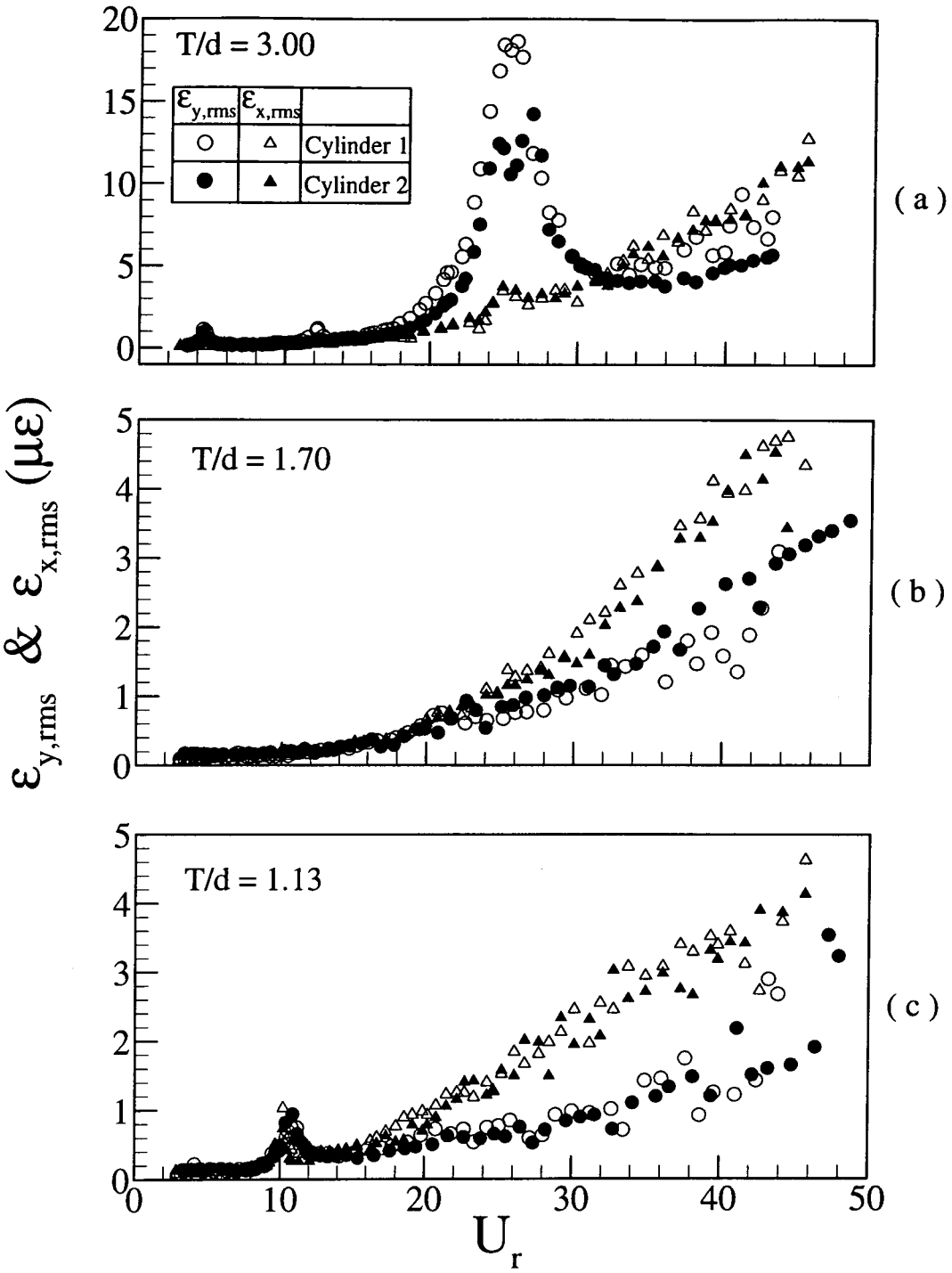

Figure 4-7 Variation of $\varepsilon_{y,rms}$ and $\varepsilon_{x,rms}$ with U_r: (a) T/d = 3.00; (b) T/d = 1.70; (c) T/d = 1.13. ○, $\varepsilon_{y,rms}$, Cylinder 1; ●, $\varepsilon_{y,rms}$, Cylinder 2; △, $\varepsilon_{x,rms}$, Cylinder 1; ▲, $\varepsilon_{x,rms}$, Cylinder 2.

E_u are shown in Fig. 4-9. All spectra exhibit a prominent peak at $f^* = fd/U_\infty = 0.2$, i. e. at the vortex shedding frequency f_s^* (c.f. E_u in Fig. 4-9c).

The occurrence of resonance is responsible for the prominent peak in E_{ey} and also that in $\varepsilon_{y,rms}$ at $U_r \approx 4.2$. Similarly, the peaks at $U_r \approx 12$ and 26 in $\varepsilon_{y,rms}$ could be identified with the result of f_s coinciding with the second- and third-mode natural frequencies of the fluid-cylinder system, respectively.

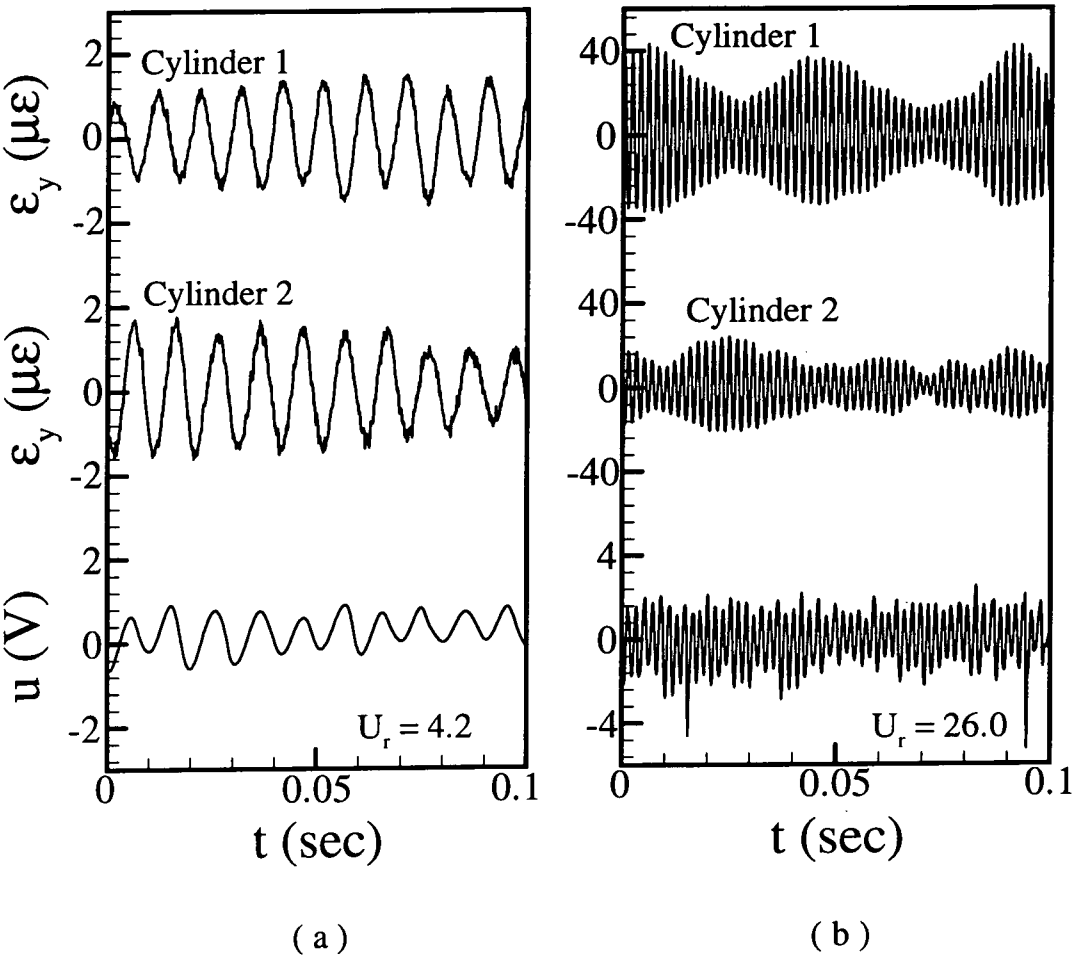

Figure 4-8 Time history of ε_y (upper trace - Cylinder 1, middle trace - Cylinder 2) and u (lower trace) at T/d = 3.00: (a) $U_r \approx 4.2$; (b) $U_r \approx 26$. The hot wire was located at x/d = 2 and y/d = 1.5.

The peak in $\varepsilon_{y,rms}$ at $U_r \approx 26$ is by far most pronounced compared to the others. It has been discussed in Chapter 3 that four reasons could be put forward to explain this behaviour. Firstly, the resonance corresponding to $f_y^{(3)}$ occur at a higher

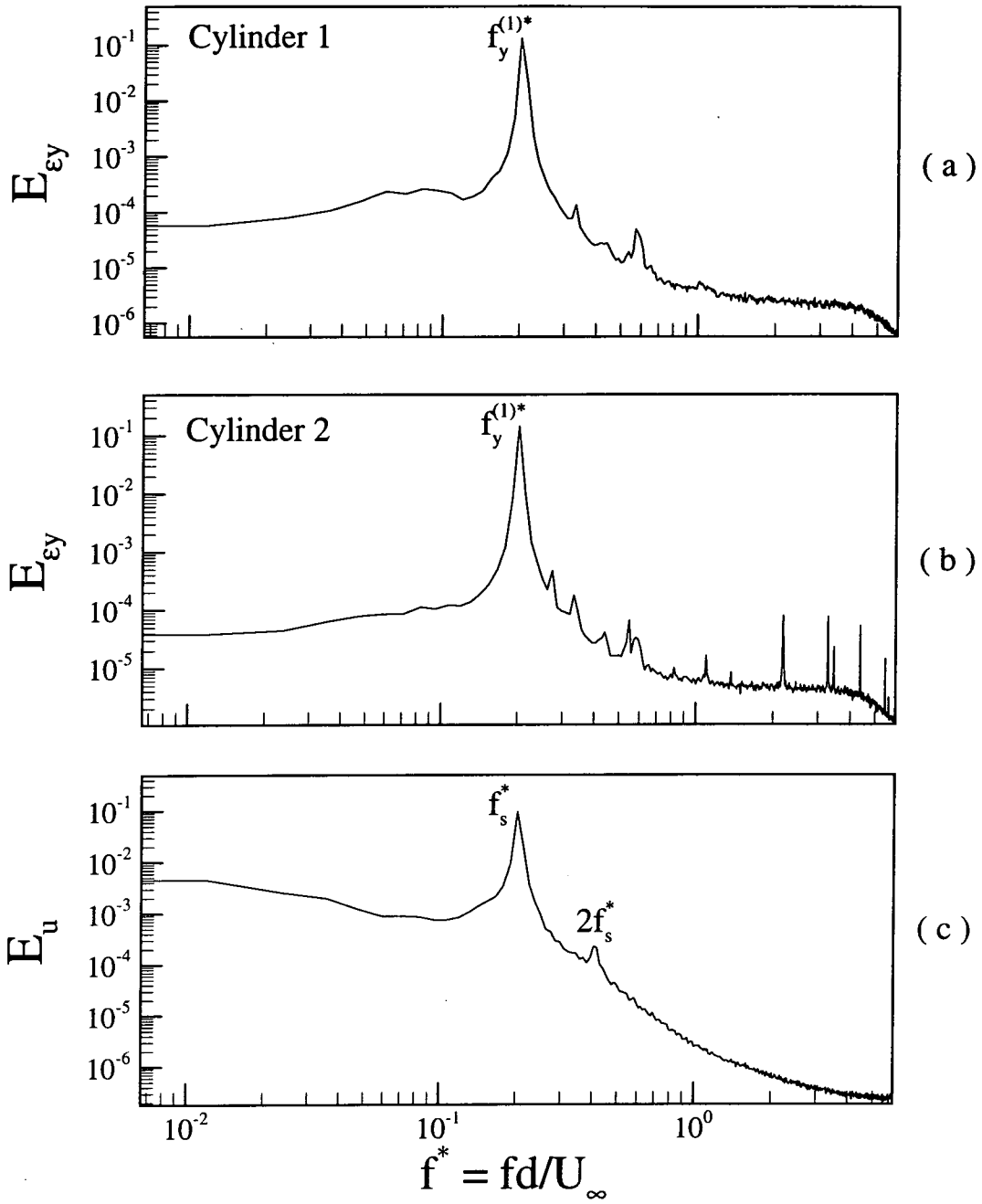

Figure 4-9 Power spectra $E_{\varepsilon y}$ (upper plate - Cylinder1, middle plate - Cylinder2) and E_u (lower plate): T/d = 3.00, $U_r \approx 4.2$. The hot wire was located at x/d = 2 and y/d = 1.5.

U_r, which is associated with much higher flow excitation energy. Secondly, the effective damping ratio, which is the sum of the structural and fluid damping ratio, corresponding to $f_y^{(3)}$ is appreciably smaller than that corresponding to $f_y^{(1)}$ or $f_y^{(2)}$

(Chapter 3). Thirdly, the fifth harmonic of $f_y^{(1)*}$ ($\approx$0.0394) is 0.197 and is very close to $f_s^* = 0.2$, thus possibly feeding additional energy to the resonance phenomenon. Finally, as previously discussed in Section 4-3, the strain, a second derivative of displacement with respect to the spanwise variation, tends to be amplified at a higher mode. In contrast, $\varepsilon_{x,rms}$ is substantially weaker at resonance, including at $U_r \approx 26$, resembling the case of an isolated cylinder.

As *T/d* reduces to 1.70, the $\varepsilon_{y,rms}$ values decrease considerably for both cylinders. Consequently, resonance does not occur (Fig. 4-7b). It can be observed from $E_{\varepsilon y}$ and $E_{\varepsilon x}$ (Figs. 4-5b and 4-6b) that a substantially weakened vortex shedding component at *T/d* = 1.70 is noticed compared to those shown at *T/d* = 3.00 (Figs. 4-5a and 4-6a). Therefore, vortices shed from the cylinders are very weak at this *T/d*. On the other hand, the intensified interaction between the narrow wake and the wide wake may lead to a loss of temporal coherence. In other words, the vortex spacing is more random and the frequency of shedding is not as well defined. Consequently, the cylinders would no longer be excited at a well-defined frequency and resonance would not be observed. It will be seen later that the two cylinders loss correlation *T/d* = 1.70 (Fig. 4-11), thus also suggesting a loss of temporal coherence. Accordingly, structural vibrations are impaired, even at resonance. This observation suggests that the structures are most stable for the range of *T/d* = 1.2 ~ 2.0 when the interaction between the flow around each cylinder weakens the vortices in the narrow and wide wakes.

As *T/d* is further reduced to 1.13, one peak in both $\varepsilon_{y,rms}$ and $\varepsilon_{x,rms}$ occurs at $U_r \approx 11$ (Fig. 4-7c). For *T/d* < 1.2, the two cylinders act like a single structure, and vortices are alternately shed only from the outer (or free stream) side of the two cylinders to form a single vortex street (Sumner *et al.* 1999). The spectrum E_u

indicates that the vortex shedding frequency is halved at T/d = 1.13, leading to $f_s^* \approx 0.09$ (Figs 4-5c and 4-6c). The spectra $E_{\varepsilon y}$, $E_{\varepsilon x}$ and E_u for T/d = 1.13 at $U_r \approx$ 11 (not shown) indicate the occurrence of the first-mode resonance, which should be responsible for the peak in both $\varepsilon_{y,rms}$ and $\varepsilon_{x,rms}$.

The peak in $\varepsilon_{x,rms}$ at $U_r \approx 11$ is quite prominent, comparable to that in $\varepsilon_{y,rms}$, which is in distinct contrast with the case of T/d = 3.00 (Fig. 4-7a) or an isolated cylinder, which will be shown later in Chapter 5. Two reasons may be responsible for this observation. Firstly, when resonance occurs at $U_r \approx 11$, the spectral phase shift between ε_{y1} and ε_{y2} at the vortex shedding frequency is near 0.5π (Chapter 3), indicating that the two cylinders do not vibrate in phase. This impairs the vibration in the lift direction, and accounts for the observation that the $\varepsilon_{y,rms}$ magnitude at the first-mode resonance ($U_r \approx 11$) for T/d = 1.13 is rather comparable with that ($U_r \approx 4.2$) for T/d = 3.00, in spite of the fact that the former occurs at a higher U_r. Secondly, for an isolated cylinder or two side-by-side cylinders at T/d = 3.00, the drag fluctuates twice as fast as the lift, implying that resonance does not occur simultaneously in the drag and lift directions. The hump or mild peak in $\varepsilon_{x,rms}$ at $U_r \approx$ 4.2, 12 and 26, where resonance occurs in the lift direction, is either due to cross talk between lift and drag or to the non-linear effect created by the violent vibration in the lift direction. At T/d = 1.13, however, vortices are shed from the outer side of the cylinders only, i.e. the drag fluctuates at the same frequency as the lift. Therefore, resonance occurs simultaneously in both directions. This explains the pronounced peak in $\varepsilon_{x,rms}$ at $U_r \approx 11$.

It is interesting to point out that $\varepsilon_{x,rms}$ tends to be larger than $\varepsilon_{y,rms}$ at higher U_r, especially for small T/d. For example, other than the occurrence of resonance,

the values of $\varepsilon_{x,rms}$ appear larger than $\varepsilon_{y,rms}$ for $U_r \approx 23.0$ and 33.0, corresponding to T/d = 1.70 and 1.13, respectively. Measurements of mean drag and mean lift on two side-by-side cylinders (Chapter 3) indicate an increasing repulsive force as the two cylinders approach each other. The increased repulsive force may lead to an increase in fluid rigidity between the two cylinders as T/d decreases, which may be partially responsible for the suppressed transverse vibrations of the two cylinders. The increased repulsive forces, however, has little effect on the drag direction vibration in the present investigation. Consequently, the value of $\varepsilon_{x,rms}$ tends to be greater than $\varepsilon_{y,rms}$ as T/d reduces.

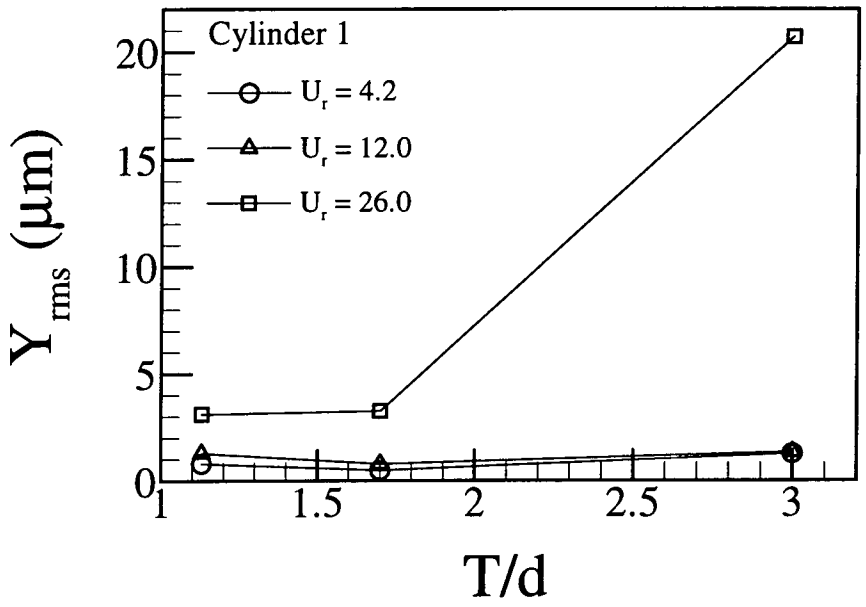

Figure 4-10 Variation of Y_{rms} with T/d at U_r = 4.2, 12.0 and 26.0.

In order to highlight the effect of T/d on the amplitude of cylinder vibration near resonance, the dependence of Y_{rms} on T/d at U_r = 4.2, 12.0 and 26.0, corresponding to the first-, second- and third-mode resonance at T/d = 3.00, respectively, is plotted in Fig. 4-10. Here, Y_{rms} were estimated based on the strain-displacement relations deduced in Section 4-3. Generally, the vibration amplitude at

T/d = 3.00 is greater than that at *T/d* = 1.70 and 1.13, indicating a suppressed vibration as the two cylinders approach each other. It can be observed that the lift direction vibration amplitude near the third-mode resonance is by far most pronounced at *T/d* = 3.00. This observation suggests that structural flexibility could have a significant impact on its instability analysis.

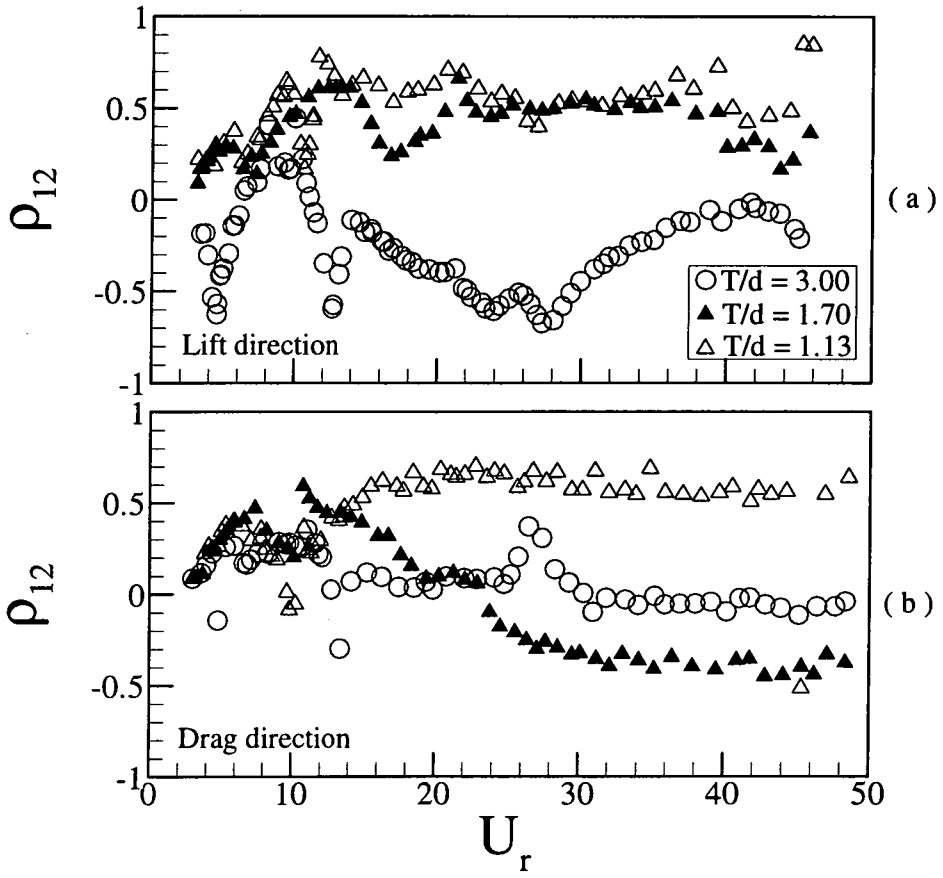

Figure 4-11 Variation of ρ_{12} with *T/d* and U_r: (a) ρ_{12} between ε_{y1} and ε_{y2}; (b) ρ_{12} between ε_{x1} and ε_{x2}. ○*T/d* = 3.00; ▲1.70, △1.13.

4.4.3 Correlations between the cylinders

In order to understand further the cylinder dynamics, the correlation coefficient ρ_{12} between the two simultaneously measured ε_y (or ε_x) from the cylinders is calculated and plotted against U_r for different *T/d* ratios in Fig. 4-11. At

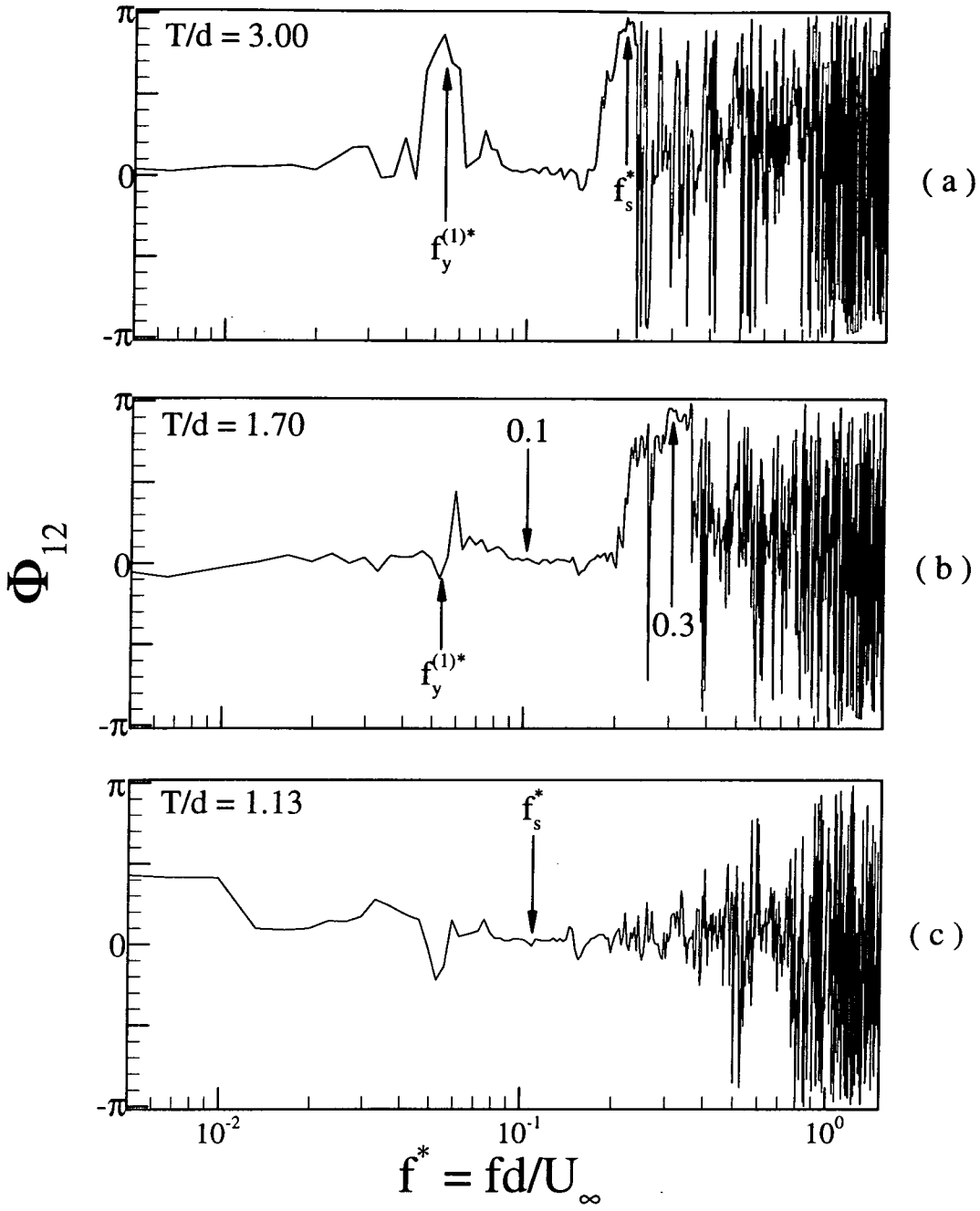

Figure 4-12 Spectral phase angles Φ_{12} between ε_{y1} and ε_{y2} at U_r = 16: (a) T/d = 3.00; (b) 1.70; (c) 1.13.

T/d = 3.00, except in the range of $6 < U_r < 12$, ρ_{12} between ε_{y1} and ε_{y2} (Fig. 4-11a) is generally negative, indicating that the two cylinders move in opposite directions. The spectral phase angle Φ_{12} between the signals ε_{y1} and ε_{y2} (Fig. 4-3) at U_r = 16

are shown in Fig. 4-12. At T/d = 3.00, Φ_{12} (Fig. 4-12a) is close to π at the first-mode natural frequency $f_y^{(1)*}$ and the vortex shedding frequency f_s^*. This observation is consistent with previously reported results (Chapters 2 and 3) showing that vortices are shed from the two cylinders predominantly in anti-phase mode. In view of the fact that, in the case of free vibrations, vortex shedding gives rise to the excitation forces, it might be concluded that the anti-phase vortex shedding from the two cylinders is responsible for the negative ρ_{12}. The troughs near $U_r \approx 4.2$, 12.0 and 26.0 are apparently linked to resonance; thus it is not surprising to see a more negative ρ_{12} nearer to resonance, where the structural vibration is 'locked' together with the predominantly symmetric vortex shedding from the cylinders. In contrast, ρ_{12} between ε_{x1} and ε_{x2} (Fig. 4-11b) is generally close to zero, except near $U_r \approx$ 4.2, 12.0 and 26.0, where resonance occur at the first-, second- and third-mode vibration frequencies, respectively. This suggests that interference between the two cylinders at T/d = 3.00 is small in the drag direction.

As T/d reduces, the interference between the two cylinders is expected to increase. At T/d = 1.70, the correlation is positive in the lift direction (Fig. 4-11a), indicating an in-phase movement of the two cylinders. At the two dominant vortex frequencies f^* = 0.3 and 0.1, Φ_{12} (Fig. 4-12b) between the signals ε_{y1} and ε_{y2} is about π and 0, respectively. However, the component at f^* = 0.1 is unlikely to make a major contribution to the positive ρ_{12}. The $E_{\varepsilon y}$ spectra (Fig. 4-5b) display rather pronounced peaks at the natural frequencies of the system but not at f^* = 0.1 or 0.3. It may be inferred that the first-mode natural frequency component, at which $\Phi_{12} \approx 0$, in ε_y contributes largely to the positive ρ_{12}. In the drag direction, the correlation is either positive or negative depending on U_r (Fig. 4-11b). The sign is

again verified to be consistent with the phase shift Φ_{12} (not shown) at $f_x^{(1)}$ and is therefore ascribed to the contribution from the $f_x^{(1)}$ component.

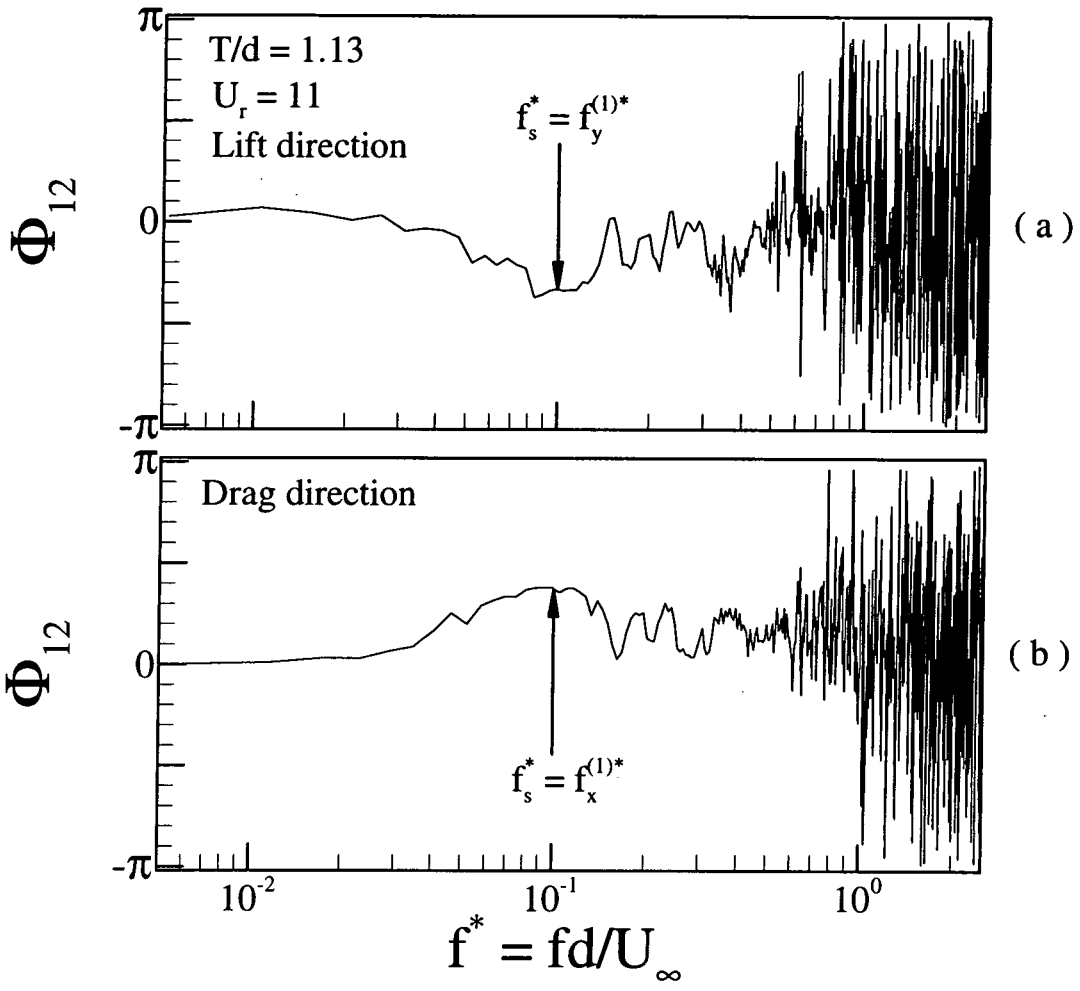

Figure 4-13 Spectral phase angles Φ_{12} at *T/d* = 1.13 when resonance occurs at $U_r = 11$: (a) between ε_{y1} and ε_{y2}; (b) between ε_{x1} and ε_{x2}.

At *T/d* = 1.13, the correlation is positive in both lift and drag directions. Their values are essentially the same, about 0.6 for $U_r > 10$. As discussed earlier, the repulsive force between the cylinders increases as *T/d* decreases. Assuming a spring-damper-mass model for the fluid-cylinder system, a rise in the repulsive force as the cylinders approach each other could be interpreted as equivalent to an increase in fluid rigidity. Consequently, an increase in correlation between the two cylinders

is expected. These results indicate that the two cylinders act like a single structure. As previously discussed, at *T/d* = 1.13, one oscillating vortex street with $f_s^* \approx 0.09$ is formed behind the cylinders (Figs. 4-5c and 4-6c). The spectral phase angles Φ_{12} (Fig. 4-12c) between ε_{y1} and ε_{y2} at *T/d* = 1.13 and $U_r = 16$ is near zero at the vortex shedding frequency $f_s^* = 0.09$, i.e. the two cylinders move in unison. This suggests that the vortices be shed alternately from the free-stream sides of the two cylinders. Note that there is a trough, near $U_r \approx 11$, in ρ_{12} for either direction. Since the natural frequency associated with Cylinder 1 is slightly different from that associated with Cylinder 2 (Section 4-2), the two cylinders do not reach resonance at exactly the same U_r. This causes a phase shift of about 0.4π (Fig. 4-13) at the vortex shedding frequency and subsequently a reduced ρ_{12} near $U_r \approx 11$.

4.5 Fluid Dynamics Effects on System Natural Frequencies

Chapter 3 studied the effect of the flow on the natural frequencies of the combined fluid-cylinder system and found that $f_y^{(1)}$, $f_y^{(3)}$, $f_x^{(1)}$ and $f_x^{(3)}$ may depend on U_r and *T/d*. Primarily, Chapter 3 focused on the natural frequencies of the fluid-cylinder system associated with Cylinder 1. In this chapter, an examination is carried out on whether the flow has the same effect on the system natural frequencies associated with each of the two cylinders.

Comparisons between the first-mode natural frequencies, $f_y^{(1)}$ and $f_x^{(1)}$, associated with Cylinder 1 and 2 are shown in Figs. 4-14 and 4-15. At *T/d* = 3.00 and 1.13, the behaviour of $f_y^{(1)}$ or $f_x^{(1)}$ is rather similar for the two cylinders. The frequencies decrease slowly with U_r but experience an abrupt change when

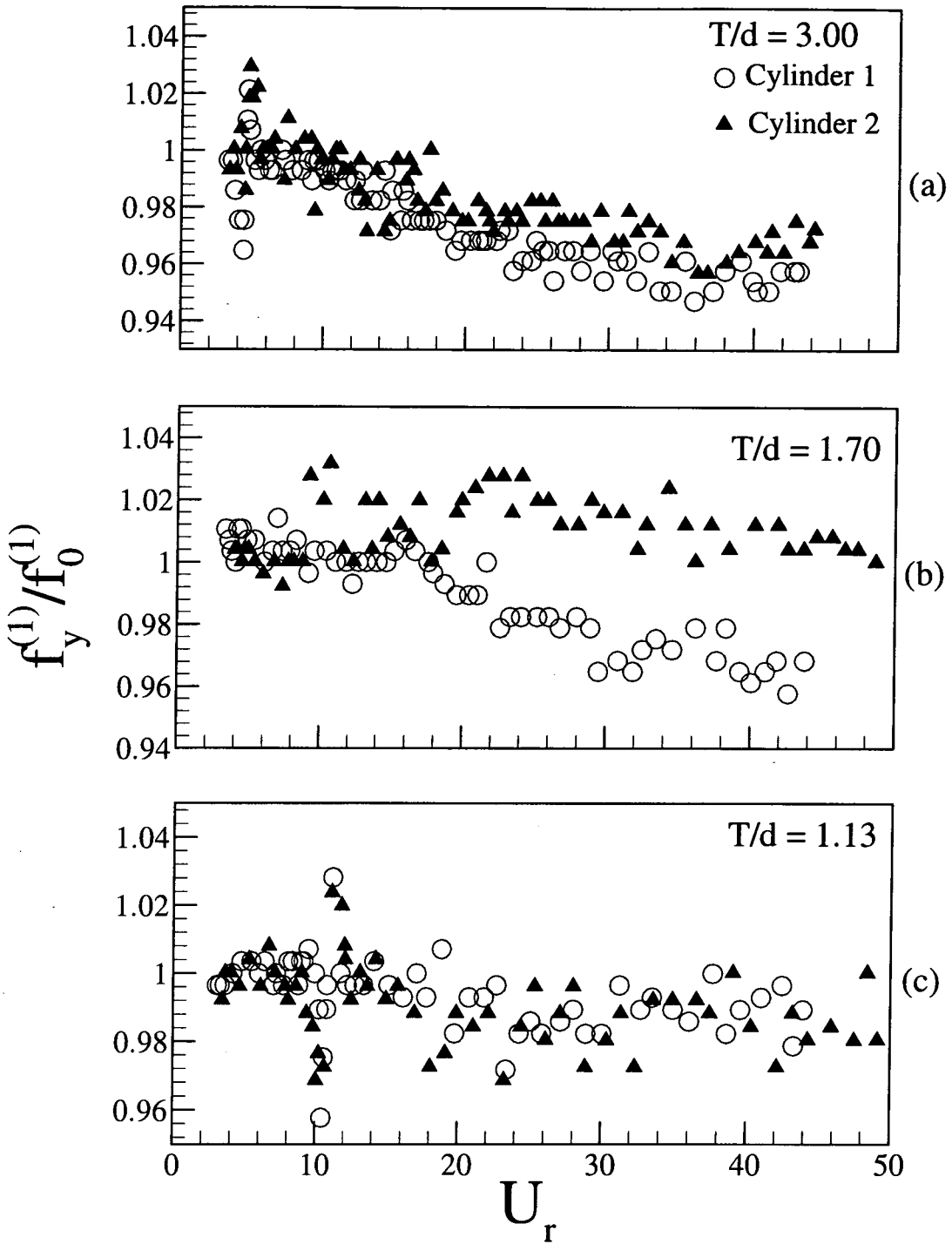

Figure 4-14 Variation of the cross-flow $f_y^{(1)}$ with T/d and U_r: ○, Cylinder 1; ▲, Cylinder 2. (a) T/d = 3.00; (b) 1.70; (c) 1.13.

resonance occurs. This behaviour has been observed and discussed in detail in Chapter 3. At T/d = 1.70, however, there is an appreciable difference, up to 5%, in

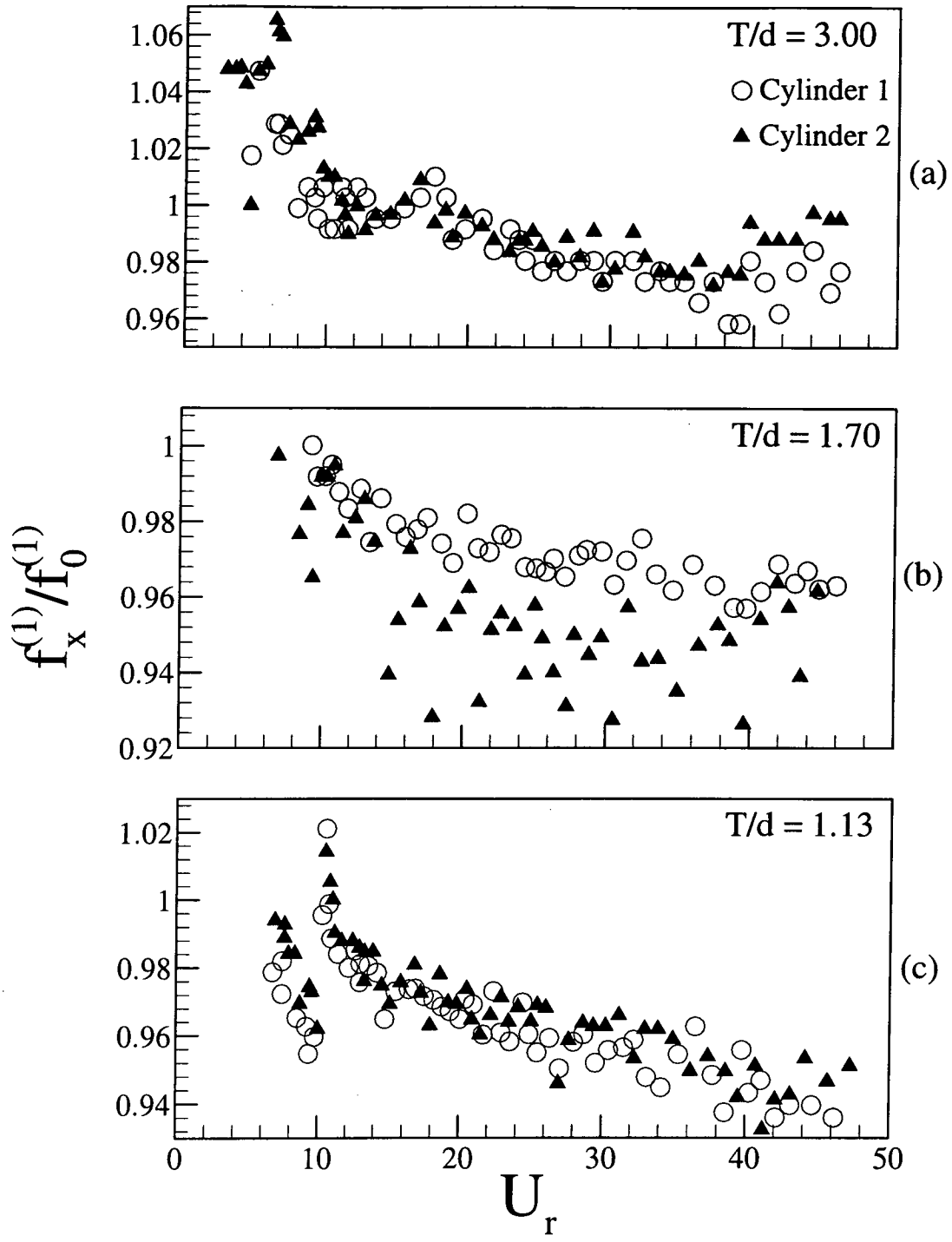

Figure 4-15 Variation of the inline $f_x^{(1)}$ with *T/d* and U_r: ○, Cylinder 1; ▲, Cylinder 2. (a) *T/d* = 3.00; (b) 1.70; (c) 1.13.

$f_y^{(1)}/f_0^{(1)}$ or $f_x^{(1)}/f_0^{(1)}$ between the two fluid-cylinder systems. The natural frequencies are determined from the fluctuating strain spectra, which were calculated

using a conventional FFT algorithm. The frequency resolution Δf, fixed by the sampling rate and the record length used in the FFT calculation, is estimated to be 0.35 Hz. The corresponding uncertainty in $f_y^{(1)}/f_0^{(1)}$ or $f_x^{(1)}/f_0^{(1)}$ is less than 0.4%. Therefore, the difference in $f_y^{(1)}/f_0^{(1)}$ or $f_x^{(1)}/f_0^{(1)}$ between the two fluid-cylinder systems cannot be attributed to experimental errors.

Considering the fluid-cylinder system as a spring-damper-mass model, both fluid and structure contribute to the system mass, stiffness and the effective damping ratio. A number of factors could alter the natural frequency of the system. One is the fluid force on the cylinder. For example, as the two cylinders approach each other, the repulsive force increases. This is equivalent to an increase in fluid rigidity. Furthermore, the increasing repulsive force between the cylinders gives rise to an increase in the tensile axial loading on the cylinder, which is fix-supported at both ends, and subsequently increases the structural rigidity (Weaver *et al*, 1989; Xu *et al.* 2001). As a result, the system natural frequency might increase. Added mass is another factor that may change the natural frequency of the system. Chen (1987) calculated the added mass on two side-by-side cylinders in a cross flow and found that, in the range of $1.13 < T/d < 4$, the added mass increases as T/d decreases, thus contributing to a decrease in the system natural frequency. Non-linear fluid damping may also affect the system natural frequency, which has yet to be better understood. The behaviour of the system natural frequency is the combined effect of varying system mass, stiffness and damping ratios with T/d. All of these factors are related to fluid dynamics, which is quite different around each cylinder for the range of T/d = 1.5 ~ 2.0 (e.g. Chapters 2 & 3). For example, at T/d = 1.70, the base pressure on one cylinder is smaller than that measured on its neighbour. The gap flow is deflected towards the cylinder with the lower base pressure, resulting in a narrow wake. Meanwhile a wide wake develops behind the neighbouring cylinder.

Correspondingly, the mean drags and lifts on the two cylinders also differ considerably. Naturally, it is not surprising to see an appreciable deviation in $f_y^{(1)}/f_0^{(1)}$ or $f_x^{(1)}/f_0^{(1)}$ between the two fluid-cylinder systems.

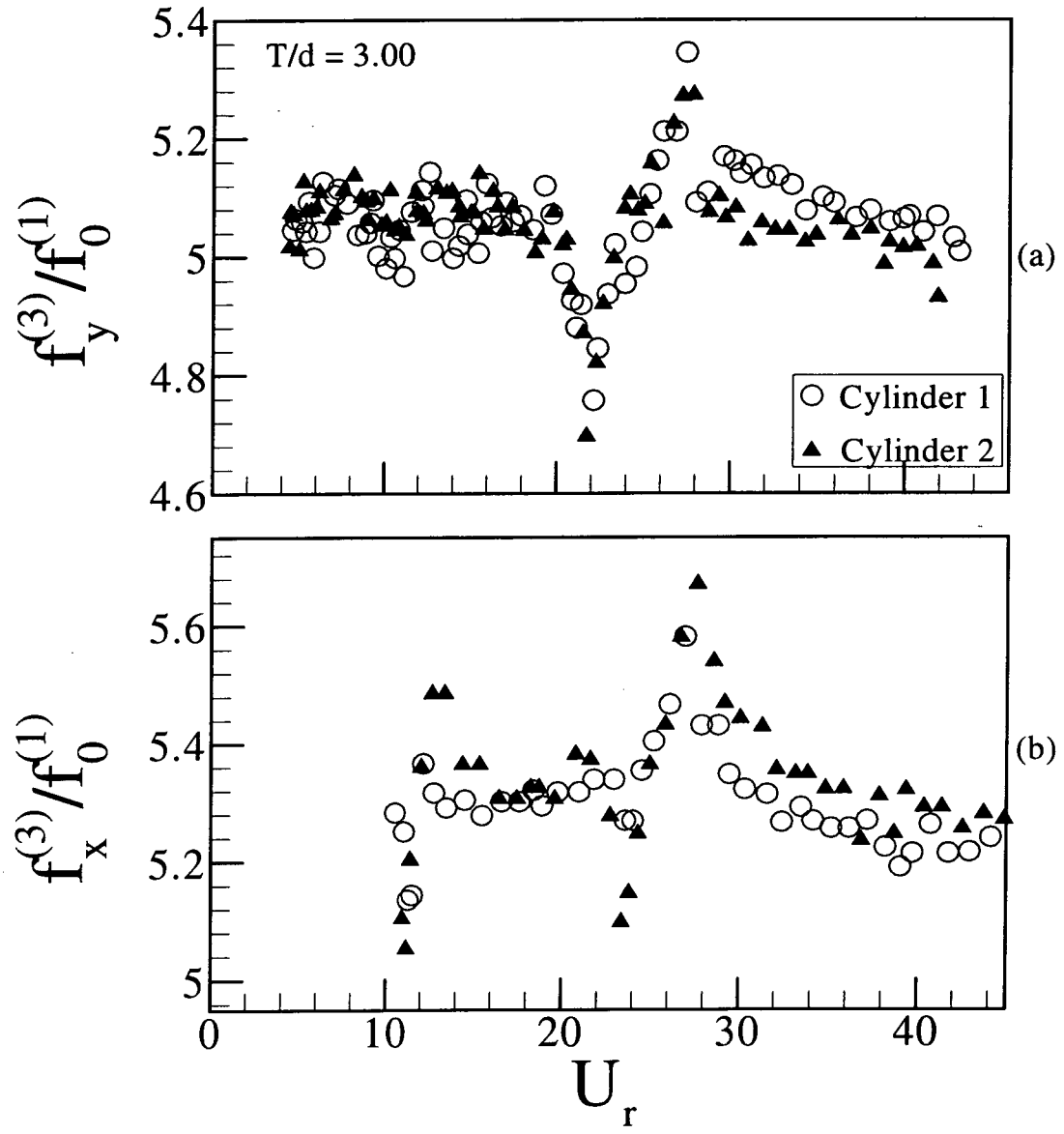

Figure 4-16 Variation of the cross-flow $f_y^{(3)}$ and inline $f_x^{(3)}$ with U_r at T/d = 3.00: ○, Cylinder 1; ▲, Cylinder 2. (a), $f_y^{(3)}$, (b) $f_x^{(3)}$.

It is interesting to note that at T/d = 3.00 the third-mode natural frequency $f_x^{(3)}/f_0^{(1)}$ (Fig. 4-16) of the fluid-cylinder system exhibits a sudden variation near

$U_r \approx 26$, where the third-mode resonance occurs in the lift direction but not in the drag direction. Furthermore, the variation in $f_x^{(3)}/f_0^{(1)}$ is rather comparable in magnitude with that of $f_y^{(3)}/f_0^{(1)}$. Since the fluctuating drag has a frequency of $2f_s^*$, the third-mode resonance in the drag direction should occur at $U_r \approx 13.0$. Indeed, a sharp variation in $f_x^{(3)}/f_0^{(1)}$ at $U_r \approx 13.0$ is observed in Fig. 4-16b for both cylinders. Two reasons could be responsible for the sudden change in $f_x^{(3)}/f_0^{(1)}$ near $U_r \approx 26$. One is a possible cross talk between lift and drag. The other is the effect of non-linearity at the occurrence of the third-mode resonance in the lift direction, which is very violent (Fig. 4-7a). The latter is most likely to be a more plausible explanation.

4.6 Conclusions

The free vibration of two side-by-side cylinders, fixed at both ends, in a cross-flow has been experimentally investigated using fibre-optic Bragg grating sensors. In the present investigation, the sensor was successfully extended to measure the dynamic strain due to the drag for a single cylinder. The strain-displacement relation is linear in the U_r range investigated. This linear relation is expected to extend well beyond the linear range ($U_r < 22$), as reported for the lift direction, in view of the substantially weaker vibration in the drag direction. The linear relation remains valid in the case of two side-by-side cylinders, but the slope changes with *T/d*. The establishment of the linear relation between strain and bending displacement facilitates the interpretation of the measured strain data. The following conclusions can then be drawn.

1. At $T/d = 3.00$, the structural vibration in the lift direction appears to overwhelm that in the drag direction, particularly when the first-, second- and third-mode resonance occurs at $U_r \approx 4.2$, 12 and 26, respectively. The vibration is especially violent at the third-mode resonance, suggesting the importance of structural elasticity in instability analysis, which has been largely overlooked in the past. The characteristics of the structural vibration resemble the case of an isolated cylinder, implying little interference at this *T/d*. The correlation coefficient ρ_{12} between ε_{x1} and ε_{x2} generally approaches zero, except near resonance where the vortex shedding frequency coincides with the system natural frequencies. The value of ρ_{12} between ε_{y1} and ε_{y2} is mostly negative and can go beyond - 0.5 near resonance, implying opposite movement of the two cylinders. This observation is consistent with previously reported in Chapter 3 that vortices shed from the two cylinders are predominantly in an anti-phase mode.
2. As *T/d* reduces to 1.70, the strength of the vortices is drastically weakened due to interactions between the flow around individual cylinders. Consequently, resonance is suppressed, and this suggests an enhanced stability. The fluid dynamics, such as fluid forces, base pressure and vortex formation, around one cylinder is very different from that around its neighbour. Consequently, the natural frequencies of the combined fluid-cylinder systems, associated with each individual cylinder, may exhibit appreciable differences, up to 5%.
3. When *T/d* is further reduced to 1.13, the structural vibration in the lift direction is significantly suppressed due to the repulsive force between the two cylinders, whereas the drag direction vibration is virtually unaffected by the neighbouring cylinder. As a result, the drag direction vibration appears dominating. The correlation coefficient ρ_{12} between ε_{x1} and ε_{x2} or ε_{y1} and

ε_{y2} is positive and increases appreciably, compared with its corresponding value for the T/d = 1.70 or 3.00. Evidently, the two cylinders tend to move in-phase, coupled together like a single structure. However, there is one important difference between one isolated cylinder and the two side-by-side cylinders at small T/d. In the former case, the drag force fluctuates twice as fast as the lift force; in the latter case the fluctuating frequency of the two forces is identical since vortices are shed from the free-stream side of the two cylinders only. Consequently, resonance occurs simultaneously in both lift and drag directions, and the peak at $U_r \approx 11$ is quite comparable for $\varepsilon_{y,rms}$ and $\varepsilon_{x,rms}$.

CHAPTER 5

FLOW SEPARATION EFFECT ON A FREELY VIBRATING CYLINDER

5.1 Introduction

Flow-structure interaction involves turbulent flow, separation behaviour and structural vibrations and, most of all, the coupling between the structural motions and the flow field. Past research has largely been focused on fluid-structure interaction problems associated with rigid cylinders (Sarpkaya 1979; Bearman and Obasaju 1982; Weaver and Fitzpatrick 1988; Williamson and Roshko 1988; Parkinson 1989; Brika and Laneville 1993). There have been few studies on the free vibration of elastic cylinders in a cross-flow. Zhou *et al.* (1999b) and So *et al.* (2000b) measured the free vibration of an elastic circular cylinder in a cross-flow and noted that the cylinder was excited at the first and third natural frequencies of the fluid-structure system. However, their studies did not consider the effect of flow separation on the structural vibration and the damping force was not measured.

It has been reviewed in Chapter 1 that the flow separation point is fixed during vortex shedding from a square cylinder (Nguyen *et al.* 1991; Naudascher and Wang 1993; Chen and Liu 1999). Whereas the point keeps moving when the boundary layer is separated from a circular cylinder (Achenbach 1968; Mei and Currie 1969; Dwyer and Mccroskey 1973; Chen 1987; Higuchi *et al.* 1989). However, it is not clear how this difference of the separation behaviours would impact on fluid-structure interaction.

The free vibration of a two-dimensional bluff body in a cross-flow is governed by several major parameters. Some of the more important ones are the

Reynolds number Re, the reduced velocity U_r, the reduced damping ratio ζ, the mass ratio M^*, the cylinder aspect ratio s/d_h, the force coefficient C_L (and C_D) and the separation behaviour (Chen 1987). Each of these parameters plays a different role in the dynamic response of the cylinder. It is obvious that if the fluid-cylinder interaction problem is to be understood thoroughly, all of these parameters need to be investigated systematically. In an experimental investigation, where the cylinder and boundary conditions are given, M^*, s/d_h, C_L and C_D are fixed. Furthermore, with the natural frequency of the structure fixed, varying Re is equivalent to changing U_r. As a result, ζ, U_r and the separation behaviour play a major role in the structural response. The effect of U_r can be investigated by simply varying the incoming flow velocity, while the separation behaviour can be examined by changing the geometry of the cylinder.

The behaviour of the effective damping ratios associated with one or two side-by-side elastic circular cylinders has been discussed in Chapter 3. However, in the square cylinder case, flow separation is quite different from that associated with a circular cylinder. Thus, one might not expect the effective damping ratios to behave similarly as the circular cylinder case, because fluid damping originates from viscous dissipation and fluid drag, i.e. resulting from flow separation and viscous shearing of the fluid at the surface of the structure. As the cylinder rotates, separation behaviour is affected, resulting in, for certain α, a flow reattachment on the sidewall of the cylinder. The issue of the effect of α on the effective damping ratios has yet to be resolved.

It has been discussed in Chapter 3 that the system natural frequencies associated with two side-by-side circular cylinders are dependent on U_r and can be modified up to 10% by the vortex shedding frequency. The same could be anticipated for the system natural frequencies associated with a square cylinder. In

the square cylinder case, an additional question is how these frequencies would be affected by α.

The purpose of this chapter is to investigate the effect of flow separation on the free vibration of an elastic cylinder, fixed at both ends (zero deflection), in a cross flow, including the effect on the damping ratios and the system natural frequencies. Both circular and square cross-section cylinders were used. While a single hot wire was used to measure the flow field, two FBG sensors were employed to measure simultaneously the lateral and longitudinal structural responses at the mid span of the cylinder. This chapter is outlined as follows. Section 5-2 provides the experimental details. The measured dynamic strains are converted to displacements in Section 5-3. Section 5-4 presents the vibration characteristics of a square cylinder compared with those of a circular cylinder. The results on system natural frequencies and damping ratios are presented in Sections 5-5 and 5-6, while the conclusions are given in Section 5-7.

5.2 Experimental Details

5.2.1 Experimental setup

The experiments were conducted in a suction-type wind tunnel with a square cross section (0.35m × 0.35m) that is 0.5 m long. In the free stream, the longitudinal turbulence intensity was measured to be approximately 0.2%. The details of the wind tunnel have been discussed in Chapter 3. An acrylic cylinder was vertically mounted in the mid-plane of the test section and 0.20m downstream of the exit plane of the contraction section (Fig. 5-1). Both square and circular cylinders were investigated in order to examine in detail the effect of fixed and moving flow separation points on the flow-induced vibration of the cylinder. The two cylinders

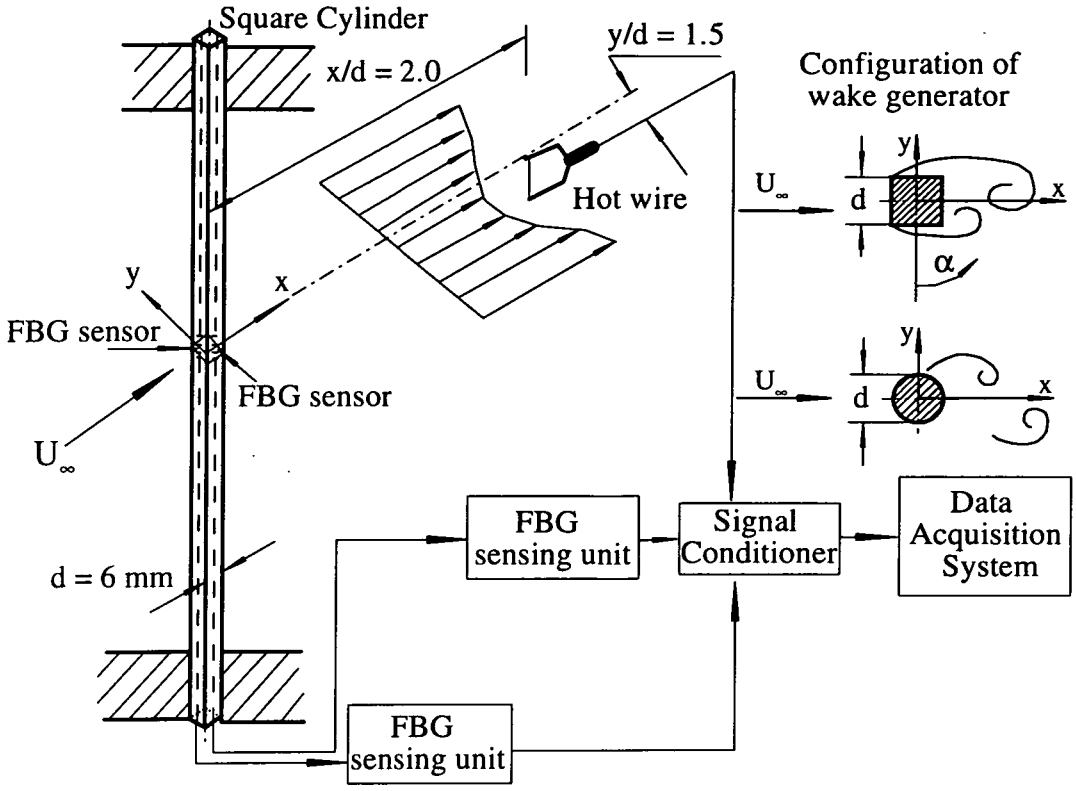

Figure 5-1 Experimental arrangement.

have identical hydraulic diameter $d_h = d = 6.0$ mm for the purpose of comparison. The first-mode structural damping ratio $\zeta_0^{(1)}$ is estimated to be 0.02 and 0.03 for the square and circular cylinders, respectively. The structural characteristics of the two cylinders are given in Table 5-1. The mounting of the cylinders was designed to provide a fixed support boundary condition at both ends, i.e. cylinder deflection at the supports was zero. The *Re* investigated varied from 800 to 10700, corresponding to a U_r range of 4 to 51. With this arrangement, blockage amounted to 2.94% for the square cylinder and 2.31% for the circular cylinder. Therefore, blockage effect on the mean drag is relatively small at the *Re* range investigated. A total of four α was investigated for the square cylinder, i.e. $\alpha = 0°$, 15°, 30° and 45°. Great care was taken during the experiments to minimise the variation of $f_0^{(1)}$ associated with

changing α. Consequently, the $f_0^{(1)}$ values of the square cylinder were found to be 90.2, 89.8, 89.2 and 88.7 Hz, corresponding to $\alpha = 0°$, 15°, 30° and 45°, respectively.

Table 5-1. Structural characteristics of cylinders.

Cylinder	Material	d_h (mm)	m (kgm^{-1})	EI (Nm^2)	M^*	$f_0^{(1)}$ (Hz)			
Square	Acrylic	6.00	0.0421	0.4739	970	$\alpha = 0$	$\alpha = 15$	$\alpha = 30$	$\alpha = 45$
						90.2	89.8	89.2	88.7
Circular	Acrylic	6.00	0.01926	0.224	565	94			

5.2.2 Dynamic strain measurements

The experimental arrangement is shown schematically in Fig. 5-1. Two optical silica fibre of diameter 125 μm built with FBG sensors were used to simultaneously measure the structural responses in the longitudinal and lateral directions. In the circular cylinder case, one optical silica fibre built with the FBG sensor was buried in a groove along the rear stagnation line of the cylinder and the other fibre along a line 90° from the rear stagnation line. The two fibres, flush with the cylinder surface using nail polish, measured the dynamic strain ε_x due to the drag and ε_y due to the lift, respectively, at the mid-span of the cylinder. Since the sensor grating has a finite length of about 10mm, the measured strain represents the average strain over this length. In the square cylinder case with α = 0°, the two optical fibres were located along the cylinder midway of the downstream surface and one side surface of the cylinder, respectively.

The sensors, labelled sensor 1 and sensor 2, simultaneously measured the strain ε_1 and ε_2 at the mid-span of the cylinder. This is true for all α tested. In principle, ε_1 and ε_2 (or ε_x and ε_y) are independent of each other. Note that the

optical fibre is extremely light and has a homogenous mass distribution. Therefore, its attachment to the cylinder will not change the structural stiffness of the cylinder. Measurements of the stream-wise fluctuating velocity u and cross-flow fluctuating displacement Y carried out by Zhou *et al.* (1999b) indicated a negligible effect of the attachment of the optical fibre on flow separation and Y. In the present experiment, the effect has been further minimised by burying the optical fibre in the cylinder. A major source of error comes from the non-linear relation between the output voltage and the dynamic strain (Zhou *et al.* 1999b; Jin *et al.* 2000). As a result, the experimental uncertainty is estimated to be ±8%.

5.2.3 Fluctuating velocity measurements

The stream-wise fluctuating velocity u was measured by a single Tungsten wire of 5 μm diameter located at $x/d = 2$ and $y/d = 1.5$. The hot wire was operated at an overheat ratio of 1.8 with a constant temperature anemometer (DISA Type 55M10).

The signals ε_x, ε_y and u or ε_1, ε_2 and u were simultaneously measured and offset, amplified and then digitised using a 12 bit A/D board and a personal computer at a sampling frequency of 6.0 kHz per channel. The duration of each record was 20s. This has been verified to be sufficiently long for the rms values $\varepsilon_{x,rms}$ of ε_x, $\varepsilon_{y,rms}$ of ε_y, $\varepsilon_{1,rms}$ of ε_1 and $\varepsilon_{2,rms}$ of ε_2 to reach approximately their stationary state, with a variation smaller than 1.0%.

5.3 Bending Displacements

Zhou *et al.* (1999b) and Jin *et al.* (2000) used the FBG sensor to measure the dynamic strain induced by the unsteady lift acting on a circular cylinder. Their

cylinder was made of the same material and has the same hydraulic diameter as the present cylinders. The strain thus obtained was compared with the Y measured using a laser vibrometer. They found that the spectra deduced from the two signals were in agreement with each other in terms of the vortex shedding frequency and the natural frequency of the fluid-cylinder system. Furthermore, the two signals showed a complete coherence at these frequencies. From their measurements, they deduced an empirical relation between Y_{rms} and $\varepsilon_{y,rms}$, i.e. $\varepsilon_{y,rms} = 0.59Y_{rms}$, for the linear portion over the range of U_r investigated. In the present investigation, this $\varepsilon - Y$ relationship was used to estimate the bending displacements from the measured dynamic strain signals in the square and circular cylinder case. Details are given below.

In the circular cylinder case, the dynamic strains ε_x and ε_y were measured using two FBG sensors (Section 5-2); the time series was given by

$$\varepsilon_x(1),\ \varepsilon_x(2),\ldots,\ \varepsilon_x(i),\ \ldots,\ \varepsilon_x(120000);$$

$$\varepsilon_y(1),\ \varepsilon_y(2),\ldots,\ \varepsilon_y(i),\ \ldots,\ \varepsilon_y(120000).$$

The bending displacements are approximated by

$$X(i) = \frac{1}{0.59}\varepsilon_x(i) = 1.6949\varepsilon_x(i),$$

$$Y(i) = \frac{1}{0.59}\varepsilon_y(i) = 1.6949\varepsilon_y(i), \qquad \text{i} = 1, 2,\ldots, 120000.$$

Similarly, the bending displacements $X'(i)$ and $Y'(i)$ of the square cylinder can be approximated by

$$X'(i) = \frac{1}{0.59}\varepsilon_1(i) = 1.6949\varepsilon_1(i),$$

$$Y'(i) = \frac{1}{0.59}\varepsilon_2(i) = 1.6949\varepsilon_2(i), \qquad \text{i} = 1, 2,\ldots, 120000.$$

When the square cylinder is placed at an incidence angle $\alpha \neq 0°$ with respect

to the free stream (Fig. 5-1), $X'(i)$ is not a displacement in the longitudinal direction, nor is $Y'(i)$ in the lateral direction. Decomposing $X'(i)$ and $Y'(i)$, the bending displacements in the longitudinal and lateral directions can be written as

$$X(i) = Y'(i)\cos(\tfrac{3}{2}\pi + \alpha) + X'(i)\cos\alpha,$$

$$Y(i) = Y'(i)\sin(\tfrac{3}{2}\pi + \alpha) + X'(i)\sin\alpha, \qquad i = 1, 2, \ldots, 120000,$$

where, $\alpha = 0°$, $15°$, $30°$ and $45°$.

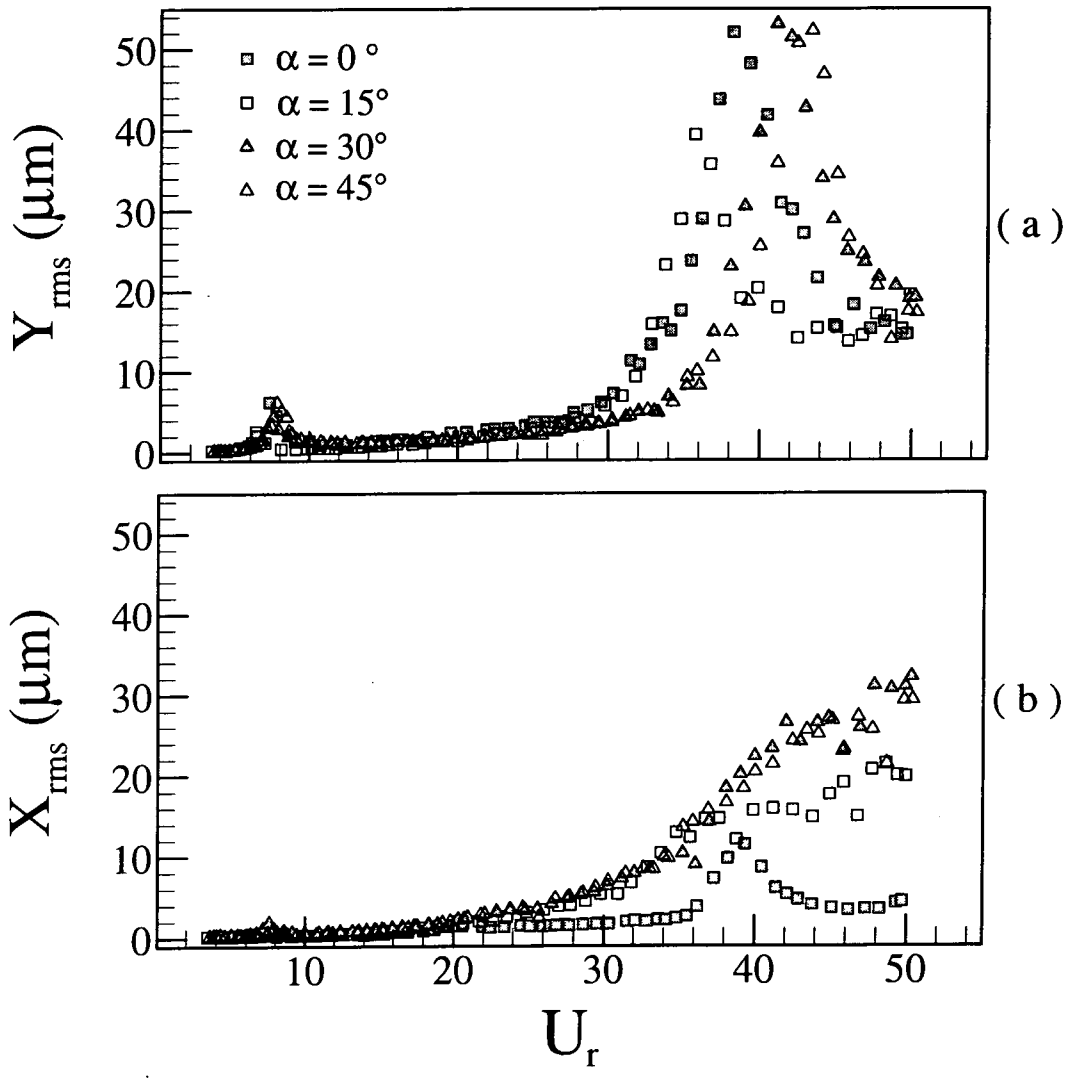

Figure 5-2 Dependence of the vibration amplitude of the square cylinder on U_r: (a) Y_{rms}; (b) X_{rms}.

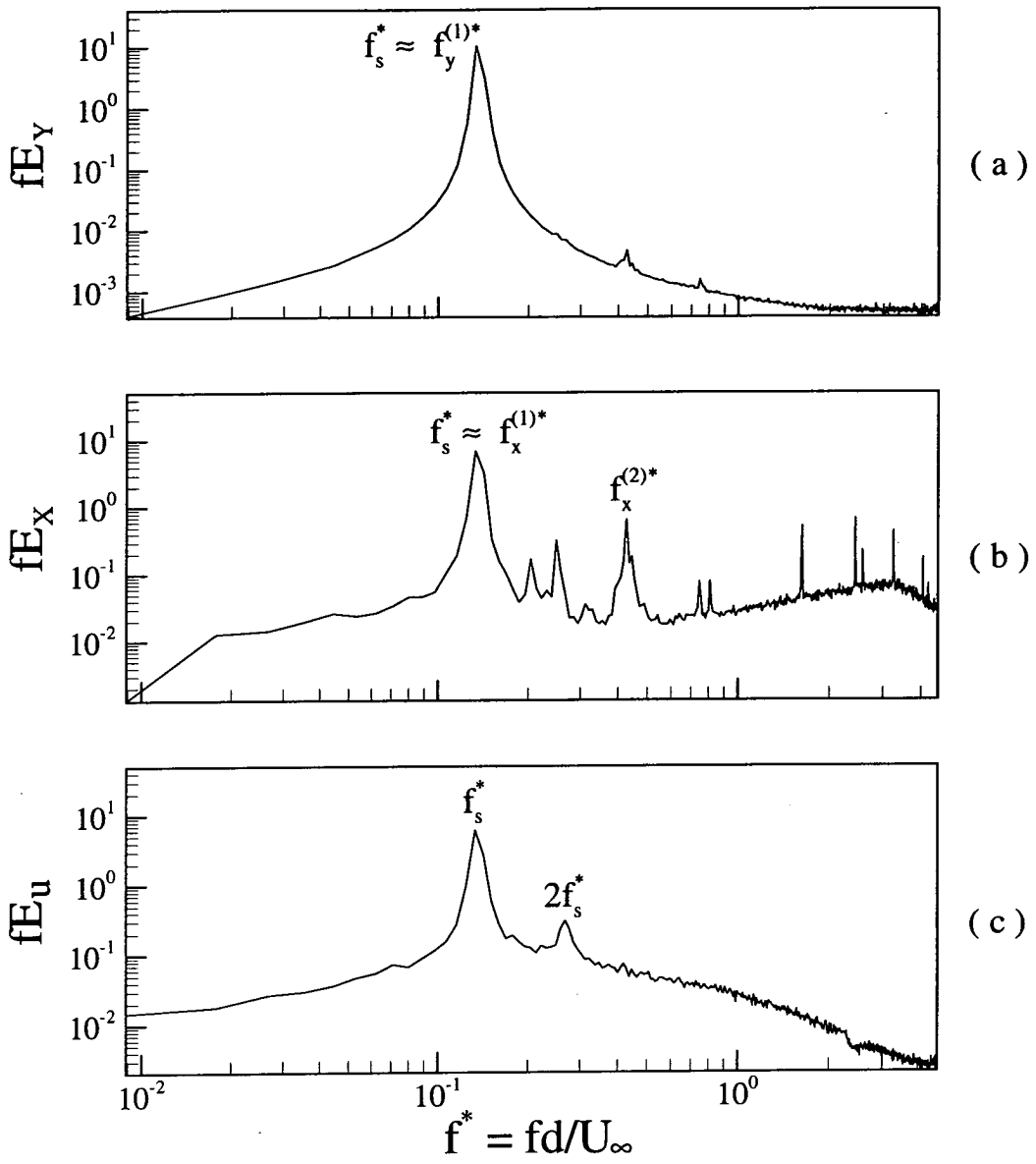

Figure 5-3 (a) Y-spectrum E_Y ; (b) X-spectrum E_X ; (c) u-spectrum E_u . (Square cylinder, $\alpha = 0°$, $U_r \approx 7.5$. The hot wire was located at $x/d = 2$ and $y/d = 1.5$).

5.4 Vibration Characteristics

Figure 5-2 presents the variation of X_{rms} and Y_{rms} with U_r for the square cylinder at various α. When $\alpha = 0°$, the variation of Y_{rms} and X_{rms} show a similar

trend. Both increase as U_r increases and their local peaks occur at the same U_r, i.e. at $U_r \approx 7.5$ and 40.

The Y_{rms} peak at $U_r \approx 7.5$ for the case $\alpha = 0°$ results from the resonance where the vortex shedding frequency f_s coincides with the first-mode natural frequency $f_y^{(1)}$ of the fluid-structure system. To substantiate this, the spectra of E_Y, E_X and E_u at $U_r \approx 7.5$ are shown in Fig. 5-3. All spectra exhibit a prominent peak at $f^* = fd/U_\infty = 0.1335$ ($f = 88$ Hz), which is consistent with the f_s of a square cylinder reported by Okajima (1982), Knisely (1990) and Zhou and Antonia (1994). The first-mode system natural frequency can be calculated by $f_y^{(1)} = f_0^{(1)}/\sqrt{1+\pi/4M^*}$ (So *et al.* 2000b). Since the added mass is very small compared to the cylinder mass in an airflow and the mass ratio M^* is quite large ($\approx$ 970), $f_y^{(1)}$ is essentially identical to $f_0^{(1)} = 90.2$ Hz (Table 5-1) or approximately equal to f_s.

In order to understand the Y_{rms} peak at $U_r \approx 40$ for the $\alpha = 0°$ case (see Fig. 5-2a), the spectra E_Y, E_X and E_u at $U_r \approx 40$ are shown in Fig. 5-4. The most prominent peak in E_Y occurs at $f = 480$ Hz or $f^* \approx 0.1354$. This frequency is approximately equal to the third-mode natural frequency $f_y^{(3)*}$ of the fluid-cylinder system, which can be estimated from $f_y^{(1)*}$ using the formula given by Chen (1987), i.e. $f_y^{(3)*}/f_y^{(1)*} = (121/22.4) = 5.402$ or $f_y^{(3)*} = f_y^{(3)} d/U_\infty = 0.1354$. Evidently, $f_y^{(3)*}$ coincides with f_s^*; the peak at $U_r \approx 40$ is the result of the third-mode resonance.

The spectra at $U_r \approx 7.5$ and 40 for $\alpha = 15°$, 30° and 45° (not shown) were quite similar to those shown in Figs. 5-3 and 5-4 ($\alpha = 0°$). They indicate the occurrence of the first- or third-mode resonance. Furthermore, the magnitude of the

peak in E_X or E_Y is larger at $U_r \approx 40$ than at $U_r \approx 7.5$, suggesting a more violent vibration corresponding to the third-mode resonance, irrespective of the α value.

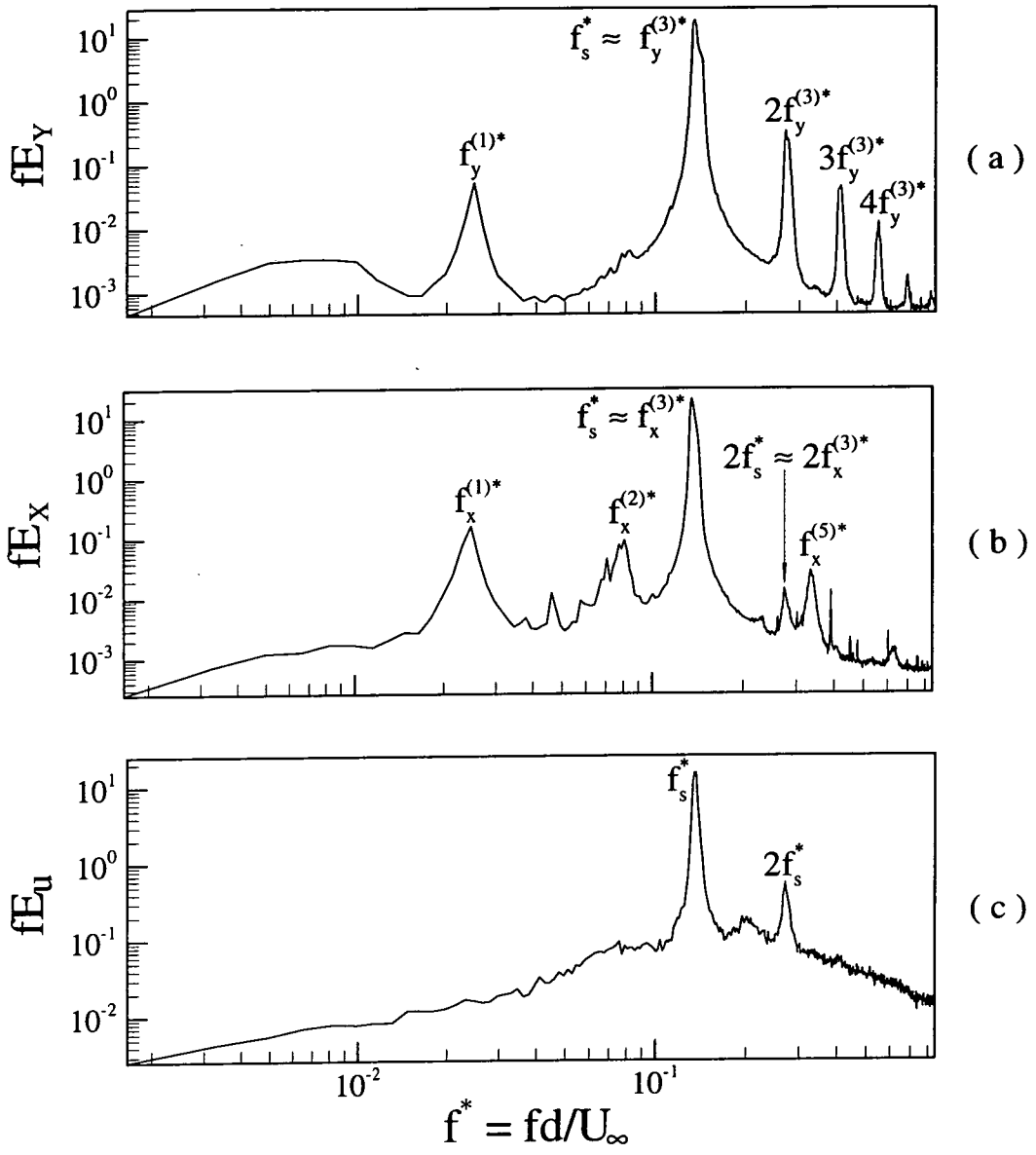

Figure 5-4 (a) Y-spectrum E_Y; (b) X-spectrum E_X; (c) u-spectrum E_u. (Square cylinder, $\alpha = 0°$, $U_r \approx 40$. The hot wire was located at $x/d = 2$ and $y/d = 1.5$).

The peak in Y_{rms} at $U_r \approx 40$ (Fig. 5-2) is by far more pronounced than that at $U_r \approx 7.5$. This may not be surprising. Firstly, the resonance corresponding to $f_y^{(3)*}$ occurs at higher U_r. Flow excitation energy, which is proportional to U_r^2, is

therefore much higher, as indicated by the more pronounced peak in E_u at $U_r \approx 40$ (Fig. 5-4c) than that at $U_r \approx 7.5$ (Fig. 5-3c). Secondly, it will be seen in Section 5-6 that the effective damping ratio, which is the sum of the structural and fluid damping ratio, associated with $f_y^{(3)*}$ is appreciably smaller than that associated with $f_y^{(1)*}$. This means that the energy dissipation, when resonance occurs at $f_s^* = f_y^{(3)*}$, could be quite small. Finally, the fifth harmonic of $f_y^{(1)*}$ ($5 \times f_y^{(1)*} = 0.124$) is quite close to f_s^*. This could feed the resonance with additional energy. The combined effect of these factors results in a much more violent vibration or instability at $U_r \approx 40$ for all α cases considered.

When α = 15°, 30° and 45°, the behaviour of Y_{rms} exhibits a similar trend as that at $\alpha = 0°$, i.e. two peaks are detected, one at a low U_r and another at a high U_r. At $\alpha = 0°$, the peak in Y_{rms} corresponding to the third mode resonance occurs at $U_r \approx$ 40. This peak shifts slightly to $U_r \approx$ 36.2, 41.4 and 42.8 for α = 15°, 30° and 45°, respectively. The peaks at the lower U_r exhibits a similar shift, occurring at $U_r \approx$ 7.50, 6.34, 7.54 and 7.94 for α = 0°, 15°, 30° and 45°, respectively. These shifts could be attributed to the variation of the vortex shedding frequency at different α. The measurements of Chen and Liu (1999) for a square cylinder showed that the variation of the Strouhal number $St = fd'/U_\infty$, where $d' = (\sin\alpha + \cos\alpha)d$ is the cross flow dimension of the cylinder of height d, depended on α and Re. For example, at Re = 8000, $St \approx 0.135$ for $\alpha = 0°$. If the square cylinder is rotated to α = 15°, St increases to 0.1814, but changes little with any further increase in α. In the present investigation, the variation in the structural natural frequency is negligibly small for different α (Table 5-1). This frequency is in general very close to the system natural frequency because of a small contribution from the air stream

(Section 5-5), implying that the third-mode resonance, where the vortex shedding frequency coincides with the third-mode natural frequency of the system, will occur at $f_0^{(3)}$ and $U_r = U_\infty / f_0^{(1)} d = f_0^{(3)} d' / S_t f_0^{(1)} d$. Noting that $f_0^{(3)} = 5.402 f_0^{(1)}$ (Chen 1987) and $d' = (\sin\alpha + \cos\alpha) d$, $U_r = 5.402(\sin\alpha + \cos\alpha)/St$, where $St = 0.135$ for $\alpha = 0°$ and about 0.1814 for $\alpha = 15°$, 30° and 45°. The subsequent calculation indicates that the third-mode resonance occurs at $U_r = 40.01$, 36.47, 40.68 and 42.11 for $\alpha = 0°$, 15°, 30° and 45°, respectively. A similar interpretation can be used to explain the shift of the peaks corresponding to the first-mode resonance.

The root mean square x-displacement, X_{rms}, at $\alpha = 15°$, 30° and 45° (Fig. 5-2b) is rather different from that at $\alpha = 0°$, exhibiting only one tiny peak at $U_r \approx 7.5$. The small peak, as compared with Y_{rms}, is consistent with the perception that fluctuating drag on a bluff body is by far smaller than fluctuating lift. Lee (1975)'s measurement showed that when the square cylinder was rotated with respect to the flow, the mean drag coefficient was minimum at $\alpha \approx 13°$ and increased with further increasing α. The fluctuating drag is also likely to increase (Vickery 1966). This may explain the increased X_{rms} as α increases (Fig. 5-2b).

For the purpose of comparison, the Y_{rms} and X_{rms} measurements of the circular cylinder were presented in Figs. 5-5 and 5-6. A detailed discussion has been given in Zhou *et al.* (1999b) about the vibration characteristics of a circular cylinder in a cross-flow and there is no need to repeat here. The following comments will focus on the difference in the vibration behaviour between the circular and square cylinders.

Firstly, three peaks at $U_r \approx 4.2$, 11.0 and 26.0 are discernible in Y_{rms} of the circular cylinder. They can be identified with the occurrence of the first-, second- and third-mode resonance (Zhou *et al.* 1999b). In contrast, the first- and third-mode

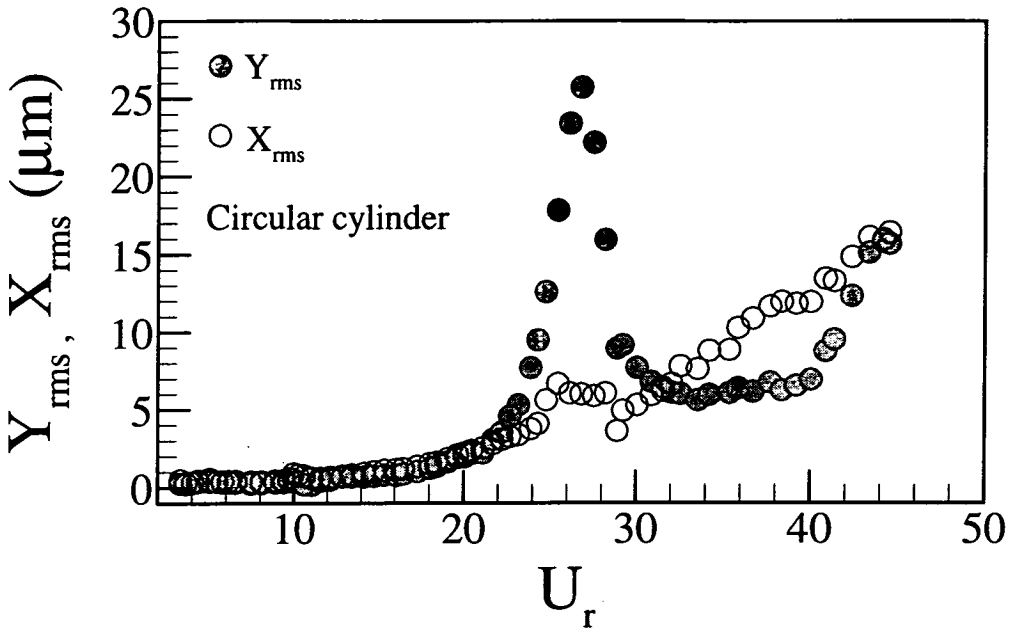

Figure 5-5 Dependence of Y_{rms} and X_{rms} of the circular cylinder on U_r.

resonances are also excited with the square cylinder, though at different U_r because of the different vortex shedding frequency. But the square cylinder data fails to show the peak corresponding to the second-mode resonance. The flow separation point from a square cylinder is fixed, that is, the shedding of vortex rolls is probably spanwise in-phase, which enhances the two-dimensionality of the vortex shedding. Presumably, the vortex excitation is spanwise uniform. The second-mode vibration could then hardly be excited, as shown in Fig. 5-2. In the circular cylinder case, however, the separation point oscillates over a range of 75°~85° (Dwyer and Mccroskey 1973). The oscillation is unlikely to be spanwise in phase, responsible at least partially for the three dimensionality of the vortex shedding. The vortex cell has a typical spanwise extent of 1~3d (King 1977; Higuchi *et al.* 1989). Therefore, the vortices shed from a circular cylinder could be less two dimensional than those from a square cylinder (Sarpkaya 1979; Zhou and Antonia 1994), thus inducing the spanwise asymmetrical excitation force and subsequently exciting the second mode of vibration.

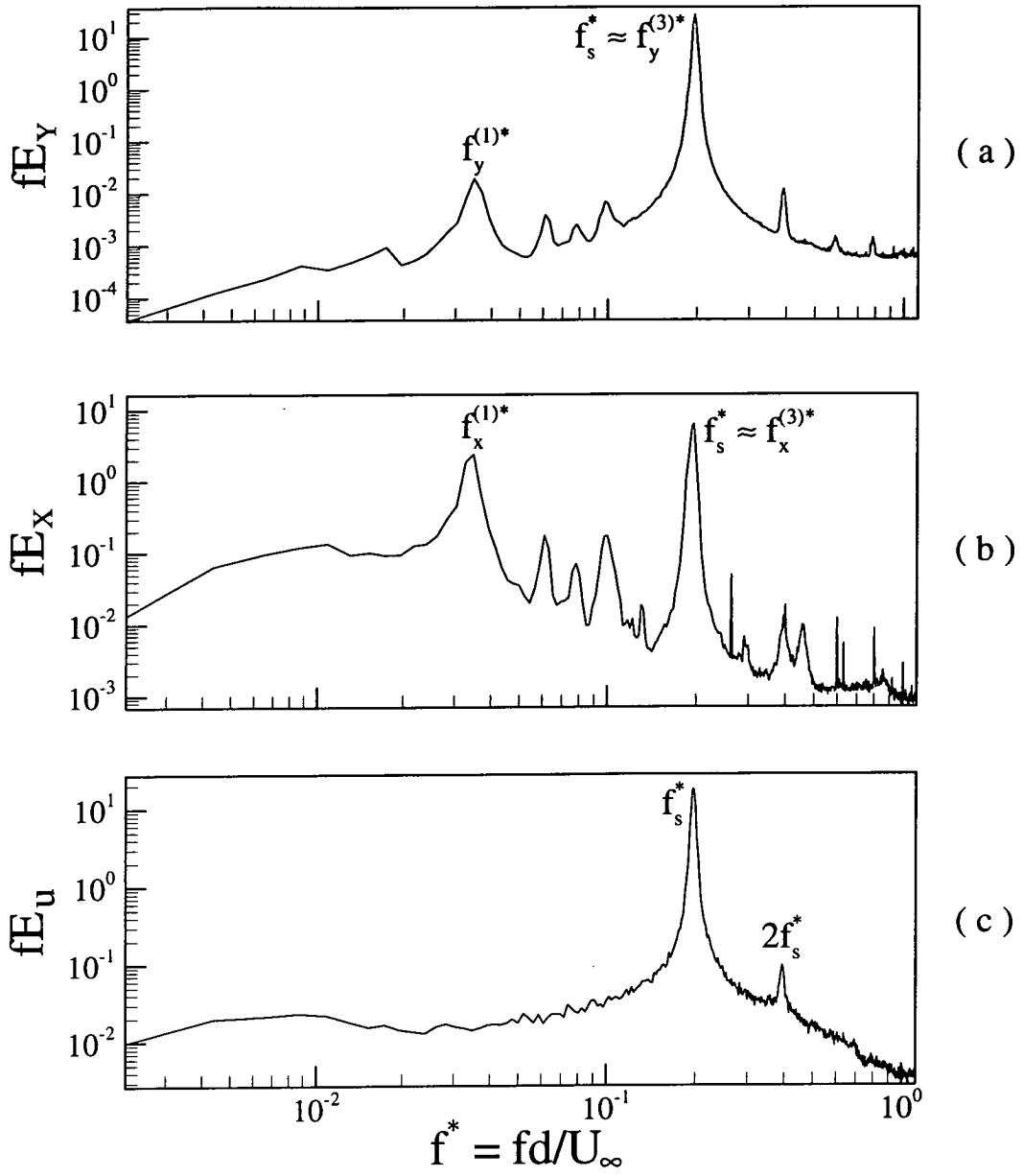

Figure 5-6 (a) Y-spectrum E_Y ; (b) X-spectrum E_X ; (c) u-spectrum E_u . (Circular cylinder, $U_r \approx 26$. The hot wire was located at $x/d = 2$ and $y/d = 1.5$).

Secondly, both cylinders show a pronounced peak in Y_{rms} at the third-mode resonance. But the peak at $U_r \approx 40$ (Fig. 5-2) for the square cylinder is about twice that at $U_r \approx 26$ (Fig. 5-5) for the circular cylinder even though the flexural rigidity of the square cylinder is larger (Table 5-1). This could be attributed to two reasons. First, for a large U_r, the galloping instability occurs for non-circular cross-section

cylinders, thus feeding in additional energy into the resonating system (e.g. Blevins 1994). Since the frequency of the galloping force is coupled with the structural vibration frequency, the occurrence of galloping and the vortex resonance may be inseparable (Bokaian and Geoola 1984a). Second, as discussed earlier, the oscillation of the separation point associated with a circular cylinder is unlikely to be spanwise in-phase. This is bound to impair the excitation force upon the structure, as compared with the spanwise in-phase shedding of vortex rolls in the square cylinder case. The combined effect results in the third-mode resonance, associated with the square cylinder, by far more violent than that associated with the circular cylinder.

5.5 Natural Frequencies of the Fluid-Cylinder System

The structural natural frequency $f_0^{(1)}$ of the square cylinder at $\alpha = 0°$ is 90.2 Hz (Table 5-1). However, the natural frequency $f_y^{(1)}$ of the fluid-cylinder system is 88.7 Hz at $U_r \approx 7.5$, as determined from the spectra (Fig. 5-3). This frequency further decreases to 86.9 Hz at $U_r \approx 40$ (Fig. 5-4). Bear in mind that the square cylinder was not remounted for the same α, implying that the natural frequency of the cylinder should remain unchanged. Since the spectra were deduced using a conventional FFT program, the frequency resolution Δf is fixed by the sampling rate and the record length used in the FFT calculation. This Δf was estimated to be 0.35 Hz. Therefore, the variation in $f_y^{(1)}$ noted above could not be attributed to experimental or calculation errors; it is more likely a genuine change in the system natural frequency because of different flow conditions.

Figures 5-7 and 5-8 show the dependence of $f_y^{(1)}/f_0^{(1)}$ and $f_x^{(1)}/f_0^{(1)}$ on α and U_r. There is a marked variation in $f_y^{(1)}/f_0^{(1)}$ and $f_x^{(1)}/f_0^{(1)}$ between $\alpha = 0°$ and

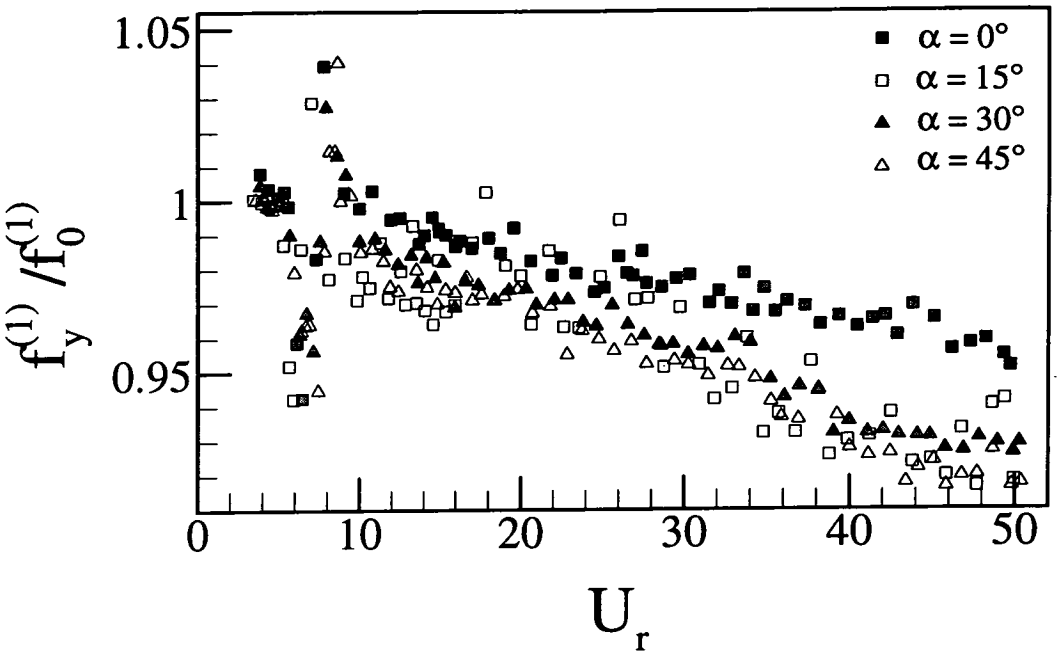

Figure 5-7 Dependence on α and U_r of $f_y^{(1)}$ associated with the square cylinder: ■, $\alpha = 0°$; □, 15°; ▲, 30°; △, 45°.

$\alpha \neq 0°$; $f_y^{(1)}/f_0^{(1)}$ and $f_x^{(1)}/f_0^{(1)}$ tend to be greater at $\alpha = 0°$ than at $\alpha \neq 0°$. This difference grows as U_r increases and become particularly evident when $U_r > 20$. Similar observation has been also made in the case of two side-by-side elastic circular cylinders (Chapters 3 and 4). From a linear analysis of the fluid-cylinder system for a circular cylinder (Zhou *et al* 2001), the system natural frequencies $f_x^{(n)}$ and $f_y^{(n)}$ can be derived as $f_x^{(n)} = f_0^{(n)}\sqrt{1-\zeta_{x,e}^2}$ and $f_y^{(n)} = f_0^{(n)}\sqrt{1-\zeta_{y,e}^2}$. It will be seen in Section 5-6 that the deduced effective damping ratios $\zeta_{x,e}^{(1)}$ and $\zeta_{y,e}^{(1)}$ corresponding to the first-mode natural frequencies $f_x^{(1)}$ and $f_y^{(1)}$ at $\alpha = 0°$ are smaller than those at $\alpha = 15°$, 30° and 45°, especially when $U_r > 20$. This could partially account for the first-mode natural frequency of the fluid-structure system greater at $\alpha = 0°$ than that at $\alpha = 15°$, 30° and 45° in both the x and y direction.

The value of $f_y^{(1)}/f_0^{(1)}$ or $f_x^{(1)}/f_0^{(1)}$ (Figs. 5-7 and 5-8) appears decreasing with the increase of U_r irrespective of the α value. The deduced $f_y^{(1)}/f_0^{(1)}$ in the

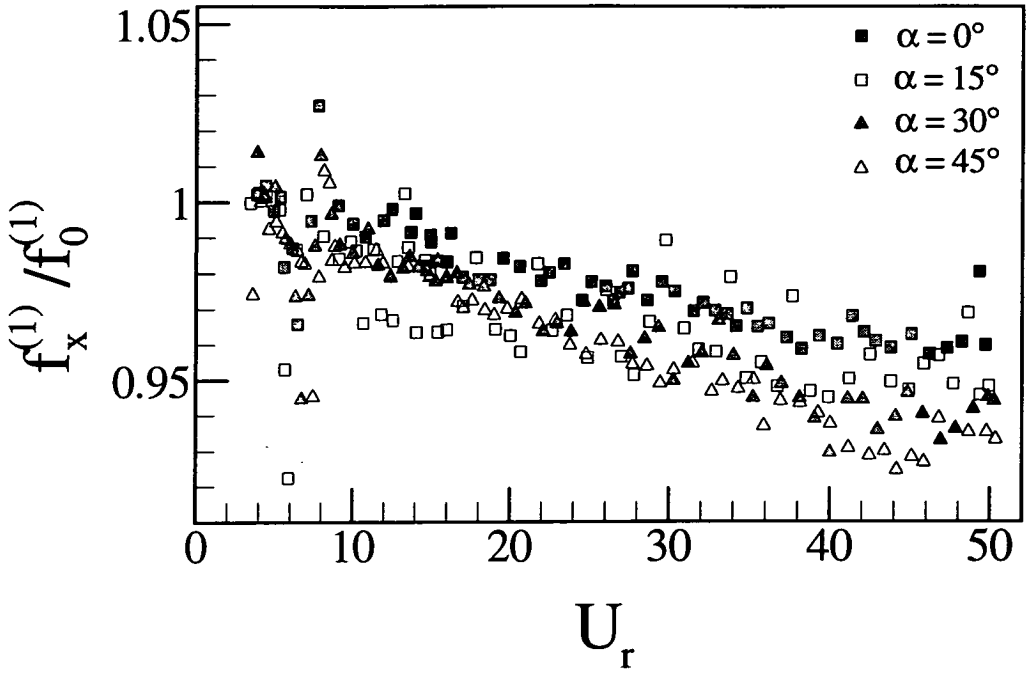

Figure 5-8 Dependence on α and U_r of $f_x^{(1)}$ associated with the square cylinder: ■, $\alpha = 0°$;□, 15°; ▲, 30°; △, 45°.

circular cylinder case is presented in Fig. 5-9a and shows a behaviour similar to the square cylinder. This result agrees with those obtained in Chapters 3 and 4 in the investigations of the interference between two side-by-side circular cylinders. Two factors may cause a variation in the system natural frequencies. Firstly, a theoretical analysis carried out by Xu *et al.* (2001) indicated that an axial force on a cylinder fixed at both ends in a cross flow could lead to an increase in the natural frequency of the fluid-cylinder system. As U_r increases, the static drag arises and subsequently causes a rise in the axial force. Therefore, the system natural frequency could rise. Secondly, it will be shown later in Section 5-6, the first-mode effective damping ratio rise as U_r increases. Zhou *et al.* (2001) carried out a linear analysis of the fluid-cylinder system and the deduced effective damping ratio. The analysis indicated that an increase in fluid damping with increasing U_r could lead to a slowly decreasing natural frequency of the fluid-cylinder system. It seems that, in present

investigations, the second factor is predominant. As a result, the system natural frequency drops, though slightly.

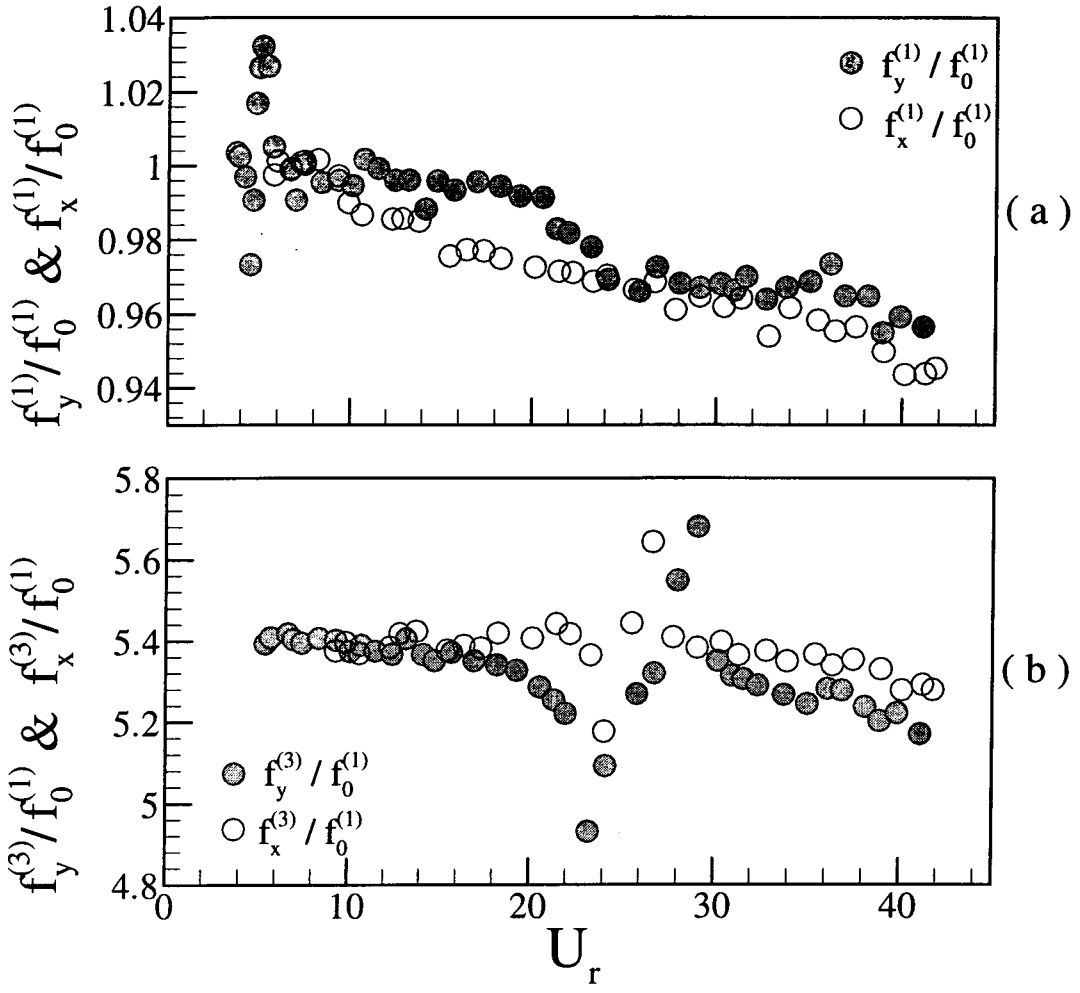

Figure 5-9 Dependence of the system natural frequencies on U_r. Circular cylinder: (a) $f_y^{(1)}$ and $f_x^{(1)}$. (b) $f_y^{(3)}$ and $f_x^{(3)}$.

It is interesting to note that, for all α tested, when resonance occurs near $U_r \approx 7.5$, $f_y^{(1)}/f_0^{(1)}$ and $f_x^{(1)}/f_0^{(1)}$ fall off sharply and then increase to a value above $f_0^{(1)}$. The variation is within $\pm 0.05 f_0^{(1)}$ in both x and y directions. A similar observation is made for the circular cylinder (Fig. 5-9a), that is, there is a rapid variation in $f_y^{(1)}/f_0^{(1)}$ and $f_x^{(1)}/f_0^{(1)}$ when the first-mode resonance occurs near $U_r \approx 4.2$. The sharp variation in $f_y^{(3)}/f_0^{(1)}$ and $f_x^{(3)}/f_0^{(1)}$ also occurs near the third-mode

resonance. It shows about 11% variation in $f_y^{(3)}/f_0^{(1)}$ (Fig. 5-10) and $f_x^{(3)}/f_0^{(1)}$ (Fig. 5-11) between U_r = 27 ~ 48 for the square cylinder and between U_r = 20 ~ 30 for the circular cylinder (Fig. 5-9b). The sharp variation does not occur at the same U_r for different α, apparently linked to the occurrence of the resonance (Fig. 5-2a), as discussed in Section 5-4.

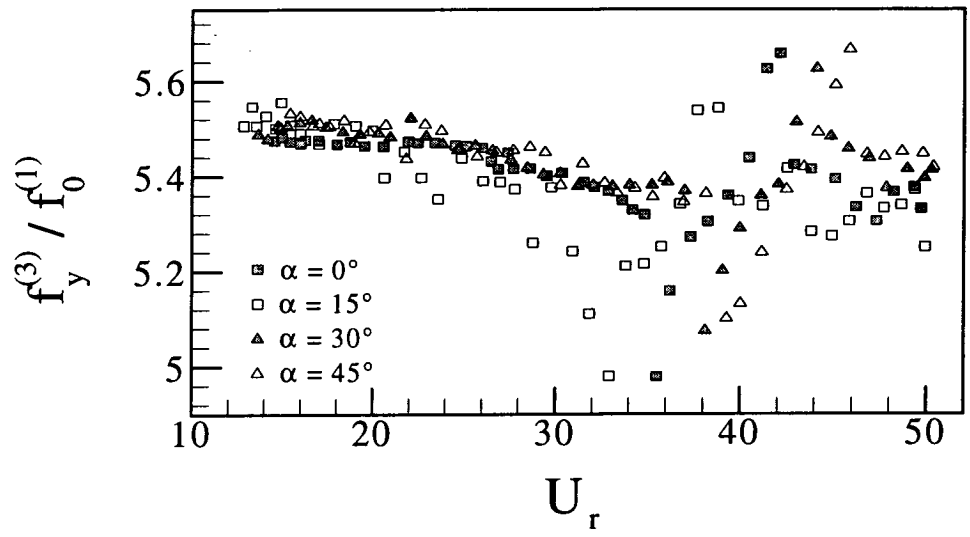

Figure 5-10 Dependence on α and U_r of $f_y^{(3)}$ associated with the square cylinder: ■, α = 0°; □, 15°; ▲, 30°; △, 45°.

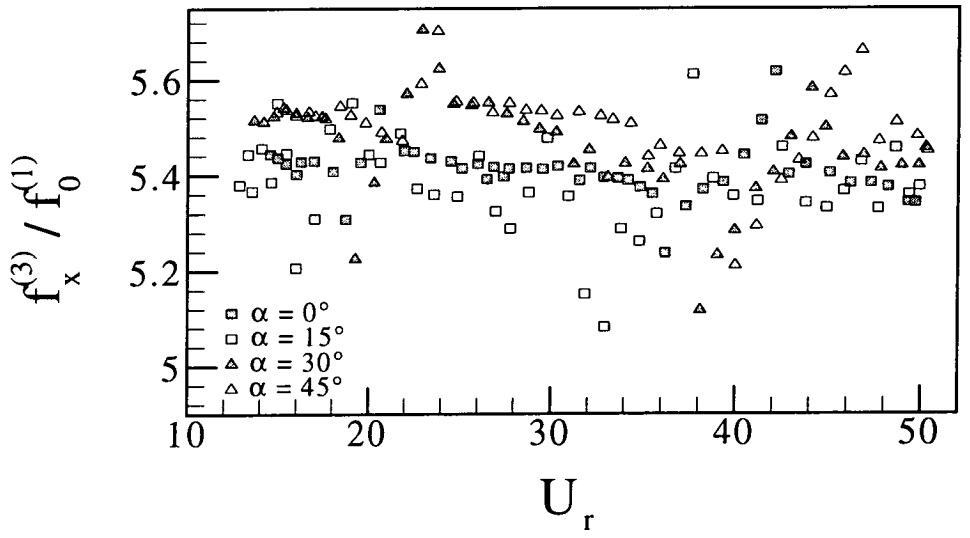

Figure 5-11 Dependence on α and U_r of $f_x^{(3)}$ associated with the square cylinder: ■, α = 0°; □, 15°; ▲, 30°; △, 45°.

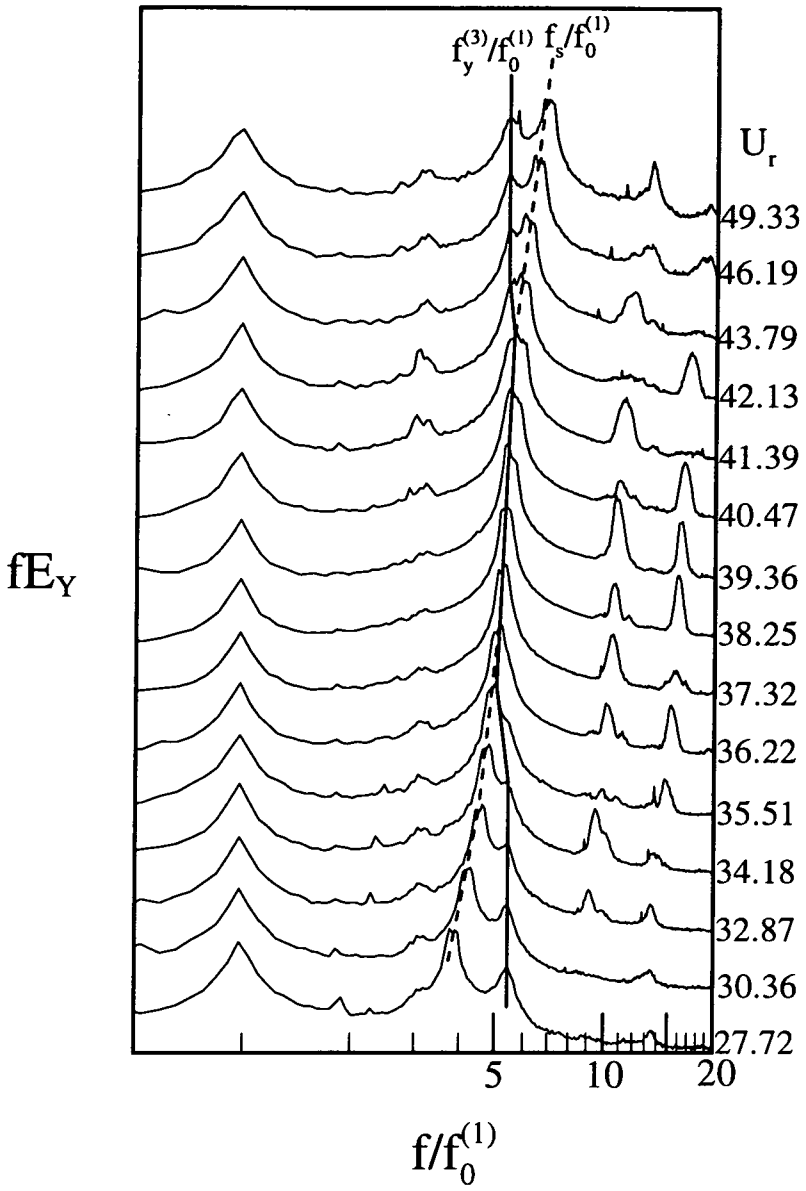

Figure 5-12 Power spectra for a range of U_r (square cylinder, $\alpha = 0°$). The lines are drawn to highlight the trend.

When a structure is forced to vibrate in a cross flow, the so-called lock-in phenomenon occurs as the vortex shedding frequency is coincident with the frequency of the external excitation force. It has been discussed in Chapters 3 and 4 that, for free vibration, it is the vortex shedding that excites the structure. In other words, the vortex-induced force dominates. To illustrate this, the *Y*-spectra of the square cylinder at $\alpha = 0°$ are presented in Fig. 5-12 for selected U_r values.

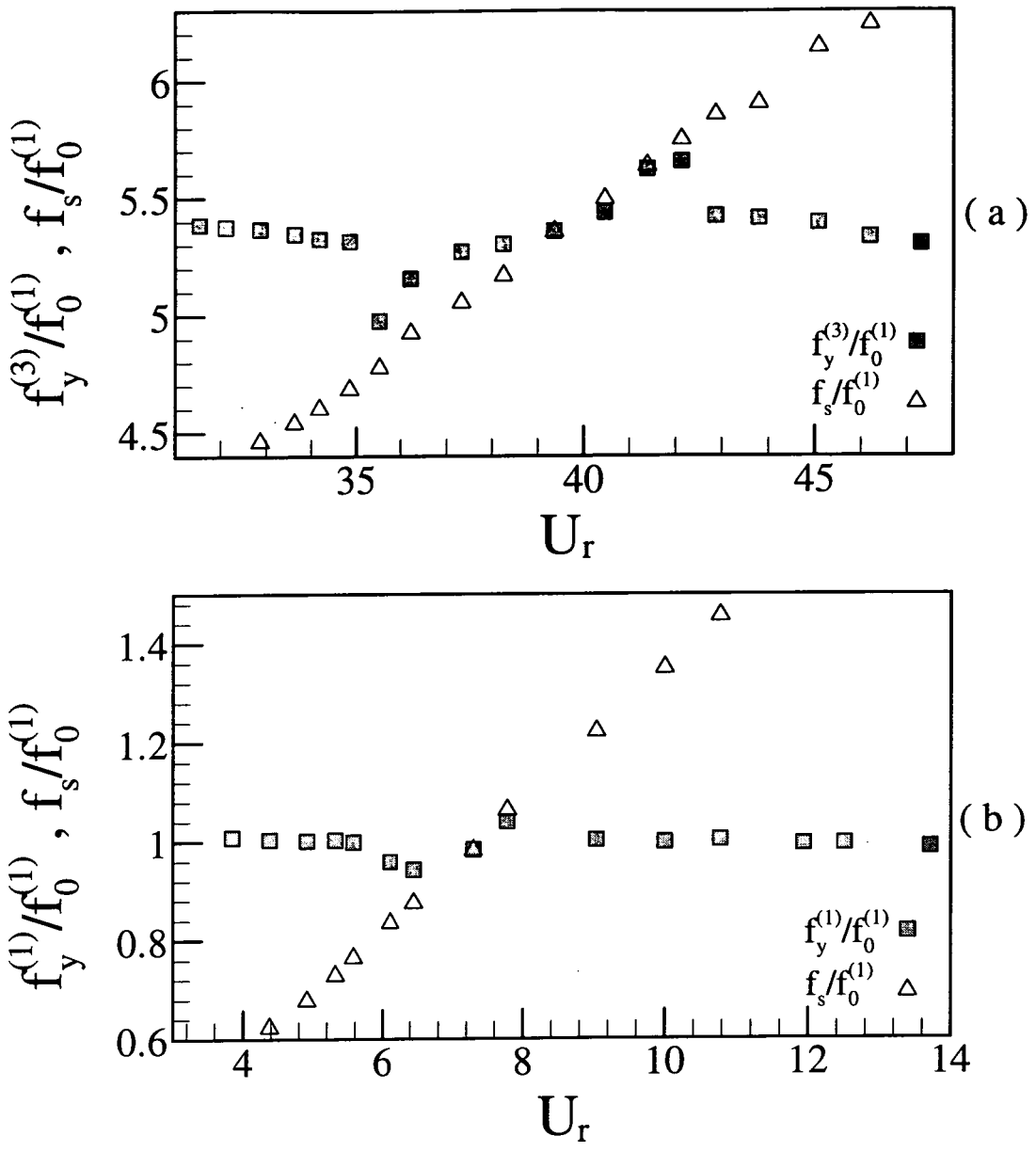

Figure 5-13 Variation of the system natural frequency (■) and the vortex shedding frequency (△) with U_r around resonance (square cylinder, α = 0°): (a) $f_y^{(3)}$ and f_s; (b) $f_y^{(1)}$ and f_s.

Evidently, the third-mode system natural frequency appears varying as the vortex shedding frequency approaches, whereas the vortex shedding frequency does not seem to be affected by the system natural frequency. This point is further highlighted in Fig. 5-13a, which compares the variation of $f_s / f_0^{(1)}$ with that of $f_y^{(3)} / f_0^{(1)}$ near the third-mode resonance. At U_r = 35.0, $f_s / f_0^{(1)}$ and $f_y^{(3)} / f_0^{(1)}$ are close enough to interact with each other and the resonance starts to occur. Influenced

by the relatively small value of $f_s / f_0^{(1)}$ = 4.7, $f_y^{(3)} / f_0^{(1)}$ drops from 5.3 to 4.96, approaching $f_s / f_0^{(1)}$. Note that $f_s / f_0^{(1)}$ remains linear with respect to U_r, implying that $f_y^{(3)}$ imposes little influence on f_s. Such interplay between f_s and $f_y^{(3)}$ continues until they are identical or synchronise at U_r = 39.5. As $f_s / f_0^{(1)}$ further increases with increasing U_r, $f_y^{(3)} / f_0^{(1)}$ follows $f_s / f_0^{(1)}$ till eventually $f_s / f_0^{(1)}$ and $f_y^{(3)} / f_0^{(1)}$ are de-coupled from each other at $U_r \approx 42.0$. The interaction between f_s and $f_y^{(1)}$ near the first-order resonance (Fig. 5-13b) is quite similar to that described above for $f_y^{(3)}$ and f_s. Clearly, vortex shedding dominates the non-linear interaction between the fluid excitation force and the structural vibration in the free vibration case, thus tuning the natural frequency of the system to the vortex shedding frequency. This observation contrasts with the lock-in phenomenon where the vortex shedding frequency is dictated by the forced vibration frequency of the cylinder. Similar behaviour also exists for the circular cylinder, as well as for the case of two side-by-side elastic cylinders (Chapter 3 and 4). Note that the third-mode system natural frequency varies over a larger U_r range than the first-mode one probably because the third-mode resonance occurs at a higher U_r than that of the first-mode resonance. The fluid excitation energy, proportional to U_r^2, is therefore by far greater.

In the square cylinder case, $f_x^{(3)} / f_0^{(1)}$ also shows a sharp variation at U_r in the range 17.1 ~ 22.1, 15.4 ~ 20.0, 17.3 ~ 24.9 and 18.4 ~ 24.8, corresponding to α = 0°, 15°, 30° and 45°, respectively (Fig. 5-11). Spectral analysis (not shown) confirms the occurrence of resonance where the fluctuating drag frequency, i.e. double vortex shedding frequency, coincides with the third-mode natural frequency

of the system. Consequently, $f_x^{(3)}/f_0^{(1)}$ is modified. However, $f_x^{(3)}/f_0^{(1)}$ associated with the circular cylinder fails to exhibit such sharp variation, albeit coincident with the fluctuating drag frequency near $U_r \approx 13$. This is probably because the resonance where $f_x^{(3)} = 2f_s$ occurs at a smaller U_r for the circular cylinder. Flow excitation energy is therefore much smaller than that associated with the square cylinder.

In summary, the natural frequency of the fluid-cylinder system may vary. The variation associated with the square cylinder shows resemblance in major characteristics to that associated with the circular cylinder, suggesting an independence of the nature (fixed or oscillating) of the flow separation.

5.6 Effective Damping Ratios

Damping models the energy dissipation of a dynamic system during vibrations; it contains an important piece of information related to motion-dependent fluid forces. Any measurements of flow-induced vibrations with no estimates of damping can only provide limited indications about fluid forces (Granger *et al.* 1993). The effective damping ratio of a fluid-cylinder system is made up of the fluid damping and the structural damping. The free vibration of an elastic structure includes multiple modes (So *et al.* 2000b). The natural frequencies corresponding to these modes may be associated with different effective damping ratios. Using the ARMA modelling technique, the effective modal damping ratios have been deduced from the measured strain signals obtained from two side-by-side elastic circular cylinders in a cross-flow (Chapter 3). In this chapter, the same technique is used to evaluate effective modal damping ratios based on the derived displacement signals from the square cylinder.

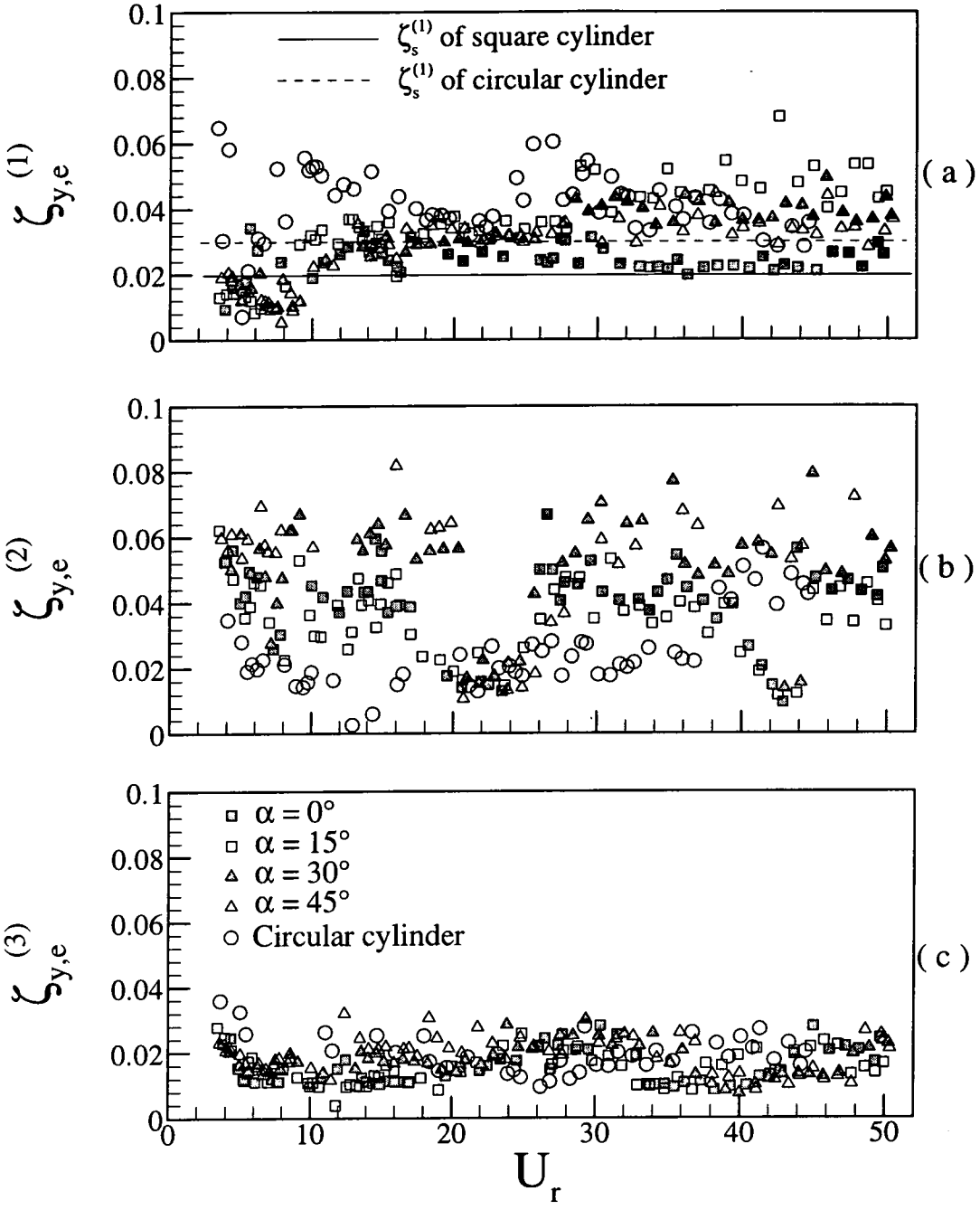

Figure 5-14 Cross-flow effective damping ratios of the fluid-cylinder system. (a) $\zeta_{y,e}^{(1)}$; (b) $\zeta_{y,e}^{(2)}$; (c) $\zeta_{y,e}^{(3)}$. ■, $\alpha = 0°$; □, $\alpha = 15°$; ▲, $\alpha = 30°$; △, $\alpha = 45°$; ○, circular cylinder; —, $\zeta_s^{(1)}$ (square cylinder of $\alpha = 0°$); ---, $\zeta_s^{(1)}$ (circular cylinder).

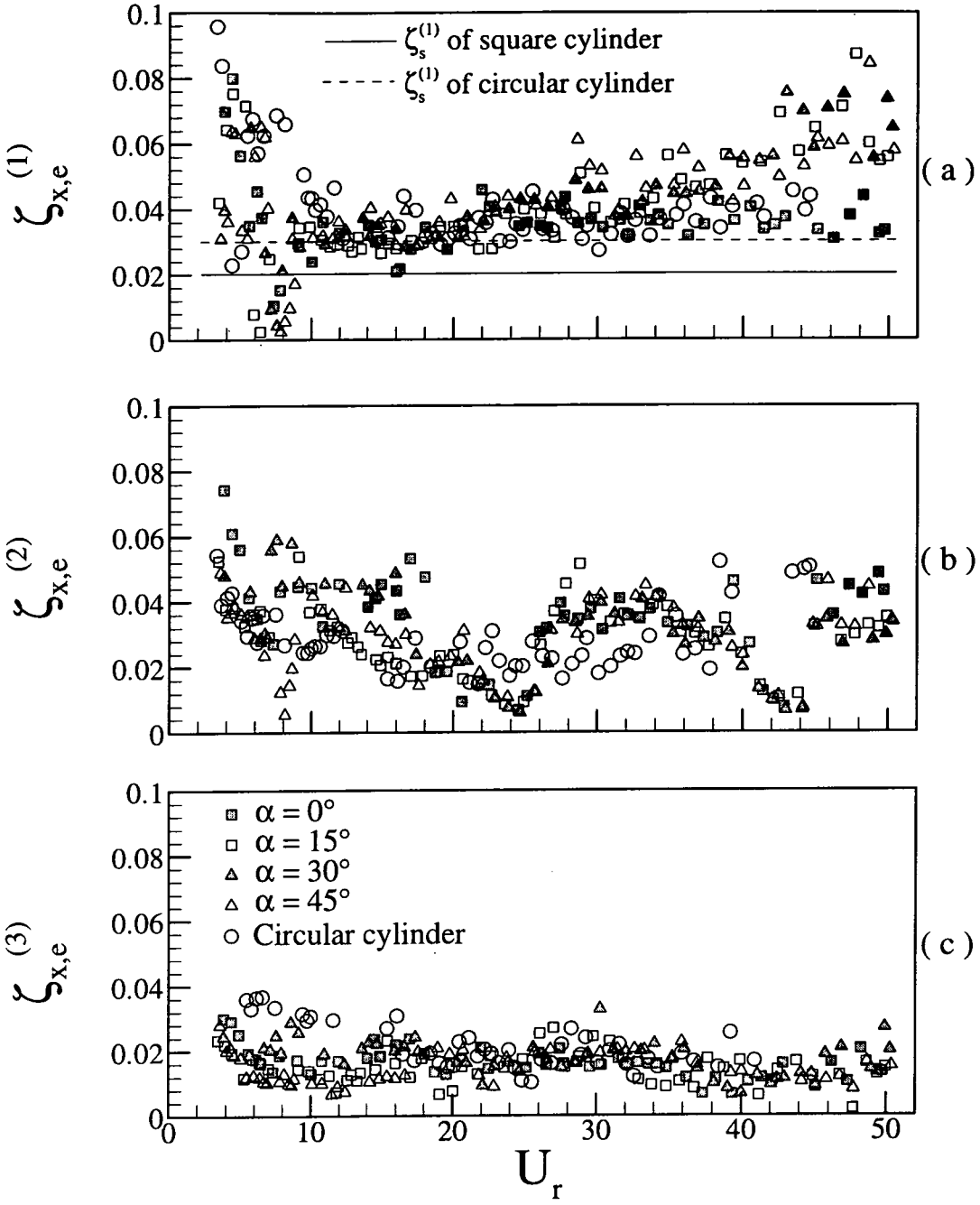

Figure 5-15 Inline effective damping ratios of the fluid-cylinder system. (a) $\zeta_{x,e}^{(1)}$; (b) $\zeta_{x,e}^{(2)}$; (c) $\zeta_{x,e}^{(3)}$. ■, $\alpha = 0°$; □, $\alpha = 15°$; ▲, $\alpha = 30°$; △, $\alpha = 45°$; ○, circular cylinder; —, $\zeta_s^{(1)}$ (square cylinder of $\alpha = 0°$); ---, $\zeta_s^{(1)}$ (circular cylinder).

Figure 5-14 presents the effective modal damping ratios along the *y*-direction, i.e. $\zeta_{y,e}^{(1)}, \zeta_{y,e}^{(2)}$ and $\zeta_{y,e}^{(3)}$ corresponding to $f_y^{(1)}, f_y^{(2)}$ and $f_y^{(3)}$, respectively. These ratios were calculated from the *Y* signal of the square cylinder. The ratios $\zeta_{x,e}^{(1)}, \zeta_{x,e}^{(2)}$ and $\zeta_{x,e}^{(3)}$ along the *x*-direction are given in Fig. 5-15.

A few observations can be made based on Figs. 5-14 and 5-15. Firstly, the effective damping ratio approaches zero when resonance occurs. Both $\zeta_{y,e}^{(1)}$ and $\zeta_{y,e}^{(2)}$ (also $\zeta_{x,e}^{(1)}$ and $\zeta_{x,e}^{(2)}$) decrease sharply near $U_r \approx 7.5$ and $U_r \approx 23.4$ for all α tested, approaching zero. Evidently, the fluid damping ratio is negative at resonance, in agreement with the measurement in Chapter 3. Note that $\zeta_{y,e}^{(3)}$ and $\zeta_{x,e}^{(3)}$ dip near $U_r \approx 40$ due to the occurrence of the third-mode resonance.

Secondly, $\zeta_{x,e}^{(1)}$ is generally larger than $\zeta_{y,e}^{(1)}$ for $U_r < 12$, implying larger fluid damping. This observation agrees with Granger *et al.* (1993)'s report for a small gap flow velocity. Based on a linear assumption that the structural vibration velocity is small relative to the free stream velocity, Blevins (1994)'s analysis indicated that the inline fluid damping was twice that of the cross-flow direction for a fluid-cylinder dynamic system. The analysis is expected to be valid for small U_r only. When $12 < U_r < 20$, $\zeta_{y,e}^{(1)}$ and $\zeta_{x,e}^{(1)}$ are nearly the same. As U_r further increases, $\zeta_{y,e}^{(1)}$ and $\zeta_{x,e}^{(1)}$ increase. However, $\zeta_{x,e}^{(1)}$ increases faster and becomes larger than $\zeta_{y,e}^{(1)}$. On the other hand, $\zeta_{x,e}^{(2)}$ and $\zeta_{x,e}^{(3)}$ are quite comparable in magnitude with their counterparts in the lift direction, probably due to the relatively small contribution from the fluid damping.

Thirdly, the effective damping ratios $\zeta_{y,e}^{(1)}$ and $\zeta_{x,e}^{(1)}$ at $\alpha = 0°$ are considerably smaller than those at α = 15°, 30° and 45°, especially when $U_r > 28$. For all α

tested, as U_r increases, $\zeta_{y,e}^{(1)}$ and $\zeta_{x,e}^{(1)}$ increase. But $\zeta_{y,e}^{(1)}$ and $\zeta_{x,e}^{(1)}$ increase even faster at $\alpha \neq 0°$ than at $\alpha = 0°$. This may contribute to the observation in Section 5-5 that $f_y^{(1)}/f_0^{(1)}$ and $f_x^{(1)}/f_0^{(1)}$ decrease faster when α is non-zero. The α effect on $\zeta_{y,e}^{(1)}$ and $\zeta_{x,e}^{(1)}$ could be related to the way the flow separates and whether it reattaches. For a square cylinder placed at an incidence angle $\alpha = 0°$, flow separates from the upstream corners and will not reattach on the side surfaces of the cylinder (Nguyen *et al.* 1991; Naudascher *et al.* 1993). When the square cylinder is rotated such as at α = 15°, 30° and 45°, the flow may impinge on the side surface of the cylinder. As a result, the boundary layer may be accelerated, separating from one upstream corner and one trailing corner of the cylinder (Hasan 1989; Chen and Liu 1999). The accelerating boundary layer will result in higher velocity gradient and hence a higher shear stress near the surface of the structure than that at $\alpha = 0°$. Since the fluid damping results from the fluid viscous shearing at the structure surface and flow separation (Blevins 1994), the higher shear stress may induce a higher fluid damping. Therefore, the effective damping ratios associated with a square cylinder at $\alpha \neq 0°$ may increase with the changes of the flow structure.

Fourthly, the first-mode, second-mode and third-mode effective damping ratios range from 0.02 ~ 0.06, 0.01 ~ 0.08 and 0.01 ~ 0.03, respectively, in both the y and x direction. The third-mode ratios are smallest, consistent with the measurement for a circular cylinder (Figs. 5-14 and 5-15). A similar observation has been made in the presence of a neighbouring cylinder (Chapter 3), which has been ascribed to the fact that the third-mode structural damping ratio was appreciably smaller than the first- or second-mode structural damping ratio (Blevins 1975) since the fluid damping ratio is small in the context of airflow. The small $\zeta_{y,e}^{(3)}$ could also partially

contribute to the observation why the third-mode resonance is by far more violent than the first-mode resonance.

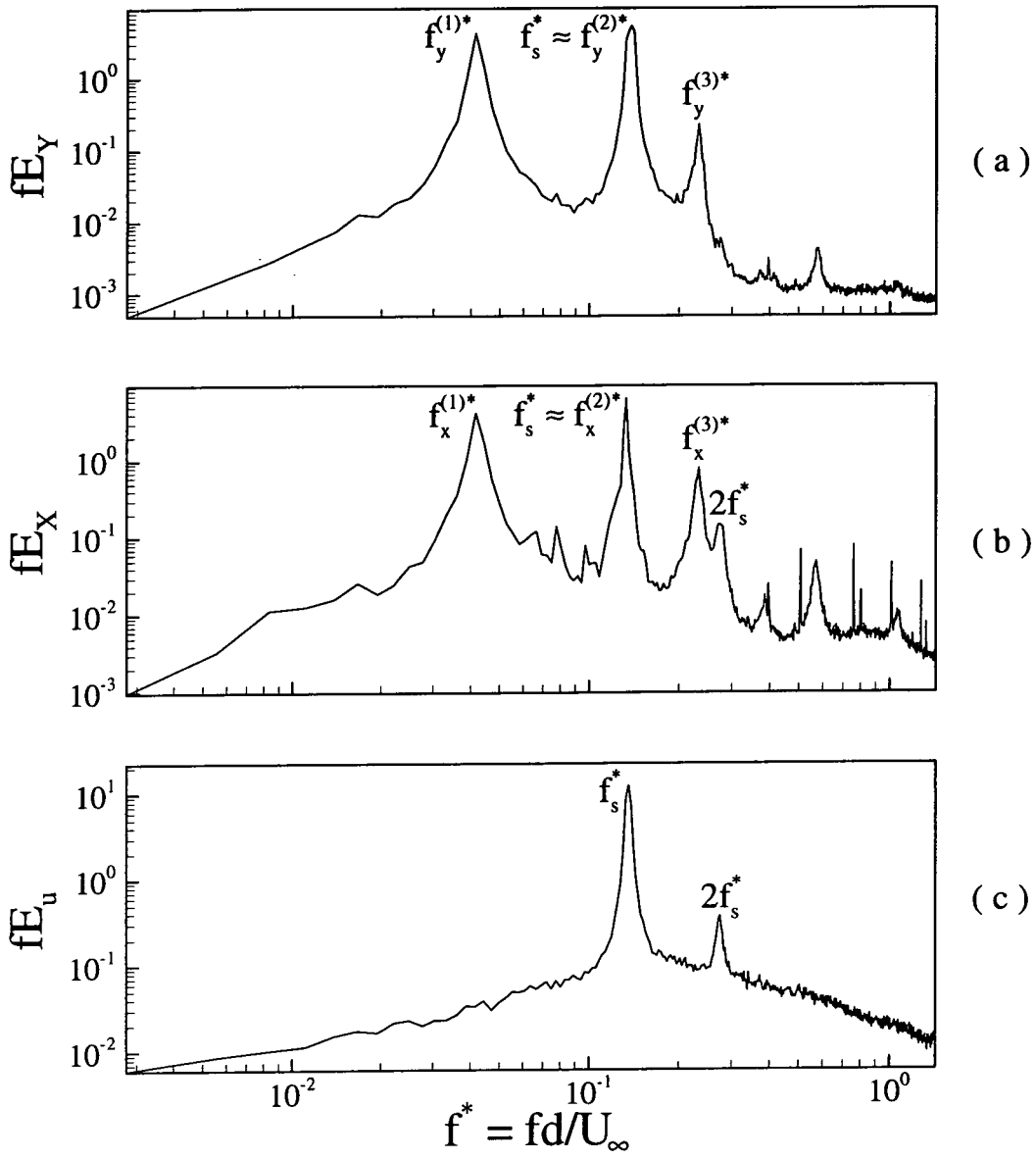

Figure 5-16 (a) Y-spectrum E_Y; (b) X-spectrum E_X; (c) u-spectrum E_u. (Square cylinder, $\alpha = 0°$, $U_r \approx 23.4$. The hot wire was located at $x/d = 2$ and $y/d = 1.5$).

Fifthly, the second-mode effective damping ratios display two troughs near $U_r \approx 20$ and 40, respectively, along both x and y directions. Spectral analysis (not shown) indicates the occurrence of the second-mode resonance and its harmonic at

$U_r \approx 20$ and 40, respectively. Fluid damping ratio will drop when resonance occurs. Away from the resonance, $\zeta_{y,e}^{(2)}$ and $\zeta_{x,e}^{(2)}$ exhibit relatively large scatter. As shown in Fig. 5-2 for the square cylinder, the second-mode resonance fails to show up for any α. The *Y*-spectrum (Fig. 5-16) indicates that even when f_s coincides approximately with $f_y^{(2)}$, the peak at $f_y^{(2)}$ does not appear to be more pronounced than those at $f_y^{(1)}$ and $f_y^{(3)}$. Evidently, the excitation for the second-mode vibration is weak compared to those for the first- or third-mode vibration. Theoretical analysis by Wang *et al.* (2001), who assumed a uniform span-wise excitation force on a cylinder, indicates that the second-mode vibration was not excited. It has been discussed in Chapter 3 that, in a real fluid-cylinder system, the vortices shed from the cylinder are not two-dimensional when *Re* is high; the span-wise extent of two-dimensionality is limited, typically from 1d to 3d (King 1977; Higuchi *et al.* 1989; Zhou and Antonia 1994). This implies a non-uniform excitation force on the cylinder, resulting in the excitation of even mode vibrations (Fig. 5-5). It seems that the excitation due to the three-dimensionality of vortices is small compared with that exciting the odd mode vibrations. Therefore, even mode resonance should be much weaker in strength than the odd mode resonance. As a result, uncertainty in estimating the even mode damping ratios is increased, resulting in relatively large scatter in $\zeta_{y,e}^{(2)}$ and $\zeta_{x,e}^{(2)}$. This uncertainty, however, should decrease at resonance, as indicated by the smaller scattering in the two troughs of $\zeta_{y,e}^{(2)}$ and $\zeta_{x,e}^{(2)}$ (Figs. 5-14b and 5-15b).

Finally, the effective damping ratios rise, though slowly, as U_r increases beyond 15, apparently resulting from the increased fluid damping.

For the purpose of comparison, the effective modal damping ratios of the circular cylinder along the *x*- and *y*-direction were included in Figs. 5-14 and 5-15.

In general, these ratios behave quite similarly to their counterparts of the square cylinder. For example, $\zeta_{y,e}^{(1)}$ approaches zero, below the structural damping ratio $\zeta_0^{(1)}$ (0.03), when the first-mode resonance occurs at the reduced velocity $U_r \approx 4.2$, implying a negative fluid damping. The $\zeta_{y,e}^{(3)}$ value is the smallest among $\zeta_{y,e}^{(1)}$, $\zeta_{y,e}^{(2)}$ and $\zeta_{y,e}^{(3)}$. The similarity could be expected since, as the resonance occurs, the flow separation from the circular cylinder is likely to be more two-dimensional, approaching the square cylinder case.

5.7 Conclusions

The effect of fixed and oscillating flow separation points on fluid-structure interactions was experimentally investigated. Flow field and structural vibration of a square cylinder, fixed at both ends, in a uniform cross-flow were measured simultaneously using a hot wire and fibre-optic Bragg grating sensors. The measurement is compared with that obtained for a circular cylinder of the same hydraulic diameter and installation conditions. The following conclusions can be drawn.

1. The vibration amplitude Y_{rms} of the square cylinder at $\alpha = 0°$ increases with U_r and displays two peaks at $U_r \approx 7.5$ and $U_r \approx 40$, respectively. The peaks were confirmed arising from the excitation of the first- and third-mode resonance. When the square cylinder was rotated, the two modes of resonance were again excited, though at slightly different U_r values because of variation in the vortex shedding frequency at different α. On the other hand, three peaks in Y_{rms} were discernible at $U_r \approx 4.2$, 11.0 and 26.0 for the circular cylinder and were identified with the excitation of the first-, second- and third-mode

resonance. The occurrence of the second-mode resonance is linked to the oscillation of the flow separation point associated with the circular cylinder. The oscillation is unlikely to be spanwise uniform, thus inducing the three dimensionality of the vortex shedding and generating the excitation force for the second-mode vibration.

2. For both cylinders, the peak in Y_{rms} due to the third-mode resonance is by far more pronounced than the others. The maximum vibration amplitude at the third-mode resonance for the square cylinder doubles that for the circular cylinder even though the square cylinder has a larger flexural rigidity. This could be attributed to two reasons. Firstly, galloping, which is coupled with the resonance, could occur for non-circular cross-section cylinders, thus feeding additional energy into the resonating system. Secondly, the oscillation of the flow separation point associated with a circular cylinder is unlikely to be spanwise in-phase. This will weaken the excitation force upon the structure, as compared with the spanwise in-phase shedding of vortex rolls in the square cylinder case.

3. The system natural frequencies slowly decrease as U_r increases except near resonance where a sudden variation occurs, up to about 10% of the structural natural frequency. The slow variation could be partially due to an increase in the structural axial loading, which is caused by increasing static drag, and partially due to an increase in fluid damping. The latter factor is predominant in present investigation. Therefore, the system natural frequency drops, though slightly. On the other hand, the sudden variation is dictated by the vortex shedding frequency. The observation is made for both cylinders, suggesting the independence of the nature (fixed or oscillating) of the flow separation point.

4. The effective damping ratios approach zero when resonance occurs at $U_r \approx$ 7.5, 21.5 and 40 for all α tested, implying a negative fluid damping. Among the effective damping ratios corresponding to the first- second- and third-mode system natural frequencies, the third-mode ratio is the smallest. Similar phenomena also exist in the circular cylinder case, indicating that it is also independent of whether the flow separation point is fixed or moving. The first-mode effective damping ratio associated with a square cylinder at $\alpha = 0°$ is smaller than that at $\alpha \neq 0°$, especially when $U_r > 28$. This is likely due to the impingement of the flow on the side walls at non-zero α, which is associated with a higher velocity gradient and hence a higher shear stress near the surface of the structure than that at $\alpha = 0°$, thus resulting in higher fluid damping.

CHAPTER 6

SUMMARY AND CONCLUSIONS

(1) Vortex Streets Behind Two Side-by-Side Cylinders

The flow behind two side-by-side circular cylinders subjected to a uniform cross-flow has been experimentally studied. Experiments were performed in a water tunnel and a closed circuit wind tunnel. Three typical *T/d* values, i.e. 3.00, 1.70 and 1.13, were investigated. At *T/d* = 3.00, two vortex streets were observed behind the cylinders. The two streets were predominantly symmetrical about the flow centreline. On the other hand, the anti-symmetrical configuration was also observed from time to time.

At *T/d* = 1.70, the gap flow between the cylinders was deflected, resulting in one narrow and one wide wake behind the cylinders. It was found that the two opposite-signed vortices in the narrow wake were typically engaged in pairing, creating a relatively low-pressure region between them and drawing in the gap vortex in the wide wake. The amalgamation of the three vortices could be at least partially responsible for the stably deflected gap flow. Two dominant frequencies, i.e. $f^* \approx 0.1$ and 0.3, were detected in the outer shear layer associated with each cylinder. The two frequencies were also identifiable in the narrow wake, but the lower frequency 0.1 only was detected in the wide wake. It was found that the secondary vortices in the shear layer coalesced to form large-scale vortices, which were shed in the narrow wake at $f_s^* \approx 0.1$, coinciding with the rolling-up frequency of the vortical structures in the wide wake. It has been proposed that vortex frequency in the wide wake is dictated by the shear layer thickness. This frequency

could feed back upstream to excite the shear layer instability and further induce the vortex shedding in the narrow wake. On the other hand, the amalgamation of the three vortices in the narrow wake involves a reduced lateral spacing between the structures, producing the frequency 0.3 in the hot-wire spectrum. The upstream influence of this frequency could excite the shear layer instability, thus resulting in a dominant frequency at $f^* \approx 0.3$. The flow visualization data suggests that the gap vortices in the narrow and wide wakes are generally in antiphase, but the one in the wide wake leads slightly that in the narrow wake and amalgamates with the pairing vortices in the narrow wake. The changeover of the gap flow deflection starts with a phase lag of the gap vortex in the wide wake behind that in the narrow wake, thus making it difficult to proceed for the gap vortex in the wide wake to amalgamate with the pairing vortices in the narrow wake. Consequently, the stability of the gap flow deflection was affected; the gap vortex grows unusually large but quickly collapses because of the increased interaction with the narrow wake. The collapse give rise to a momentarily weak interaction between the two wakes, thus allowing the narrow wake to expand laterally. The process was repeated for a few vortex-shedding cycles and eventually the narrow wake pushes the gap flow to the other side and completes the changeover.

For small cylinder spacing, $T/d = 1.13$, there are no gap vortices generated and the vortices are shed only from the free-stream side of the two cylinders, resulting in a single vortex street. This flow was asymmetrical about the centreline in terms of the mean velocity and Reynolds stresses under the effect of the biased gap bleeding between the cylinders. When the bleeding was biased towards one cylinder, vortices were shed alternately from the free-stream side of the two cylinders; when unbiased, the symmetric vortex shedding occurred, though unstable and quickly reverting to alternate shedding. The bleeding is invisible at about $x/d = 5$. Its effect

however persists, giving rise to the asymmetrical distributions of the mean velocity and Reynolds stresses at least up to x/d = 10. The observation is in marked contrast with the single cylinder case, where vortices are always shed alternately from the cylinder.

(2) Free Vibrations of Two Side-by-Side Cylinders in a Cross Flow

Fluid-structure interactions of two side-by-side elastic cylinders with fixed support at both ends placed in a cross-flow were experimentally investigated using FBG sensor, flow visualization and hot wire technique. Three identical T/d ratios with (1) were investigated. It was found that the structural vibration behaviour is closely linked to the flow characteristics. At T/d = 3.00, the spectral phase shift Φ_{12} between the vibrations of the two cylinders is $\pm\pi$, in consistent with previously reported results that vortex pairs are symmetrically formed and shed from the two cylinders for a sufficiently large cylinder spacing. Accordingly, the two vortex streets immediately behind the cylinders are predominantly in the anti-phase mode, in addition, this finding is found to be independent of Re. As T/d reduces to 1.70, one narrow and one wide wake were observed and the corresponding normalized dominant frequencies, as seen from velocity spectra, were 0.31 and 0.105, respectively. Flow visualization results suggest that vortices are shed from both sides of each cylinder at the same frequency, i.e. $f_s^* \approx 0.1$, while the normalized frequency 0.31 could be ascribed to the amalgamation of the two paring vortices in the narrow wake and the gap vortex in the wide wake. This result is in consistent with (1). At T/d = 1.13, Φ_{12} is generally near zero, indicating a dominance by the alternate vortex shedding.

Vibration characteristics of the elastic cylinders contrast distinctly with those of rigid ones. At T/d = 3.00, the occurrence of the first-, second- and third-mode resonance were identified in present investigations. The third-mode resonance is far more violent due to the combined effect of higher flow energy, smaller effective damping ratio, and synchronization of vortex shedding with the fifth harmonic of $f_y^{(1)}$. The inline vibration appears to be far less violent for the third-mode resonance than the cross-flow one. When $T/d < 3.00$, the vibration is suppressed because of the weakening strength of the vortices.

It is found that the characteristics of the system modal damping ratios, including both structural and fluid damping, and natural frequencies depend on T/d and vary slowly with U_r as a result of fluid-structure interactions. The natural frequencies of the combined fluid-cylinder system experience a rather sudden variation, up to 10%, near resonance. The variation always displays the pattern of a dip followed by a rise, indicates that, in the free vibration case, when the vortex shedding and system natural frequency components approach each other, the system natural frequency is modified so as to adapt to the vortex shedding frequency. This observation contrasts with the lock-in phenomenon where the vortex shedding frequency is tuned to the forced vibration frequency of a cylinder. Furthermore, the cross-flow natural frequencies of the system increase when the transverse spacing ratio is decreased. The observed increase in the repulsive force between the cylinders as they approach each other could be seen as an increase in fluid stiffness, thus causing a rise in the cross-flow natural frequency of the system. This behaviour of the system natural frequencies persists even in the case of the single cylinder and does not seem to depend on the interference between cylinders. In addition, the natural frequencies of the fluid-cylinder system appear decreasing, albeit slowly, as U_r increases, which could be partially attributed to the increased fluid damping as U_r

increases. The first-mode effective damping ratios $\zeta_{y,e}^{(1)}$ approach zero when resonance occurs near $U_r \approx 11$ for $T/d = 1.13$ and near $U_r \approx 4.2$ for $T/d = 3.00$, so is $\zeta_{y,e}^{(3)}$ near $U_r \approx 26$, thus indicating negative fluid damping. For relatively large U_r (> 15), the ratios are quite comparable in the lift and drag directions, probably the result of a small fluid damping in the present investigation. The cross-flow fluid damping becomes significant at $T/d = 1.13$, accounting for about one half of the effective damping. The third-mode effective damping ratio $\zeta_{y,e}^{(3)}$ is appreciably smaller than that corresponding to the first- or second-mode. This can be attributed to a substantial decrease of the structural damping ratios for higher modes of vibrations.

(3) Vortex-Induced Vibration Characteristics of Two Fix-Supported Elastic Cylinders

The interference effects on structural dynamics and vibration characteristics of two fix-supported side-by-side elastic cylinders were experimentally investigated using two FBG sensors, a Polytec Series 3000 Dual Laser Beam Vibrometer and a single hot wire. Three identical transverse spacing ratios as mentioned in (1) and (2), $T/d = 3.00$, 1.70 and 1.13, were investigated. The FBG sensor was successfully extended to measure the dynamic strain due to the drag for a single cylinder. The strain-displacement relation is linear in the U_r range investigated. This linear relation is expected to extend well beyond the linear range ($U_r < 22$), as reported for the lift direction, in view of the substantially weaker vibration in the drag direction. The linear relation remains valid in the case of two side-by-side cylinders, but the slope changes with T/d. The establishment of the linear relation between strain and bending displacement facilitates the interpretation of the measured strain data.

At T/d = 3.00, the characteristics of the structural vibration resemble the case of an isolated cylinder, implying little interference. The correlation coefficient ρ_{12} between ε_{x1} and ε_{x2} generally approaches zero, except near resonance where the vortex shedding frequency coincides with the system natural frequencies. The value of ρ_{12} between ε_{y1} and ε_{y2} is mostly negative and can go beyond – 0.5 near resonance, implying opposite movement of the two cylinders, in consistent with previous result in (1) and (2) that vortices shed from the two cylinders are predominantly in an antiphase mode. As the two cylinders approach each other, T/d = 1.70, the strength of the vortices is drastically weakened due to interactions between the flow around individual cylinders. Consequently, resonance is suppressed, suggesting an enhanced stability. The fluid dynamics around one cylinder is very different from that around its neighbour at this T/d. As a result, the natural frequencies of the combined fluid-cylinder systems, associated with each individual cylinder exhibit an appreciable difference of about 5%. When T/d is further reduced to 1.13, the structural vibration in the lift direction is significantly suppressed due to the repulsive force between the two cylinders, whereas the drag direction vibration is virtually unaffected by the neighbouring cylinder. Consequently, the drag direction vibration appears dominating. The correlation coefficient ρ_{12} is positive and increases appreciably, compared with its corresponding value for the T/d = 1.70 or 3.00, in both cross-flow and streamwise directions. Evidently, the two cylinders tend to couple together like a single structure. However, there is one important difference between one isolated cylinder and the two side-by-side cylinders at small T/d. In the former case, the drag force fluctuates twice as fast as the lift force, while in the latter case the fluctuating frequency of the two forces is identical since vortices are shed from the free-stream side of the two cylinders only. Consequently, resonance occurs simultaneously in both lift and drag directions.

(4) Flow Separation Effect on a Freely Vibrating Cylinder

Flow field and structural vibration of an elastic square cylinder, associated with fixed flow separation points, fixed at both ends, in a uniform cross-flow were simultaneously measured using hot wire and FBG sensors. The measurement is compared with that obtained for a circular cylinder, from which the flow separation points keep moving when the boundary layer is separated, of the same hydraulic diameter and installation conditions, in an effort to understand the effect of the nature of flow separation on fluid-structure interactions. In square cylinder case, the vibration amplitude increases with U_r and displays two peaks arising from the excitation of the first- and third-mode resonance, though at slightly different U_r values for different α because of variation in the vortex shedding frequency. On the other hand, three peaks in Y_{rms} were discernible for the circular cylinder, corresponding to the occurrence of the first-, second- and third-mode resonance, respectively. The occurrence of the second-mode resonance is linked to the oscillation of the flow separation point associated with the circular cylinder. The oscillation is unlikely to be spanwise uniform, thus inducing the three dimensionality of the vortex shedding and generating the excitation force for the second-mode vibration. Furthermore, the maximum vibration amplitude at the third-mode resonance for the square cylinder doubles that for the circular cylinder even though the square cylinder has a larger flexural rigidity. This could be attributed to two reasons. Firstly, galloping, which is coupled with the resonance, could occur for non-circular cross-section cylinders. Secondly, the oscillation of the flow separation point associated with a circular cylinder is unlikely to be spanwise in-phase, which will weaken the excitation force upon the structure. In addition, the first-mode effective damping ratio associated with a square cylinder at $\alpha = 0^{\circ}$ is smaller than

that at $\alpha \neq 0^{\circ}$, especially when $U_r > 28$. This is due to the impingement of the flow on the side walls at non-zero α, which is associated with a higher velocity gradient and hence a higher shear stress near the surface of the structure than that at $\alpha = 0^{\circ}$, thus resulting in higher fluid damping.

It is found that the system natural frequencies slowly decrease as U_r increases except near resonance where a sudden variation occurs, up to about 10% of the structural natural frequency. The slow variation could be partially due to an increase in the structural axial loading and partially due to an increase in fluid damping. The latter factor is predominant in present investigation. Therefore, the system natural frequency drops, though slightly. On the other hand, the sudden variation of the system natural frequency is dictated by the vortex shedding frequency. In either circular cylinder or square cylinder cases, the effective damping ratios approach zero when resonance occurs, implying a negative fluid damping. Among the effective damping ratios corresponding to the first- second- and third-mode system natural frequencies, the third-mode ratio is the smallest. These observations are made for both cylinders, suggesting the independence of the nature (fixed or oscillating) of the flow separation point.

References

Achenbach, E. 1968 Distribution of local pressure and skin friction around a circular cylinder in a cross-flow up to $Re = 5\times10^6$. *Journal of Fluid Mechanics* **34**(4), 625-639.

Achenbach, E. and Heinecke, E 1981 On vortex shedding from smooth and rough cylinders in the range of Reynolds numbers 6×10^3 to 5×10^6. *Journal of Fluid Mechanics* **109**, 239-251.

Andjelic, M. and Popp, K. 1989 Stability effects in a normal triangular cylinder array. *Journal of Fluids and Structures* **3**, 165-185.

Antonia, R.A. and Fulachier, L. 1989 Topology of a turbulent boundary with and without wall suction. *Journal of Fluid Mechanics* **198**, 429-451.

Baban, F. and So, R. M. C. 1991 Recirculating flow behind and unsteady forces on finite-span circular cylinders in a cross-flow. *Journal of Fluids and Structures* **5**, 185-206.

Baban, F., So, R. M. C. and Otugen, M. V. 1989 Unsteady forces on circular cylinders in a cross-flow. *Experiments in Fluids* **7**, 293-302.

Bearman, P. W. and Obasaju, E. D. 1982 An experimental study of pressure fluctuations on fixed and oscillating-square section cylinders. *Journal of Fluid Mechanics* **119**, 297-321.

Bearman, P. W. and Wadcock, A. J. 1973 The interference between a pair of circular cylinders normal to a stream. *Journal of Fluid Mechanics* **61**, 499-511.

Biermann, D. and Herrnstein, W. H., Jr. 1933 The interference between struts in various combinations. National Advisory Committee for Aeronautics, Technical Report Number 468.

Bisset, D. K., Antonia, R. A. and Britz, D. 1990 Structure of large-scale vorticity in a turbulent far wake. *Journal of Fluid Mechanics* **218**, 463-482.

Blackburn, H. M. and Melbouren, W. H. 1996 The effect of free-stream turbulence on sectional lift forces on a circular cylinder. *Journal of Fluid Mechanics* **306**, 267-292.

Blevins, R. D. 1975 Vibration of a loosely held tube. *Journal of Engineering for Industry* **97**, 1301-1304.

Blevins, R. D. 1994 *Flow-induced vibration*. Krieger Publishing Company, Malabar, Florida, USA.

Blevins, R. D. and Burton, T. E. 1976 Fluid forces induced by vortex shedding. *Journal of Fluids Engineering* **98**, 19-26.

Bloor, M. S. 1964 The transition to turbulence in the wake of a circular cylinder. *Journal of Fluid Mechanics* **19**, 290-304.

Bokaian, A. R. and Geoola, F. 1984a Hydroelastic instabilities of square cylinders. *Journal of Sound and Vibration* **92**(1), 117-141.

Bokaian, A. and Geoola, F. 1984b Wake-induced galloping of two interfering circular cylinders. *Journal of Fluid Mechanics* **146**, 383-415.

Bokaian, A. and Geoola, F. 1984c Proximity-induced galloping of two interfering circular cylinders. *Journal of Fluid Mechanics* **146**, 417-449.

Brika, D and Laneville, A. 1993 Vortex-induced vibrations of a long flexible circular cylinder. *Journal of Fluid Mechanics* **250**, 481-508.

Brown, G. L. and Roshko, A. 1974 On density effects and large-scale structure in turbulent mixing layers. *Journal of Fluid Mechanics* **64**, 775-816.

Cantwell, B. and Coles, D. 1983 An experimental study of entrainment and transport in the turbulent near wake of a circular cylinder. *Journal of Fluid Mechanics* **136**, 321-374.

Chang, K. S. and Song, C. J. 1990 Interactive vortex shedding from a pair of circular cylinders in a transverse arrangement. *International Journal for Numerical Methods in Fluids* **11**, 317-329.

Chen, J. M. and Liu, C. H. 1999 Vortex shedding and surface pressures on a square cylinder at incidence to a uniform air stream. *International Journal of Heat and Fluid Flow* **20**, 592-597.

Chen, S. S. 1975 Dynamic responses of two parallel circular cylinders in a liquid. *Journal of Pressure and Vessel Technology* **97**, 78-83.

Chen, S. S. 1986 A review of flow-induced vibration of two circular cylinders in crossflow. *Journal of Pressure Vessel Technology* **108**, 382-393.

Chen, S. S. 1987 *Flow-Induced Vibration of Circular Cylindrical Structures.* Hemisphere Publishing Corporation, Washington, USA.

Chen, S. S. and Jendrzejczyk, J. A. 1979 Dynamic response of a circular cylinder subjected to liquid cross flow. *Journal of Pressure Vessel Technology* **101**, 106-112.

Chen, S. S. and Jendrzejczyk, J. A. 1981 Flow velocity dependence of damping in tube arrays subjected to liquid cross flow. *Journal of Pressure Vessel Technology* **103**, 130-135.

Chen, S. S., Zhu, S. and Cai, Y. 1995 An unsteady flow theory for vortex-induced vibration. *Journal of Sound and Vibration* **184**, 73-92.

Chen, Y. N. 1972a Fluctuating lift forces of Karman vortex streets on single circular cylinders and in tube bundles: Part 1 - The vortex street geometry of the single circular cylinder. *Journal of Engineering for Industry* **94**, 603-612.

Chen, Y. N. 1972b Fluctuating lift forces of Karman vortex streets on single circular cylinders and in tube bundles: Part 2 - Lift forces of single cylinders. *Journal of Engineering for Industry* **94**, 613-622.

Chen, Y. N. 1972c Fluctuating lift forces of Karman vortex streets on single circular cylinders and in tube bundles: Part 3 - Lift forces in tube bundles. *Journal of Engineering for Industry* **94**, 623-628.

Dwyer, H. A. and Mccroskey, W. J. 1973 Oscillating flow over a cylinder at large Reynolds number. *Journal of Fluid Mechanics* **61**(4), 753-767.

Englar, R.J. 1975 Circulation control for high-lift and drag generation on STOL aircraft. *Journal of Aircraft* **12**, 457-464.

Evangelinos, C. and Karniadakis, G. E. 1999 Dynamics and flow structures in the turbulent wake of rigid and flexible cylinders subject to vortex-induced vibrations. *Journal of Fluid Mechanics* **400**, 91-124.

Evangelinos, C., Lucor, D. and Karniadakis, G. E. 2000 DNS-derived force distribution on flexible cylinders subject to vortex-induced vibration. *Journal of Fluids and Structures* **14**, 429-440.

Feireisen, J. M., Mongomery, M. D. and Fleeter, S. 1994 Unsteady aerodynamic forcing functions: a comparison between linear theory and experiment. *Journal of Turbomachinery* **116**, 676-685.

Gerrard, J. H. 1966 The mechanics of the formation region of vortices behind bluff bodies. *Journal of Fluid Mechanics* **25**, 401- 413.

Granger, S. 1990 A new signal processing method for investigating fluidelastic phenomena. *Journal of Fluids and Structures* **4**, 73-97.

Granger, S. and Paidoussis, M. P. 1995 An improvement to the quasi-steady model with application to cross-flow induced vibration of tube arrays. *Flow-Induced Vibration* (Ed. Bearman), Balkema, Rotterdam. 339-350.

Granger, S., Campistron, R. and Lebret, J. 1993 Motion-dependent excitation mechanisms in a square in-line tube bundle subject to water cross-flow: an experimental modal analysis. *Journal of Fluids and Structures* **7**, 521-550.

Griffin, O. M. 1980 Vortex-excited cross-flow vibrations of a single cylindrical tube. *Journal of Pressure Vessel Technology* **102**, 158-166.

Griffin, O. M. and Koopmann, G. H. 1977 The vortex-excited lift and reaction forces on resonantly vibrating cylinders. *Journal of Sound and Vibration* **54**(3), 435-448.

Griffin, O. M. and Ramberg, S. E. 1974 The vortex-street wakes of vibrating cylinder. *Journal of Fluid Mechanics* **66**(3), 553-576.

Hara, F. 1989 Unsteady fluid dynamics forces acting on a single row of cylinders vibrating in a cross flow. *Journal of Fluids and Structures* **3**, 97-113.

Hasan, M. A. Z. 1989 The near wake structure of a square cylinder. *International Journal of Heat and Fluid Flow* **10**(4), 339-348.

Higuchi, H., Kim, H. J. and Farell, C. 1989 On flow separation and reattachment around a circular cylinder at critical Reynolds numbers. *Journal of Fluid Mechanics* **200**, 149-171.

Ho, C. M. and Huerre, P. 1984 Perturbed free-shear layers. *Annual Review of Fluid Fechanics* **16**, 365-424.

Hori, E. 1959 Experiments on flow around a pair of parallel circular cylinders. *Proceedings of 9th Japan National Congress for Applied Mechanics*, Tokyo, pp. 231- 234.

Hussain, A. K. M. F. 1986 Coherent Structures and Turbulence. *Journal of Fluid Mechanics* **173**, 303-356.

Ishigai, S., Nishikawa, E., Nishmura, K. and Cho, K. 1972 Experimental study on structure of gas flow in tube banks with tube axes normal to flow (Part 1, Karman vortex flow around two tubes at various spacings). *Bulletin of the JSME* **15**, 949-956.

Jadic, I., So, R. M. C and Mignolet, M. P. 1998 Analysis of fluid-structure interactions using a time-marching technique. *Journal of Fluids and Structures* **12**, 631-654.

Jendrzejczyk, J. A., Chen, S. S. and Wambsganss, M. W. 1979 Dynamic response of a pair of circular tubes subjected to liquid cross flow. *Journal of Sound and Vibration* **67**(2), 263-273.

Jin, W., Zhou, Y., Chan, P. K. C. and Xu, H. G. 2000 A fibre-optic grating sensor for the study of flow-induced vibrations. *Sensors and Actuators*. **79**, 36-45.

Kamemoto, K. 1976 Formation and interaction of two parallel vortex streets. *Bulletin of the JSME* **19**, 283-290.

Kersey, A. D., Davis, M. A., Patrick, H. J., Leblanc, M., Koo, K. P., Askins, C. G., Putnam, M. A. and Friebele, E. J. 1997 Fibre grating sensors. *Journal of Lightwave Technology* **15**, 1442-1462.

Kim, H. J. and Durbin, P. A. 1988 Investigation of the flow between a pair of circular cylinders in the flopping regime. *Journal of Fluid Mechanics* **196**, 431-448.

King, R. 1977 A review of vortex shedding research and its application. *Ocean Engineering* **4**, 141-171.

Kiya, M., Arie, M., Tamura, H. and Mori, H. 1980 Vortex shedding from two circular cylinders in staggered arrangement. *Journal of Fluids Engineering* **102**, 166-173.

Knisely, C. W. 1990 Strouhal numbers of rectangular cylinders at incidence: A review and new data. *Journal of Fluids and Structures* **4**, 371-393.

Kolář, V., Lyn, D. A. and Rodi, W. 1997 Ensemble-averaged measurements in the turbulent near wake of two side-by-side square cylinders, *Journal of Fluid Mechanics* **346**, 201-237.

Kourta, A., Boisson, H. C., Chassaing, P. and Ha Minh, H. 1987 Nonlinear interaction and the transition to turbulence in the wake of a circular cylinder. *Journal of Fluid Mechanics* **181**, 141-161.

Kumada, M., Hiwada, M., Ito, M. and Mabuchi, I. 1984 Wake interference between three circular cylinders arranged side by side normal to a flow. *Trans. JSME* **50**, 1699-1707 (in Japanese).

Landweber, L. 1942 Flow about a pair of adjacent, parallel cylinders normal to a stream. D. W. Taylor Model Basin, Department of the Navy, Report 485, Washington, D.C.

Laneville, A. and Mazouzi, A. 1995 Ovalling oscillations of cantilevered cylindrical shells in cross-flow: new experimental data. *Journal of Fluids and Structures* **9**, 729-745.

Lee, B. E. 1975 The effect of turbulence on the surface pressure field of a square prism. *Journal of Fluid Mechanics* **69**, 263-282.

Livesey, J. L. and Dye, R. C. F. 1962 Vortex excited vibration of a heat exchanger tube row. *Journal of Mechanical Engineering Science* **4**, 349-352.

Luo, S. C. and Teng, T. C. 1990 Aerodynamic forces on a square section cylinder that is downstream to an identical cylinder. *The Aeronautical Journal* **94**, 203-212.

Maekawa, T. and Mizuno, S. 1967 Flow around the separation point and in the near-wake of a circular cylinder. *Phys. Fluids Suppl.* S184.

Mei, V. C. and Currie, I. G. 1969 Flow separation on a vibrating circular cylinder. *The Physics of Fluids* **12**(11), 2248-2255.

Mendes, P. A. and Branco, F. A. 1999 Analysis of fluid-structure interaction by an arbitrary Lagrangian-Eulerian finite element formulation. *International Journal for Numerical Methods in Fluids* **30**, 897-919.

Meneghini, J. R., Saltara, F. Siqueira, C. L. R. and Ferrari, J. A. 2001 Numerical simulation of flow interference between two circular cylinders in tandem and side-by-side arrangement. *Journal of Fluids and Structures* **15**, 327-350.

Michalke, A. 1984 Survey on jet instability theory. *Progress in Aerospace Sciences* **21**, 159-199.

Mignolet, M. P. and Red-Horse, J. R. 1994 ARMAX identification of vibrating structures: model and model order estimation. *Proceedings of the 35th Structures, Structural Dynamics, and Material Conference, AIAA/ASME*, Hilton Head, South Carolina, April 18-20, 1628-1637.

Mittal, S. and Kumar, V. 1999 Finite element study of vortex-induced cross-flow and in-line oscillations of a circular cylinder at low Reynolds numbers. *International Journal for Numerical Methods in Fluids* **31**, 1087-1120.

Moretti, P. 1993 Flow-induced vibration in arrays of cylinders. *Annual Review of Fluid Mechanics* **25**, 99-114.

Naudascher, E. and Wang, Y. 1993 Flow-induced vibrations of prismatic bodies and grids of prisms. *Journal of Fluids and Structures* **7**, 341-373.

Newman, D. J. and Karniadakis, G. 1997 A direct numerical simulation study of flow past a freely vibrating cable. *Journal of Fluid Mechanics* **344**, 95-136.

Nguyen, T. D. and Naudascher, E. 1991 Vibration of beams and trashracks in parallel and inclined flows. *Journal of Hydraulic Engineering* **117**(8), 1056-1076.

Norberg, C. 1987 Effect of Reynolds number and a low-intensity freestream turbulence on the flow around a circular cylinder. *Publ.* 87/2. Dept. Applied Thermodynamics and Fluid Mechanics, Chalmers University of Technology.

Okajima, A. 1982 Strouhal numbers of rectangular cylinders. *Journal of Fluid Mechanics* **123**, 379-398.

Okamoto, S., Hirose, T. and Adachi, T. 1981 The effect of sound on the vortex-shedding from a circular cylinder. *Bulletin of the JSME* **24**, 45-53.

Ongoren, A. and Rockwell, D. 1988a Flow structure from an oscillating cylinder, Part 1: mechanisms of phase shift and recovery in the near wake. *Journal of Fluid Mechanics* **191**, 197-223.

Ongoren, A. and Rockwell, D. 1988b Flow structure from an oscillating cylinder, Part 2: mode competition in the near wake. *Journal of Fluid Mechanics* **191**, 225-245.

Paidoussis, M. P. 1982 A review of flow-induced vibrations in reactors and reactor components. *Nuclear Engineering and Design* **74**, 31-60.

Parkinson, G. 1989 Phenomena and modelling of flow-induced vibrations of bluff bodies. *Progress in Aerospace Sciences* **26**, 169-224.

Perry, A. E., Chong, M. S. and Lim, T. T. 1982 The vortex-shedding process behind two-dimensional bluff bodies. *Journal of Fluid Mechanics* **116**, 77-90.

Prandtl, L. 1976 The Mechanics of Viscous Fluid. In *Aerodynamics Theory: A General Review of Progress* (Editor: Durand, W. F.). Gloucester Mass., Peter Smith Publisher. (Republication of the work first published in 1935 by Julius Springer).

Prasad, A. and Williamson, C. H. K. 1997 The instability of the shear layer separating from a bluff body. *Journal of Fluid Mechanics* **333**, 375-402.

Price, S. J. and Paidoussis, M. P. 1989 The flow-induced response of a single flexible cylinder in an in-line array of rigid cylinders. *Journal of Fluids and Structures* **3**, 61-82.

Price, S. J., Paidoussis, M. P., Macdonald, R. and Mark, B. 1987 The flow-induced vibration of a single flexible cylinder in a rotated square array of rigid cylinders with pitch-to-diameter ratio of 2·12. *Journal of Fluids and Structures* **1**, 359-378.

Qaudflieg, H. 1977 Vortex induced load on the cylinder pair at high *Re*. *Forsch. Ing. Wes.* **43**, 9-18.

Richter, A. and Naudasher, E. 1976 Fluctuating forces on a rigid circular cylinder in confined flow. *Journal of Fluid Mechanics* **78**, 561-576.

Rockwell, D. 1983 Invited lecture: Oscillations of impinging shear layer. *AIAA Journal* **21**, 645-664.

Roshko, A. 1954 On the drag and shedding frequency of bluff cylinders. Nat. Adv. Comm. Aero., Wash., Tech. Note 3169.

Roshko, A. 1976 Structure of turbulent shear flows: A new look. *AIAA Journal* **14**, 1349-1357.

Sarpkaya, T. 1979 Vortex-induced oscillations — A selective review. *Journal of Applied Mechanics* **46**, 241-258.

Schewe, G. 1983 On the force fluctuations acting on a circular cylinder in crossflow from subcritical up to transcritical Reynolds numbers. *Journal of Fluid Mechanics* **133**, 265-285.

So, R. M. C., Liu, Y., Chan, S. T. and Lam, K. 2000a Numerical studies of a freely vibrating cylinder in a cross flow. *Journal of Fluids and Structures* (to appear).

So, R. M. C. and Savkar, S. D. 1981 Buffeting forces on rigid circular cylinders in cross flows. *Journal of Fluid Mechanics* **105**, 397-425.

So, R. M. C., Zhou, Y. and Liu, M. H. 2000b Free vibrations of an elastic cylinder in a cross flow and their effects on the near wake. *Experiments in Fluids* **29**, 130-144.

Spivac, H. M. 1946 Vortex frequency and flow pattern in the wake of two parallel cylinders at varied spacing normal to an air stream. *Journal of the Aeronautical Sciences* **13**, 289-301.

Sumner, D., Wong, S. S. T., Price, S. J. and Paidoussis, M. P. 1999 Fluid behaviour of side-by-side circular cylinders in steady cross-flow. *Journal of Fluids and Structures* **13**, 309-338.

Sumner, D., Price, S. J. and Païdoussis, M. P. 2000 Flow-pattern identification for two staggered circular cylinders in cross-flow. *Journal of Fluid Mechanics* **411,** 263-303.

Trethewey, M. W., Sommer, H. J. and Cafeo, J. A. 1993 A dual beam laser vibrometer for measurement of dynamic structural rotations and displacemnents. *Journal of Sound and Vibration* **164**, 67-84.

Vickery, B. J. 1966 Fluctuating lift and drag on a long cylinder of square cross-section in a smooth and in a turbulent stream. *Journal of Fluid Mechanics* **25**(3), 481-494.

Wang, X. Q., So, R. M. C. and Liu, Y. 2001 Flow-induced vibration of an Euler-Bernoulli beam. *Journal of Sound and Vibration* (to appear).

Weaver, D. S. and Abd-Rabbo, A. 1984 A flow visualization study of a square array of tubes in water cross-flow. *Proceedings Symposium on Flow-Induced Vibrations,* Vol. 2 (Editors: Paidoussis, M. P., Au-Yang, M. K. & Chen, S. S.), pp. 165-177.

Weaver, D. S. and Fitzpatrick, J. A. 1988 A review of cross-flow induced vibrations in heat exchanger tube arrays. *Journal of Fluids and Structures* **2**, 73-93.

Weaver, W., Timoshenko, S. P. and Young, D. H. 1989 *Vibration Problems in Engineering. Fifth edition.* John Wiley & Sons, Inc. pp. 54-55, 366, 426-432 & 454-456.

Weaver, D. S. and Yeung, H. C. 1984 The effect of tube mass on the flow induced response of various tube arrays in water. *Journal of Sound and Vibration* **93**, 409-425.

Wei, T and Smith, C. R. 1986 Secondary vortices in the wake of circular cylinders. *Journal of Fluid Mechanics* **169**, 513-533.

West, G. S. and Apelt, C. J. 1997 Fluctuating lift and drag forces on finite lengths of a circular cylinder in the subcritical Reynolds number range. *Journal of Fluids and Structures* **11**, 135-158.

Williamson, C. H. K. 1985 Evolution of a single wake behind a pair of bluff bodies. *Journal of Fluid Mechanics* **159**, 1-18.

Williamson, C. H. K. and Roshko, A. 1988 Vortex formation in the wake of an oscillating cylinder. *Journal of Fluids and Structures* **2**, 355-381.

Winant, C. D. and Browand, F. K. 1974 Vortex pairing, the mechanism of turbulent mixing layer growth at moderate Reynolds number. *Journal of Fluid Mechanics* **63**, 237- 255.

Xu, S. J., Zhou, Y. and So, R. M. C. 2001 Theoretical analysis of the structural dynamics of a cylinder in a cross flow. *Journal of Fluids and Structures.* (Submitted).

Yiu, M.W., Zhou, Y. and Zhang, H. J. 2001 Flow Topology and Heat Transport in a Turbulent Two-Cylinder Wake, *Turbulence and Shear Flow Phenomena-2,* Stockholm. (Accepted).

Zdravkovich, M. M. 1977 Review of flow interference between two circular cylinders in various arrangements. *Journal of Fluids Engineering* **99,** 618-633.

Zdravkovich, M. M. 1984 Classification of flow-induced oscillations of two parallel circular cylinders in various arrangements. *Symposium on flow-induced vibrations*, Vol.2, pp. 1-18.

Zdravkovich, M. M. 1985 Flow-induced oscillations of two interfering circular cylinders. *Journal of Sound and Vibration* **101**, 511-521.

Zdravkovich, M. M. 1987 The effects of interference between circular cylinders in cross flow. *Journal of Fluids and Structures* **1**, 239-261.

Zdravkovich, M. M. and Pridden, D. L. 1977 Interference between two circular cylinders; series of unexpected discontinuities. *Journal of Industrial Aerodynamics* **2**, 255-260.

Zhang, H. J. and Zhou, Y. 2001 Effect of unequal cylinder spacing on vortex streets behind three side-by-side cylinders. *Physics of Fluids* (submitted).

Zhang, H. J., Zhou, Y. and Antonia, R. A. 2000 Longitudinal and spanwise vortical structures in a turbulent near wake. *Physics of Fluids* **12**(11), 2954-2964.

Zhou, C. Y., So, R. M. C. and Lam, K. 1999a Vortex-induced vibrations of an elastic circular cylinder. *Journal of Fluids and Structures* **13**, 165-189.

Zhou, C. Y., So, R. M. C. and Mignolet, M. P. 2000a Fluid damping of an elastic cylinder in a cross-flow. *Journal of Fluids and Structures* **14**, 303-322.

Zhou, Y. and Antonia, R. A. 1992 Convection velocity measurements in a cylinder wake. *Experiments in Fluids* **13,** 63-70.

Zhou, Y. and Antonia, R. A.1993 A study of turbulent vortices in the wake of a cylinder. *Journal of Fluid Mechanics* **253**, 643-661.

Zhou, Y. and Antonia, R. A. 1994 Effect of initial conditions on structures in a turbulent near-wake. *AIAA Journal,* **32,** 1207-1213.

Zhou, Y., Antonia, R.A. and Tsang, W.K. 1998 The effect of the Reynolds number on a turbulent far-wake. *Experiments in Fluids* **25**, 118-125.

Zhou, Y., So, R. M. C., Jin, W., Xu, H. G. and Chan, P. K. C. 1999b Dynamic strain measurements of a circular cylinder in a cross flow using a fibre Bragg grating sensor. *Experiments in Fluid*, **27,** 359 - 367.

Zhou, Y., So, R. M. C., Liu, M. H. and Zhang, H. J. 2000b Complex turbulent wakes generated by two and three side-by-side cylinders. *International Journal of Heat and Fluid Flow* **21,** 125-133.

Zhou, Y., Wang, Z. J., So, R. M. C., Xu, S. J. and Jin, W. 2001 Free vibrations of two side-by-side cylinders in a cross-flow. *Journal of Fluid Mechanics* (In press).

Ziada, S. and Staubli, T. (Editors) 2000 *Flow-Induced Vibration.* A. A. Balkema, Rotterdam, Netherlands.

Appendix:

List of Publications Already Published, Accepted or Submitted

Refereed Journals:

Wang, Z. J. and Zhou, Y. 2001 Vortex streets behind two side-by-side cylinders. *Journal of Fluid Mechanics* (Submitted).

Wang, Z. J., Zhou, Y. and Li, H. 2001 Flow-visualization of a two side-by-side cylinder wake. *International Journal of Flow Visualization and Image Processing* (In press).

Wang, Z. J., Zhou, Y and So, R. M. C. 2001 Vortex-induced vibration characteristics of two fix-supported elastic cylinders. *Journal of Fluids and Structures* (Submitted).

Wang, Z. J., Zhou, Y., So, R. M. C. and Jin, W. 2000 Flow separation effect on a freely vibrating cylinder. *Journal of Fluids and Structures* (submitted).

Zhou, Y., Wang, Z. J., So, R. M. C., Xu, S. J. and Jin, W. 2001 Free vibrations of two side-by-side cylinders in a cross flow, *Journal of Fluid Mechanics* **443**, 197 - 229.

Refereed conference proceedings:

Wang, Z. J. and Zhou, Y. 2001 Incidence angle effects on effective damping of square cylinder in a cross flow. 2001 *ASME Fluids Engineering Division Summer*

Meeting, New Orleans, Louisiana, May 29- June 1, Paper no. FEDSM2001-18142.

Wang, Z. J., Zhou, Y., So, R. M. C. and Jin, W. 2000 An experimental study of dynamics of a square cylinder in a cross-flow using optical fibre Bragg grating sensors. 2000 *ASME Fluids Engineering Division Summer Meeting*, Boston, Massachusetts, June 11 - 15. Paper No. FEDSM00-11039.

Zhang, H. J., Zhou, Y., So, R. M. C., Mignolet, M. P. and Wang, Z. J. 2000 Measurement of fluid and structural damping using an ARMA technique. *Proceedings of International Conference on Advances in Structural Dynamics,* Vol. 2, pp. 1109-1116. Hong Kong.

Zhou, Y., So, R. M. C., Wang, Z. J. and Jin, W. 2000 Free vibrations of two side-by-side cylinders in a cross-flow. *7th International Conference on Flow Induced Vibrations, FIV 2000*, Lucerne, Switzerland, 19-21 June 2000.